Characterisation of VUV-sensitive Silicon Photomultipliers for the $0\nu\beta\beta$ experiment nEXO

der naturwissenschaftlichen Fakultät
der Friedrich-Alexander-Universität Erlangen-Nürnberg
zur

Erlangung des Doktorgrades Dr. rer. nat.

vorgelegt von

Michael Thomas Wagenpfeil
aus Fürth

ECAP-2020-006

Characterisation of VUV-sensitive Silicon Photomultipliers for the $0\nu\beta\beta$ experiment nEXO

Charakterisierung VUV-sensitiver Silicon Photomultiplier für das $0\nu\beta\beta$ Experiment nEXO

der naturwissenschaftlichen Fakultät
der Friedrich-Alexander-Universität Erlangen-Nürnberg
zur

Erlangung des Doktorgrades Dr. rer. nat.

vorgelegt von

Michael Wagenpfeil
aus Fürth

Als Dissertation genehmigt

von der naturwissenschaftlichen Fakultät
der Friedrich-Alexander-Universität Erlangen-Nürnberg

Tag der mündlichen Prüfung: 25.03.2021

Vorsitzender des Promotionsorgans: Prof. Dr. Wolfgang Achtziger

Gutachter/in: Prof. Dr. Gisela Anton
Prof. Dr. Christian Weinheimer

Mündliche PrüferInnen: Prof. Dr. Gisela Anton
Prof. Dr. Stefan Funk
Prof. Dr. Michael Schmiedeberg

Abstract

Silicon Photomultipliers are pixelated semiconductor photosensors with single photon resolution and are regarded as very promising technology to construct next-generation, cutting-edge detectors for low-background experiments in astroparticle physics. The energy resolution for any particle interaction that occur in the detector is a crucial parameter of such experiments and depends on the capability of the detector to collect as much scintillation light from the events as possible. The detector needs to be designed thoroughly to maximise the light yield and the optical behaviour of the Silicon Photomultipliers in the detector medium plays a key part in detector simulations.

This work presents extensive reflectivity studies with Silicon Photomultipliers and other samples in liquid xenon at vacuum ultraviolet wavelengths. A dedicated setup at the University of Münster has been used that allows to acquire angular reflection spectra of various samples immersed in liquid xenon with 0.45° resolution. The reflectivity is determined to 25–36 % at an angle of incidence of 20° for the four samples investigated in this work. The reflectivity increases with angle of incidence for all samples but one. The highest reflectivity was measured for a wafer sample with 70 % at 76°.

This work also reports on the determination of basic Silicon Photomultiplier properties via diode IV-characteristics investigated at different temperatures. Such characteristics can also be used to establish a method to use Silicon Photomultipliers as direct sensors for the very own pn-junction temperature.

Contents

1. Introduction

The work presented in this thesis has been performed within the nEXO collaboration which plans to operate a 5 tonne liquid xenon detector to search for the neutrinoless double beta decay of ^{136}Xe. The neutrinoless double beta decay is a hypothetical second-order weak transition that is only possible in case the neutrino is its own antiparticle. The Standard Model of particle physics comprises no such Majorana fermions so a potential discovery would infer physics beyond the Standard Model. This makes this decay particularly interesting. Its potential discovery is highly difficult due to the extreme half-life of second-order weak interactions. The current half-life limit is roughly 10^{16} times larger than the age of the universe. In nEXO, only a handful of events are expected in one tonne of xenon per year. One decisive detector property is the energy resolution of nEXO which is closely correlated to the efficiency to collect the liquid xenon scintillation photons released during particle interactions. nEXO is designed to maximise this collection efficiency based on extended optical simulations of the detector geometry.
The light collection efficiency depends strongly on the optical properties of the Silicon Photomultipliers (SiPMs) operated as scintillation photon sensors in nEXO. Knowing their angular reflectivity is of paramount interest since any reflected photons may be detected by another SiPM within the detector. Any photons that are not absorbed by one SiPM without generating a signal therefore get a second chance to be detected. The detector geometry has to be optimised accordingly so that reflected photons interact as little as possible with any non-SiPM components. Precise knowledge of the SiPM reflectivity is essential to perform these optimisations and run extended detector simulations to improve the event reconstruction.
SiPMs are one of the most promising photosensors developed within the last decades. SiPMs are pixelated semiconductor sensors that achieve single photon resolution via avalanche breakdown in the Geiger operation mode. Unlike photomultiplier tubes, SiPMs offer a compact geometry, low operation voltage and work in magnetic fields. Despite their size below $1\,\mathrm{cm}^2$, the decreasing market price and the possibility to connect SiPMs in photo-sensitive tiles allow for a high scalability of SiPM based photo-detecting systems. The high internal gain provides low noise levels at low temperatures. The photo detection efficiency of current SiPM models exceeds 60 % and first SiPMs with reasonable efficiency for ultraviolet photons became available recently. For these reasons, SiPMs increasingly replace older photosensors while further research and technological improvements are still on the way.

SiPMs are particularly interesting for liquid noble gas based, low-background experiments e.g. for neutrinoless double beta decay experiments as nEXO or for dark matter searches. Liquid noble gas detectors benefit from the excellent chemical and physical properties of the noble gases. Advantages of liquid noble gases are – among others – the easy chemical application, the chemical stability, the well-understood energy deposition process of energetic particles and – for xenon – the high density and stopping power. Liquid noble gas detectors require photosensors capable of being operated within the cryogenic medium. Photosensors also have to be sensitive for the deep ultraviolet scintillation light emitted by liquid noble gases if penetrated by energetic particles. UV-sensitive SiPMs fulfil both requirements. Low-background experiments must avoid significant radioactive contaminations in the detector whose decays may produce signals that are undistinguishable of the events the experiment is looking for. This can severely affect the sensitivity of such experiments and with it the discovery potential for new physics. Liquid argon and xenon are suitable detector materials due to the absence of long-lived radionuclides. The possibility to produce SiPMs from extremely radiopure materials makes them ideal photosensors for low-background experiments. Several experiments already operate or plan to operate large-scale SiPM-based photo-detectors in liquid noble gases and significant pioneering work has been accomplished recently.
This work presents results from the first reflectivity studies with ultraviolet-sensitive SiPMs in liquid xenon. The studies have been performed with a dedicated reflection setup at the University of Münster. A synopsis of the setup components, an overview of the mathematical framework to describe the angular reflection spectra, investigations of sources of systematic uncertainties and the results obtained with various reflection samples are presented in chapter 3. The results are of great interest to perform precise optical simulations of the planned nEXO detector.
Chapter 4 focuses on the investigation of SiPM IV-characteristics. nEXO will require tens of thousands single SiPM dies for its photo-detector and all of them need to be examined individually prior to being employed. A fast method to check the uniformity of all SiPMs is necessary to perform such examinations in a reasonable time frame. IV-characteristics allow to examine various SiPM properties with a simple setup and at arbitrary temperatures. A mathematical model of a SiPM is established to fit IV-characteristics and deduce several parameters of the investigated SiPMs. Additionally, a method to use SiPMs as direct sensors for the temperature of their pn-junction is developed and explored experimentally.
Before, chapter 2 gives an overview of the theoretical background of the topics related to the presented studies. The background comprises an explanation of neutrinoless double beta decay and the experimental difficulties of its discovery, an overview of nEXO and its physics goals, a summary of the properties of liquid xenon as detector material and a brief review on the working principle of SiPMs.

2. Theoretical background

Table of contents:

The following chapter provides an overview of the physic background relevant for the topics discussed in this work. Section 2.1 explains the nature of the hypothetical neutrinoless double beta decay and highlights the experimental requirements to discover this transition. Section 2.2 focuses on the detector and physics goals of the nEXO-experiment which motivated the studies presented in this work. The

properties of liquid xenon as a detector material are discussed in section 2.3 along with the scintillation process after penetration with charged particles. Finally, section 2.4 gives an overview of Silicon Photomultipliers with an emphasis on the physics of avalanche breakdown in reverse-biased solid state detectors and the detection of ultraviolet photons in such devices.

2.1. Neutrinoless double beta decay

Double beta decay are very rare, second order weak interaction processes whose half-lives are several orders of magnitude larger than the age of the universe. This transition is energetically allowed for only 35 nuclides and has been observed directly or via geochemical measurements for about half of these [302]. Double beta decay is consistent with the Standard Model (SM) of particle physics however the hypothetical neutrinoless double beta decay is not. Its discovery would imply new physics and has the potential to explain some mysteries of the universe e.g. the matter-antimatter-asymmetry.
The following pages can only give a short introduction of the complex nature of double beta decays. More information can be found in several reviews about (neutrinoless) double beta decays focusing on theory and phenomenology [61, 75, 149, 244], the connection to neutrino physics [263] or the experimental sensitivity [148]. A recent brief review of current experimental searches can be found in [236] while the discovery potential of such experiments is discussed in [11].

2.1.1. Double beta decay phenomenology

A double beta decay can occur if a regular single beta decay is forbidden by energy conservation but two beta decays result in a nucleus with a smaller mass than the parent nucleaus. This is schematically shown in figure 2.1.
Phenomenologically, in a $\beta^-\beta^-$-decay, a nucleus X with mass number A and proton number Z decays to a nucleus Y with A and $Z+2$ with the emission of two electrons and two electron-antineutrinos (compare to fig. 2.3):

$$ {}^{A}_{Z}\mathrm{X} \rightarrow {}^{A}_{Z+2}\mathrm{Y} + 2\,\mathrm{e}^- + 2\,\bar{\nu}_\mathrm{e} \tag{2.1} $$

This decay is also known as the neutrino-accompanied double beta ($2\nu\beta^-\beta^-$)-decay to distinguish it from the neutrinoless alternative explained below. In the neutrino-accompanied mode, the neutrons undergoing the transition are uncorrelated but decay simultaneously [149]. Besides this process, other similar, SM-conform decays as double positron decay ($2\nu\beta^+\beta^+$), double electron capture (2νECEC) or mixtures as $2\nu\beta^+$EC decays have been either observed or proclaimed. Experimental studies are performed for several of these channels however the $2\nu\beta^-\beta^-$-decay remains

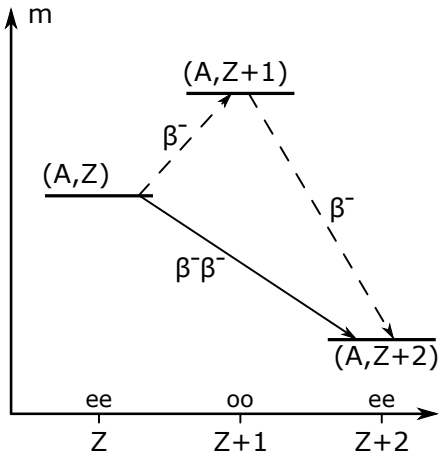

Figure 2.1.: Energy level diagram of a $\beta^-\beta^-$ transition from A,Z to A,Z+2.

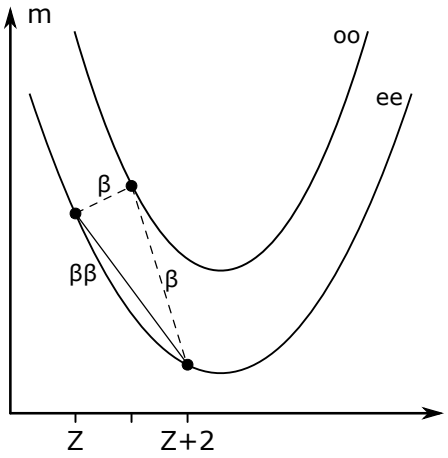

Figure 2.2.: $\beta\beta$-decay in the Weizsäcker mass parabola interpretation.

the most prominent variant with the lowest half-lives. 88 nuclides are known to be theoretically able to undergo second order weak interactions but only 35 of them undergo $2\nu\beta^-\beta^-$-decay [302].
All $\beta\beta$ nuclides have even proton and neutron numbers (ee-nuclei) and an even nucleon number A [302]. For even A systems, the pairing term of the Weizäcker mass formula generates different mass parabolas for ee- and oo-nuclei [74]. Any β-decay implies a change between these two parabolas as shown in in figure 2.2. This can cause the very situations, where the single-β-daughter nucleus has more mass and only $\beta\beta$-decays are possible.
The released decay energy (Q-value) is shared as kinetic energy among the electrons and antineutrinos. The recoil energy of the daughter nucleus can be neglected. The observable shape of the $2\nu\beta^-\beta^-$ energy spectrum is continuous spanning from 0 to the Q-value and peaked below $Q/2$ [149] ((1) in figure 2.5).
The $\beta\beta$ process currently holding the record for the longest half-life ever measured is the double electron capture of ^{124}Xe with $T_{1/2}^{2\nu\mathrm{ECEC}} = (1.8\pm0.5\pm0.1)\times10^{22}$ yr [45]. The $2\nu\beta^-\beta^-$-decay has only been observed – either directly or geochemically – in about 16 nuclides with half-lives spanning from 10^{18} to 10^{21} yr [302]. Some of these nuclides are listed in table 2.1. In the following, $2\nu\beta\beta$ is equivalent to $2\nu\beta^-\beta^-$.

While the $2\nu\beta\beta$-decay is perfectly explained by weak interaction, the hypothetical neutrinoless double beta ($0\nu\beta\beta$) decay would violate the Standard Model for several reasons. In a neutrinoless $\beta\beta$-decay, two neutrons decay to two protons with only two electrons in the final state (compare to fig. 2.4):

$$ {}^{A}_{Z}\mathrm{X} \rightarrow {}^{A}_{Z+2}\mathrm{Y} + 2\,\mathrm{e}^- \tag{2.2} $$

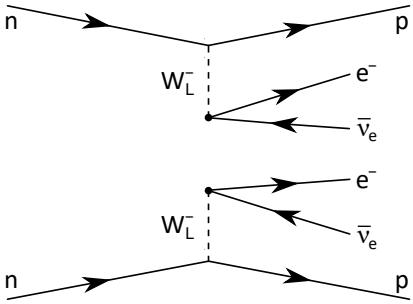

Figure 2.3.: Feynman diagram of the double beta ($2\nu\beta^-\beta^-$) decay.

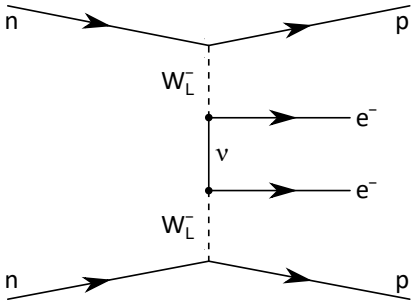

Figure 2.4.: Feynman diagram of the neutrinoless mode ($0\nu\beta^-\beta^-$).

This process is only possible, if massive Majorana neutrinos exist and lepton number conservation is violated. Since the Standard Model regards the neutrino as massless Dirac-particle, any observation of $0\nu\beta\beta$-decays would automatically imply new physics beyond the Standard Model. $0\nu\beta\beta$-decay is the most practical way to test the possible Majorana-nature of the neutrino.
$0\nu\beta\beta$-decays can be distinguished experimentally from $2\nu\beta\beta$-decay events only via the sum energy of the emitted electrons. In $0\nu\beta\beta$-decay, the spectrum is a single δ-peak at the Q-value ((2) in fig. 2.5) since no kinetic energy is carried away by any neutrinos [272]. The current half-life limits for $0\nu\beta\beta$-decays are more than 5 orders of magnitude higher than for the corresponding $2\nu\beta\beta$-decay. As a consequence, the $0\nu\beta\beta$ energy spectrum is very tiny in comparison. One of the main challenges for any $\beta\beta$-experiment therefore is to achieve a good enough energy resolution to identify the $0\nu\beta\beta$-peak in the end point spectrum of the $2\nu\beta\beta$-decay, which is always a background component that cannot be suppressed by any means.
Besides $0\nu\beta\beta$-decay all other $\beta\beta$-like processes mentioned above can be hypothetically neutrinoless as well however with significantly larger half-lives. $0\nu\beta\beta$-decay therefore presents the best discovery probability among all neutrinoless processes. Still, other $\beta\beta$-transitions are investigated including highly exotic transitions as neutrinoless quadruple beta decay [53].

2.1.2. Neutrinoless double beta decay mechanism

There are plenty of theories for physics beyond the Standard Model. Several mechanisms may lead to the lepton number violation required for $0\nu\beta\beta$-decays. Three of these mechanism are shown in figure 2.6. The so-called m_ν-mechanism on the left requires a non-zero neutrino mass. A right-handed anti-neutrino is emitted in the β^--decay at the upper vertex, a helicity flip occurs and it is absorbed as a left-handed neutrino at the lower vertex. The probability of this transition

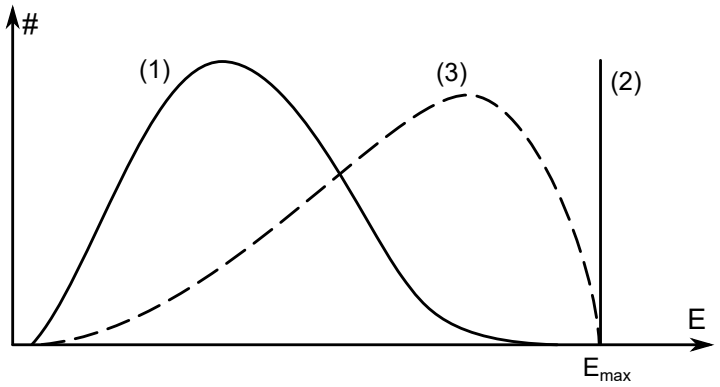

Figure 2.5.: Schematic energy spectrum of a neutrino accompanied $2\nu\beta\beta$-decay (1), a neutrinoless $0\nu\beta\beta$-decay via Majorana neutrino helicity flip (2) and a neutrinoless $0\nu\beta\beta$-decay under emission of a hypothetical Majoron (3). Redrawn from [272].

scales with the small fraction of opposite chirality in the anti-neutrino spinor, that is present in all particles with non-zero rest mass. This means, the 0ν-coupling constant depends on the neutrino mass.
The second mechanism in the middle requires a non-zero weak coupling constant to right-handed currents. No helicity flip occurs but the interaction at one vertex happens via the exchange of a right handed W_R. The 0ν-coupling depends on the right handed weak coupling strength. The last mechanism postulates the emission of a hypothetical Majoron M^0. While all scenarios show a different interaction model on particle level, they all have in common: if $0\nu\beta\beta$-decay is observed experimentally it always implies Majorana neutrinos and new physics. This is called the *black box theorem* or Schechter-Valle theorem [269].
Neither right handed weak currents nor M^0 particles have not been observed yet. However, we know from the observation of neutrino oscillations that neutrinos have small, but non-zero rest masses which is in conflict with the Standard Model [76, 125, 137, 284]. The neutrino sector and specifically any process requiring massive neutrinos therefore is prone to require physical mechanisms beyond the Standard Model what makes the m_ν-mechanism with a light neutrino exchange the most interesting to elaborate. In this mechanism, an effective Majorana neutrino mass $m_{\beta\beta}$ is defined as:

$$m_{\beta\beta} \equiv \left| \sum_{i=1}^{3} U_{ei}^2 \, m_i \right| \tag{2.3}$$

where U_{ei} are elements of the PMNS-matrix [204]. $m_{\beta\beta}$ depends on the values of the neutrino mass eigenstates m_i (i=1,2,3) and the neutrino mixing angles θ_{12}, θ_{23} and θ_{13}. It also depends on one Dirac-phase and two Majorana phases α_{21} and

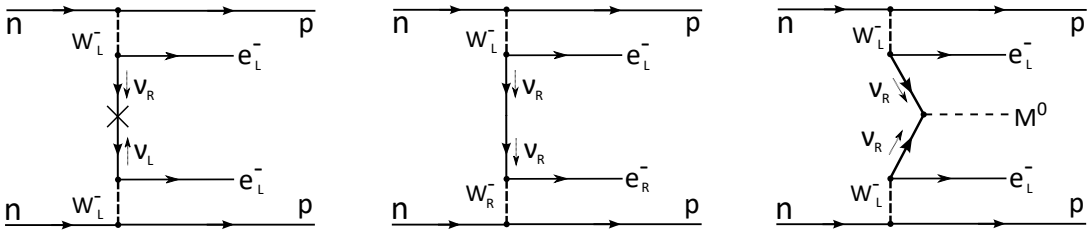

Figure 2.6.: Different potential $0\nu\beta\beta$-mechanisms [272]. Left: m_ν-mechanism allowing a neutrino-antineutrino-transition; Middle: RHC-mechanism with right-handed weak coupling; Right: M^0-meachnism with emission of a hypothetical Majoron.

α_{31} as contained in the extended PMNS-matrix (including the possibility of light Majorana neutrinos). $m_{\beta\beta}$ is the effective mass that governs the opposite helicity fraction in the m_ν-mechanism and thus the probability of the $0\nu\beta\beta$-decay. This probability can be expressed in terms of a half-life $T^{0\nu}_{1/2}$ via:

$$(T^{0\nu}_{1/2})^{-1} = G_{0\nu}(Q_{\beta\beta}, Z) \cdot |\mathcal{M}_{0\nu}|^2 \cdot m^2_{\beta\beta} \tag{2.4}$$

where the phase-space factor $G_{0\nu}$ depends on both Z of the specific nuclide and the Q-value $Q_{\beta\beta}$. $|\mathcal{M}_{0\nu}|$ is the dimensionless nuclear matrix element (NME) for the transition from the initial (A,Z) to the daughter nucleus (A,Z+2) [148]. While $G_{0\nu}$ can be calculated exactly for any nuclide, $|\mathcal{M}_{0\nu}|$ depends on a specific nucleon model. This leads to large systematic uncertainties in the experimental sensitivity to $m_{\beta\beta}$ [122, 149]. Phase-space values for the most common $\beta\beta$-nuclides are listed in table 2.1 and nuclear matrix mixing element calculations are shown in figure 2.9.

2.1.3. Consequences of neutrinoless double beta decay

The observation of $0\nu\beta\beta$-decay would open another window to physics beyond the Standard Model. It implies the Majorana-nature of the neutrino and proves the existence of Majorana fermions. Additionally, if the values of the neutrino mass eigenstates are known from other experiments, the combination with $m_{\beta\beta}$ derived from $0\nu\beta\beta$-experiments would yield information about the potentially CP-violating phases in the PMNS-matrix.
The measurement of the $0\nu\beta\beta$ half-life also sheds light on the neutrino mass hierarchy i.e. the ordering of the individual neutrino mass eigenstates. In the normal hierarchy, the neutrino mass ordering is m_1, m_2, m_3 and the lightest two mass eigenstates have the smallest mass separation. In the inverted hierarchy, the ordering is m_3, m_1, m_2 and the two most massive eigenstates have the smallest separation. Both scenarios are shown in figure 2.7. The allowed regions for $m_{\beta\beta}$ are shown in dependence of the lightest neutrino mass eigenstate m_l. The regions

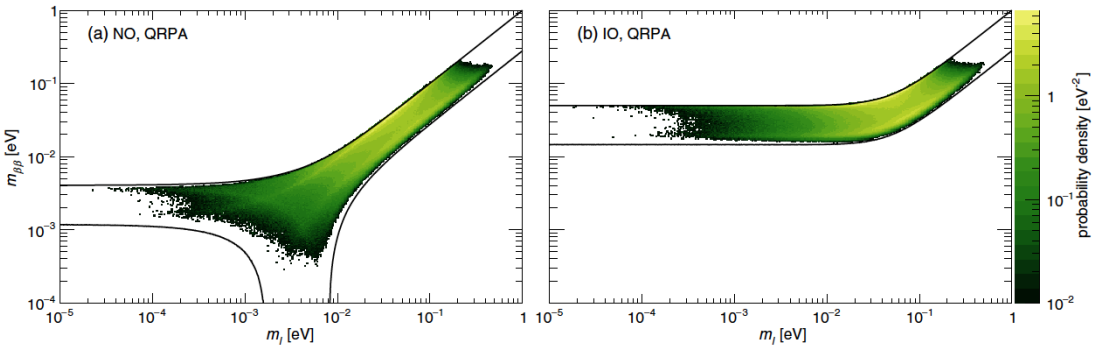

Figure 2.7.: Allowed 3σ parameter space for the Majorana neutrino mass $m_{\beta\beta}$ in dependence on the lightest neutrino mass m_l [11]. The normal hierachy (ordering) is shown on the left (a), the inverted on the right (b). The nuclear matrix elements are calculated assuming the Quasiparticle Random Phase Approximation (QRPA) model. The colour scale indicates the probability density of the $m_{\beta\beta}$ combinations.

are not populated uniformily but represent the density of possible combinations of m_i based on equation 2.3. The hierarchies are quasi-degenerate above 100 meV but split up below. The current limits on the sum of all neutrino masses $\sum m_\nu$ is about 0.3 eV [9]. As a consequence, $m_{\beta\beta}$ is mostly independent on m_l for the inverted hierarchy and proportional to m_l in the normal hierarchy if $m_l \gtrsim 10$ meV.
$0\nu\beta\beta$-experiments reach out to measure the half-life $T^{0\nu}_{1/2}$ of the given $0\nu\beta\beta$-decay. The determined half-life limit can be converted to an upper limit in the physical observable $m_{\beta\beta}$ shrinking down the allowed parameter space from the top in the hierarchy plots. The measurement of the $0\nu\beta\beta$-decay half-life therefore not only yield information about the absolute neutrino mass scale, it could also allow to rule out one of the hierarchy scenarios. For example, if a given experiment is sensitive enough to cover the entire parameter space of the inverted hierarchy but fails to detect any $0\nu\beta\beta$-decay event, the normal hierarchy must be realised in nature given that the neutrino is a Majorana particle. On the other side, if the decay has been detected, the distinction cannot be made without further cuts on m_l or $\sum m_\nu$ due to the degeneration of both hierarchies at large Majorana neutrino masses.
Another question is why neutrino masses are so small compared to the masses of the charged fermions. The answer can be the so-called *Sew-Saw mechanism* that adds a right-chiral neutrino field to the Standard Model Lagrangian. As a consequence, neutrinos become Majorana particles with three generations of light, active neutrinos and one additional heavy neutrino around several MeV that does not participate in the weak interaction (sterile neutrino) [149]. This simple mechanism not only introduces massive Majorana neutrinos with only small extensions to the Standard Model, it could also explain a much more profound problem. If heavy neutrinos are their own anti-particles, they can decay into light

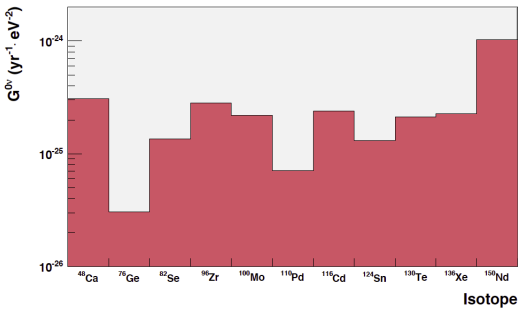

Figure 2.8.: $0\nu\beta\beta$-decay phase space factors $G_{0\nu}$ of various $\beta\beta$-nuclides [149]. The values are calculated in units of the electron mass squared. The y-axis is logarithmic.

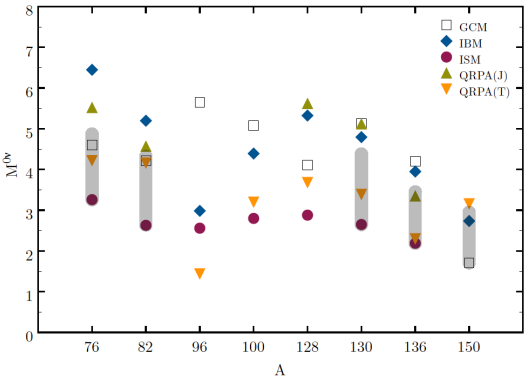

Figure 2.9.: NMEs for $0\nu\beta\beta$-nuclides calculated with different nucleus models [148]. The spread in the experimental limits on $m_{\beta\beta}$ originates from the uncertainty on the NME.

leptons plus a Higgs-particle with $l_\alpha\,\Phi$ or $\bar{l}_\alpha\,\bar{\Phi}$ in the final state. An asymmetry in both decay channels would lead to an asymmetry in the lepton sector and a net leptogenesis during the inflationary epoch of the evolution of the universe. Since the lepton and baryon sector are coupled via *sphaleron processes*, such lepton-generating mechanisms may explain the observable matter-antimatter asymmetry [116, 149].

2.1.4. Neutrinoless double beta decay experiments

There are various $0\nu\beta\beta$-experiments in operation, construction and planning. These kind of experiments have to care about several key properties.
First, there are 35 nuclides known to undergo $0\nu\beta\beta$-decay [302] but only a couple of them can be used in a large-scale detector. The 9 most commonly used nuclides are listed in table 2.1. The choice of the nuclide is a trade-off between several advantageous or problematic characteristics of each nuclide. An ideal nuclide has a large Q-value to reduce background and a high natural abundance. Since $2\nu\beta\beta$-decays present a non-suppressible background component, a large half-life $T^{2\nu}_{1/2}$ is desirable. Additionally, according to equation 2.4, large phase-space factors $G^{0\nu}$ and NMEs are preferable (see figures 2.8 and 2.9). There is no ideal nuclide for $0\nu\beta\beta$-decay search as table 2.1 shows. Beyond nuclear physics characteristics, it is also important to account for the scalability and extraction possibilities of the material, the possibility to enrich the detector material in the $\beta\beta$-isotope, its robustness to external background radiation, its chemical stability and of course the availability on the world market. All this considered, ^{76}Ge and ^{136}Xe are the most interesting nuclides for large-scale, next-generation $0\nu\beta\beta$-experiments.

Nucl.	Q-value (keV)	Abund.	$T^{2\nu}_{1/2}$ (yr)	$[G_{0\nu}]^{-1}$ (yr eV^2)	$T^{0\nu}_{1/2}$ lim. (yr)	References
^{48}Ca	4271	0.187 %	$(4.4^{+0.6}_{-0.5})\times10^{19}$	4.10×10^{24}	5.8×10^{22}	[99], NEMO-3 [303]
^{76}Ge	2039.006(50)	7.61 %	$(1.65^{+0.14}_{-0.12})\times10^{21}$	4.09×10^{25}	8.0×10^{25}	[121], GERDA [13]
^{82}Se	2995.8(15)	8.73 %	$(9.2\pm0.7)\times10^{19}$	9.27×10^{24}	2.4×10^{24}	[232], CUPID-0 [63]
^{96}Zr	3356.097(86)	2.80 %	$(2.3\pm0.2)\times10^{19}$	4.46×10^{24}	9.2×10^{21}	[17], NEMO-3 [69]
^{100}Mo	3034.40(17)	9.63 %	$(7.1\pm0.4)\times10^{18}$	5.70×10^{24}	1.1×10^{24}	[250], NEMO-3 [49]
^{116}Cd	2813.50(13)	7.49 %	$(2.87\pm0.13)\times10^{19}$	5.28×10^{24}	2.2×10^{23}	[251], Aurora [68]
^{130}Te	2526.97(23)	34.08 %	$(6.9\pm1.3)\times10^{20}$	5.89×10^{24}	1.5×10^{25}	[251], CUORE [29]
^{136}Xe	2458.10±0.31	8.87 %	$(2.19\pm0.06)\times10^{21}$	5.52×10^{24}	1.07×10^{26}	KamLAND-Zen [142]
^{150}Nd	3371.38(20)	5.6 %	$(8.2\pm0.9)\times10^{18}$	1.25×10^{24}	2.0×10^{22}	[184], NEMO-3 [51]

Table 2.1.: List of the most important ββ nuclides used in current experiments. Q-values (except for ^{136}Xe; see section 2.2.1) and current best 0νββ limits are taken from the references in the last column. Natural abundances are taken from [199], 2νββ half-lives from [66]. The phase space factors $G^{0\nu}$ are taken from [315]. Unlike in figure 2.9, the table lists the inverted values since $T^{0\nu}_{1/2}$ scales with $[G_{0\nu}]^{-1}$.

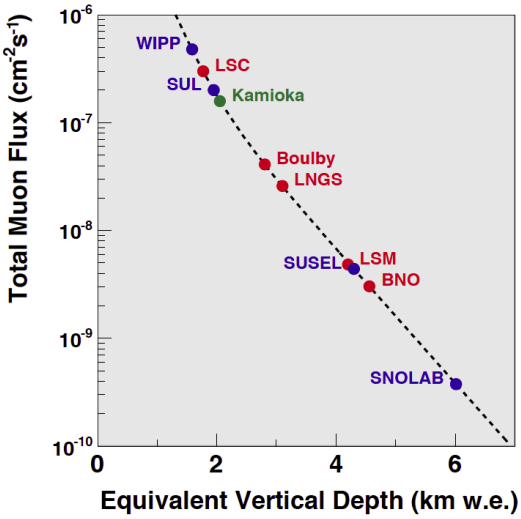

Figure 2.10.: Total muon flux in underground labratories for particle physics over their vertical depth in kilometer water equivalents [149]. Muon induced background can be critical in low-background experiments so detectors greatly benefit from the reduced total muon flux if operated deep underground.

Secondly, the energy resolution ΔE is a crucial feature when it comes to suppressing external and internal background. In particular, $2\nu\beta\beta$-events cannot be reduced through thorough radioassay studies but only distinguished via the sum energy of the two emitted electrons near the Q-value. The energy resolution strongly depends on the detector type and geometry. $0\nu\beta\beta$-experiments operating scintillation detectors with ^{136}Xe as EXO-200 [37] have a poor resolution compared to semiconductor-diodes using ^{76}Ge as GERDA [13] or bolometers using ^{130}Te as CUORE [28]. The choice of the $\beta\beta$-nuclide goes hand in hand with any intended detector design.

At last, the background contribution b is decisive for $0\nu\beta\beta$-decay searches. $0\nu\beta\beta$-experiments must be low-background or background-free experiments due to the extreme half-lives of $0\nu\beta\beta$-decays. Internal background must be reduced by a stringent choice of all detector materials with regard to their radiopurity and through thorough purification efforts of the signal material. External background is reduced by operating the $0\nu\beta\beta$-experiments in an underground laboratories. External background consists of secondary particles induced by cosmic radiation or radioactive activated materials close to or within the detector. Figure 2.10 shows the muon flux over the vertical depth with several underground laboratory sites hosting particle physics experiments.

All in all, any $0\nu\beta\beta$-experiment running with a total fiducial mass M of a nuclide with atomic weight m_A and for a live-time (integrated data acquisition time) t expects a total number of $0\nu\beta\beta$-events of:

$$N = \log 2 \cdot \frac{N_A}{m_A} \cdot \epsilon \cdot \frac{M{\cdot}t}{T^{0\nu}_{1/2}} \tag{2.5}$$

where N_A is the Avogadro constant and ϵ the signal detection efficiency [148]. Any lower limit in observed $0\nu\beta\beta$-events can be transferred to an upper limit in $T^{0\nu}_{1/2}$. The more relevant physical observable $m_{\beta\beta}$ can be derived via equations 2.4 and 2.5:

$$m_{\beta\beta} = K_1 \cdot \sqrt{\frac{N}{\epsilon\, M\, t}} \tag{2.6}$$

where K_1 is a constant that depends only on the atomic weight m_A, phase-space $G_{0\nu}(Q_{\beta\beta}, Z)$ and NME $\mathscr{M}_{0\nu}$ of the $\beta\beta$-nuclide. The limit in $m_{\beta\beta}$ scales with the square-root of the exposure $M{\cdot}t$ so $0\nu\beta\beta$-experiments need to collect large masses of the $\beta\beta$-nuclide to increase sensitivity.

Table 2.2 shows leading $0\nu\beta\beta$-experiments most of which are currently running or have been until recently. The table contains information about:

- the individual nuclide of choice of each experiment,
- the fiducial mass in this nuclide (which in some cases is not given in the publications but calculated from information in several sources),
- the energy resolution of the experiments (ranges in the resolution are due to more than one read-out systems),
- the background index in counts per keV, kg fiducial mass and year. This index is not given in more meaningful terms of FWHM since in most of the listed experiments, this information is not available. Also, the index is a subject to background flatness and fiducial cuts.
- the current limit in the $0\nu\beta\beta$-decay half-life at 90 % C.L.,
- the current limit in the Majorana neutrino mass $m_{\beta\beta}$ (the large uncertainties are due to uncertainties in the NME calculation – a significant source of systematic errors for all experiments when (measured) half-life limits are converted to limits on $m_{\beta\beta}$)
- and references to most recent publications.

$0\nu\beta\beta$-experiments can be characterised by their sensitivity to the $0\nu\beta\beta$-decay half-life after a certain live-time (in years) or exposure $M{\cdot}t$ (in kilogram-years). This sensitivity refers to the average upper limit in $T^{0\nu}_{1/2}$ (or a lower limit in the Majorana neutrino mass value) at a certain confidence level. The confidence level is determined via Feldman-Cousins confidence intervals based on a large ensemble

Experiment	Nucl.	Mass (kg)	Energy res.	Bg. (cts/keV/kg/yr)	$0\nu\beta\beta$ lim. (yr)	$m_{\beta\beta}$ lim. (meV)	Ref.
CANDLES	^{48}Ca	0.0076	(4–6) %	0.38×10^{-3}	5.8×10^{22}	3500–22000	[303]
CUORE	^{130}Te	206	0.28 %	$(1.38\pm0.07)\times10^{-2}$	3.2×10^{25}	75–350	[28, 8]
CUORICINO	^{130}Te	11.2	(0.16–1.03) %	$< 9\pm6$	2.8×10^{24}	300–710	[35]
CUPID-0	^{82}Se	5.13	0.17 %	$3.6^{+1.9}_{-1.4}\times10^{-3}$	2.4×10^{24}	376–770	[63]
EXO-200	^{136}Xe	74.7	1.15 %	$\leq (1.9\pm0.2)\times10^{-3}$	3.5×10^{25}	93–286	[37]
GERDA	^{76}Ge	31	(0.15–0.20) %	$1.0^{+0.6}_{-0.4}\times10^{-3}$	8.0×10^{25}	140–300	[13]
HDM	^{76}Ge	9.54	(0.11–0.14) %	0.19 ± 0.01	1.9×10^{25}	< 350	[182]
KamLAND-Zen	^{136}Xe	346	4.66 %	0.584×10^{-3}	1.07×10^{26}	61–165	[56, 142]
Majorana	^{76}Ge	29.7	0.12 %	$1.6^{+1.2}_{-1.0}\times10^{-3}$	1.9×10^{25}	240–520	[3]
NEMO	^{48}Ca	0.00699	(2.8–3.5) %	0.49	2.0×10^{22}	6000–26000	[50]
	^{82}Se	0.932	(3.4–4.2) %	$(3.5\pm0.03)\times10^{-3}$	2.5×10^{23}	1200–3000	[54]
	^{96}Zr	0.0094	(3.2–3.9) %	4.775 ± 0.0079	9.2×10^{21}	7200–19500	[46]
	^{100}Mo	6.914	(3.3–4.1) %	$(1.1\pm0.03)\times10^{-3}$	1.1×10^{24}	330–620	[49]
	^{116}Cd	0.410	(3.5–4.3) %	$(84.2\pm4.0)\times10^{-3}$	1.0×10^{23}	1400–2500	[52]
	^{130}Te	0.661	(3.6–4.5) %	0.125 ± 0.011	1.3×10^{23}	N/A	[48]
	^{150}Nd	0.0366	(3.2–3.9) %	1.06 ± 0.009	2.0×10^{22}	1600–5300	[51]
SOLOTVINO	^{116}Cd	≈ 0.1	7.75 %	0.04	1.7×10^{23}	< 1900	[112]
CUPID	^{100}Mo	253	0.2	10^{-4}	1.5×10^{27}	10–17	[47]
DARWIN	^{136}Xe	≈ 450	≤ 1.0 %	$\leq 3.96\times10^{-6}$	$\geq 2.4\times10^{27}$	18–64	[10]
LEGEND-200	^{76}Ge	200–1000	0.12 %	2.4×10^{-4}	$> 10^{28}$	< 17	[126]
nEXO	^{136}Xe	≈ 3600	≤ 1.0 %	$\leq 1.49\times10^{-5}$	$\geq 9.2\times10^{27}$	5.7–17.7	[32]
NEXT-100	^{136}Xe	≈ 87	< 1 %	$\leq 4\times10^{-4}$	$\geq 2.8\times10^{25}$	80–160	[205]
SNO+	^{130}Te	≈ 1300	N/A	$\approx 5.83\times10^{-5}$	$> 1.9\times10^{26}$	< 50.6	[132]

Table 2.2.: Most prominent $0\nu\beta\beta$ experiments including the fiducial mass of their $\beta\beta$-nuclides, energy resolution ΔE at the Q-value, background index, $0\nu\beta\beta$ limit and the limit on the Majorana neutrino mass $m_{\beta\beta}$. Past and running experiments are shown with current half life limits. Projected limits are given for the future experiments on the bottom.

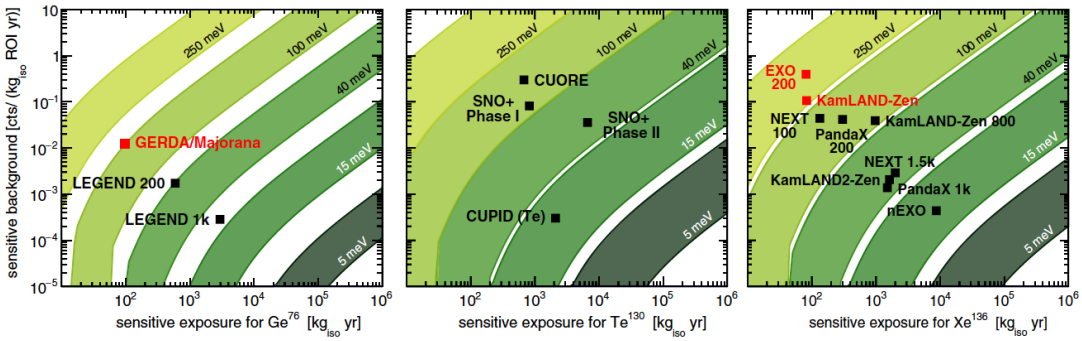

Figure 2.11.: Discovery sensitivity of various $0\nu\beta\beta$-decay experiments using ^{76}Ge, ^{130}Te or ^{136}Xe after 5 years of live-time [11]. The probability is plotted in terms of $m_{\beta\beta}$ (greenish bands) depending on the exposure and background rate of the experiment. Currently running experiments are shown in red (as of 2017).

of identical replicas of such an experiment that all experience different background levels (details in [148]). These intervals allow to set confidence interval limits for null-results (i.e. no observation) and represents the standard frequentist approach used in $0\nu\beta\beta$-experiment analyses. In case of a null-result, only background events are expected. The upper limit on $m_{\beta\beta}$ scales with the square-root of the number of background events b. This transforms equation 2.6 to:

$$m_{\beta\beta} = K_2 \cdot \sqrt{\frac{b^{1/2}}{\epsilon\, M\, t}} = K_2 \cdot \sqrt{1/\epsilon} \cdot \left(\frac{c \cdot \Delta E}{M\, t}\right)^{1/4} \tag{2.7}$$

where K_2 again is a constant that only depends on the nuclide and $b = c \cdot M\, t \cdot \Delta E$ is the number of background events which depends on the background rate c, the exposure and the width ΔE of the region of interest (ROI) [148]. This means, that for any background rate that cannot be interpreted as consistent with zero, the sensitivity for the Majorana neutrino mass does not scale with the square of the exposure but with its forth root. For this reason, future-generation $0\nu\beta\beta$-experiments as those listed in table 2.2 aim to be as background-free as possible so that the sensitivity improves faster with $M{\cdot}t$ [12].

Another way to characterise a $0\nu\beta\beta$-experiment is to calculate the discovery probability i.e. the probability of actually detecting a $0\nu\beta\beta$-decay event with a significance of at least $3\,\sigma$. This discovery probability combines the sensitivity of a certain detector design (see equation 2.7) and the probability distribution of $m_{\beta\beta}$ shown in figure 2.7. Figure 2.11 shows the discovery sensitivity of some experiments using ^{76}Ge, ^{130}Te or ^{136}Xe after 5 years of live-time as a function of the sensitive exposure and the expected sensitive background. The discovery sensitivity is given in terms of $m_{\beta\beta}$ where the bands represent the range of considered NME values.

2.2. The nEXO experiment

nEXO is a next-generation, multi-tonne, liquid xenon $0\nu\beta\beta$-experiment planned to increase the half-life sensitivity for the $0\nu\beta\beta$-decay of ^{136}Xe to 10^{28} yr [27]. nEXO will improve the sensitivity to $m_{\beta\beta}$ to $\mathcal{O}(1\,\text{meV})$ and will cover most if not all the parameter space of the inverted hierarchy shown in figure 2.7. The experiment is scheduled to start taking data around 2024. A comprehensive overview of the detector R&D progress is found in the pre-Conceptional Design Report published by the nEXO-collaboration [32] and a publication foccussing on the sensitivity [27]. nEXO is the successor of the EXO-200 experiment, which serves in many ways as a very successful prototype [58, 31]. EXO-200 was the first experiment to observe the $2\nu\beta\beta$-decay of ^{136}Xe [7] and derived the most precise measurement of its half-life with $T_{1/2}^{2\nu\beta\beta} = 2.165\pm0.016\,(\text{stat.})\pm0.059\,(\text{sys.})\times10^{21}$ yr [18]. This value is still more accurate than the most recent value from the significantly larger KamLAND-Zen detector [143]. EXO-200 sets a lower limit on the $0\nu\beta\beta$-decay half-life of 3.5×10^{25} yr [37]. This is consistent with the currently leading KamLAND-Zen limits [142]. An informative overview of EXO-200 can be found in [19] while previous $0\nu\beta\beta$-results are reported in [59] and [25].

2.2.1. Overview of nEXO

nEXO will be a liquid xenon (LXe) based time-projection-chamber (TPC) – a detector design first conceived in the Gotthard-experiment [309]. Unlike EXO-200, nEXO will be single-sided with a cathode at the cylinder cap and not in the centre. nEXO will be a single-phase TPC with its detector volume entirely filled with LXe – unlike the detectors operated by the XENON-collaboration (see e.g. [42]).
The detector will be a cylindrical TPC with a height and diameter of about 1.3 m contained in a spherical carbon-fibre cryostat filled with hydrofluoroether (HFE) which acts as a cooling agent (see fig. 2.12). The cryostat is vacuum insulated from the outside and installed in a huge water tank with a height and diameter of about 13 m. The tank acts as active muon-veto and as a shield against external ionising radiation. The minimum HFE- and water shielding thickness is 0.76 m and 4.25 m, respectively. nEXO is planned to be constructed in SNOLab, Canada, in a depth of 2070 m which corresponds to about 6000 m.w.e. [285].
nEXO will us 5109 kg of enriched xenon of which 4038 kg is used as fiducial volume. The remaining xenon is (a) discarded due to the short distance to any non-xenon detector material (e.g. the readout systems, cryostat) where the background level is higher and the electric field quality poor or (b) contained in the re-liquefying and purifying system constantly circulating the xenon out and back into the detector. The ^{136}Xe abundance is planned to be at least 90 %. nEXO will be operated at 165 K. nEXO will use the $\beta\beta$-decaying xenon as detector material at the same

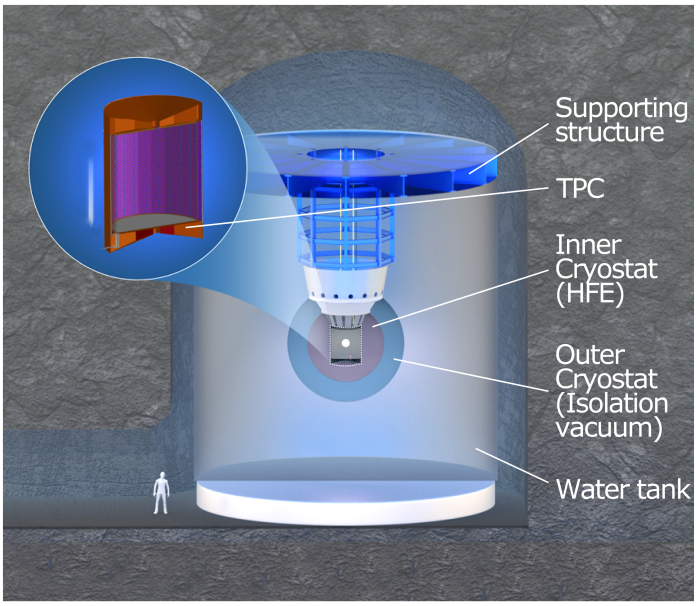

Figure 2.12.: Conceptual scheme of the nEXO detector in an underground cavern. The TPC (zoom) sits inside a cylindrical cryostat (violet) which is surrounded by an insulation vacuum (blue). The entire construction is placed in a water tank (white). The mechanical attachment and electrical connections are realised from the ceiling.

time so that the xenon is used to detect its very own decays. This allows to design a very compact and efficient detector. All numbers are from table 3.1 in [32].
^{136}Xe is well suited as $\beta\beta$-nuclide. It might not be an ideal nuclide considering its low NME and Q-value and mediocre phase space factor. However, xenon has a large stopping power and density if liquid, is chemically stable and has no long-lived β-decaying nuclides which makes xenon very convenient as detector material (see section 2.3). Xenon is further available in large masses from air liquefaction plants and can be purified and enriched rather easily [118]. The Q-value of ^{136}Xe has been reported by two groups to be (2457.83±0.37) keV [258] and (2458.73±0.56) keV [207] yielding a weighted average mean of (2458.10±0.31) keV.
The first $0\nu\beta\beta$-experiments using ^{136}Xe have been conducted in the late 80s in a high pressure ionisation chamber [67] and a proportional chamber [73] and derived half-lives around 10^{22} yr. The current limit is 1.07×10^{26} yr established by the KamLAND-Zen-Collaboration [142] while the best limit of EXO-200 is 3.5×10^{25} yr [37]. Both collaborations also examined the $2\nu\beta\beta$-spectrum more closely. The KamLAND-Zen-Collaboration investigated the spectral shape in detail to derive further information about the weak axial vector coupling g_A and possible quenching effects [18, 143]. The quenching factor q reduces the Gamov-Teller matrix element in the $2\nu\beta\beta$-transition via ^{136}Cs [131] and has been recorded to

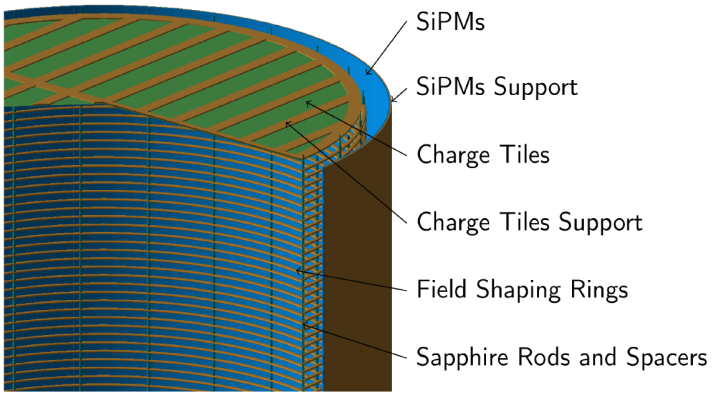

Figure 2.13.: Geometry of the top part of the nEXO TPC taken from the GEANT4 detector simulation [32]. Secondary electrons are drifted to the charge tiles on the detector top (green). The drift field is generated by concentrically stacked field shaping rings (brown). SiPMs (blue) detect the xenon scintillation light.

be about 0.74 for ^{136}Xe [168]. q is believed to play no major role for the $0\nu\beta\beta$-transition for several reasons. If this is true, the projected $0\nu\beta\beta$ half-life would benefit enormously [127, 173].

2.2.2. The nEXO detector and working principal

The two electrons from any $\beta\beta$-decay in the detector volume ionise and excite xenon atoms along their trajectory. Each electron carries a maximum initial energy of half the Q-value at 2458.10 keV yielding in a CSDA range (Continuous Slowing Down Approximation) of about 2.9 mm in LXe [129]. The energy dissipation of the kinetic energy is dominantly due to electron collisions with xenon atoms. An electric field around 400 Vcm^{-1} parallel to the cylinder axis drifts the secondary electrons ripped from their mother xenon atoms through the LXe tow the charge readout system located at the top of the cylinder (see figure 2.13). Depending on the ionisation density, a certain fraction of these electrons will however recombine with positively charged xenon ions. This produces xenon dimers that eventually decay under the emission of scintillation light (see section 2.3.3).
Electron drift in xenon is well understood. The drift velocity increases with the electric field strength [23, 220]. Diffusion and xenon purity affect the drifting electron cluster. Diffusion increases the size of the cluster during the drift thus reducing the lateral resolution of the initial secondary electron distribution. Diffusion coefficients in liquid xenon have been measured by the EXO-200 collaboration to several 10s of cm^2/s. The transversal diffusion acts about 2.3 times stronger than the lateral component at the field strength in EXO-200 and nEXO [23, 231]. Impurities in the

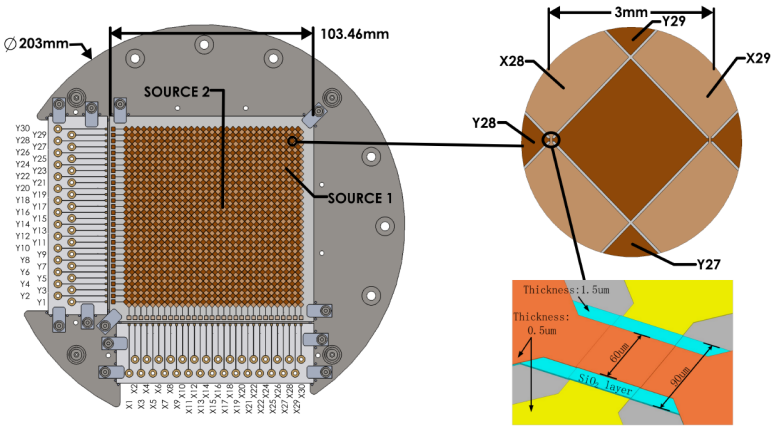

Figure 2.14.: CAD drawing of the charge readout tile prototyp. Several x- and y-strips are daisy-chained in a checker-board topology and read out at two sides. The zoom shows the geometry and the vertical insulation of the strip crossings [175].

xenon will trap or absorb drifting electrons and cause distortions of the charge-only energy signal. The electron lifetime is 3 ms at 778 $\mathrm{Vcm^{-1}}$ in EXO-200 [18, 118]. nEXO plans to reach more than 10 ms [32] to account for the larger drift length of 125 cm. The electric field in nEXO is generated by a cathode plane at the bottom and the anode charge collection system at the top. Its homogeneity is ensured by 58 concentrically stacked, sapphire-insulated field shaping rings at the edge of the TPC with a thickness of 4 mm and a pitch of 2 cm.

The drift electrons are detected with an array of anode tiles at the top of the TPC with a position resolution of 3 mm (see figure 2.14). Each tile consists of two perpendicular sets of Au/Ti-strips deposited onto a 300 µm silica wafer surface. The strips are about 10 cm long, spaced 3 mm centre-to-centre and are daisy-chained at the corners forming a checkerboard-style anode tile to maximise the charge-sensitive metallic surface to about 96 %. Both strip planes are insulated with 1.5 µm of SiO_2 at the crossings. The strips are read out individually or in groups at the backside of the substrate so that the modular tiles can be put very close to each other in the final charge collection system. Check [32] for more information, [175] for prototype results and [200] for simulations of nEXO with segmented charge readout tiles.

Some secondary electrons are not drifted to the anode tiles but collide with positive xenon ions and undergo recombination. This produces excited xenon-dimers that relax under the emission of vacuum ultraviolet (VUV) scintillation photons at around 178 nm [95]. The same happens to xenon atoms that are not ionised but excited by the penetrating particle. Details of the scintillation process are given in section 2.3.3. Xenon is transparent for its own scintillation light. The Rayleigh scattering length is comparable to the dimensions of nEXO (see table 2.4).

The inner surface will be photo-sensitive to register the VUV scintillation photons. The mantle surface of the TPC will be covered with VUV-sensitive silicon photomulitpliers (SiPMs) which are shown in blue in figure 2.13. The SiPMs will be connected in 10 cm wide tiles that are stacked together to SiPM staves comprising 2 times 12 tiles. 24 of these staves form a photo-sensitive icositetragon-based barrel between the field shaping rings and the TPC shell. There are important design specifications for the field shaping rings to minimise shadowing of the SiPMs. An additional highly VUV-reflective coating is anticipated for any non-photo-sensitive surfaces in the TPC (e.g. the rings or the cathode) to maximise the photon transport efficiency (PTE), i.e. the average fraction of emitted photons that manage to hit a SiPM somewhere. A large solid angle coverage of the photo-sensitive surface and a good PTE is the precondition for a good light collection efficiency and with it a good energy resolution of the entire detector [174].
The lateral position reconstruction in x and y (perpendicular to cylinder axis) is accomplished with the charge-only signal. At least two 3 mm anode panels have to be in coincidence to trigger data acquisition. The lateral position resolution is $3\,\mathrm{mm}/\sqrt{12} = 0.87\,\mathrm{mm}$ in theory but will most likely be larger than 1.0 mm based on the findings in EXO-200 (see [18], VIII, C). Clusters originating from closer than 1.5 cm to the inner edge of the TPC field cage are removed by a fiducial cut to account for electric field inhomogeneities and large background levels. The axial z-position is calculated via the electron drift time (derived from the time difference between the light and charge signals) and the known drift velocity at the specific field strength. The accuracy will be close to the one in EXO-200 with 0.42 mm [18].

2.2.3. Analysis and Backgrounds

nEXO as EXO-200 will use the combined light- and charge-signal to reconstruct the event energy. Both signal are anti-correlated. The more secondary electrons escape recombination and contribute to the charge signal, the less scintillation light is emitted and vice versa. The combination of both signals is independent of any fluctuations in the recombination probability and yields the overall deposited energy [104]. nEXO will also use the so-called *standoff distance* which is the distance of an event position to any non-xenon component in the detector. The larger it is, the smaller the contribution from internal background induced by the materials of these components. Additionally, the multiplicity and particle information are registered for each event. The multiplicity refers to the topography of the charge cluster which can be about the size of one anode tile pad (single-site) or spanning over more than two pads or triggering completely independent pads if there are multiple depositions (multi-site). Electron tracks in liquid xenon are rather short so $\beta\beta$ events are likely to yield single-site events while multi-site events are more

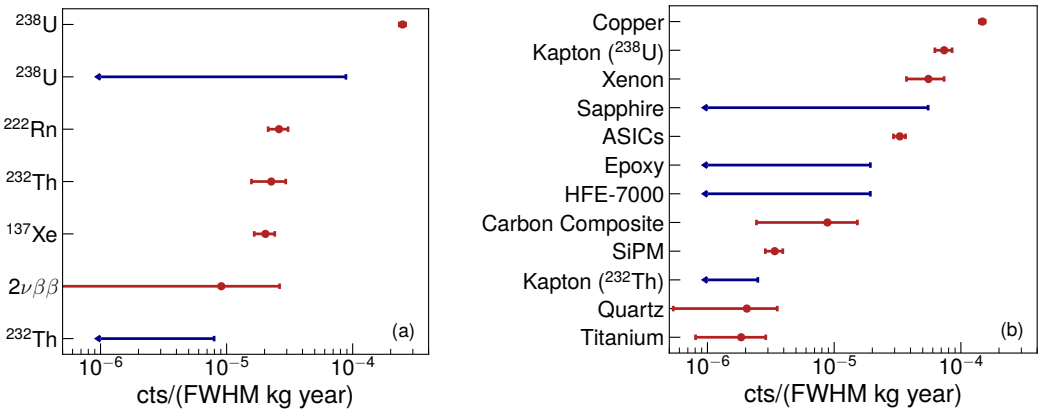

Figure 2.15.: Measured background levels for event energies within $Q_{\beta\beta} \pm \mathrm{FWHM}/2$ and in the inner 2000 kg of LXe [27]. The background contribution is grouped by the individual radionuclides (a) and detector materials (b). Blue arrows indicate 90 % C.L. upper limits and red circles present measurements including 1σ uncertainties.

background-like. The particle identification makes use of the different interaction channels and ionisation potential of different particles.
Backgrounds in nEXO are sources that emit particles with an energy of larger than the Q-value of ^{136}Xe and live long enough to be pronounced in steady-state of the detector. This can be long-lived radionuclides, cosmogenically-created radionuclides or neutrino-induced backgrounds [27]. The most important sources are grouped by radionuclide and material in figure 2.15 and comprise:

- the 2448 keV γ-line of ^{214}Bi which is a part of the ^{238}U–^{222}Rn decay chain and very close to the Q-value of ^{136}Xe,
- the ^{232}Th decay chain including ^{220}Rn which gets dissolved in the LXe,
- muon-induced radionuclides as ^{137}Xe [21],
- the neutrino-accompanied $\beta\beta$ decay of ^{136}Xe – a background that cannot be reduced in any way except a supreme energy resolution,
- some other nuclides as ^{137}Cs, ^{60}Co and ^{40}K [194].

The biggest contributors in terms of detector components are the copper from the TPC vessel, ^{238}U in the Kapton especially in the charge module and SiPM cabling, the field rings and the xenon itself. More details are found in [27].
Background radionuclides undergoing α-decay can be discriminated efficiently via the particle identification. There are only few β-emitters around the Q-value of ^{136}Xe so γ decays within the ROI are the dominant background source. At these energies, γ-particles predominately undergo Compton-scattering which mainly

results in multi-site events. The actual γ-background therefore only refers to the small fraction of γ events in the ROI that against all odds end up as single-site events and are indistinguishable from $0\nu\beta\beta$-events. This fraction can be quite significant – even after extensive background modelling and large efforts in component material screening – given the tiny expected $0\nu\beta\beta$-rate.
The construction material for all detector components have to be chosen carefully in terms of their purity – especially if the components are close to or within the xenon. Extensive radionuclide screening assessments have to be performed to evaluate which materials can be used or need to be avoided to contruct the detector. The assessments also determine the precise radioactive impurity concentrations to refine the detector simulations [193, 194].
The γ-particle attenuation length at the Q-value of ^{136}Xe is about 8.4 cm in LXe [310]. This means, that the background contribution of the detector components are increasingly attenuated towards the detector centre. This is met by introducing a running background index – which describes the background counts per energy interval, kg LXe and time – instead of a classical fiducial cut. Such a running index is characterised not by a single number but by a position dependent function that gets smaller towards the centre. The signal analysis exploits all four event characteristics via a combined, multidimensional fit on the energy, position, multiplicity and particle ID distributions and discriminates the events in signal- and background-like. The discrimination power can be set to depend on the background index thus accounting for the varying background level within the detector volume. As a result, nearly the entire xenon inventory can be used as active medium instead of only a fiducial mass fraction. The outer background-dominated part of the xenon as well as all events beyond the ROI can be used to simultaneously constrain the individual background contributions eventually optimising the discrimination power for events in the detector centre and ROI [32].
The single-site background rate will be about 8.6×10^{-4} cts./(FWHM $\cdot$ kg $\cdot$ yr) in nEXO for the inner 3000 kg of the xenon but only 1.4×10^{-4} cts./(FWHM $\cdot$ kg $\cdot$ yr) in the inner 1000 kg as shown in figure 2.16. The FWHM will be roughly 30 keV which is much larger than for bolometric $0\nu\beta\beta$-experiments but still very good for scintillator-based detectors. The numbers are based on the profound radioassay program of candidate materials for EXO-200 [193, 194].

2.2.4. nEXO Physics Goal

nEXO aims at a $0\nu\beta\beta$ half-life sensitivity of $T_{1/2} = 9.2\times10^{27}$ yr corresponding to a sensitivity on the Majorana neutrino mass of $\langle m_{\beta\beta}\rangle = (5.7\text{–}17.7)$ meV (depending on the NME model) at 90 % C.L. [32]. The numbers refer to a live-time of 10 years of data-taking. The sensitivity over live-time is shown in figure 2.17.

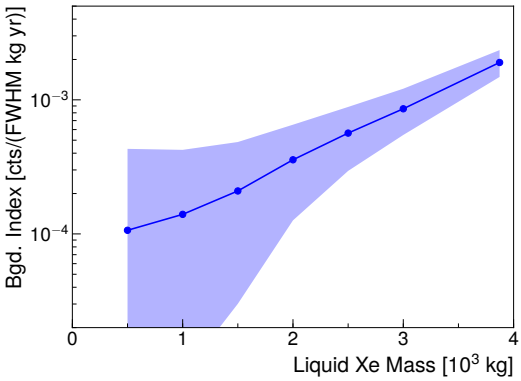

Figure 2.16.: Runnning backgorund index and 95 % confidence belt of nEXO derived from toy-MC simulations [27]. The index decreases strongly towards the centre of the detector.

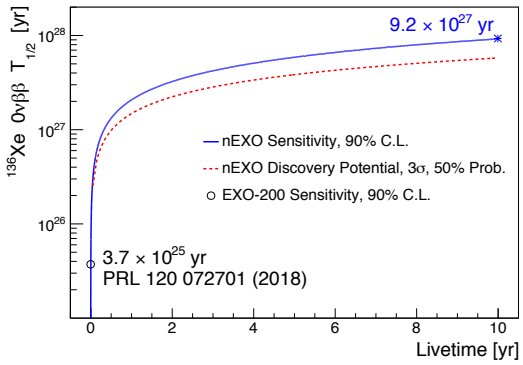

Figure 2.17.: Median sensitivity at 90 % C.L. and 3σ discovery potential of nEXO over live-time. [27]. The plot includes the EXO-200 full-dataset limit from 2018 [25].

The capability to exploit several event characteristics in a multidimensional fit combined with the cutting-edge background index (especially in the detector core) leads to a competitive $0\nu\beta\beta$ discovery potential which is shown to be the best among next-generation $0\nu\beta\beta$-experiments in simulations [11]. The 3σ discovery potential is $T_{1/2} = 5.7{\times}10^{27}$ yr or $\langle m_{\beta\beta}\rangle = (7.3\text{–}22.3)$ meV after 10 yr.
The goal in terms of energy resolution is 1 % at the Q-value in the combination of the anti-correlated charge and light signals, i.e. better than 25 keV. At this level, the $2\nu\beta\beta$ background contribution is compatible with zero and the half-life sensitivity barely improves with resolution. The main radionuclide background is the γ-decay of ^{214}Bi only 10 keV off the ^{136}Xe Q-value. Its discrimination based on the deposited energy would require a hypothetical resolution of 0.4 % and would increase the sensitivity to about $4{\times}10^{28}$ yr [27]. This goal might however be achieved using Barium-tagging in a possible upgrade to nEXO in the far future [92, 222]. More realistic improvements can be made by introducing machine learning tools as deep neuronal networks in the analysis which has already been investigated for EXO-200 [115]. This could improve the sensitivity to about $1.2{\times}10^{28}$ yr [200].
A decent energy resolution is still necessary to reliably distinguish a possible signal from various kinds of background events. The nEXO design addresses the efficiency requirements on the charge and light collection systems as the most important R&D challenge. While close to 100 % of all secondary electrons can be registered by the anode tiles, only a small fraction of VUV-photons will be detected due to shadowing effects, large non-photo-sensitive surfaces and the poor photon detection efficiency (PDE) of SiPMs in the VUV. nEXO aims at at least 3 % light collection efficiency (i.e. the product of PTE and PDE) to reach its energy

resolution goals. The R&D is focused on (a) an optimal shape and reflectivity of all non-photo-sensitive TPC components to maximise the PTE and (b) extended SiPM characterisation studies to find a candidate model with a high PDE to make the scintillation light detection as efficient as possible [141, 174, 237]. The requirement for the SiPM are among others a PDE of better than 15 % at a bias voltage that results in a correlated avalanche probability of less than 20 % within 1 µs [32]. SiPMs must also be tested for their robustness towards the high electric fields occuring in the vicinity of the field shaping rings [292]. Finally, the detector response for different event energies and positions must be simulated properly with a so-called *light-map* to improve the event reconstruction [113]. More information on SiPMs is found in section 2.4.
nEXO will also undergo studies for other exotic processes such as the $\beta\beta$-decay of ^{136}Xe to excited states [20], the $\beta\beta$-decay of ^{134}Xe [24], the first-forbidden non-unique β-transition from ^{137}Xe to ^{137}Cs [30], nucleon decays [26] and Lorentz violation [22]. Furthermore, the exact shape of the $2\nu\beta\beta$-spectrum can be investigated in detail to gain further knowledge about the axial vector coupling g_A which significantly influences the sensitivity for $\langle m_{\beta\beta} \rangle$ [261].

2.3. Properties of liquid xenon as detector material

Xenon is a colourless, dense noble gas group element. It is generally unreactive while some chemical compounds with fluor and oxygen are known [274]. Xenon has a high Z and a standard atomic weight of 131.293(6) [213]. Xenon is produced as a side product of air liquefaction with a concentration in air of only 0.09 vol. ppm [40] and a mass concentration in the geosphere[1] of about 0.02 ppbw [133]. The thermodynamic properties of xenon are discussed in section 2.3.1.
Xenon has the highest Z for any non-radioactive, non-metal element making it an excellent detector material for ionising radiation. The most relevant parameters of liquid xenon as a detector medium are discussed in section 2.3.2.

2.3.1. Thermodynamic properties of xenon

Table 2.3 lists some basic thermodynamic properties of xenon. The boiling and melting point refer to atmospheric pressure and can differ significantly for other conditions (see figure 2.18). The triple point (TP) of xenon has been investigated regularly since the earliest study in 1941 [100]. Most values agree very well within experimental uncertainties. The critical point (CP) is also known precisely.

[1] Defined as the lithosphere down to a depth of 16 km, the hydrosphere including the cryosphere, the atmosphere and the biosphere combined.

The density ρ of liquid xenon increases with falling temperature from 1155 kg m^{-3} at the critical point to about 3100 kg m^{-3} at the triple point (see for example figure 2.1 in [40]). The density increase continues for solid xenon yet less intense [145]. The liquid xenon density is about a factor 500 larger than gaseous xenon at normal conditions.

Quantity	State	Value	Reference
T_x	T_b	165.2 K	[312] tab. 7
	T_m	161.385 K	[216] fitted
TP	T_T	161.39 K	[201] tab. 2; [179] tab. 1
	p_T	(816.08±0.08) mbar	[135] tab. 1
CP	T_C	(289.726±0.002) K	[314]
	p_C	(58.400±0.005) bar	[156]
	ρ_C	1099 kg m^{-3}	[282], tab. 12
ρ	gas	5.8989 kg m^{-3}	at 273 K, 1 bar [218]
		5.897 kg m^{-3}	at 273 K, 1 atm [72] tab. I
		5.85942 kg m^{-3}	Ideal gas law at 273 K, 1 atm
	liquid	3084 kg m^{-3}	at TP [166] tab 28; [245]
		2906.1 kg m^{-3}	at 170 K, sat. [290] tab. 3
	solid	3540 kg m^{-3}	at TP [102] tab. 7
		3407 kg m^{-3}	at 160 K [145]
c_p	gas	0.1608 kJ kg^{-1} K^{-1}	at 273 K, 1 atm [217] tab. X
	liquid	0.3397 kJ kg^{-1} K^{-1}	at 165.9 K [101] tab. 3
	solid	0.041 kJ mol^{-1} K^{-1}	at 160 K [301]
λ_{th}	gas	5.15 mW K^{-1} m^{-1}	at 0 °C [177] tab. 3
	liquid	70.3 mW K^{-1} m^{-1}	at 172 K [180] tab. 1
	solid	461 mW K^{-1} m^{-1}	at 77 K (interpol.) [186]
H_{lat}	fusion	(2.315±0.045) kJ mol^{-1}	at T_T [275]
	vapor.	(12.52±0.04) kJ mol^{-1}	at 165.066 K [93]
	sublim.	(15.04±0.08) kJ mol^{-1}	at T_T [110] tab. IX
α	liquid	2.34×10^{-3} K^{-1}	at 170 K, saturated [290]

Table 2.3.: Overview of some thermodynamic properties of xenon especially at cryogenic conditions. The quantities are: the boiling and melting point, the triple and critical point, the density ρ, the thermal capacity c_p, the thermal conductivity λ_{th}, the latent heat values H_{lat} and the expansivity α. The values given in the table are obtained from the references presented in the right column, calculated from formulas given there or interpolated from data tables.

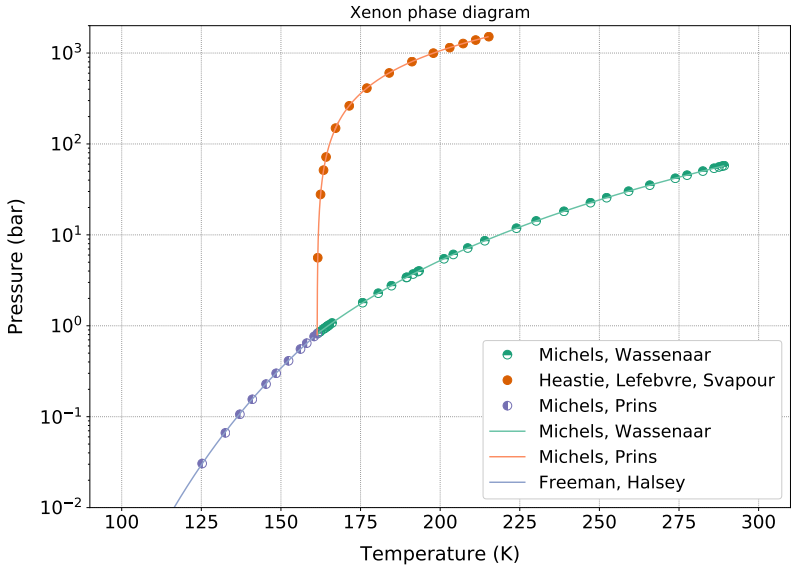

Figure 2.18.: Phase diagram of xenon. The plot includes the vapour pressure curve and data (green) [216], the solid-liquid phase curve and data (red) [161] as well as data [215] and a fitted function [136] for the melting curve (blue).

The isochoric specific thermal capacity c_p, the thermal conductivity λ and the latent heat of phase transitions H_{lat} are reported for all physical states. All values are rather small compared to most other elements or substances. c_p and λ of xenon are the smallest values among the noble gases.

The phase diagram in figure 2.18 shows the physical state for any temperature and pressure. The diagram combines data with fitted thermodynamic equilibrium equations for the vapour pressure curve [216], the solid-liquid phase curve [161] and the melting curve [136, 215]. A melting point T_m of 161.385 K and a boiling point T_b of 164.8 K can be derived from the fits for a pressure of 1 bar.

Xenon is always super-critical if stored at room temperature and the ideal gas law cannot be used to describe the behaviour of any xenon quantity at these conditions. This means that no pressure beyond 59 bar will be reached in storage gas bottles if no overfilling occurs. On the other hand, the ideal gas law cannot be used to avoid any overfilling. Instead, gas companies use technical fill factors to determine the maximum gas mass allowed for a specific gas bottle volume. The fill factor for xenon is 1.24 kg per litre container volume according to Air Liquide [priv. comm.]. This is highly important for the design of xenon liquefaction setups.

Detailed information about the physical properties of xenon can be found in the *Rare Gas Solids* series [183] where thermodynamic information is dominantly found in [110] and [185]. Encyclopaedic overviews are found in [170] and [274] while [230] and [282] provide extended thermodynamic data tables including further literature.

2.3.2. Detector relevant properties of xenon

Table 2.4 shows several parameters of liquid xenon that are relevant for the detection process of ionising radiation. The reference for each parameter is listed along with uncertainties if reported in the publications. The table contains:

1. the average ionisation and excitation potential, E_i and E_ex, the probability fraction of ionisation vs. excitation $\alpha = N_\mathrm{ex}/N_\mathrm{i}$ and the average kinetic energy of ionised charge carriers $\bar{\epsilon}_\mathrm{i}$,
2. the average energy required for one secondary electron-hole pair W_i, the minimal energy required for one scintillation photon W_sc and the combined W-value $W_\mathrm{i+sc}$,
3. the Fano-factor F, energy band gap E_g and radiation length X_0 in LXe,
4. the peak scintillation wavelength λ_scint and the width of the scintillation light spectrum $\Delta\lambda_\mathrm{scint}$ in both xenon gas and liquid,
5. the electron mobility μ_LF, the speed of sound u_sound, the saturation drift velocity of electrons $v^\mathrm{sat}_\mathrm{drift}$, the transversal and longitudinal diffusion coefficients D_T and D_L, the scattering length a_scat and the mean free path ℓ for electrons,
6. the absorption length λ_abs and Rayleigh scattering length λ_Ray for scintillation light in liquid xenon,
7. and various reported values for the refractive index in liquid xenon in the UV (178 nm if not specified otherwise).

Light particle as electrons lose energy due to inelastic interaction with atomic electrons of the detector medium. This kind of energy dissipation can be expressed with the Platzman equation [248]:

$$E_\mathrm{dep} = N_\mathrm{i} E_\mathrm{i} + N_\mathrm{ex} E_\mathrm{ex} + N_\mathrm{i} \bar{\epsilon}_\mathrm{i} \tag{2.8}$$

where the energy deposited in the detector media E_dep partly creates N_i electron-hole pairs with ionisation potential E_i and kinetic energy $\bar{\epsilon}_\mathrm{i}$ as well as N_ex excitations with the average excitation potential E_ex. Dividing Platzman's equation by N_i yields the W-value for electron-hole-pairs produced by primary ionising radiation:

$$W_\mathrm{i} = E_\mathrm{i} + \alpha E_\mathrm{ex} + \bar{\epsilon}_\mathrm{i} \tag{2.9}$$

where the initial ratio of the number of exitons and ionisations $\alpha = N_\mathrm{ex}/N_\mathrm{i}$ has been calculated from theory to be 0.06 [296] but measured to be 0.20 [120] while the most probable value is expected to be 0.13 [120]. The W-value is known to vary with density [80]. The extrapolation of W_i measured in Xenon gas under high

	Quantity	Value	Reference
Platzman parameters	E_i	10.5 eV	[296], calc. from tab. I.
	E_ex	8 eV	[296], calc. from tab. I.
	α	0.13	[120] tab. III
	$\bar{\epsilon}_\mathrm{i}$	(4.65–5.25) eV	depending on model [119]
W-values	W_i	(15.6±0.3) eV	[296]
		(14.2±0.2) eV	[233] tab. 1
		15.8 eV	[80]
	W_sc	(13.8±0.9) eV	[120]
		(13.46±0.29) eV	[283]
	$W_\mathrm{i+sc}$	(11.5±0.5) eV	[38]
Other excitation parameters	F	0.041–0.059	depending on model [119]
	E_g	(9.22±0.01) eV	[55]
	X_0	2.872 cm	[297]
Scintillation properties	λ_scint	174.52 nm	Gas at 300 K [176]
	$\Delta\lambda_\mathrm{scint}$	14.92 nm	
	λ_scint	178.00 nm	Liquid at 160 K [176]
	$\Delta\lambda_\mathrm{scint}$	14.26 nm	
Electron propagation	μ_LF	2200 $\mathrm{cm^2\,s^{-1}\,V^{-1}}$	at 163 K, [220] tab. I
	u_sound	650.58 $\mathrm{m\,s^{-1}}$	at 163 K, [62] tab. III
	$v_\mathrm{drift}^\mathrm{sat}$	2.9×10^3 $\mathrm{m\,s^{-1}}$	at 163 K, [220] tab. I
	D_T	(48.5–60.9) $\mathrm{cm^2 s^{-1}}$	for low E-fields, [23] fig. 7
	D_L	(23.8–41.0) $\mathrm{cm^2 s^{-1}}$	at $\mathcal{O}$(100V/cm) [231] fig. 7
	a_scat	4.2×10^{-9} cm	at 163 K, [55] tab. II
	ℓ	3.3×10^{-6} cm	at 163 K, [55] tab. II
Light propagation	λ_abs	$>$ 100 cm	at 165 K, [64] tab. I
	λ_Ray	(29 − 50) cm	[172, 81, 150, 286, 96]
Refractive index	n_LXe	1.65	at 163.2 K, [291]
		1.59	[81]
		1.6	for 170 nm at 161 K, [96]
		1.5655±0.0082	for 180 nm at TP, [71]
		1.72±0.02	[276]
		1.69±0.02	at 170 K, [286]
		1.69±0.04	[150]

Table 2.4.: Overview of various liquid xenon properties relevant for the detection process of particles. The individual quantities are explained in detail in the text.

pressure to liquid xenon densities agrees perfectly with the measurements in LXe. An overview of various measurements of W_i can be found in [38].
The Fano factor F accounts for variations in the number of electron-ion-pairs produced by an ionising particle at a certain energy if all the energy is absorbed in a monoatomic gas [130]. The value of F depends strongly on the energy dissipation model. The band gap energy E_g of condensed xenon is known precisely with only a small difference between liquid and solid xenon [55]. The radiation length X_0 has been calculated from theory by the particle data group [297].
The scintillation process and its relevant parameters are explained in section 2.3.3. Electron propagation in liquid xenon is well-understood thanks to various studies at LXe-based experiments. The low-field electron mobility μ_LF and the speed of sound u_sound in LXe has been measured in the 60s [62, 220]. The drift velocity increases with electric field strength [154, 220] and reaches a saturated drift velocity $v_\mathrm{drift}^\mathrm{sat} = 3000\,\mathrm{m\,s^{-1}}$ above roughly $10^4\,\mathrm{Vcm^{-1}}$ – a small value among the liquid noble gases [220]. The mobility corresponds to the proportional factor between v_drift and the field strength and describes the resistance of a specific material for drifting charge carriers. The mobility in xenon is rather large for a condensed noble gas [220]. A good symposium of various measurements can be found in [23] including values from the EXO-200-, XENON- and LUX-collaborations. There are indications that the drift velocity decreases for higher temperatures [231]. The EXO-200- and nEXO collaborations also determined the transversal and lateral diffusion coefficient D_T and D_L [23, 231]. The electron mobility in liquid xenon is limited by elastic scattering with a scattering length a_scat. In contrast, the mean free path ℓ describs the momentum transfer rate [55]. The lifetime of drifting electrons depends strongly on the xenon purity since electrons can be trapped by electronegative impurities. The EXO-200 collaboration achieved an electron lifetime of better than 3 ms at $778\,\mathrm{Vcm^{-1}}$ [18] while the nEXO-collaboration aims at a lifetime higher than 10 ms at about $400\,\mathrm{Vcm^{-1}}$ [32]. Lastly, electrons in LXe can be extracted out of the liquid phase if electric fields higher than $1.75\,\mathrm{kVcm^{-1}}$ are applied [153]. more details about the emission process can be found in [155].
A large range for the Rayleigh scattering length λ_Ray for 178 nm photons in LXe is reported in literature. Studies without explicit cleaning procedure of all LXe wetted surfaces prior to the experiment tend to deliver lower values (29 ± 2 cm in [172]) compared to those that perform considerate baking and xenon purification efforts (> 50 cm in [96]). Overviews of different λ_Ray measurements can be found in [64, 150, 276].
There is no clear picture for the refractive index n_LXe as well. Especially values obtained in recent studies don't agree within their uncertainties. Due to the strong dependence on the specific wavelength achieved in experiments, this might be a systematic effect [165]. Also, the refractive index is known to depend on temperature [206] which is yet to be examined in detail.

Xenon is an excellent detector material – especially for large-scale low background experiments. It has the highest Z for any non-radioactive, non-metal element and a high density if liquefied. This results in a large energy dissipation potential and good stopping power i.e. a high ability to stop or absorb ionising radiation. The average energy required for secondary electron-ion pairs or scintillation photons is relatively small compared to other noble gases [40] so the number of secondary particles per MeV energy deposited by a penetrating particle is large (see [95], fig. 11). The monoatomic character of xenon further prevents any dissipation to vibrational states [220].
Another excellent property of xenon is its scalability. This allows to conceive tonne-scale but still monolithic detectors such as nEXO, XENONnT, LZ or DARWIN all of which are low-background experiments [32, 44, 1]. Such experiments rely massively on their improving background levels towards the detector centre where the sensitivity is highest. Since external background radiation is increasingly damped by the outer volume, monolithic detectors are the best choice to profit from xenon's high stopping power. The scalability also allows for various detector sizes from table-top, proof-of-principle detectors with a mass of about 10 kg like XENON10 [36] to huge future-generation detectors like DARWIN [1] requiring several global annual production quantities of xenon.
Unlike krypton, xenon has no long-lived unstable isotopes (apart from double beta decaying nuclei) with the longest half-lives being in the order of a few weeks. This drastically reduces internal background levels in any xenon detector. The downside is the complicated energy calibration of a tonne-scale detector volume whose centre is barely penetrated by external calibration sources (see [32] sec. 4.4). For $0\nu\beta\beta$-decay experiments, β-decaying nuclei are particularly undesired since their energy spectrum inevitably overlaps with the $\beta\beta$-spectrum or the ROI. The most long-lived β-decaying xenon nuclei is ^{133}Xe with a half-life of only 5.243 d and a Q-value of 427.4 keV [131]. The most long-lived β^--decaying xenon nuclei with a Q-value larger as the one of ^{136}Xe is ^{138}Xe with a half-life of 14.08 min and a Q-value of 2770 keV [131].
Finally, xenon is easy to purify, This allows to reduce any potentially radioactive non-xenon impurities and to enrich (or deplete) the detector material in a specific isotope with particularly interesting (unwelcome) properties. For example, nEXO profits from a high abundance of ^{136}Xe [32] while for XENON1T, it is the largest background source [45].

Comprehensive reviews of xenon as a particle detector material have been done by C. Gruhn [151], W. Schmidt [271], E. Aprile, A. Bolotnikov, A. Bolozdynya and T. Doke [40], E. Aprile and T. Doke [39] as well as V. Chepel [95]. Information about the simulation of a liquid xenon detector response with NEST (Noble Element Simulation Technique) has been published by M. Szydagis [295].

2.3.3. Scintillation in liquid xenon

As all liquid noble gases, liquid xenon is known to scintillate if penetrated by fast electrons. The light originates from the relaxation of xenon dimers that are formed as a consequence of the excitation or ionisation of xenon atoms. Depending on the initial energy deposition on the atomic level, two processes can be distiguished [95]:

Direct excitation branch:

$$
\begin{aligned}
e^- + Xe &\rightarrow Xe^* + e^- \\
Xe^* + Xe &\rightarrow Xe_2^{*,v} \\
Xe_2^{*,v} + Xe &\rightarrow Xe_2^* + Xe \\
Xe_2^* &\rightarrow Xe + Xe + h\nu
\end{aligned}
$$

Excited xenon atoms form dimers with vibrational excitation (v) that mostly relax non-radiative. Scintillation photons are emitted during the dissociation of the electrically excited dimer Xe_2^*.

Ionisation-recombination branch:

$$
\begin{aligned}
e^- + Xe &\rightarrow Xe^+ + 2\,e^- \\
Xe^+ + Xe + Xe &\rightarrow Xe_2^+ + Xe \\
e^- + Xe_2^+ &\rightarrow Xe^{**} + Xe \\
Xe^{**} + Xe &\rightarrow Xe^* + Xe + \text{heat} \\
Xe^* + Xe + Xe &\rightarrow Xe_2^* + Xe + \text{heat} \\
Xe_2^* &\rightarrow Xe + Xe + h\nu
\end{aligned}
$$

Xenon ions form molecular ions that recombine and relax to the same excited xenon dimer formed in the excitation process. The dimers dissociate via the emission of scintillation photons.

Excited xenon dimers Xe_2^* emit scintillation light during the transition from their lowest electronic excited states to the ground state $^1\Sigma_g^+$. The transition can occur from either a singlet $^1\Sigma_u^+$ or a triplet excited state $^3\Sigma_u^+$. Direct transition from the triplet is forbidden but can occur via spin-orbital coupling [187] resulting in a much larger decay time constant (about (27±1) ns for the triplet compared to about (2.2±0.3) ns for the singlet [189]). This is depicted in figure 2.19. The relative population of both excited states is difficult to measure but is reported to be around than 0.05 in favour of the triplet which increases the effectiv scintillation decay time significantly [189]. There are additional non-exponential time components of roughly 40 ns and up to 2 µs due to the time delay imposed by the recombination process [164, 187]. The population of the singlet and triplet states is not necessarily the same for both branches.

The relative fraction of the direct excitation branch and the ionisation-recombination branch can be measured by switching an electric field on and off to change the number of electrons escaping recombination. The zero-field recombination fraction has been reported to lie between 67 % [188] and 71 % [189] in liquid xenon. If electric fields are applied, less electrons contribute to recombination and the scintillation yield decreases by a factor up to about 3 [95]. The effective scintillation

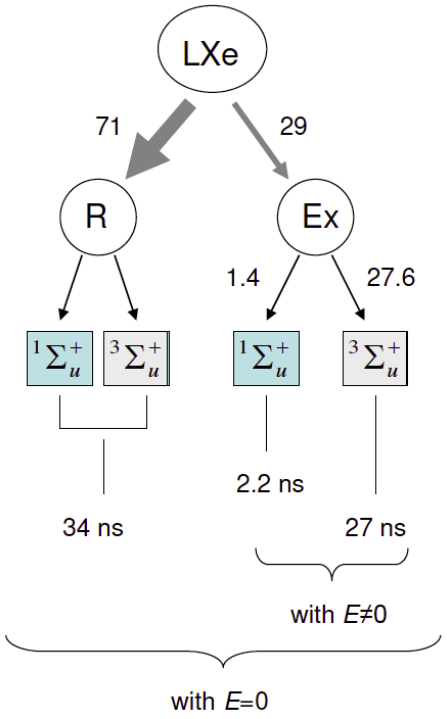

Figure 2.19.: Observalble fraction (in %) for recombination (R) and excitation (Ex) events for energy deposition by 0.5–1 MeV electrons in LXe [95].

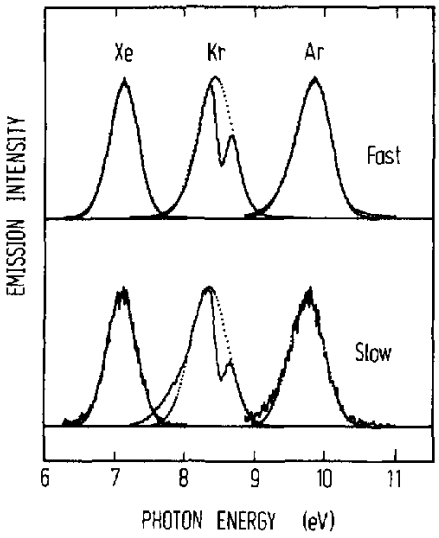

Figure 2.20.: VUV scintillation light spectrum of liquid xenon, krypton and argon [223]. The xenon spectrum peaks at 6.97 eV or 178 nm.

time constant also changes due to a different ratio of the excitation and recombination branches. These quantities are likely to also depend on the angle between the trajectory of the penetrating electron and the electric field due to columnar recombination effects [270].

Liquid xenon emits VUV scintillation light around 178.00 nm with a peak witdh $\Delta\lambda_{\text{scint}}$ of 14.35 nm [176]. The VUV spectrum is shown in figure 2.20. A small fraction of infrared photons of $\gtrsim$0.2 photons/keV (estimation from [95]) with wavelengths around 1.3 µm have also been observed [82, 83]. Their origin is not fully understood however they are believed to originate from the atomic transition from higher excited (vibrational) levels to the first excited state in the direct excitation branch [95].

The scintillation light yield depends on the interacting particle type and its stopping power with a minimum scintillation photon W-value of $W_{\text{sc}}^{\text{min}} = 13.8\,\text{eV}$ for baryons (see fig. 11 in [95]). For ^{207}Bi-electrons at 0.976 MeV, the scintillation light yield is significantly smaller with a W-value of 21.6 eV corresponding to a yield of 46.3 photons/MeV [120].

2.3.4. Liquid xenon detectors

Many experiments use xenon or liquid xenon as detector material to profit from the excellent properties of xenon as detector material. Pioneering work to establish xenon detectors has been accomplished with the Gotthard, EXO-200 and MEG detectors [309, 58, 219]. Table 2.5 lists some present and future liquid xenon detectors with scintillation light readout using Silicon Photomultipliers (SiPMs) or Photomultiplier Tubes (PMTs).
Most of the experiments search for new physics such as dark matter (DM) and $0\nu\beta\beta$-decay or more exotic processes as the neutrinoless μ-decay. Other detector types are conceived to investigate coherent elastic neutrino-nucleon scattering (CEνNS) or for medical applications as LXe-based positron emission tomography.

2.4. Silicon Photomultiplier

Silicon Photomultiplier (SiPMs) are pixelated semiconductor photosensors with single-photon resolution. They consist of an array of individual Single Photon Avalanche Diodes (SPADs) that share the same silicon substrate. Each SPAD is operated in Geiger-mode above the reverse current breakdown voltage of the pn-junction. Several publications provide an overview of the basic SiPM structure and characteristics, e.g. from D. Renker [259, 260], V. Saveliev [268] or G. Barbarino et al. [70]. Other names for SiPMs are *Geiger Avalanche Photo-Diodes* (G-APD), *micro-channel APD* or *Multi Photon Pixel Counters* (MPPC).
SiPMs offer a compact and robust geometry, low power consumption, insensitivity to magnetic fields and easy scalability [241]. SiPMs can be manufactured with high radiopurity materials [237] and recent developments also led to new SiPM models that exhibit a reasonable PDE in the VUV-regime [174]. All this makes SiPMs particularly interesting for photosensitive systems in liquid noble gas based, low-background experiments e.g in the $0\nu\beta\beta$-decay or dark matter search community. SiPMs also exhibit much smaller levels of electronics noise due to their high gain. They increasingly replace Avlanache Photo-Diodes (APD) and promise improved energy resolution performances [174, 226].

2.4.1. Solid state photon detectors

Solid state photon detectors have been conceived first in the early 1960s by McIntyre [208] and Haitz [158] who developed the first p-i-n-photodiodes. Such diodes convert incoming light into current to detect photons. p-i-n-photodiodes consist of a semiconductor crystal, typically silicon, with a p- and n-doping layer separated by a broad intrinsic layer as shown in figure 2.21. The doping provides majority charge carriers to form a depletion region in the intrinsic layer that acts

Experiment	Application	Status	Fid. mass	Signal type	PD type	Reference
XMASS	DM	Operation	835 kg	Scint.	PMT	[4]
XENON1t	DM	(Operation)	1042 kg	Scint. + Charge	PMT	[44]
LUX	DM	Operation	370 kg	Scint. + Charge	PMT	[14]
PandaX-II	DM	Operation	580 kg	Scint. + Charge	PMT	[111]
KamLAND-Zen	$0\nu\beta\beta$	Operation	343 kg	Scint.	PMT	[143]
XENON-nT	DM	Start in 2020	6000 kg	Scint. + Charge	PMT	[44]
LZ	DM	Start in 2020	7000 kg	Scint. + Charge	PMT	[211]
DARWIN	DM++	Design	50000 kg	Scint. + Charge	R&D	[1]
EXO-200	$0\nu\beta\beta$	Operation	250 kg	Scint. + Charge	APD	[58]
nEXO	$0\nu\beta\beta$	Design	5000 kg	Scint. + Charge	SiPM	[32]
RED-100	CEνNS	unclear	100 kg	Scint. + Charge	SiPM	[16]
MEG-II	$\mu \rightarrow e\gamma$	Construction	300 kg	Scint.	SiPM	[65]
XEMIS2	PET	Construction	200 kg	Scint. + Charge	PMT	[139]
PETALO	PET (TOF)	Concept	200 kg	Scint.	SiPM	[264]

Table 2.5.: List of current and future experiments using liquid xenon as detector materials. The table contains the application of the detectors along with their current status, the (fiducial) liquid xenon mass, the signal which is exploited (Scintillation and/or charge) and the type of photosensor used for the xenon scintillation light detection.

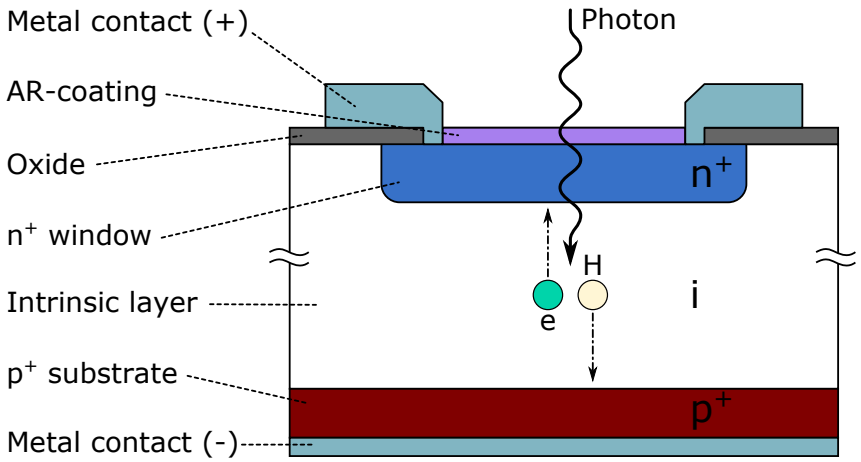

Figure 2.21.: Schematic planar p-i-n-photodiode according to Haitz [158, 159]. A silicon substrate is equipped with a p^+ bottom layer and an n^+ top region. They are separated by a large intrinsic layer to form a photo-absorbing, depleted volume. Incident photons will transfer their energy to the substrate and create pairs of electrons (e) and holes (H).

as absorption volume for incoming photons. A reverse bias voltage V_{bias} is applied to metal contacts on one side to increase the potential of the pn-junction and to deplete the entire intrinsic layer. The doping concentration can be increased by several orders of magnitude (p^+ and n^+) to reduce the thickness of the doping layers required for full depletion. Additional anti-reflective (AR) coatings can be applied to match the refractive indices of silicon and air.

Incoming photons with an energy exceeding the band gap of the semiconductor (1.124 eV at 300 K for silicon [77]) can be absorbed in the diode via the photoelectric effect. The photon energy is transferred to an electron which is excited to the conduction band resulting in an electron-hole-pair. The electron is drifted to the n-doping layer due to the intrinsic electric field while the hole drifts to the p-layer resulting in a net photo-current. Recombination does not occur within the depletion region due to the absence of free charge carriers emphasising the importance of fully depleted diode volumes. Electron-hole-pairs produced outside of the depletion region do not contribute to the photo-current due to the absence of a drift field unless they manage to diffuse into the depletion region. The photo-current is proportional to the intensity of the incoming photon flux. p-i-n-photodiodes can be used at relatively high fluxes starting at a signal of about 200 electron-hole-pairs [260].

Photodiodes can be made sensitive to lower photon fluxes via internal multiplication of the electron-hole-pairs. Internal multiplication or gain can be achieved with higher internal electric fields – strong enough to start avalanches in the silicon matrix [158]. If the field strength is sufficient, drifting charge carriers gain enough

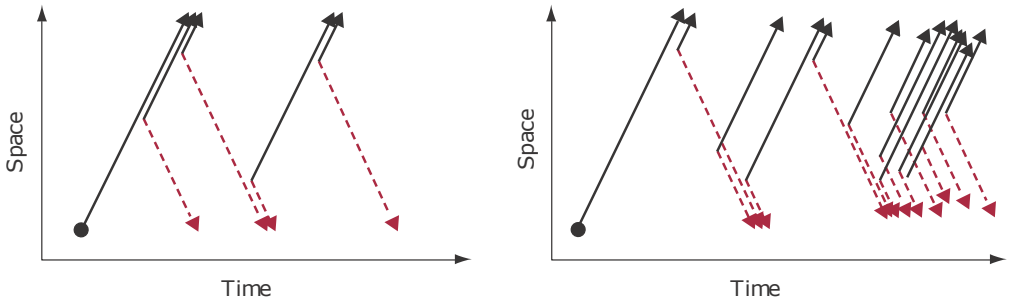

Figure 2.22.: Schematic representation of a simple avalanche below (left) and a self-sustaining avalanche above (right) the breakdown voltage of the pn-junction. Electrons are drawn with black lines and holes with red dashed lines [60].

kinetic energy to create secondary electron-hole-pairs via impact ionisation. These secondary pairs are accelerated again and create additional charge carriers and so on. An example charge carrier avalanche is depicted in the left in figure 2.22. Both electrons and holes or electrons alone may ionise additional electron-hole-pairs depending on the material and field [60]. The strength of this internal gain depends linearly on the external bias voltage in first approximation and can be manipulated accordingly. Detectors making use of internal multiplication via avalanches are called Avalanche Photodiodes (APD) and operate at gains of 50–200. They are sensitive to signals of about 10 photoelectrons [260].

To achieve single-photon sensitivity, the external bias voltage has to be increased above the so-called breakdown voltage V_{bd} [294]. In this regime, the production rate of electron-hole-pairs exceeds their extraction rate from the diode leading to an exponential increase in the photocurrent as shown in the right in figure 2.22. The avalanche becomes self-sustaining and transposes the entire available diode capacitance. This leads to an infinite gain if the avalanche remains unquenched. Such diodes are called *Single Photon Avalanche Diode* (SPAD). Self-sustaining avalanches can be a serious threat to the integrity of the SPAD but also provide the multiplication factors necessary to detect single photons. The avalanching quenching and the bias voltage above breakdown need to be operated in a sweetspot to consider both effects. The SPAD is completely insensitive to new photons during most of the avalanche breakdown so quenching is also required to re-activate the SPAD and reduce dead time. This operation regime is called Geiger-mode [60] and corresponds to the working principle of PMTs. The voltage exceeding the breakdown voltage is called overvoltage $\Delta V = V_{\mathrm{bias}} - V_{\mathrm{bd}}$. The operation regimes are schematically shown in figure 2.24.

SPADs are usually realised as *reach-through* structure where a second pn-junction is introduced to form the Geiger-mode region [208]. A schematic SPAD cross section is shown in figure 2.23. An additional p-layer is added to the typical

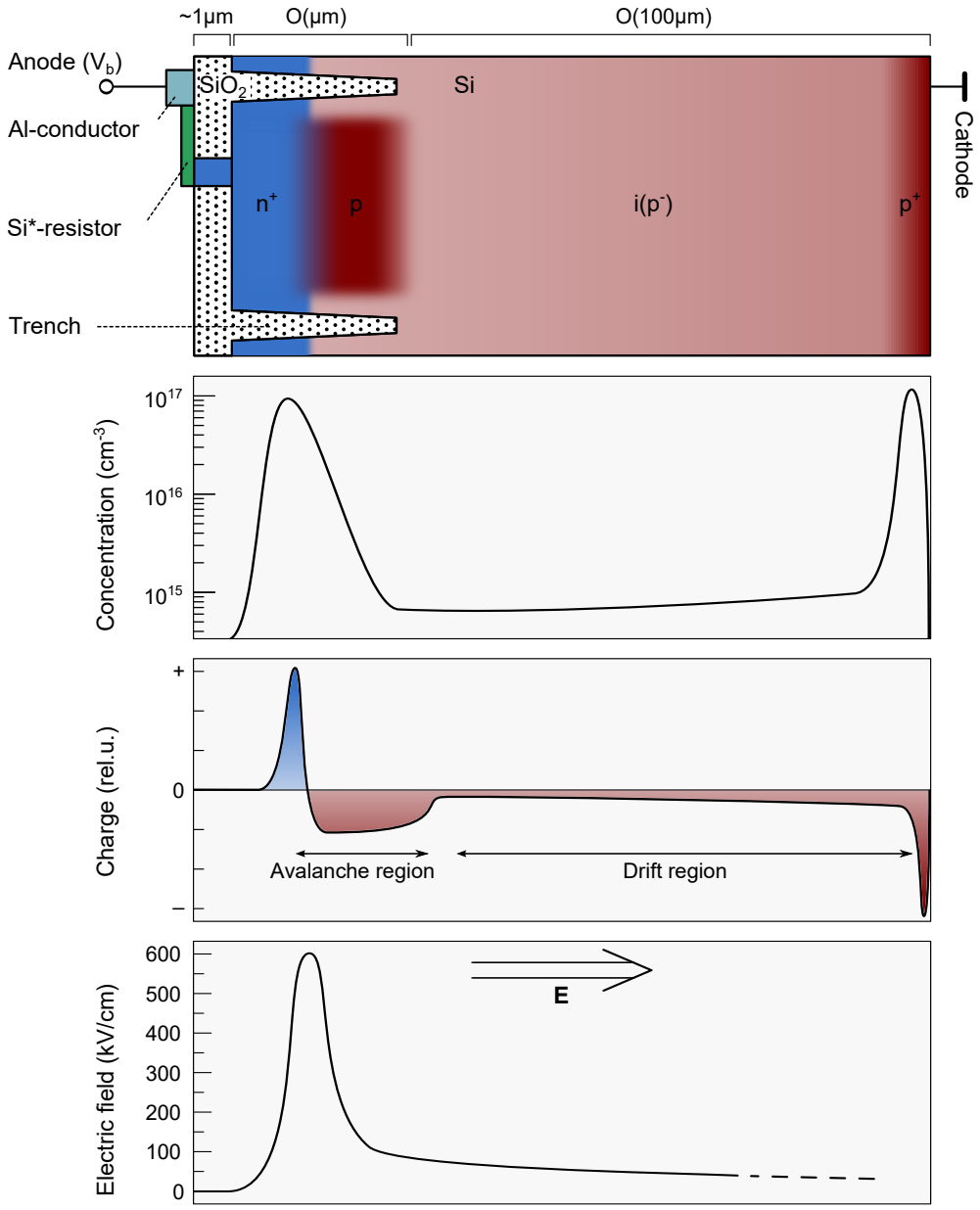

Figure 2.23.: Schematic view of a SPAD. The SPAD consits of a compact high doping concentration pn-junction at the top and a deep slightly doped substrate beneath (adopted from [6] and [86]). The high doping concentration pn-junction provides a large charge density and high electric field for the avalanche breakdown while the intrinsic layer (i) acts as photon absorber. Photoelectrons released within the substrate are drifted to the avalanche region to trigger avalanche breakdown. The doping profile is taken from [279], the electric field profile from [86] and [279].

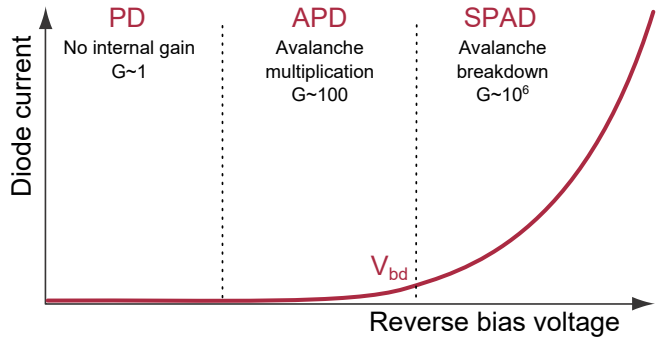

Figure 2.24.: Scheme of the different operation regimes of solid state detectors based on their internal multiplication. To realise avalanche breakdown in SPADs, a reverse bias voltage above the breakdown voltage V_{bd} is required. Plot based on [158].

p-i-n doping profile in close proximity to the n^+ region. This creates a compact pn-junction with high doping concentrations and a high electric field strength where avalanche breakdown can occur. This avalanche region (sometimes also multiplication or high-field region) has a width in the order of micrometers. The lateral dimension of a SPAD is determined by the size of the p-layer. The SPAD is limited by n^+ guard rings at the edges of the p-layer or virtual guard rings [147]. This prevents edge-breakdown but also introduces a source of large leakage currents. The intrinsic substrate is slightly p-doped (p^-) providing a monotone field gradient. Photons absorbed in this layer create charge carriers that are drifted along the electric field lines ("reached through") to the multiplication region and trigger the breakdown. This drift region comprises most of the detector and provides a large photon absorbing volume. Electron-hole-pairs created in a part of the substrate not covered by the p-layer are not drifted to the avalanche region and cannot be detected. The geometric fraction of photo-active to total surface is called *fill-factor* (FF) and is an important characteristic parameter. SPADs have lateral dimensions between 5 and 75 µm [6, 146] and FFs up to 80 % [6]. The p^+ layer at the bottom is electrically contacted to apply the external bias voltage V_{bias}. The n^+ layer is electrically connected via a polysilicon resistor to quench avalanches.

2.4.2. Avalanche breakdown in SPADs

The SPAD pulse shape is strongly connected with the evolution and quenching of the avalanche breakdown. It can be separated in different stages depicted schematically in figure 2.25. The figure shows a part of the IV-characteristics around the breakdown voltage (red) in the upper left and an electrical circuit model of a SPAD according to [158] in the lower left. The plots in the right show the current and voltage evolutions.

In **off condition**, the switch S in the diode circuit is open, the diode capacitance is fully charged and no current is flowing: $I_D = I_Q = 0$. The diode voltage V_D is equal to the applied external voltage V_{bias}. Avalanche breakdown is triggered via photoelectric or thermal excitation of substrate electrons to the conduction band.

As soon as a charge carrier is excited within or drifted to the avalanche region, the switch S is closed and avalanche breakdown ocurs with a certain turn-on probability p_{01} or **triggering probability** p_{trig} [158, 209]. p_{trig} depends strongly on the electric field profile, the overvoltage ΔV [234] and the impact ionisation rate α [103]. p_{trig} is significantly larger for electrons than holes which is why SPAD doping profiles are designed with an n-layer on top and the photo-absorbing volume below so that electrons trigger the avalanche breakdown [234]. Avalanche triggering is a field of active research as various processes are still not understood in detail [140].

If an avalanche is triggered, **breakdown** occurs and charge carriers are accelerated in the Geiger-mode pn-junction. They create new carrier pairs via impact ionisation and an exponential growth in the diode current starts (arrow 1). The free carrier density is called a *microplasma* [266] – a well studied phenomenon in reverse biased silicon [208, 98]. The microplasma evolves quickly longditudinally along the electric field lines passing through the entire high-field region [287]. Currents get up to $\mathcal{O}(\mu A)$ within $\mathcal{O}(ps)$ [103]). The lateral spread of the microplasma is governed by diffusion with durations around $\tau_{on} = \mathcal{O}(100\,ps)$ [277] but produce the majority of the avalanche current ($\mathcal{O}(10\mu A)$) [103]). The typical size of a microplasma is 10 µm. Additional microplasmas can be triggered via emission of photons within the avalanche process [98, 144, 227]. The diode current I_D is shown in blue in figure 2.25. The exponential increase in current only happens if the impact ionisation rate exceeds the extraction rate of the free carriers from the diode. This is the best definition for the Geiger-regime [60].

In **on condition**, the exponential increase of the diode current stops as soon as the free carrier density lowers the electric field of the pn-junction. The ionisation rate drops since it scales with the overvoltage ΔV [287]. The maximum current is $\Delta V/R_D$. The entire diode capacitance C_D discharges to V_{bd} with a time constant of $\tau_{bd} = R_D{\cdot}C_D$ (arrow 2). The diode resistance R_D corresponds to the series resistance of the space charge region and the silicon bulk. τ_{bd} is much larger than the carrier transit time in the microplasma so the evolution speed of the plasma is large [234]. While the diode current I_D decreases due to the reduced field, the external current I_Q starts to grow due to the increasing free carrier density (cyan in figure 2.25). The voltage V_Q over the quenching resistor R_Q increases and the diode voltage V_D available for the microplasma drops. As soon as V_D reaches V_{bd}, an equilibrium between ionisation and extraction rate is reached and the microplasma evolution ends maintaining a constant diode current $\Delta V/(R_D + R_Q)$ via self-sustaining avalanches.

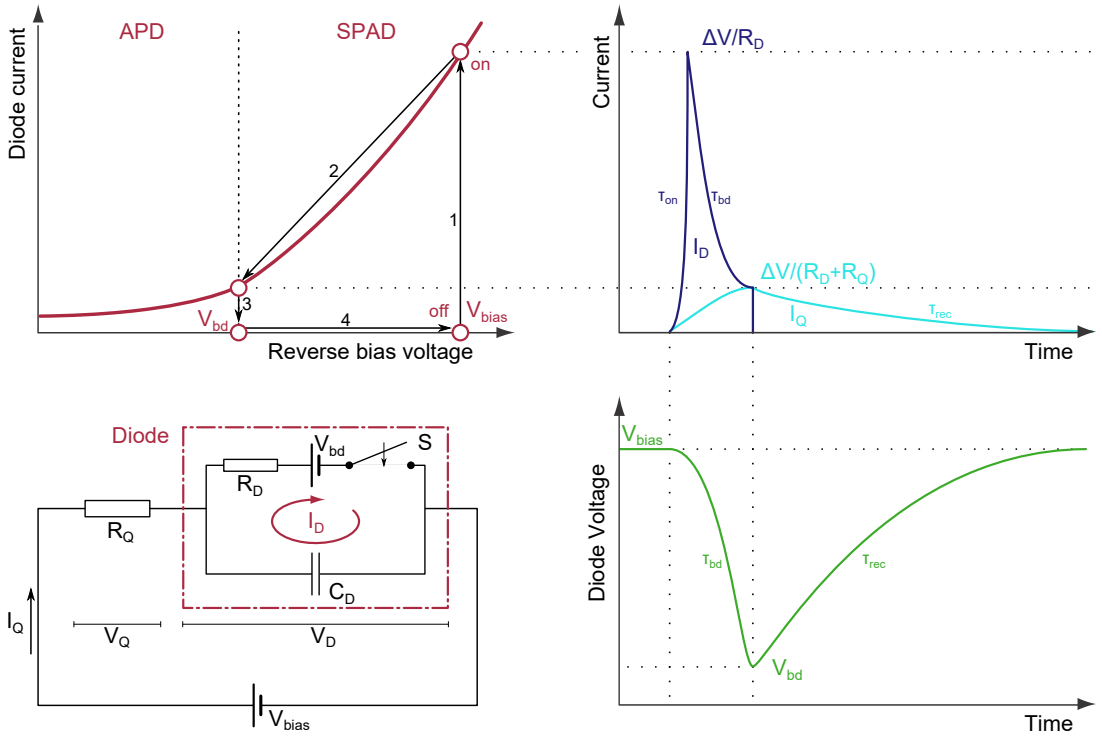

Figure 2.25.: Schematic overview of a SPAD pulse cycle. *Bottom left:* electronic circuit model for a SPAD consisting of the diode the a quenching resistor R_Q. *Top left:* IV-characteristics above the breakdown voltage V_{bd}. The avalanche breakdown cycle starts in the off-condition followed by the microplasma evolution, the quenching process, the turn-off and the SPAD recovery. *Right:* schematic evolution of the diode current I_D, the external current I_Q and the diode voltage V_D.

At the breakdown voltage V_{bd}, there is a non-zero **turn-off probability** p_{10} for a fluctuation of the number of charge carriers in the avalanche region to zero [158]. This correponds to re-opening switch S (arrow 3). The quenching resistor R_Q guarantees that the diode voltage V_D cannot exceed V_{bd}. This shuts off the external energy source driving the impact ionisation rate and boosts p_{10}. The resistance R_Q is typically 100 kΩ up to 10 MΩ [108, 146]. Compared to the recovery time, the turn-off time is very short for such R_Q values with about $\mathcal{O}$(1ns) [103, 158]. Active electronics can be used to quench avalanches externally. This requires more complex circuits but avoid downsides of the slow SPAD recovery [108].

Finally, the SPAD **recovers** via R_Q to its full capacitance with a time constant $\tau_{rec} = R_Q \cdot C_D$. Charge carriers released during the recovery may trigger new avalanches. These *correlated avalanches* experience a reduced triggering probability and a reduced avalanche current due to the smaller V_D which has not yet recovered to V_{bias}. The full recovery time is typically around $5\,\tau_{rec}$.

The multiplication factor of a SPAD is called gain G. The gain represents the total number of charge carriers released in one avalanche breakdown:

$$G = Q/\mathrm{e} = C_\mathrm{D}\,\Delta V\,/\,\mathrm{e} \sim 10^6 \tag{2.10}$$

The gain depends linearly on ΔV for bias voltages not too close to V_bd. A large gain produces stronger signals but is also prone to increasing noise as explained below in section 2.4.4. The optimal operation ΔV has to be chosen to take both effects into account. The gain is independent of the ambient temperature T at fixed overvoltage.
The response of a SPAD to an avalanche breakdown can be monitored via the external current I_Q. The pulse shape is equal to the shape of the diode voltage V_D shown in figure 2.25 with a fast rise time τ_bd and a slow exponential recovery governed by τ_rec [158]. Both time constants depend on temperature since they couple to the resistances R_D and R_Q. SPAD pulses can reveal two time constants for the recovery part with a narrow spike at the pulse maximum [103, 238]. This is due to a small parasitic capacitance of the quenching resistor [107]. In this case, this parasitic capacitance C_Q provide a fast current supply path in the beginning of the avalanche and dominates I_Q until C_Q is discharged and the slower SPAD recovery takes over. The parasitic time constant and the fraction of the pulse amplitude dominated by the parasitic spike both depend on temperature.
The total charge processed in one breakdown is always $C_\mathrm{D}\,\Delta V$. Microplasmas may evolve differently e.g. depending on the position of the plasma relative to the edge of the p-layer or if the avalanche breakdown is initiated by two or more photoelectrons [249]. This slightly affects the response pulse shape but not the total charge. SPADs are fully digital in the sense that either there is a breakdown or not – however if there is one, the response signal is always the same. This means, that SPADs lacks the ability to distinguish how many photons are absorbed and the output signal is independent of the number of incident photons. This is a characteristic property of Geiger-mode sensors [260]. On the positive side, this operation mode gives the high gain values required for single-photon detection.
The SPAD gain is independent of temperature [304] while the breakdown voltage is not [239, 256]. Both SPAD capacitance and quenching resistor depend on temperature as well which also affects the recovery time constant [239].

2.4.3. Working principle of SiPMs

Silicon Photomultiplier consist of 100–100 000 individual SPADs with a total surface area of 1–10 mm^2. The SPADs share the same silicon bulk and backside substrate (p^+ layer in figure 2.23) but are separated by intrinsic silicon between the p-layers forming the individual avalanche regions. Each SPAD is equipped with an own

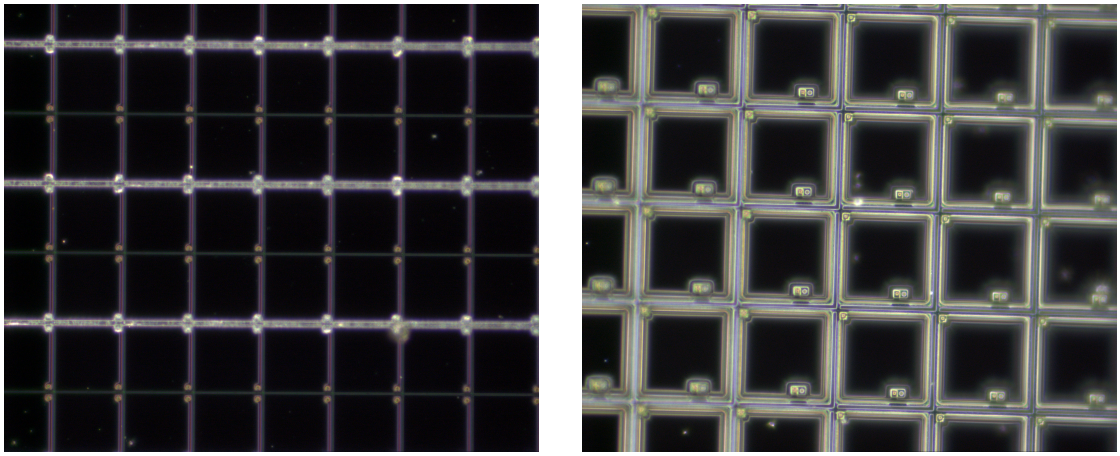

Figure 2.26.: Microscope pictures of SiPM models from different manufactures. *Left:* VUV-HD LF from FBK with a pixel pitch of 35 µm [147]. The horizontal conduction lines are shown in white and connect microcells on both sides via polysilicon resistors (purple). The microcells are mechanically separated by grooves (green). *Right:* MPPC S13370 4th generation (VUV4) from Hamamatsu with a pixel pitch of 50 µm [146]. The micro-structure is much more prominent and isotropic. The microcell connectors are attached close the centre of the microcell edge.

quenching resistor. The bias voltage is applied via conducting strips on the surface (bluish in figure 2.23) to all SPADs thus connecting the SPADs in parallel. Each SPAD including the resistor and bias strip connector corresponds to one microcell in the pixel matrix of the SiPM. The pixel sizes vary between 5 and 75 µm depending on the SiPM model [6, 146].

Modern SiPM models are equipped with additional trenches to optically decouple the SPADs from photons emitted during avalanche breakdown (black polka dots in figure 2.23) [144, 227]. Trenches are cut into the material for the full depth of the high-field region or deeper and covered with metallic films with a high photo-absorption coefficient [242].

The quenching resistor and bias strip layout is designed to cover the non photo-sensitive regions of the SPAD below (trenches and guard rings) to maximise the geometric fill-factor FF. Typical quenching resistors are made of polysilicon with a custom resistance while aluminium is chosen for the bias strips. Together, they constitute the surface micro-structure. The layout and shape of this micro-structure varies strongly among the SiPM manufacturers as shown in figure 2.26.

The arrangement of SPADs within the SiPM matrix with a parallel connection scheme allows SPADs to remain photo-active while another SPAD undergoes avalanche breakdown. This allows SiPMs to count single photons. The second crucial property is the microcell uniformity. Each SPAD is required to produce the

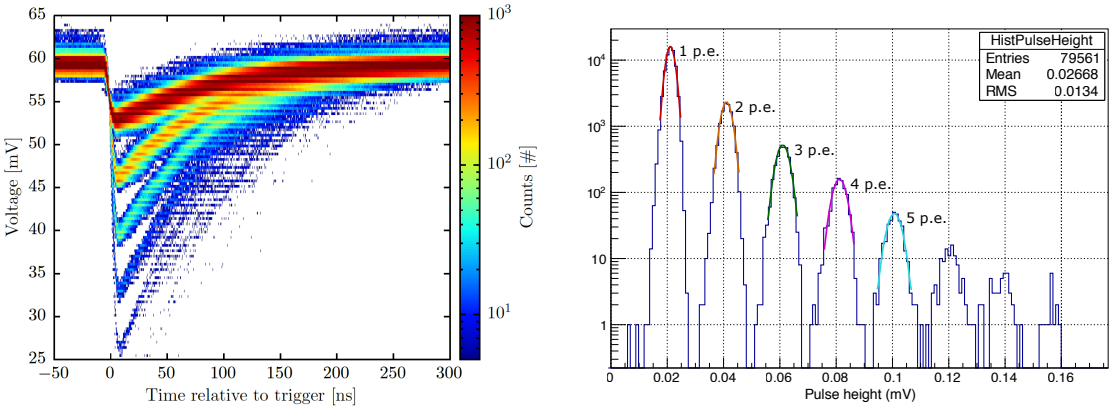

Figure 2.27.: Left: Example set of SiPM waveforms (signal amplitude vs. time) taken from [313]. The pulses are obtained with a scope using a trigger on an amplitude close to the baseline. **Right**: Pulse height histogram of a different set of waveforms which can be obtained e.g. via a projection on the y axis of the maxima of each waveform or with multi-exponential fit models [237, 224]. The individual waveform bands (left) and pulse height peaks (right) correspond to photoelectron-equivalent (p.e.) levels. The p.e. levels are well separated if good cell-to-cell uniformity is achieved.

same response signal if breakdown occurs. Individual photons can then be counted via the combined signal of different but uniformly responding SPADs. Figure 2.27 shows an example set of waveforms from a typical SiPM. The timestamp at which pulses pass the trigger threshold is set to 0 ns, the colour corresponds to the density of the waveforms. All pulses have a steep drop associated with the microplasma evolution and a long recovery tail. If good cell-to-cell gain and electric uniformity is achieved, all pulses have the same shape and amplitude (about 7 mV). If two SPADs are triggered at the same time, the pulse has twice the height but the same exponential constants (amplitude around 14 mV) and so on. Eventually, each band corresponds to an increasing number of simultaneously fired microcells – denoted by photo-electron equivalents (p.e.). It can not be decided whether a microcell has been triggered by an actual photo-electron or via thermal excitation.

Figure 2.27 also shows a pulse height histogram of the amplitudes of a different data set recorded with a KETEK PM3350 SiPM at −20 °C and 5.3 V overvoltage. Pulse height histograms are essentially a y-projection of a set of waveforms (e.g. left in figure 2.27). Again, due to the good cell-to-cell uniformity, the response of a SiPM to a photon flux shows excellent separation of the peaks in a pulse height spectrum [235]. The peaks are spaced equidistantly due to the discrete nature of the SiPM response.

A matrix of SPADs introduces new capacitive couplings of each SPAD to the other microcells and to the parasitic grid capacitance. This requires a careful microcell and

micro-structure layout to avoid deterioration of the output pulses [107]. Electrical noise contributions due to these couplings are one reason for the increasing peak width with increasing p.e.-level in the histogram in figure 2.27. Current SiPM models allow single-photon resolution up to 22 p.e. and more before the individual pulse height peaks intermingle [174].
SiPMs show non-linear behaviour for medium and large photon fluxes due to the unavailability of a fraction of microcells during breakdown and recovery. Saturation occurs and the pulse height does not depend on the incident photon rate as soon as the rate is large in relation to the available number of microcells N_{px}. The mean number of fired pixels for a photon rate N_{ph} is given by

$$\bar{N}_{\mathrm{fired}} = N_{\mathrm{px}} \cdot \left[1 - \exp\left(\frac{-\,\mathrm{PDE}\cdot N_{\mathrm{ph}}}{N_{\mathrm{px}}}\right)\right] \tag{2.11}$$

where the PDE is the photon detection efficiency of the SPADs (see below) [265]. Non-linearity is a well-known problem for SiPMs and its modelling is a topic of current research [86, 138, 249].
The photon detection efficiency PDE is one of the most important characteristic properties of any SiPM. It describes the probability for an incident photon to get detected via an avalanche breakdown current pulse and can be written as:

$$\mathrm{PDE}(\Delta V, \lambda, \theta) = p_{\mathrm{trig}}(\Delta V) \cdot \mathrm{QE}(\lambda, \theta) \cdot \mathrm{FF} \tag{2.12}$$

which is the product of the triggering probability p_{trig} to start avalanche breakdown once a charge carrier pair is created, the quantum efficiency QE and the geometric efficiency or fill factor FF. The QE describes the probability for a photon to get absorbed within the silicon via the photoelectric effect. As explained above, p_{trig} strongly depends on the overvoltage while the FF predominantly depends on the doping layout of the high-field region. The QE depends:

- on the wavelength λ via the light absorption length $1/\alpha$ in silicon. $1/\alpha$ spans from 4 to 12 µm for optical wavelengths [57]. High-field regions are typically less deep to ensure that photons are predominantly absorbed below the high-field region. This is important to achieve electron triggered avalanches to benefit from their higher triggering probability. The QE becomes zero for photon energies above the silicon band gap (1.124 eV at 300 K for silicon [77]) [252] and for very short wavelengths where photons are absorbed in undoped surface layers without electric field. An example PDE curve of an FBK NUV-HD with a 40 µm pitch is shown in figure 2.28.
- on the angle of incidence θ since reflection occurs at the SiPM surface reducing the photon flux transmitted into the silicon substrate. Photons may be reflected at the microcell surface i.e. bare silicon or silicon compounds as SiO_2

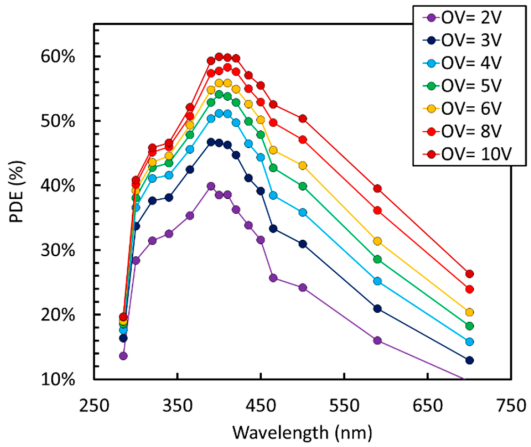

Figure 2.28.: PDE of an FBK NUV-HD SiPM with 40 µm pitch. The wavelength dependence is governed by the QE and depends on the light absorption length. The overvoltage (OV) dependence is governed by the triggering probability [147].

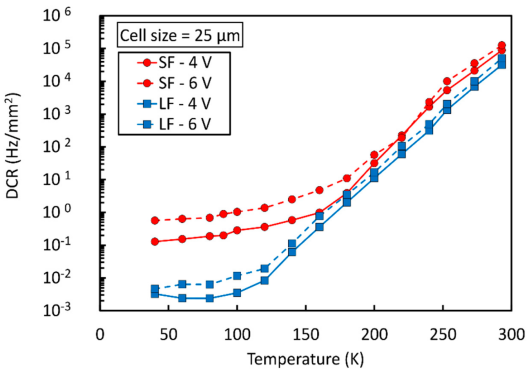

Figure 2.29.: Dark count rate (DCR) over temperature for two FBK NUV-HD models. Dark noise occurs via thermal excitation of electrons to the conduction band which leads to the exponential branch. At low temperatures, inter-band tunneling dominates [147].

or SiC. Photons are also reflected by the micro-structure producing complex scattering patterns due to the periodicity of the pixel pitch. Understanding the reflection profile of SiPMs is crucial to understand the PDE and the response of a SiPM to a light field with various angles of incidence as it occurs in nEXO (see [32], section 4.1.4.1). This eventually influences the whole detector design which aims to maximise the photon collection efficiency. This is the motivation for chapter 3 of this thesis.

2.4.4. SiPM noise sources

There are three main noise sources in SiPMs: dark noise, electronic noise and correlated avalanches. Dark noise is produced by thermally generated charge carriers pairs, electronic noise is induced by capacitive couplings or induction and correlated avalanches are additional avalanches that occur in correlation with an initially triggered pixel.

Dark noise (DN) originates from thermally generated charge carriers in the silicon that trigger an avalanche without any external photons [159]. DN-induced breakdown cannot be distinguished from photo-electron events. Dark noise depends exponentially on temperature with a freeze-out around 150 K with inter-band tunnelling dominating below (see figure 2.29). The tunnelling regime is strongly

field-dependent due to field-assisted effects [103]. A large fraction of dark noise events have been shown to originate from few faulty SPADs due to defects or sub-micro-cells. Excluding such regions can reduce the dark noise rate by one order of magnitude [128].
Electronic noise is induced by external electromagnetic radiation or imperfections in the electric components of both SiPM micro-structure and pre-amplification stages. Additionally, parasitic capacitive coupling contributes to this noise source as discussed above [107].
There are two main effects resulting in correlated avalanches. *Crosstalk* occurs in pixels neighbouring an initially triggered microcell due to optical coupling [87]. This can happen as prompt crosstalk or with a certain drift time delay depending on the depth in which the neighbouring cell is triggered. *Afterpulses* occur in initially triggered pixels some time after the initial avalanche [259]. The correlated avalanche probability is the sum of the probabilities for all processes that lead to additional avalanches subsequent to an initial breakdown.

Crosstalk occurs via the emission of photons in a microplasma triggering additional avalanche breakdowns in neighbouring microcells. Light emission from reversed-biased silicon pn-junctions during breakdown is a well-studied phenomenon [98, 227]. However, there is still no generally accepted understanding of the details of the emission process [87, 221]. Three main emission mechanisms have been proposed so far: (1) photon-assisted inter-band transitions (recombination), (2) direct radiative transitions between different sub-valence-bands (intra-band hole transitions) and (3) bremsstrahlung of hot electrons [157, 300]. Theoretical frameworks for all mechanisms exist with band structures and carrier temperatures taken into account [144, 84, 306]. Reported emission spectra however differ strongly and there is no agreement on a specific dominant mechanism or multi-mechanism model [15]. Published studies reported emission in the infrared [157, 240] or visible regime [227, 98, 152, 190][2] with carrier temperatures between 2000 and 7000 K [240, 98, 114][3]. The emission efficiency is reported to be in the order of 10^{-5} photons per charge carrier crossing the pn-junction [190, 221, 240]. Disagreements yet still exist in the spectral part evaluated for emission efficiency estimations [221]. There are good arguments that only a narrow energy range is relevant for crosstalk since higher energetic photons are likely to be absorbed within the initial microcell while photons with long wavelengths are not absorbed at all. These considerations yield a relevant range between 1.15 and 1.4 eV and an emission efficiency of 3×10^{-5} [240]. As a consequence, a breakdown microplasma with a typical gain around 10^6 emits about 30 photons potentially triggering additional microcells.

[2] Citations sorted chronologically.
[3] Citations sorted by temperature.

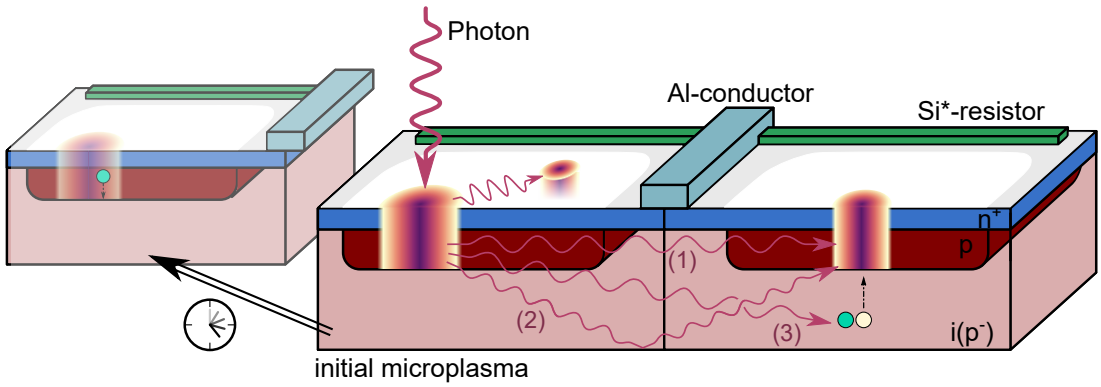

Figure 2.30.: Schematic view of an array of SPADs suffering from correlated avalanches. The initially triggered microplasma (centre) emits photons that trigger crosstalk in a neighbouring cell (right). Crosstalk can be prompt – via direct optical coupling (1) or internal reflection (2) – or delayed if a photon emitted in the microplasma is absorbed in the intrinsic layer and the charger carrier first need to drift to the avalanche region (3). Afterpulsing occurs if a charge carrier is trapped within the avalanche region and triggers a second avalanche in the initial microcell after a certain trapping time (left).

Optical coupling between microcells can occur in three main ways shown in figure 2.30: (1) direct coupling of two high-field regions, (2) optical coupling of two high-field regions via reflection on the bottom of the silicon bulk [257] and (3) if the emitted photon is absorbed in the intrinsic region of another microcell instead of the high-field region. Coupling (1) and (2) lead to prompt crosstalk which coincides with the initial pulse resulting in higher p.e.-levels as in figure 2.27 even under dark conditions. Coupling (3) leads to *delayed crosstalk* with additional 1 p.e. pulses delayed by the drift time it takes the charge carriers to reach the avalanche region which in turn depends on the depth of absorption. The direct high-field region coupling (1) can be drastically reduced with the introduction of trenches to mechanically separate the microcells. Oxide fillings and high Z metallic depositions at the trench-substrate interfaces are used to establish high absorption cross-sections for photons responsible for crosstalk [242]. Such trenches are also depicted earlier in figure 2.23.

Crosstalk is undesirable source of noise since a single incident photon is counted as if two or more incident photons trigger a similar number of avalanches. This poses a problem for light readout systems of SiPM based photo-detectors [87, 123]. The crosstalk probability p_{CT} can be determined via the probability of one initial cell to produce crosstalk in general, or as an average number of additionally triggered avalanches. The latter corresponds to the overall charge contribution due to crosstalk (example studies can be found in [123, 239, 254, 304]). Both metrics are found in literature and show different overvoltage dependencies [203]. Crosstalk

can also be modelled analytically via combinatoric considerations of a photo-active SPAD array [138, 307]. Comparisons with data show that the main contribution to crosstalk comes from the four nearest neighbour pixels around the initially triggered microcell [138].

Afterpulsing occurs if charge carriers within an avalanche get trapped by crystal defects, impurities or other local trapping centres in the avalanche region. These carriers are released after a certain trapping time and may trigger additional but delayed breakdowns in the same microcell. This is depicted in the left in figure 2.30. The characteristic trapping time depends on the kind of trapping centre. Several time constants have been found to manifest in pulse timestamp analyses ranging from several nm to more than 1 µm [237]. Afterpulses with short time delays contribute little to the SiPM response as the microcell is not yet fully recovered from the initial breakdown. This reduces both the triggering probability and the afterpulse amplitude [259]. As a consequence and unlike as for crosstalk, the mean number of afterpulses is not equal to the correlated charge contribution since the additional released charge depends on the recovery state of the microcell [174]. This affects the definition of the afterpulsing probability p_{AP} and, again, different interpretations exist in literature.

Correlated avalanches are key characteristics in SiPM studies and various publications focus on these properties [174, 239, 254, 304]. Mathematical frameworks and useful notations are established in [85, 123, 237, 174]. Figure 2.31 shows a helpful summary of a SiPM response including correlated avalanches. Each dot represents one fitted pulse amplitude of a large set of SiPM waveforms. The amplitudes are converted to the charge released in a breakdown with photoelectron equivalent (p.e.) as unit. Initial pulses can suffer from prompt crosstalk (blue) resulting in pulses at higher p.e.-levels, or delayed crosstalk (purple) some time after the timestamp of prompt pulses. Afterpulses (orange) occur in the initially triggered microcells and show a smaller amplitude following the recovery state of the cell. Late pulses (green) are either afterpulses in fully recovered microcells or new initial avalanches triggered via dark noise. All individual effects can suffer from prompt crosstalk. This causes the characteristic distribution at and below 1 p.e. to repeat at higher p.e.-levels yet with reduced intensity (dashed).

Both crosstalk and afterpulsing increase with ΔV. Crosstalk increases due to the larger gain resulting in a larger number of photons emitted during breakdown while afterpulsing is booste by the larger number of electrons experiencing trapping. Afterpulsing time constants depend on field gradients in the multiplication region [109, 123, 304]. Crosstalk and afterpulsing probabilities do not change with incoming photon flux (down to dark conditions) nor with photon wavelength [280]. Temperature dependencies are observed for afterpulsing and delayed crosstalk but prompt crosstalk varies only little [239, 253]. The number of correlated avalanches

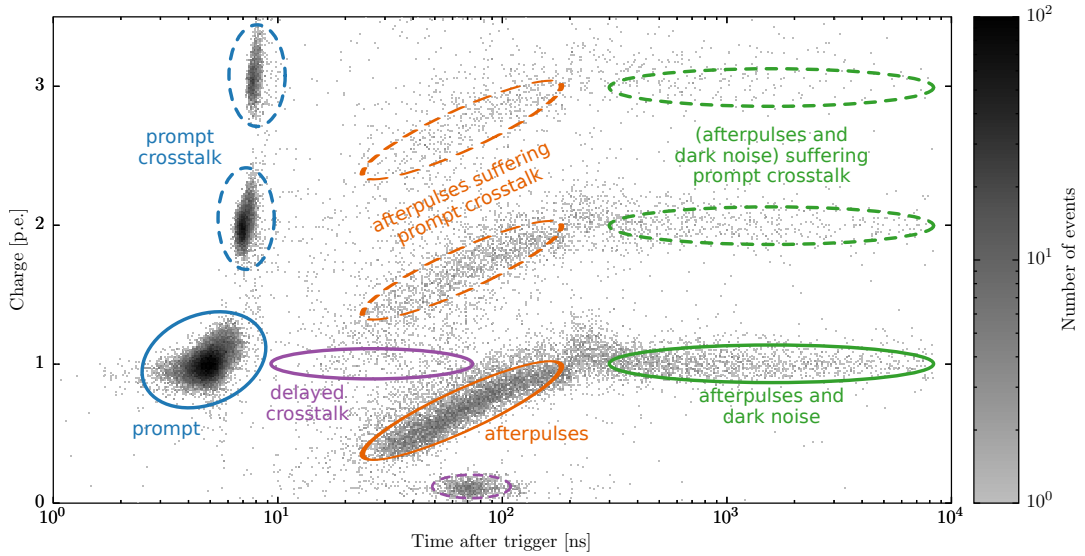

Figure 2.31.: Distribution of a set of SiPM pulse amplitudes in units of photoelectron equivalents (p.e.). Initial, prompt pulses (blue) are followed by delayed crosstalk events (purple) and afterpulses as a function of the time since trigger. Fast afterpulses (orange) present smaller pulse amplitudes following the recovery of the SPAD. Late afterpulses and dark count events (green) process the full SPAD charge inventory. Crosstalk (dashed) leads to a repeating pattern at higher p.e.-levels. Figure taken from [174].

has been found to decrease with temperature [34] while the charge contribution is independent [304]. Afterpulsing trapping times are reported to strongly increase at lower temperature [259].

2.4.5. VUV-light detection with SiPMs

UV light detection in silicon detectors is challenging due to the large absorption coefficient of silicon in this regime [57]. In fact, the absorption depth in silicon is less than 10 nm for wavelengths between 90–360 nm [311]. Incident UV photons are absorbed above the multiplication region and charge carriers need to be collected from a depth of $\mathcal{O}(1\,\mathrm{nm})$ for efficient UV detection. Additional surface depositions as passivation layers may too pose high absorption cross-sections – especially in the VUV – and carriers photo-generated there are not drifted to the multiplication region due to the absence of field gradients in these undoped layers [311]. This is shown in figure 2.32 where the simulated electric field of a SiPM is shown over the depth and compared with the fraction of UV photons surviving absorption. For this reason, standard commercial SiPMs usually present a rather low UV PDE – especially in the deep UV i.e. for LXe and LAr scintillation light [235].

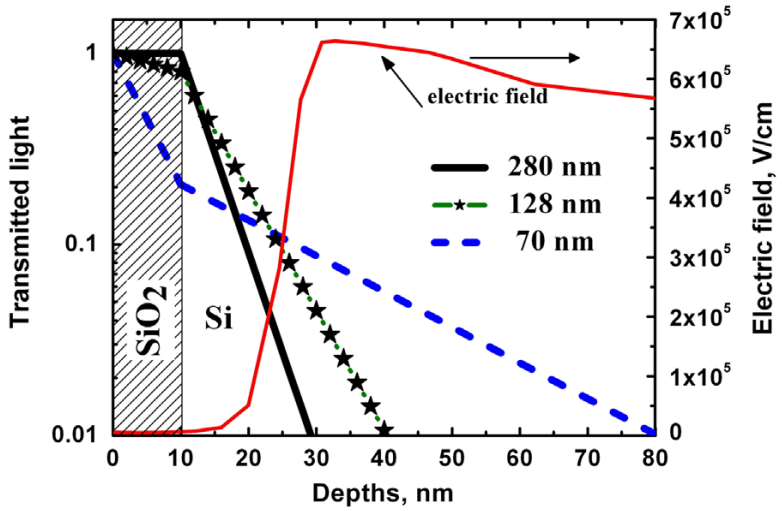

Figure 2.32.: Simulated vertical electric field profile of an example SiPM with a 20 nm pn-junction and a 10 nm passivation layer [311]. The plot also shows the photon distribution surviving absorption in the silicon and silicon dioxide for three example wavelengths. Reflection losses are not taken into account.

Several methods allow to adapt SiPMs for UV and VUV light detection and to improve the PDE in this wavelength regime:

- The thickness of anti-reflective coatings and passivation layers need to be minimal (i.e. $\mathcal{O}(1\,\text{nm})$) [235, 311]. As a drawback, electronic noise and reflection loses can be larger.
- The p-n junction needs to be as close to the surface as possible to achieve a larger field gradient in the first few nanometers and to increase the carrier collection efficiency by minimising the recombination probability in the undoped surface layers [247].
- Due to the higher triggering probability for electrons compared to holes, the vertical doping profile needs to be inverted [268]. In this *p-on-n* configuration, electrons are photo-generated above the high-field region and are allowed to trigger the avalanches just like they do in n-on-p configuration at larger wavelengths [6]. This requires an inverse pn-junction in an n^- substrate. This technique is also used for SiPMs optimised for blue light detection [247].
- Since avalanches are triggered from above, edge breakdown in the dead region between the multiplication region and the trenches becomes more likely. To avoid the reduced gain associated with edge breakdown, the doping concentration in the avalanche region needs to be increased [294]. This results in a thin high-field region and an abrupt pn-junction – a concept called *shallow*

doping [311]. As a result, the breakdown voltage is decreased significantly [294]. The optimisation via shallow doping is limited by tunnelling breakdown [247].

- The additional application of delta-doping layers very close to the SPAD surface likely increases the internal quantum efficiency significantly [229]. Delta-doping layers have a width of only a few Ångström and a large doping concentration to extend the influence of the internal electric field well to the SPAD surface.
- The quenching resistance, the optical insulation of the trenches and the optical matching to the operation medium need to be optimised. The fill factor needs to be improved via narrow dead regions. These statements are valid for every wavelength but especially important for VUV detection [235, 247].

2.4.6. VUV-sensitive SiPMs in Research and Industry

Large-scale liquid noble gas detectors have been successfully designed and operated in the last decades but require large photosensitve areas for the observation of rare particle interactions. Pioneering work in this field has been accomplished by EXO-200 [58], MEG [65] and XENON [43]. SiPMs with competitive photon detection efficiency for the VUV scintillation light of liquid xenon and argon [176] are now available. Large-area SiPM systems are operated or considered in various next-generation particle detectors, e.g. nEXO, DarkSide-20k, DUNE and the successful pioneering experiment MEG-II. The good single-photon resolution of SiPMs is suitable for experiments with very low photon rates while the fine pixel structure allows to introduce an additional reconstruction tool by analysing the light map of a large-scale detector precisely [113]. On the other hand, large-area photo-sensors require a large number of channels and feedthroughs which poses a challenge from

Experiment	Mat.	SiPM model	Photo. area	Ref.
MEG-II	LXe	Hamamatsu VUV2	0.589 m^2	[65]
nEXO	LXe	FBK, Hamamatsu, 3DdSiPM	4.5 m^2	[32]
DARWIN	LXe	SiPMs are one option	8.1–12.0 m^2	[1]
DarkSide-20k	LAr	FBK NUV-HD	13.0 m^2	[2]
Argo	LAr	SiPM is baseline option	$\approx$ 200 m^2	[210]
Proto-DUNE-SP	LAr	Hamamatsu and SensL	Light guide	[255]
DUNE	LAr	R&D	Light guide	[5]

Table 2.6.: List of particle physics detectors based on liquid noble gases as detector material that are using or planning to use SiPMs for photon readout. The experiments are sorted by their photosensitive areas.

the background level point. A compromise must be found between photo-active area and granularity of the photo-sensor channels. Table 2.6 lists some current and future particle detectors using SiPMs including their photo-active area.
nEXO aims at 1 % energy resolution (σ) at the Q-value. This requires a photon collection efficiency of at least 3 % [32]. A PDE of at least 15 % at 178 nm and at a bias voltage that results in a probability for correlated avalanches of less than 20 % within 1 µs is necessary to achieve the energy resolution goal. Additionally, the SiPM dies are required to be at least 1 cm^2 in size and need to be ganged to SiPM tiles to keep the number of readout channels reasonable. The nEXO collaboration has investigated different SiPM prototypes manufactured by FBK and Hamamatsu in the recent years and essential progress has been made to meet above requirements [237, 174, 140]. Additionally, the dynamic range of possible overvoltages with stable amplification has been seen to increase [256] and the radioactive contamination of SiPM materials has been sucessfully reduced [237].
Manufacturers as Hamamatsu from Japan, FBK from Italy and SensL from Ireland are among the world leaders in this UV photosensor technology. The development of VUV-sensitive SiPMs is currently driven by the astroparticle physics community, however there are possible applications in other fields from material sciences to medical imaging. For example, time-of-flight positron-emission-tomography (TOF-PET), UV lithography monitors and Laser-Induced Breakdown Spectroscopy (LIBS) could profit from UV-sensitive, pixelated semiconductor photo-sensors.
SiPMs have gained a lot of attention in the last decade considering both particle detectors and industrial applications and are seen as a strong candidate for the ultimate low light-level photosensor. The Horizon 2020 funded SENSE project sees an enormous innovation potential when it comes to a replacement of PMTs by the new SiPM technology according to their roadmap [278]. The future development process of UV-SiPMs for industrial applications will be focused on the increase of the PDE in the UV-region and the radiation hardness of the bulk material.

3. UV-Reflectivity of SiPMs in Liquid Xenon

Table of contents:

The proper simulation of events in the nEXO detector is crucial to prove that the claimed efficiency goals can be reached. The simulation also plays an important role when it comes to the proper reconstruction of events based on their charge and light signal. The light collection efficiency from events in the detector depends on the event location (the so-called light map) but also on the optical properties of all internal components. Reflection at the SiPM surface drastically reduces the photon detection efficiency (PDE), as outlined in section 2.4.3, and affects the photon transport efficiency (PTE) in nEXO. The simulation of the light map and the optimisation of the internal detector to maximise the PTE require precise knowledge of the SiPM reflectivity. In this chapter, the first-ever systematic reflectivity studies of SiPMs in liquid xenon and for VUV-wavelengths are presented. The measurement setup and analysis are explained beforehand.

3.1. Reflection Phenomena

3.1.1. Definition

There is one general agreement on the terms *reflection* and *reflectance* defined by the US National Bureau of Standards [228]:

> "*Reflection* is the process by which electromagnetic flux (power), incident on a stationary surface or medium, leaves that surface or medium from the incident side without change in frequency; *reflectance* is the fraction of the incident flux that is reflected."

Typically, reflectance describes the behaviour of a thin layer of a reflecting material while the term reflectivity is used for larger samples as examined in this thesis. The electromagnetic flux can be seen as an incident beam $\boldsymbol{k}_\mathrm{i}$ hitting a sample surface with normal $\boldsymbol{n}$ under a polar angle θ_i and an azimuthal angle ϕ_i with a total flux of Φ_i. This is depicted in figure 3.1. A fraction of the incident flux is reflected off the surface as $\boldsymbol{k}_\mathrm{r}$ with a specific angular distribution in θ_r and ϕ_r i.e. $\Phi_\mathrm{r}/\partial\Omega\left(\theta_\mathrm{i}, \phi_\mathrm{i}, \theta_\mathrm{r}, \phi_\mathrm{r}\right)$. The total reflected flux Φ_r can be calculated by integrating over an entire half sphere. The angular reflectivity r and the total reflectivity R can be calculated by forming the quotient of incident and flux Φ_i and Φ_r:

$$r\left(\theta_\mathrm{i}, \phi_\mathrm{i}, \theta_\mathrm{r}, \phi_\mathrm{r}\right) = \frac{\Phi_\mathrm{r}/\partial\Omega\left(\theta_\mathrm{i}, \phi_\mathrm{i}, \theta_\mathrm{r}, \phi_\mathrm{r}\right)}{\Phi_\mathrm{i}} \tag{3.1}$$

$$R\left(\theta_\mathrm{i}, \phi_\mathrm{i}\right) = \frac{\Phi_\mathrm{r}\left(\theta_\mathrm{i}, \phi_\mathrm{i}\right)}{\Phi_\mathrm{i}} = \frac{1}{\Phi_\mathrm{i}} \cdot \int_0^{2\pi} \int_0^{\pi/2} r\left(\theta_\mathrm{i}, \phi_\mathrm{i}, \theta_\mathrm{r}, \phi_\mathrm{r}\right) \mathrm{d}\theta_\mathrm{r}\, \mathrm{d}\phi_\mathrm{r} \tag{3.2}$$

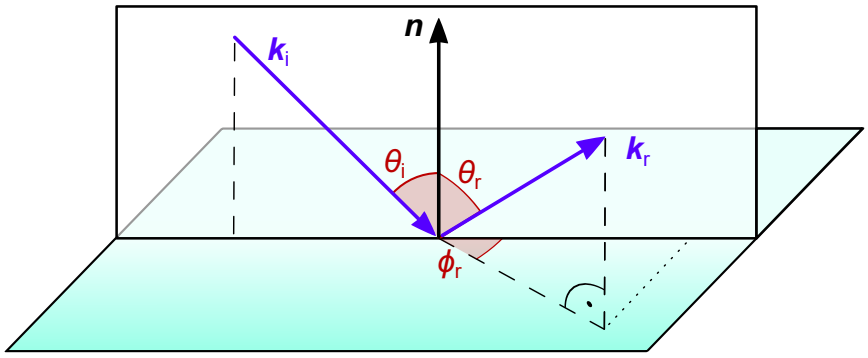

Figure 3.1.: Basic scheme of a reflection process. The incident beam (blue) with polar angle of incidence θ_i is reflected off a sample surface (turquoise) under a polar angle θ_r and azimuthal angle ϕ_r. The plane of incidence is defined by $\boldsymbol{n}$ and $\boldsymbol{k}_i$.

The azimuthal angle ϕ_i of the incident beam can be discarded for isotropic surfaces but not for SiPMs. This angle carries information about the orientation of the surface micro-structure of the SiPMs relative to the incident photon beam.
The SiPM reflectivity is characteristic to the specific sample surface and its mechanical composition. Different photosensors show different reflection properties and can be distinguished from isotropic surfaces as plain wafers that are investigated later. The reflectivity also depends on the processing of the sensor material during manufacturing as well as the mechanical influences during usage and storage of the samples. This may imply significant differences in the reflectivity among samples of the same SiPM model.
All results presented here have been accomplished with a monochromatic VUV light source. All samples are either photosensors (with or without micro-structure) or unprocessed wafer samples with a SiO_2 coating. All wavelength-dependencies of the reflectivity are therefore unconsidered and so are wavelength changing processes like fluorescence. All measurements used a photomultiplier monitor in counting mode to scan the light beam. Equation 3.1 can then be rewritten as:

$$R(\theta_i, \phi_i) = \frac{\Phi_r(\theta_i, \phi_i)}{\Phi_i} = \frac{\dot{N}_r(\theta_i, \phi_i) \cdot E_\gamma}{\dot{N}_i \cdot E_\gamma} = \frac{\dot{N}_r(\theta_i, \phi_i)}{\dot{N}_i}. \tag{3.3}$$

3.1.2. Reflection types

Two different types of reflection phenomena can be distinguished: specular and diffuse reflection. Figures 3.2 and 3.3 show schemes of these two types.

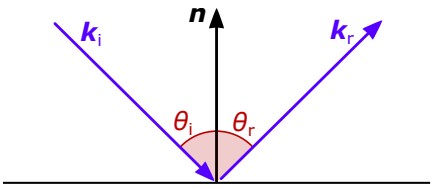

Figure 3.2.: Specular reflection

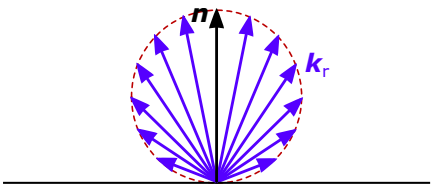

Figure 3.3.: Diffuse reflection

Specular reflection implies that a light beam is reflected by the same polar angle under which the incident beam hits the sample surface: $\theta_i = \theta_r$. The reflected beam lies in the plane of incidence defined by $\boldsymbol{n}$ and $\boldsymbol{k}_i$. This is well known from regular mirrors. *Diffuse reflection* occurs from the microscopic roughness of a given sample. The incident photons with initial intensity I are reflected diffusely with an angular distribution following Lambert's cosine law:

$$\mathrm{d}I(\theta_r) = I_r \theta_r \, \mathrm{d}\Omega \tag{3.4}$$

The intensity reflected under the solid angle $\mathrm{d}\Omega$ is the initial intensity I multiplied by the cosine of the monitored angle θ_r.
The reflection behaviour of most materials is a mixture of specular and diffuse reflection under different proportions. Compared to many other materials, SiPMs present very planar surfaces – even at microscopic levels. This is due to the wafer manufacturing process aiming at a defect-free crystal pattern and good microcell uniformity. It will be shown later that no diffuse reflection component occurs with SiPM samples so only specular reflection will be regarded in the further analysis.

3.2. Reflectivity Measurement Setup and Principle

The determination of the total reflectivity of a sample requires to scan the angular reflectivity r in the entire hemisphere above the sample surface. SiPMs show no diffuse reflection component. This means, the reflectivity can be measured by only scanning the reflected flux in the plane of incidence. This requires a position dependent photon flux monitor.
The following section presents an overview of the reflectivity setup used for the reflection measurements presented in this thesis. The setup is operated at the University of Münster. The assembly of the individual components of the setup has been discussed extensively in the PhD-theses from K. Bokeloh [79] and C. Levy [195] and one publication [33]. The following points focus on the basic details of the setup components including all changes to the setup compared to these theses.

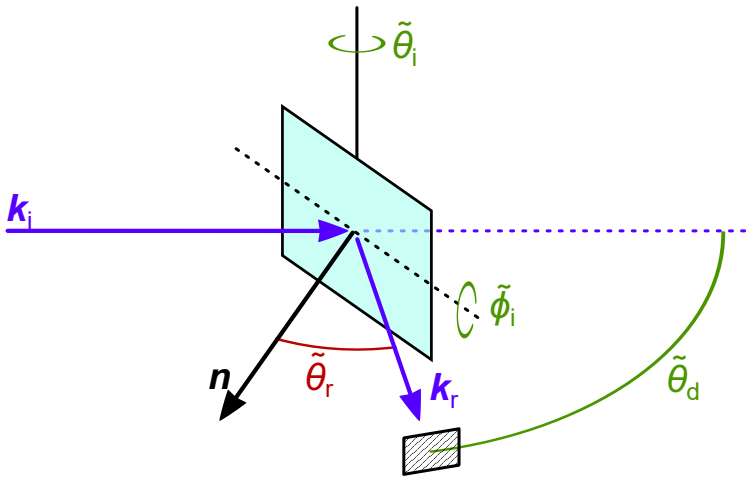

Figure 3.4.: Scheme of the physical reflection angle (red) and hardware setup angles (green). The reflectivity of a sample (turquoise) is investigated with a detector (black striped rectangle). The sample tilt is described by $\tilde{\phi}_i$ and the angle of incidence is set with $\tilde{\theta}_i$. The detector rotates around the sample described with $\tilde{\theta}_d$.

3.2.1. Reflectivity Setup

Geometry

To investigate the reflectivity $r\,(\theta_i, \phi_i, \theta_r, \phi_r)$, the setup needs to provide three free axes of movement to change the angle of incidence (AOI) θ_i and to scan the hemisphere above the sample surface. ϕ_i is defined relative to the SiPM micro-structure. The schematic principle of the setup is shown in figure 3.4. The designated VUV light source is rather complex so the incident light beam $\mathbf{k}_i$ is left untouched and the AOI is controlled by turning the sample via $\tilde{\theta}_i$. The easiest way to scan the hemisphere above the sample is to move a monitoring detector around the sample on a circle (via $\tilde{\theta}_d$) and change the tilt angle $\tilde{\phi}_i$ of the sample as a second dimension.

The relationship between the setup angles $\tilde{\theta}_i$, $\tilde{\phi}_i$ and $\tilde{\theta}_d$ and the reflection angles θ_i, θ_r and ϕ_r is calculated thoroughly in [79]. Diffuse reflection plays no role with SiPMs so only the plane of reflection is of relevance. The tilt angle $\tilde{\phi}_i$ can then be set to 0° and the relationships simplify to:

$$\begin{aligned} \tilde{\theta}_r &= \tilde{\theta}_d + \tilde{\theta}_i - 180° \\ \theta_i &= \tilde{\theta}_i \\ \theta_r &= \tilde{\theta}_r \\ \phi_r &= 0 \end{aligned} \tag{3.5}$$

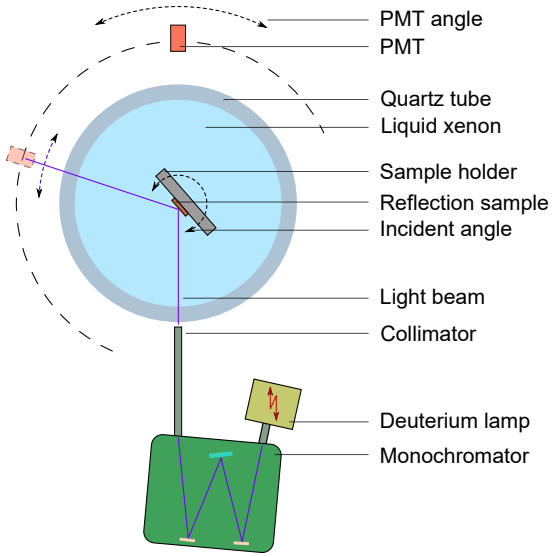

Figure 3.5.: Schematic overview of the reflection setup at the University of Münster. A light system produces a narrow VUV spectrum. The photons are guided to a quartz tube filled with liquid xenon. The light is reflected by a sample in the rotation axis of the tube. Reflected photons are registered by a PMT orbited around the tube.

Setup overview

The experimental setup is schematically shown in figure 3.5. The light is produced by a deuterium lamp. A narrow wavelength band in the VUV regime is selected by a monochromator. The VUV photons are collimated and guided into a VUV-transmissive quartz tube filled with liquid xenon. The reflection sample is attached in the centre of the tube so that the rotation axis of the tube lies on the sample surface. The angle of incidence (AOI) can be changed via rotating the entire tube. The angular reflection spectrum is scanned with a PMT in counting mode rotated around the tube. Figure 3.6 shows a photograph of the setup. The components are explained in the caption and details are given in the following.

Light source

The SiPMs are examined in a VUV photon field. The light system consists of a deuterium plasma light source attached to a plane grating vacuum scanning monochromator. The light source provides continuous emission above 170 nm (see figure 3.7). A 1200 grooves/mm grating with a blaze wavelength of 150 nm is installed in the monochromator to extract a narrow emission spectrum at the peak LXe scintillation wavelength. The reciprocal linear dispersion is 26.5 Å/mm and a slit height of 2 mm has been chosen. The spectral width is 5.3 nm ie. about one third of the width of the LXe scintillation spectrum (see table 2.4). The calibration

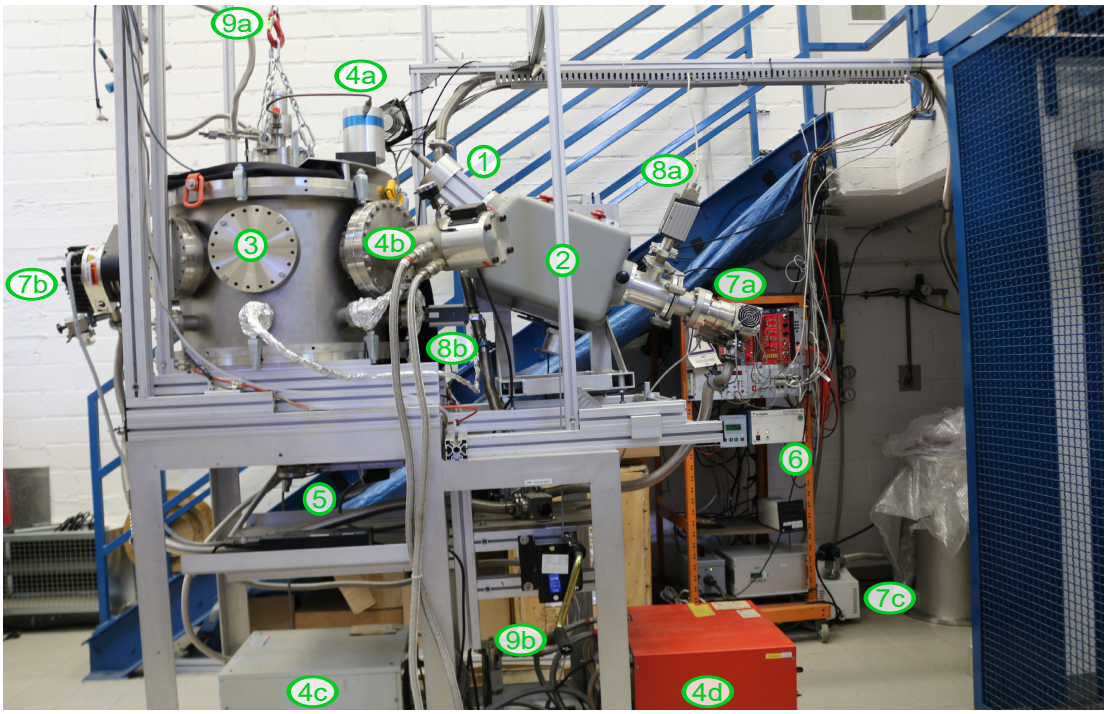

Figure 3.6.: The reflection setup at the University of Münster in 2019. It consists of the deuterium lamp (1), the monochromator (2), the light guide (behind PMT cryohead), the main chamber (3), the cryohead for the xenon liquefaction (4a) and PMT plus cold shield (4b), the PMT feedthrough (5) as well as the electronic readout, controls and DAQ interfaces (6). Compressors for the cryoheads are on the bottom (4c/d). Turbopumps for the monochromator (7a) and main chamber (7b) are connected to a common scroll pump (7c). Digital pressure sensors monitor both vacuum systems (8a/b). The inner chamber is lifted via a pulley (9a) and a manual wrench (9b).

of the light source and the validation of the output spectrum was performed in [288] (equation 4.1) and the monochromator is set to 1797 Å.
The VUV light is guided inside the main reflection chamber via a vacuum T-piece incorporating an uncoated quartz lens. The lens is adjusted so that the VUV light is focused onto the rotation axis of the sample holder in the quartz tube in the main chamber. The focal length is 80 mm at a wavelength of 178 nm and the diameter is 25 mm to exploit all photons exiting the monochromator. The light enters the main chamber via a collimator including a 1 mm diameter aperture. The light guide system is shown in figure 3.8.
The monochromator and the main chamber are separated by a MgF_2 window directly after the monochromator exit to avoid residual gas exchange between both volumes. MgF_2 has a transmittance of more than 87 % at 178 nm [162] so only a small fraction of light is lost in the light guide system.

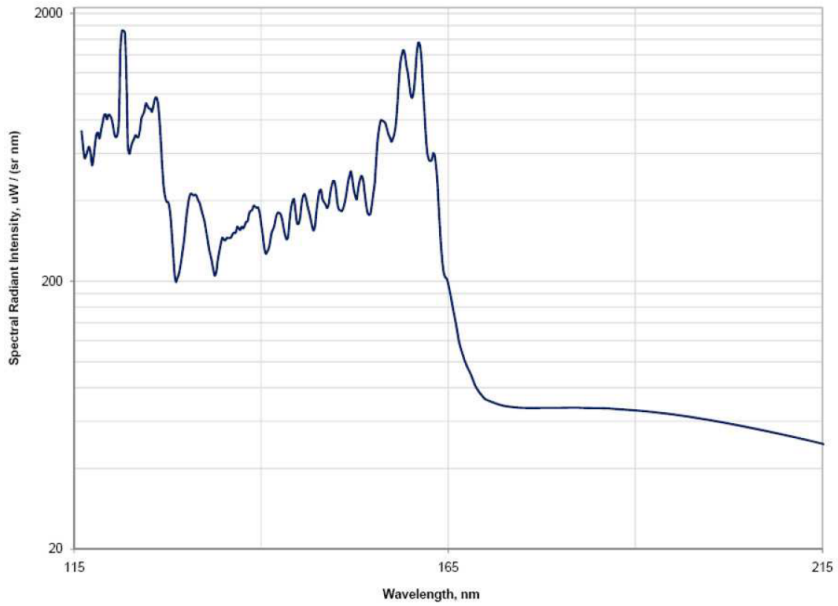

Figure 3.7.: Emission spectrum of the deuterium plasma light source used in the reflectivity setup. The spectrum is continuous above 170 nm [212].

Main chamber

The main chamber shown in figure 3.9 consists of a large vacuum vessel with an outer diameter of 630 mm and a height of about 400 mm. The vessel is equipped with various CF-flanges distributed evenly over the cylinder [79]. CF160 flanges are connected to a turbo molecular pump evacuating the chamber and the cold head used to cool down the cold shield and the PMT. A third CF160 flange is sealed with a vacuum window to provide a view inside the chamber when evacuated. A CF40 flange is connected to the light guide system containing the VUV lens. The chamber is sealed to a bottom and a top plate with two Viton O-rings. Both plates are equipped with additional access flanges. The top plate houses a second window and the rotational feedthrough for the quartz tube. The bottom plate provides the 4-axis feedthrough for the PMT movement as well as electric feedthroughs for the PMT power supply and electrical readout. All mechanical feedthroughs are placed in the plate centres thus sharing a mutual rotational axis.

The chamber contains the PMT and its movable suspension as well as the VUV light collimator at the end of the light guide system. The collimator is shown in figure 3.10. It has an inner diameter of 14 mm and is equipped with an exchangeable aperture with a diameter of 1.5 mm. The distance between the apterture and the central cylinder axis where the sample will be located is about 45 mm [195, 288].

A cold shield surrounds the inner part of the chamber to reduce thermal radiation from the vacuum vessel walls to the liquid xenon in the centre. The cold shield

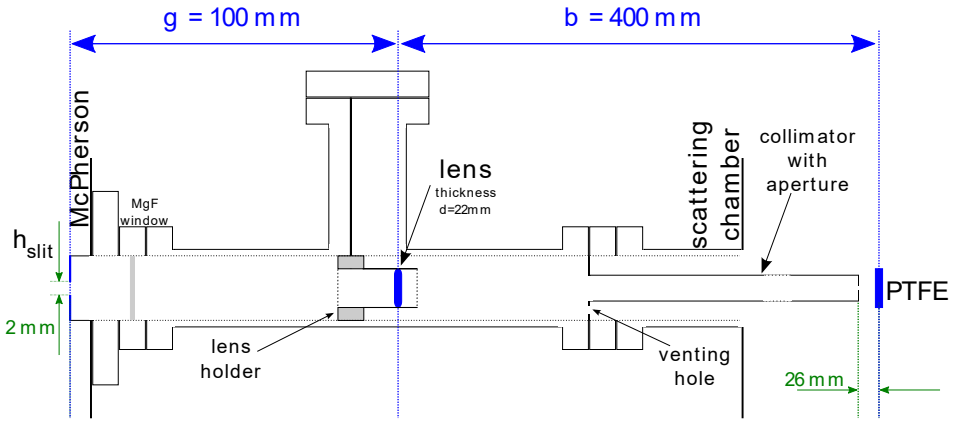

Figure 3.8.: Scheme of the light guide system showing the McPherson monochromator exit on the left and the main (scattering) chamber on the right [79]. The light is focused with an uncoated quartz lens. The distance between collimator and sample is now larger due to the incorporation of the quartz tube.

is closed at the top and bottom only leaving holes for the quartz tube, PMT suspension, collimator and side vacuum window. The upper cap of the cold sheet has been removed in figure 3.9. A Leybold cold head is used to cool down the shield and the PMT (see table 3.1). The shape, mass and material of the cold shield has been chosen with respect to the geometry of the setup and the power of the cold head [79, 288]. The temperature of the cold sheet is kept around the LXe temperature and is monitored via PT100 RTDs and silicon diode temperature sensors.

Vacuum

VUV light is affected by large absorption cross sections in matter as outlined in section 2.4.5. The air constituents with the strongest VUV absorption strength are oxygen and water vapour with a cross section σ of about $6{\times}10^{-21}\,\mathrm{cm}^2$ [169] and $2{\times}10^{-18}\,\mathrm{cm}^2$ [97], respectively, for xenon scintillation light ($\sim 7\,\mathrm{eV}$). The mean free path in air is $\ell = (\sigma\, n)^{-1}$ where n is the particle density of the constituents in air. It is calculated via $n = \rho/M{\cdot}\eta$ where ρ is the matter density, M the average molecular mass of air and η the abundance of the specific constituents of air ($\sim 21\,\%$ for oxygen, $\sim 2\,\%$ for water vapour). The mean free path is then about 1 cm for water vapour and 32 cm for oxygen making the evacuation of water paramount. The chamber is evacuated to about $3{\times}10^{-5}\,\mathrm{mbar}$ increasing the mean free path significantly to avoid any VUV light loss. The vacuum chamber has been cleaned prior to the measurement campaigns to also avoid residual gas impurities. The rotational feedthroughs of both PMT and quartz tube are attached with vacuum grease. This might introduce photo-absorbing residual gas components.

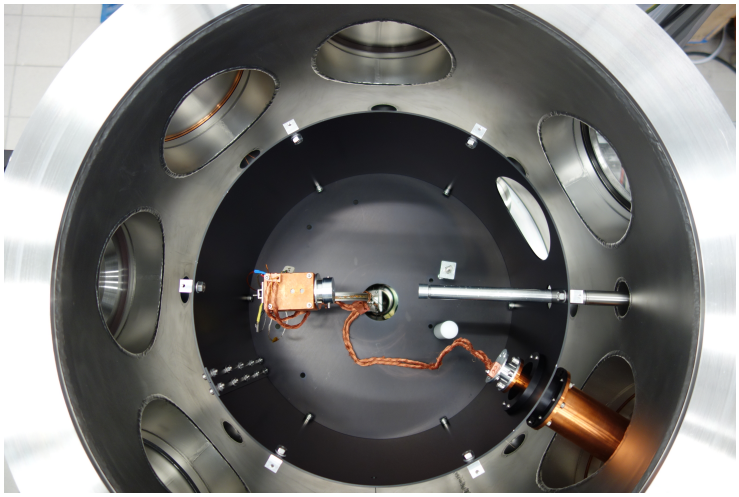

Figure 3.9.: Top view into the main chamber. The quartz tube will be located between the collimator (right) and the PMT (left). The PMT cold head can be seen in the lower right. A black cylindrical cold shield surrounds the inner part of the chamber.

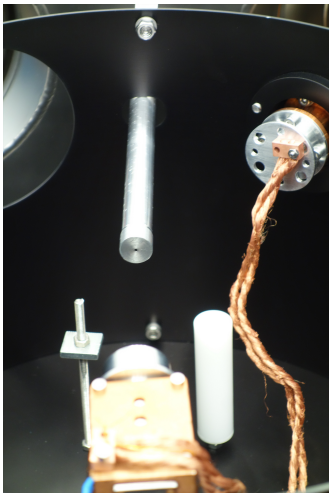

Figure 3.10.: An entry aperture attached to the end of the VUV light collimator.

The depositions of water molecules within the residual gas on the cold quartz tube can be avoided by evacuating the chamber below the saturation vapour pressure of water. The lowest LXe temperature used in the reflection measurements is −94 °C where the H_2O saturation pressure is about 4.3×10^{-5} mbar [78]. No ice depositions have been experienced at any point on any surfaces of the quartz tube and the PMT housing during the campaigns.

The monochromator is evacuated with an additional vacuum system. Both vacuum systems are separated from the chamber via the MgF_2 window in the light guide. This protects the PMT from grease depositions from the grating feeds in the monochromator. Unlike the monochromator system, only conflat (CF) flanges are used in the main chamber to achieve a vacuum well below the saturation vapour pressure of water. Additionally, a larger pumping speed is installed for the main chamber. Due to the significantly larger evacuated volume and the usage of vacuum grease, the vacuum in the main chamber is only slightly better than the one in the monochromator system (about 8×10^{-5} mbar). Still, the light path can be considered completely evacuated. Both vacuum systems are evacuated with turbomolecular pumps that share the same prevacuum pump.

Quartz Tube

The samples are attached within a UV-grade quartz tube with a height of 50 mm, an inner diameter of 40 mm and a thickness of 3 mm. The tube has been purchased

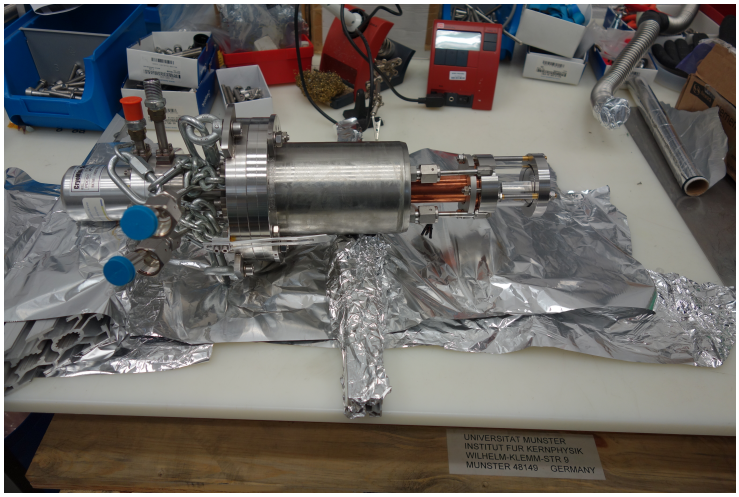

Figure 3.11.: Sealed quartz tube, copper cold finger, rotational feedthrough bearing, LXe pipes and cold head motor unit (right to left).

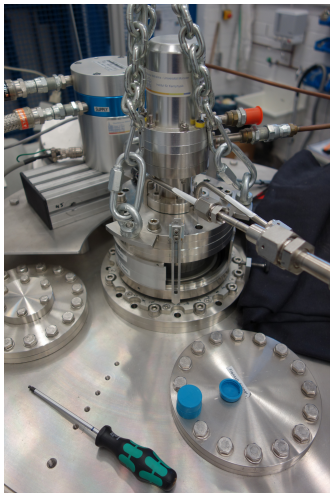

Figure 3.12.: The Cold head with the helium pump in the back.

from *Aachener Quarzglas-Technologie Heinrich*. The tube material HPFS® has a refractive index of 1.591533234 at 178 nm according to the Sellmeier Dispersion Equation constants stated by manufacturer Corning and a transmittance of $\geq$ 80 % · cm at 185 nm [106]. This yields about 87 % for the quartz tube thickness for this wavelength. Measurements done in [195] indicate that at 178 nm, the true transmittance is rather 80 %. This agrees very well with the Fresnel equation for normal incidence and the above refractive index. The Rayleigh scattering length for fused silica is about 3.7 m for 178 nm photons using the formula, the photoelastic constant and the isothermal compressibility reported in [94]. Photonic absorption is therefore the dominant attenuation process in the quartz and close to no scattering is expect to contribute to the off-peak rate.

The quartz tube is sealed with two CF40 flanges and Viton O-rings (very right in figure 3.11). The flanges are pressed together via three M6 threaded rods evenly spaced by 120°. A torque wrench set to 7 Nm proved to be sufficient to properly seal the tube if the bolts are tightened evenly and gently. Vacuum leakage tests have been performed prior to all measurement campaigns and no xenon loss has been experienced if cooled down. The upper CF40 flange is attached to a cold finger out of copper which in turn is connected to a cold head (very left in figure 3.11). The entire system is attached to a vacuum rotational feedthough. The feedthrough also accommodates gas ports for the xenon in- and outlet – the so-called xenon feed and bleed ports. These ports can be seen protected by blue caps in figure 3.11. They lead to the top flange to directly access the volume in the quartz tube. This volume is pumped and filled/emptied with xenon via these gas pipes. Xenon gas

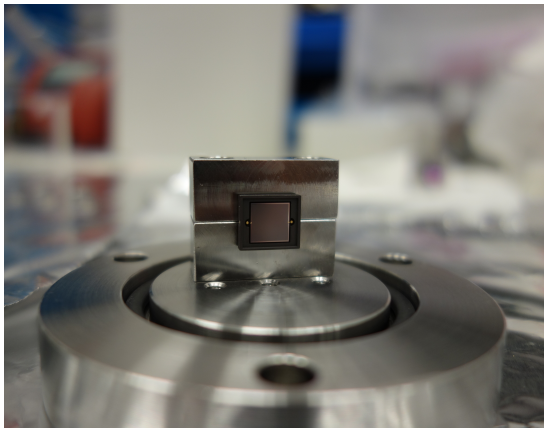

Figure 3.13.: VUV4 sample SiPM attached to the bottom flange. The groove later accommodates the O-ring to seal the quartz tube via three rods located in the outer borehole circle.

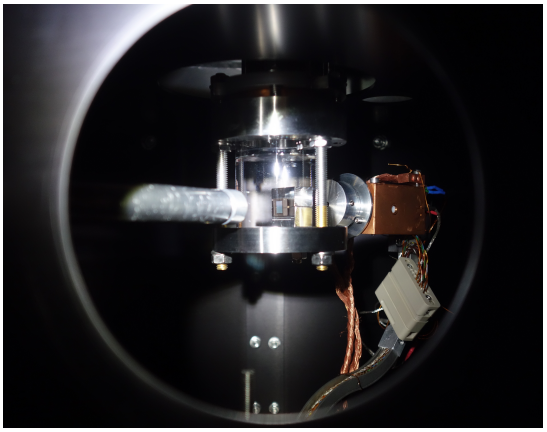

Figure 3.14.: Sealed quartz tube filled with liquid xenon inside the main chamber. The collimator is on the left, the PMT housing on the right. The tube height is set to reflection position.

from the feed connector getting in contact with the cold finger will loose thermal energy eventually liquefying, dropping down and cooling the bottom flange via evaporation until the entire sealed quartz tube reaches the desired temperature.

Inner Chamber

Figure 3.12 shows this entire inner chamber set in place in the main chamber. The rotational feedthrough sits exactly in the centre of the top plate. The feedthrough can be rotated and changed in height within the bearing of the flange. The current rotation angle is indicated by a pointer connected to the cold head flange and a scale on the main chamber top plate. The scale is arbitrary and the corresponding angle is called *Xenon angle* in the following ($-20°$ in figure 3.12). The xenon pipes are connected to the feed and bleed systems via flexible pipes – or short flexpipes – and the cold head is connected to a helium motor unit in the back. All flexpipes as well as the cold head with its motor unit have to be rotated along with the feedthrough for changing the angle of the quartz tube. The xenon temperature can be manipulated via the temperature control of the cold head. The xenon pressure will follow any temperature change according to the vapour pressure curve shown in figure 2.18. The pressure can be monitored with a digital pressure gauge located at one of the external feed pipes. It has an offset of 0.36 bar.
The photograph in figure 3.13 shows a VUV4 SiPM mounted on a sample holder that is attached to the bottom flange. The holder is designed so that the sample surface lies exactly in the tube's cylinder axis and thus the rotation axis of the inner system. The groove will accommodate the Viton O-ring used to seal the

quartz tube. The boreholes on the edge of the flange will accommodate the three rods tightening both flanges. Figure 3.14 shows a look into the main chamber if the quartz tube and the cold finger are attached. The VUV photons enter through the collimator on the left, cross the tube and are registered by the PMT on the right. A SiPM is attached in the centre of the quartz tube. The tube is filled with liquid xenon with the phase separation level visible at the top of the tube. The cold finger can be spotted on the top vanishing within the rotational feedthrough flange. The entire inner system can be changed in height to either let the VUV beam cross the tube above the sample holder or hit the sample and reflect. This is done via a manual wrench connected to the cold head flange and several spacer between cold head and feedthrough flange to relieve the wrench off any forces during the measurement campaigns. Since the sample holder is firmly attached to the bottom flange, rotating the feedthrough means to change the angle of incidence.

Light detector

The reflected VUV-light was monitored with a UV-sensitive Hamamatsu R8520 PMT with 10 dynode stages. It achieves a gain of about 10^6 at t maximum supply voltage of 900 V and features a synthetic silica entry window and a bialkali photocathode. The spectral response ranges down to 160 nm. The quantum efficiency (QE) for xenon scintillation light has been measured to be around 31 % [41]. The PMT can be operated at temperatures down to −110 °C. The QE has been seen to improve up to 10 % during cooling [41].

The PMT is cooled via the same cold head that cools down the cold shield. A flexible copper belt is attached to both cold head and PMT to transfer cooling power while still allowing the PMT to rotate around the quartz tube. The PMT is located in a copper housing to evenly cool down the entire detector. The housing can be seen in figure 3.15. A diode temperature detector is accommodated in the housing to monitor the PMT operation temperature. More information about the initial installation of the PMT can be found in [79].

The PMT housing can be closed with an exchangeable aluminium collimator as shown in figure 3.16. An aperture collimator with a diameter of 2 mm has been used for most measurements. A slit collimator with a slit height of 16.9 mm and a width of 1.5 mm has been used for the VUV4 campaigns. The PMT housing is wrapped with a sheet of mu-metal to decrease the influence of the Earth's magnetic field. This is important since the orientation of the dynodes to the magnetic field changes during the measurements of the angular spectra which would introduce a scanning angle dependent gain. The mu-metal coating has been carried out following the instructions in chapter 2.4.2. in [273].

The PMT housing is mechanically attached to the PMT suspension visible in the bottom in figure 3.15. The suspension is connected to the 4-axis feedthrough on

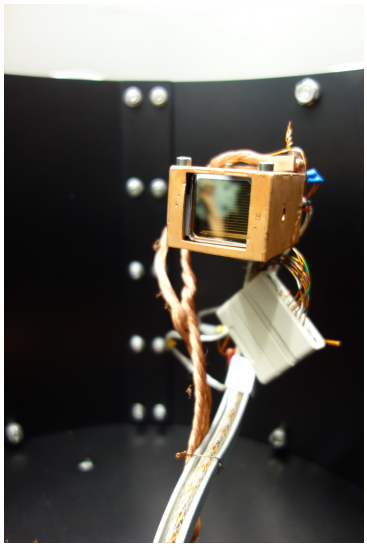

Figure 3.15.: The VUV-sensitive PMT in the copper case with the aperture detached.

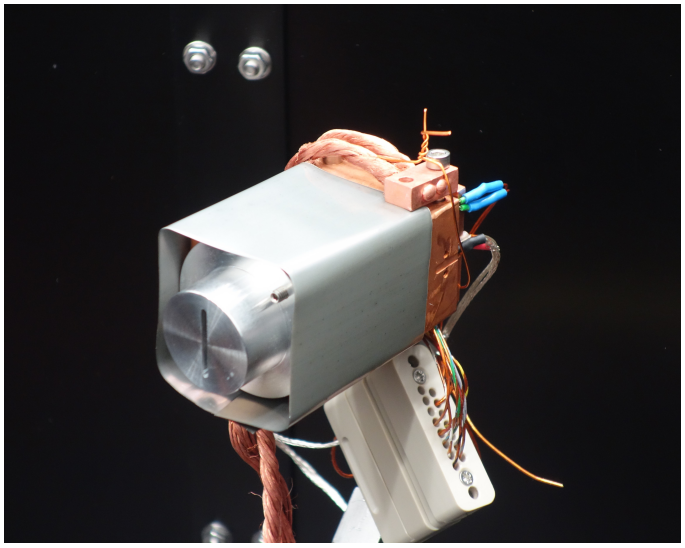

Figure 3.16.: PMT case including slit aperture unit and mu-metal magnetic shielding. The PMT holder and the electronic connections for PMT power supply and readout can be seen below.

the bottom of the main chamber (see figure 3.17). The feedthrough provides four degrees of movement, namely the rotation of the PMT around the quartz tube as well as the lateral movement of the whole PMT suspension and housing in x, y and z. With this, the centre point of the PMT rotation can be moved. The x and y coordinates have to be set during the alignment of the PMT to align the rotation axes of the PMT and the quartz tube. The z coordinate has to be set to align the rotation plane of the PMT with the plane of reflection. The z-coordinate may be varied to scan a beam profile. The distance between the PMT aperture and the quartz tube cylinder axis is 40.5 mm. The main chamber is equipped with Teflon bumpers on both sides of the collimator as shown in figure 3.9 to protect the PMT housing from colliding with the collimator.

Electronics

The rotation axis of the PMT feedthrough is connected to a stepping motor via a chain string as shown in figure 3.17. The stepping motor has an accuracy of 200 steps per rotation. The transmission to the feedthrough has a gear ratio of 4. This results in an angular spectral resolution of 0.45° for the scanning PMT. All angular spectra in this work are acquired with this resolution.

The electronic readout systems are shown in figure 3.18. The PMT signal is first amplified by a factor of 10 in a fast amplifier before being processed in a leading edge discriminator (LED). An LED width of 255 mV and a threshold of 100 mV

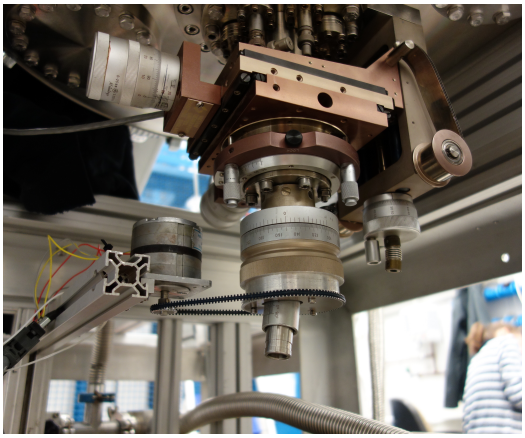

Figure 3.17.: 4-axial feedthrough for the PMT suspension on the bottom of the main chamber. The stepping motor can be seen on the left.

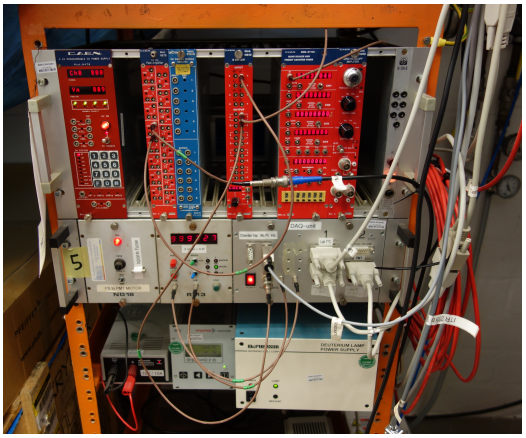

Figure 3.18.: Electronic control devices, power supplies, DAQ box and PMT pulse readout system for the reflection setup.

proved to yield plausible and consistent results [289]. The discriminated pulses are recorded with a counting unit. A digital oscilloscope is used to check the proper shape of the PMT and LED output pulses.
The LED is connected to a custom-made data acquisition (DAQ) unit. The DAQ unit processes (1) the LED signal, (2) the signal of two vacuum gauges monitoring the pressure in the monochromator and chamber vacuum system, and (3) the temperatures of the PMT, the cold shield and the laboratory. The DAQ unit communicates via a USB link with a LabView interface on a computer. The interface processes all the data delivered by the DAQ unit and controls the rotational speed and direction of the stepping motor. The motor can be moved to arbitrary angle positions for a certain acquisition time. A stabilisation time of several seconds is set before starting the data acquisition to let the PMT suspension ring down after each angle step. The vacuum gauge within the main chamber has to be switched off during measurements due to the parasitic emission of light.
The electronics rack further comprises the stepping motor power supply and the stepping motor control which is controlled via the DAQ unit (second row) as well as the turbomolecular pump controls and the deuterium lamp power supply and control (bottom row).

Setup Components

A list of all setup components used in the reflection setup at the University of Münster is provided in table 3.1. The table includes model numbers and the manufacturers of the individual components. Links to the manuals are given in the references if available.

Component	Model	Manufacturer	References
Light source	632 Deuterium lamp	McPherson	[212]
Monochromator	Model 218	McPherson	Priv. comm.
VUV lens	NT48-297 DCX-UV 25x100 UNCTD	Edmund optics	[124]
Prevacuum pump	Scrollvac SC 5 D	Leybold	[197]
Monochr. turbo pump	TMU 071 P	Pfeiffer	[246]
Chamber turbo pump	TW 300	Leybold	[198]
Gas inlet valves	SS-8BG-VCR	Swagelok	[293]
Quartz tube	Fused Silica Standard Grade 7980	Corning	[106]
Xenon purifier	MonoTorr PS3-MT3	SAES	[267]
Coldhead	Model PDC 08	Iwatani	N/A
Motor Unit	Model 601	Iwatani	N/A
Compressor	Model SA101	Iwatani	N/A
Temperature controller	336	LakeShore	[191]
PMT	R8520-406	Hamamatsu	[160]
Power supply	N470	CAEN	[89]
Coldhead	RPK 1500 E	Leybold Heraeus	[196]
Motor Unit	RG 210	Leybold Heraeus	[196]
Compressor	RW2	Leybold Heraeus	[196]
Fast amplifyer	N979	CAEN	[91]
LED	N840	CAEN	[90]
Counter timer	N1145	CAEN	[88]

Table 3.1.: List of the components of the reflection setup at the University of Münster used in this work.

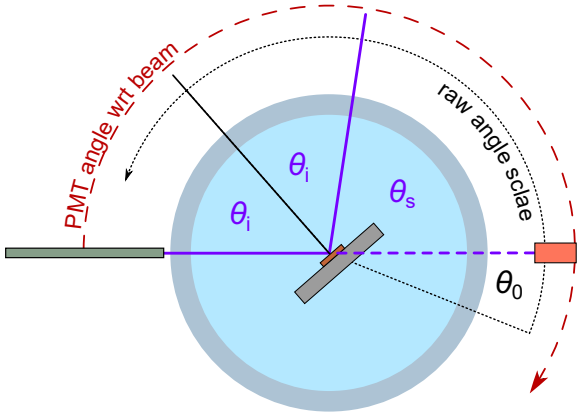

Figure 3.19.: Scheme of the PMT angle scales in the reflection setup. θ_i is the angle of incidence and θ_0 the zero angle of the PMT scale. The beam enters at $180°+\theta_0$ in the raw scale (black dotted). The specular angle θ_s is the angle between the exiting specular beam and 180° on the PMT angle wrt beam scale (red dashed).

3.2.2. Measurement Principle and Data Processing

The specular reflection of VUV photons at the sample surface does change the mean angle of the photon beam but not the beam shape. The reflected photons may however experience different incident angles due to the components of the micro-structure on the sample surfaces. The beam is however broadened by the defocusing power of the LXe filled quartz lens. Rayleigh scattering is non-directional and introduces background.

The angular reflection spectra are scanned with the UV-sensitive PMT. The PMT rotates counter-clockwise around the quartz tube within the reflection plane. This is called the *PMT orbit*. The raw PMT angle scale ranges from some zero point θ_0, which only depends on the hardware settings of the PMT suspension, to the bumper protecting the PMT from colliding with the collimator. The raw PMT angle scale is shown with a black dotted line in figure 3.19. This scale is converted to the PMT angle scale with respect to the beam by subtracting raw angles from the beam position at $180°+\theta_0$ (red dashed line). These *PMT angles wrt beam* will be shown on all following angular spectra. Physical angles are shown in purple.

The height of the quartz tube including the sample can be changed to hit the sample surface or to withdraw the sample entirely from the VUV photon beam. The first mode is called *reflection mode*. In the second mode, the photon flux is unaltered and can be used to establish a reference spectrum corresponding to a reflectivity of 100 % (*reference mode*). The reference peaks are integrated and the constant dark rate and other background are subtracted. The position of the reference peaks is used to set the zero point θ_0 of the PMT angle scale.

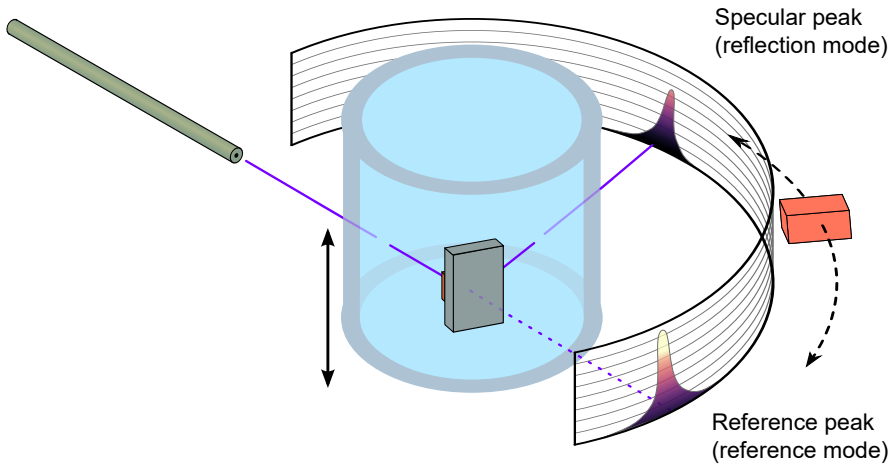

Figure 3.20.: Scheme of the reflectivity measurement principle. The PMT scans the angular spectrum in reference or specular mode, depending on the height of the quartz tube that contains the sample. The VUV beam either crosses the liquid xenon above the sample holder (reference mode) or directly hits the sample (reflection mode).

The reflection of the examined samples is purely specular. No diffuse spectral distributions have been observed for any sample. There is one prominent specular peak for each incident angle. This peak is again integrated and cleared from background. The specular peak is located at a raw angle of $\theta_0+\theta_s$. From this, the angle of incidence (AOI) θ_i can be calculated if the zero point is fixed via the reference peak position. The specular reflectivity r of the given sample at a certain AOI θ_i is calculated by dividing the integral of specular peaks by the integral of the reference peaks:

$$r = \frac{I_{\text{spec}}}{I_{\text{refr}}} \tag{3.6}$$

The peak integral of the specular peaks is always smaller than the peaks in reference position since a fraction of light gets absorbed by the sample. The quartz tube is a cylinder and the photon path in the tube is the same for the reference and the reflection mode. Additionally, photons always pass the quartz tube perpendicularly in both modes. This measurement principle is shown schematically in the 3D scheme in figure 3.20 where the setup works in reflection mode producing a peak in specular position (upper peak) while the reference peak is shown vis-à-vis the collimator where it would appear if the quartz tube is lowered.
The total reflectivity R is very close to r due to the absence of a diffuse reflection component. However, secondary specular peaks have been observed for some samples. These secondary peaks point to components of the surface micro-structure that exhibit a different slope compared to the dominant plain microcell surface.

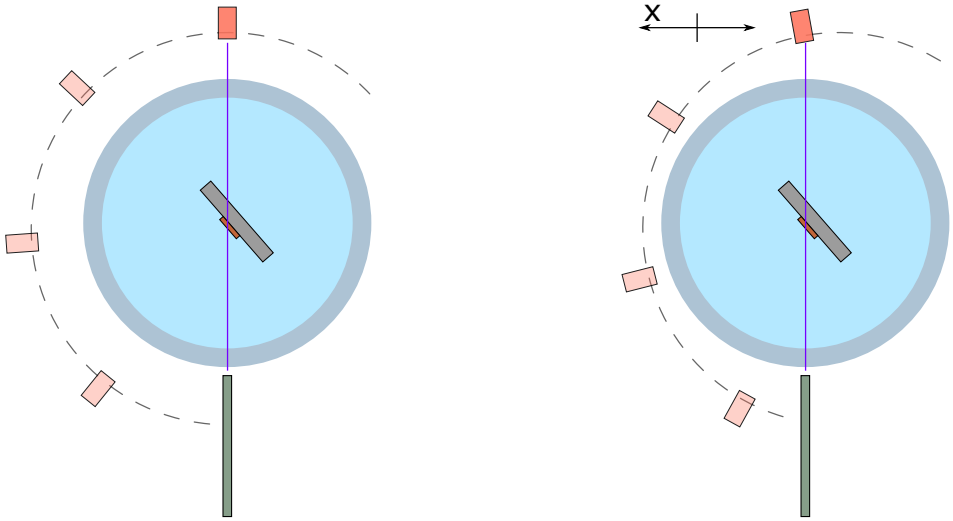

Figure 3.21.: Scheme of the PMT orbit alignment procedure in x-direction. On the left, the setup is properly aligned and the PMT always faces the rotation axis. On the right, the PMT orbit is shifted in x resulting in a reduced effective opening area of the PMT collimator depending on the scanning angle.

In the following, the notation *campaign* is used for a set of measurements with one specific sample (e.g. VUV4 campaign). The notation *run* is used for every acquired angular spectrum. Runs can be reference runs (in reference mode) or reflection runs (in reflection mode at a specific AOI). Reference peaks are acquired several times between reflection runs to monitor the reference peak stability.

3.2.3. Setup Alignment

The setup has to be carefully aligned prior to the measurements. The alignment procedures can be extensive and time-consuming and in some cases led to alignment settings that were visually off. A wrong alignment leads to large systematic errors during scanning angular spectra. The alignment has been done as thorough as possible by eye before confirming the alignment settings with measurements. Systematic errors have been estimated for the final data to account for any remaining inaccuracies in the alignment.
The alignment procedure has been explained in [195] in much detail and is roughly depicted in figure 3.21. Basically, the centre axis of the PMT orbit and the rotation axis of the quartz tube (and with it the surface of the reflection sample) have to be aligned so that they share a mutual rotation axis. This can be done by varying the x- and y-component of the PMT suspension. If the alignment is not performed properly, as in the right of figure 3.21, the reflected light will not arrive

perpendicularly at the PMT aperture for most angles. The PMT will register less photons corresponding to the projected aperture area seen by the reflected light beam. This results in a systematic reduction in reflectivity depending on the AOI. This effect is used to set the alignment by scanning reference or specular peaks with varying x- and y-coordinate eventually choosing the one (x,y) pair that yields the highest photon rate.

The same principle can be used to set the z-coordinate. The reference peak is scanned for varying heights of the PMT orbit until the highest peak maximum is found. A misalignment in z is not dramatic since it just decreases the overall light flux for both reference and reflection position. However, the PMT orbit may be slightly tilted compared to the plan of reflection. In this case, the z-alignment has to be adapted along each change between runs in reference and reflection mode.

3.3. Mathematical Description of Light Propagation

The specular and reference peaks in the angular spectra can be described with an analytical function based on the integration of the VUV light beam with the aperture window of the scanning PMT. The light propagation in the quartz tube can also be described analytically via introducing a scaling factor that contains the refractive index of the material in the tube. The following section presents the mathematics leading to the analytical function and the description of the light propagation within the setup. The effects on the angular spectra of both the beam containment on the reflectivity samples as well as the micro-structure on the SiPM surface are also discussed.

3.3.1. Analytical Shape of Peaks

The PMT scans the angular reflection spectra counter-clockwise. The beam is broadened due to scattering, defocusing and other reasons but still exhibits an approximately Gaussian shape at the position of the PMT orbit [79]. The PMT has an aluminium aperture with a diameter and a thickness of 2 mm. It only counts photons within the plane in which the PMT scans the angular spectra as depicted in figure 3.22.

A mathematical function can be derived to describe the peak shape based on the integration of a 2D-Gaussian. There is no analytical solution for the integration of a 2D-Gaussian with a circular aperture so rectangular integration limits have been chosen so that the rectangle area equals the one of the aperture. The integration limits are $\pm\sqrt{\pi}r/2$ where r is the radius of the PMT aperture:

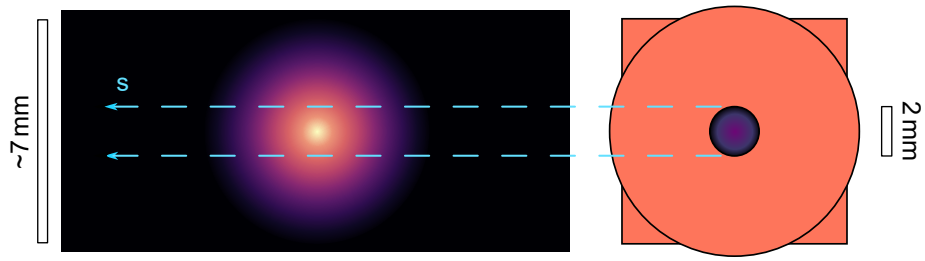

Figure 3.22.: Scheme showing the PMT (right) scanning a peak (left) along axis s (blue) in the reflection setup. The PMT has an 2 mm diameter aperture. The entire peak is approximately 7 mm in diameter with the dominant amount of photons concentrated on the inner 2 mm. The PMT scans the peaks counter-clockwise.

$$f(s) = \iint_{-\sqrt{\pi}r/2}^{+\sqrt{\pi}r/2} \exp\left(-\frac{(x-s)^2}{2\sigma^2}\right) \cdot \exp\left(-\frac{y^2}{2\sigma^2}\right) \mathrm{d}x\,\mathrm{d}y \tag{3.7}$$

where s is the parametrisation of the path of the scanning PMT and σ is the Gaussian width of the light beam. The integral can be solved with the antiderivative of the Gaussian function i.e. the difference of two error-functions containing the integral limits as numerator. This yields:

$$f(s) = \pi\,\sigma^2 \cdot \mathrm{erf}\left(\frac{\sqrt{\pi}r}{\sqrt{8}\sigma}\right) \cdot \left[\mathrm{erf}\left(\frac{\sqrt{\pi}r/2 - s}{\sqrt{2}\sigma}\right) - \mathrm{erf}\left(\frac{-\sqrt{\pi}r/2 - s}{\sqrt{2}\sigma}\right)\right] \tag{3.8}$$

The function can be normalised to yield a maximum of 1 at s=0 and scaled with amplitude A. Additionally, an x-offset M is introduced to account for arbitrary peak positions on the angular scale of the PMT. The final formula is:

$$f(s, M) = \frac{A}{2\,\mathrm{erf}\left(\frac{\sqrt{\pi}r}{\sqrt{8}\sigma}\right)} \cdot \left[\mathrm{erf}\left(\frac{\frac{\sqrt{\pi}r}{2} - (s-M)}{\sqrt{2}\sigma}\right) - \mathrm{erf}\left(\frac{-\frac{\sqrt{\pi}r}{2} - (s-M)}{\sqrt{2}\sigma}\right)\right] \tag{3.9}$$

This function will be fitted to all angular spectra presented later in this chapter. The formula will be referenced to as *Gaussian integral* or short *GaussInt*. The area $F(M)$ under this function can be derived by integrating $f(s, M)$ using the antiderivative of the error-function and L'Hôpital's rule to arrive at:

$$F(M) = A\sqrt{\pi}r \cdot \mathrm{erf}^{-1}\left(\frac{\sqrt{\pi}r}{\sqrt{8}\sigma}\right) \tag{3.10}$$

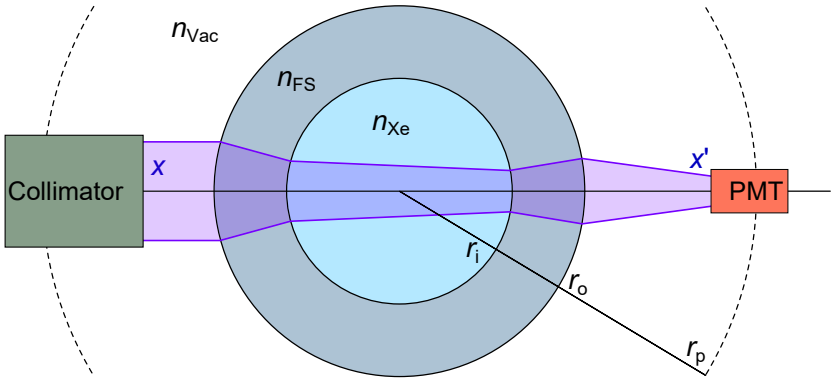

Figure 3.23.: Scheme of the off-axis VUV light propagation in the quartz tube. The light beam is focused due to the refractive indices n_{FS} and n_{Xe} of the fused silica of the tube and the liquid xenon inside the tube. The radii of the tube and the PMT orbit are give in section 3.2.1.

3.3.2. Light Propagation in the Quartz Tube

The VUV light beam traverses four boundary surfaces when crossing the quartz tube: twice the vacuum-quartz boundary at the outer tube radius r_o and twice the quartz-LXe boundary at the inner tube radius r_i. The light will be (de)focused at any of these boundaries as outlined in figure 3.23. This leads to a change in the object size x to the image size x' at the position of the PMT orbit r_p. The change in size can be calculated via extended trigonometric methods and expanded around the optical axis, i.e. for small object sizes x. The result is:

$$\frac{x}{x'}(x\to 0) = \frac{2r_p}{r_o}\left(\frac{1}{n_{FS}} - 1\right) + \frac{2r_p}{r_i}\left(\frac{1}{n_{Xe}} - \frac{1}{n_{FS}}\right) + 1 \tag{3.11}$$

where n_{FS} and n_{Xe} are the refractive indices of the fused silica and liquid xenon. The approximation around the optical axis is motivated considering the small beam diameter of 2–3 mm compared to the inner diameter of the quartz tube r_i which is 40 mm. Primary angles at the first transition from vacuum to fused silica are smaller than 5°. Inserting the values for both refractive indices yields:

$$\frac{x}{x'}(x\to 0) = \begin{cases} +1.1960 & \text{for} \quad n_{Xe} = 1.00 \text{ (Vacuum)} \\ -0.4575 & \text{for} \quad n_{Xe} = 1.69 \text{ (Liquid xenon)} \end{cases} \tag{3.12}$$

This means that the beam is slightly broadened if the quartz tube is evacuated while the liquid xenon implies a strong focusing power and focuses the beam on an aspherical focal point prior to reaching the PMT orbit. This leads to a compression of the Gaussian beam in the polar component x while the component z in direction

of the cylinder axis of the tube is unaffected. The beam profile can be investigated experimentally via a set of angular spectra at equidistant heights of the PMT orbit. Mathematically, the compression can be accounted for by introducing two beam width parameters in equation 3.9: x for the polar component within the PMT orbital plane and z for the (cylinder-) axial component. This yields:

$$\begin{aligned} f(s, M_x, M_z) = \frac{A}{4} \cdot \mathrm{erf}^{-1}\left(\frac{\sqrt{\pi}r}{\sqrt{8}\sigma_x}\right) \mathrm{erf}^{-1}\left(\frac{\sqrt{\pi}r}{\sqrt{8}\sigma_z}\right) \cdot \\ \left[\mathrm{erf}\left(\frac{\sqrt{\pi}r/2 - (s - M_x)}{\sqrt{2}\sigma_x}\right) - \mathrm{erf}\left(\frac{-\sqrt{\pi}r/2 - (s - M_x)}{\sqrt{2}\sigma_x}\right)\right] \cdot \\ \left[\mathrm{erf}\left(\frac{\sqrt{\pi}r/2 - (s - M_z)}{\sqrt{2}\sigma_z}\right) - \mathrm{erf}\left(\frac{-\sqrt{\pi}r/2 - (s - M_z)}{\sqrt{2}\sigma_z}\right)\right] \end{aligned} \tag{3.13}$$

where σ_x is the width in polar and σ_z in axial direction. Since x is affected by the compression while z is not, both variables are related via the compressing factor from equation 3.11:

$$\sigma_x = \sigma_z \cdot \frac{x}{x'}(x \to 0)$$

3.3.3. Beam Containment on the Sample

At large AOIs, the VUV light beam will start to partly miss the sample with width w due to the decreasing projected sample surface that reflects VUV photons. This reduced beam containment can be accounted for with a correction factor with respect to both the AOI θ_i and the beam width. The beam width is progressively decreasing due to the focusing effect of the tube and the xenon as shown in figure 3.24. The beam width needs to be calculated for both corners of the sample surface, i.e. at an angle of θ_i for the corner pointing towards the PMT and $-\theta_\mathrm{i}$ for the other side of the optical axis. The beam width σ_w at the y-position of the sample corner is then calculated via:

$$\begin{aligned} \sigma_w(\theta_\mathrm{i}) = \sigma \cdot n_\mathrm{FS}^2\, r_\mathrm{o}^2\, r_\mathrm{i}^2 \cdot \\ \Big\{ n_\mathrm{Xe} n_\mathrm{FS}^2 r_\mathrm{o}^2 r_\mathrm{i}^2 \;+\; \sigma^2 \cdot \Big[n_\mathrm{Xe} n_\mathrm{FS}^2 r_\mathrm{o}^2 r_\mathrm{i}^2 + n_\mathrm{FS} r_\mathrm{o}^2 - (n_\mathrm{FS} - 1)\,(n_\mathrm{Xe} - n_\mathrm{FS})\, r_\mathrm{o} r_\mathrm{i} \Big] + \\ +\; \sigma^4 + \sigma \cdot \Big[(n_\mathrm{FS} - 1)\, n_\mathrm{FS} n_\mathrm{Xe} r_\mathrm{o} r_\mathrm{i}^2 + (n_\mathrm{Xe} - n_\mathrm{FS})\, n_\mathrm{FS} r_\mathrm{o}^2 r_\mathrm{i} \Big] \cdot \tan(\theta_\mathrm{i}) + \\ +\, \sigma^3 \cdot \left[(n_\mathrm{FS} - 1)\, r_\mathrm{o} + (n_\mathrm{Xe} - n_\mathrm{FS})\, r_\mathrm{i} \right] \cdot \tan(\theta_\mathrm{i}) \Big\}^{-1} \end{aligned} \tag{3.14}$$

The beam containment can be calculated with the same integration formula shown in equation 3.13 but for a rectangle with lateral edge length $w \cos\cdot(\theta_\mathrm{i})$ and axial

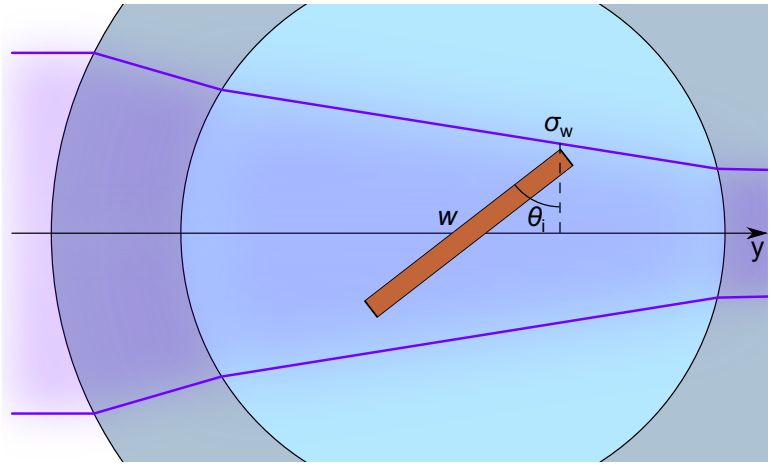

Figure 3.24.: For large AOI θ_i, the VUV beam is not entirely contained on the sample surface with width w but partly propagates straight on without being reflected. The beam width σ_w at the position of the sample corners is different for both sides of the optical axis (y) due to the increasing beam focusing.

length w to account for the projection. The integration has to be carried out separately for both sides of the optical axis due to the decreasing beam width resulting in two different widths $\sigma_w(\theta_\mathrm{i})$ and $\sigma_w(-\theta_\mathrm{i})$. This leads to a containment correction factor of:

$$F_\mathrm{con}(\theta_\mathrm{i}) = \frac{\sigma_w(\theta_\mathrm{i})\,\mathrm{erf}\left(\frac{w\cos(\theta_\mathrm{i})}{\sqrt{8}\sigma_w(\theta_\mathrm{i})}\right) + \sigma_w(-\theta_\mathrm{i})\,\mathrm{erf}\left(\frac{w\cos(\theta_\mathrm{i})}{\sqrt{8}\sigma_w(-\theta_\mathrm{i})}\right)}{\sigma_w(\theta_\mathrm{i})\,\mathrm{erf}\left(\frac{w}{\sqrt{8}\sigma_w(\theta_\mathrm{i})}\right) + \sigma_w(-\theta_\mathrm{i})\,\mathrm{erf}\left(\frac{w}{\sqrt{8}\sigma_w(\theta_\mathrm{i})}\right)} \tag{3.15}$$

which is 1 as long as the beam is contained entirely on the sample surface but decreases for larger AOIs. F_con is plotted over the angle of incidence θ_i in figure 3.25.

3.3.4. SiPM surface micro-structure

SiPMs are equipped with a complex micro-structure on the surface to distribute power over the microcells and read out signals. Usually, parallel strips of power lines are connected to the microcells via quenching resistors on the surface. As a result, the surface includes various surface slopes apart from the dominant flat microcell surface. This affects the reflection behaviour. Additional shadowing effects occur if a part of the microcell surface is blocked from the incident light by the micro-structure strips.

This situation is shown geometrically in figure 3.26. A SiPM profile is hit by incident light under an AOI θ_i of about 60°. The SiPM surface micro-structure consists of equidistant strips perpendicular to the plan of incidence. The strips

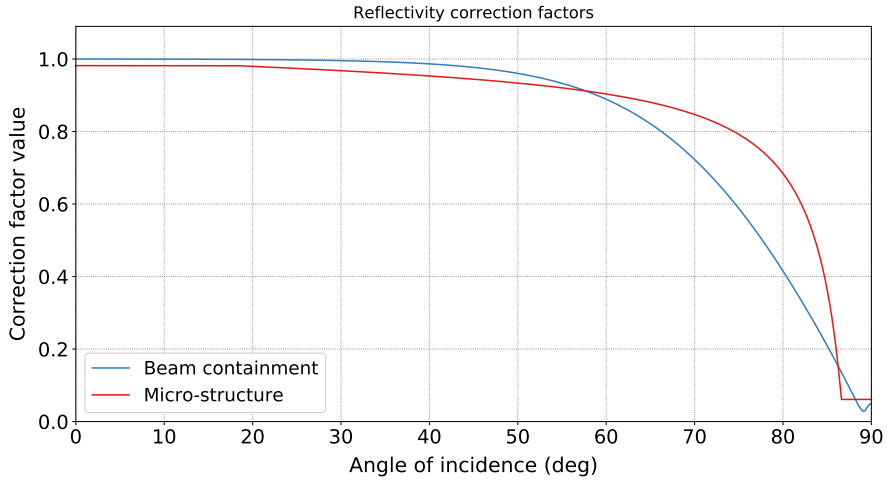

Figure 3.25.: Beam containment and micro-structure correction factor plotted over the angle of incidence. The FBK micro-structure values are taken as an example.

have a height h, a top width t and a side slope α. The pixel pitch is p. The incident light beam can be divided in four domains:

1. Domain 1 (green) is reflected by the microcell surface region s. The part Δt on the right lies in the shadow of the micro-structure strip. The reflected light will be observed in the specular peak.
2. Domain 4 (green) is reflected by the top face of the micro-structure strips. This surface is roughly parallel to the microcell surface and the reflected light may also contribute to the specular peak.
3. Domain 2 (red) hits the SiPM surface in the region Δt left of s where the light is reflected onto the edge of the micro-structure strips and reflected again under an angle of 270°-θ_i-2α. These photons are expected at an angle of 180°-2α relative to the incident light in the angular reflection spectra.
4. Domain 3 (blue) is reflected back by the edge of the micro-structure strip under an angle of 2α-θ_i-90°. The reflected light is (1) either directly reflected back under an angle of 2θ_i-2α relative to the incident light for large AOI, or (2) reflected again at the microcell surface resulting in an total relative angle of 2α-180° for small AOI, (3) or reflected by the micro-structure strip vis-à-vis also contributing to the specular peak. This third case holds for an AOI between 2α-90°-arctan $\left(\frac{2h}{p-t}\right)$ and 2α-90°+arctan $\left(\frac{h}{p-t-h/\tan(\alpha)}\right)$.

The pixel pitch p and the height of the micro-structure h of the SiPMs investigated in this work are such that photons hitting the detector in domains 2 and 3 are not detectable due to the limited scanning angle range of the setup. To take account for

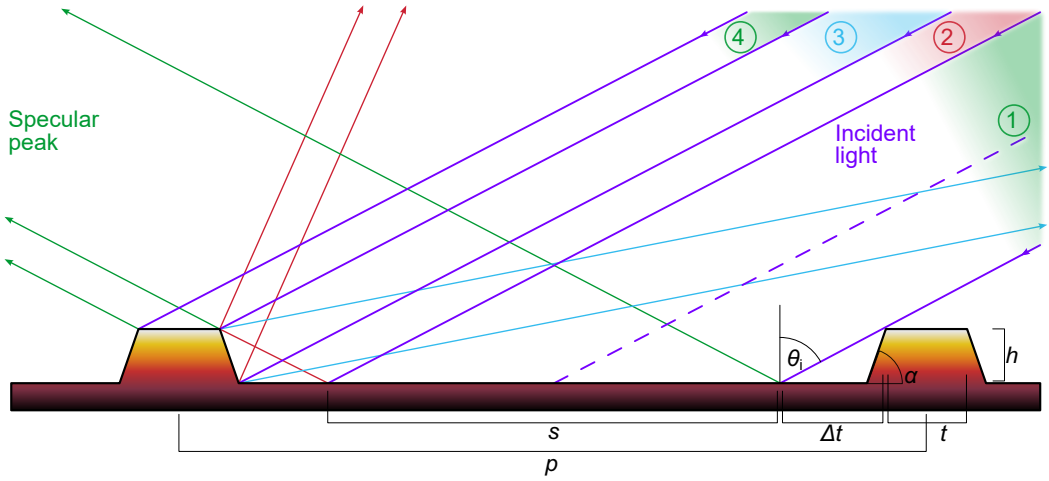

Figure 3.26.: Scheme of incident light (purple) interacting with the SiPM surface micro-structure. Domains 1 and 4 are reflected under the angle of incidence θ_i and result in the specular peak (green). Domain 2 (red) and 3 (blue) are reflected otherwise. The specular peak integral drops at large angles of incidence due to increasing shadowing by the micro-structure.

the loss of detectable photons due to the effects of the micro-structure, a geometric correction factor can be deduced:

$$c_{\mathrm{ms}}(h, p, \theta_i) = \frac{s+t}{p} = \frac{p - 2 \cdot \Delta t}{p} = 1 - \frac{2h}{p} \cdot \tan(\theta_i) \tag{3.16}$$

The correction facto depends on the architecture of the micro-structure and the angle of incidence θ_i. Figure 3.25 shows $c_{\mathrm{ms}}(h, p, \theta_i)$ plotted over the AOI based on the geometry of the FBK VUV-HD micro-structure. The specific geometric values are discussed later in section 3.5.3. The correction factor differs from equation 3.16 for angles smaller 90°-α where it is constant at $c_{\mathrm{ms}}(h, p, 90°\text{-}\alpha)$ since no shadowing occurs yet. It is also constant at t/p for angles above arctan$[(p\text{-}t)/2h]$ where the entire microcell surface is shadowed.

3.4. Measurements of setup systematics

Various sources of systematic uncertainties and their potential effect on the reflectivity measurements have been investigated in the course of this work. The systematics are discussed in the following and calculations of the uncertainties are given where possible.

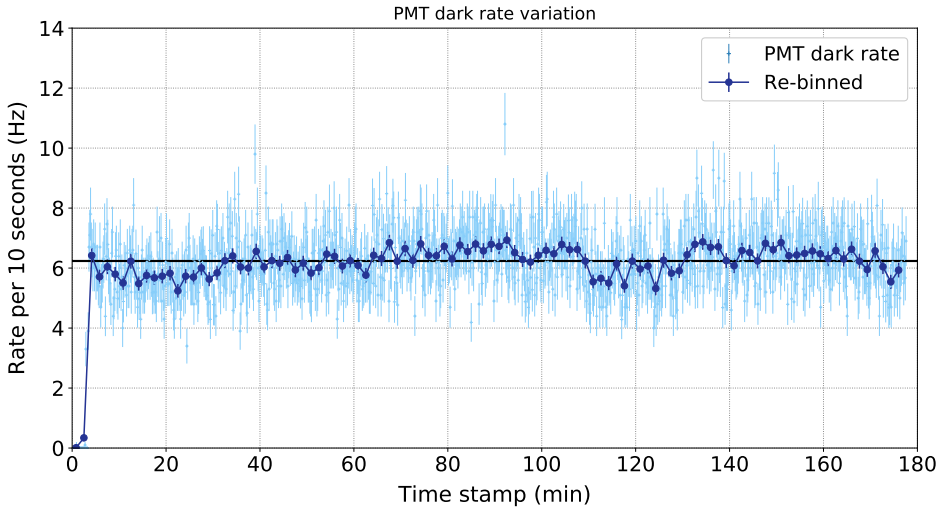

Figure 3.27.: Measurement of the PMT dark rate over time. The rate is averaged over every 10 data bins to smooth out random fluctuations. The dark rate is observably stable within several hours with relative fluctuations up to 14.7 %.

3.4.1. PMT dark rate

The PMT dark rate has been investigated for fluctuations with an acquisition time of about 3 hours and at a PMT temperature of −19 °C. Both deuterium lamp and main chamber vacuum gauge are switched off and all vacuum windows are light-tightened thoroughly. The data acquisition is started prior to ramping up the bias voltage to 811 V to also examine the PMT's response time to full gain. The stepping motor is turned off to keep the PMT at the same position. The quartz tube has been filled with xenon gas at 2.61 bar pressure gauge reading. The LED threshold was lowered to 10 mV to get an upper dark count rate limit.
The plot in figure 3.27 shows the PMT dark rate evolution with an acquisition time of 10 s per data point. The data is also re-binned averaging over 10 data points. The bias voltage has been turned on at 3 minutes. The PMT responds quickly and reaches a stable dark rate after about 3.5 minutes. The dark rate is stable afterwards at about (6.24±0.92) Hz. The xenon cold head has been cooling down to −80 °C between minute 22 and 46 reducing the xenon pressure to 2.47 bar. As expected, there is no significant effect on the dark rate.
Muons from cosmic ray interactions in the atmosphere will trigger scintillation processes in the xenon. The muon rate at sea level is about $130\,\mathrm{m^{-2}\,s^{-1}}$ [297]. This yields a muon interaction rate of 0.16 Hz in the liquid xenon when scaled to the quartz tube cross section. The contribution from muon induced scintillation to the dark rate is less than 3 % and is therefore neglected for further considerations of the PMT dark rate.

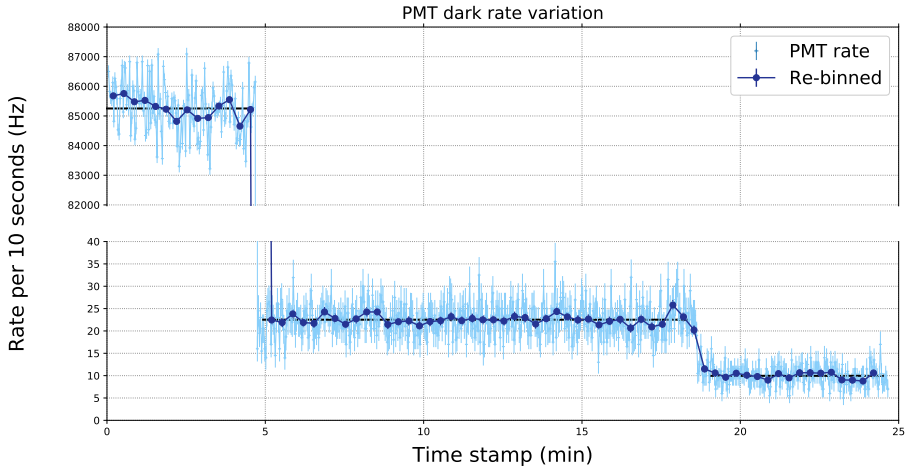

Figure 3.28.: PMT dark rate before and after the deuterium lamp is switched off. Each 10 data points are again averaged for a smoother curve. The dark rate is stable over 15 minutes but drops when the PMT is moved from the reference position.

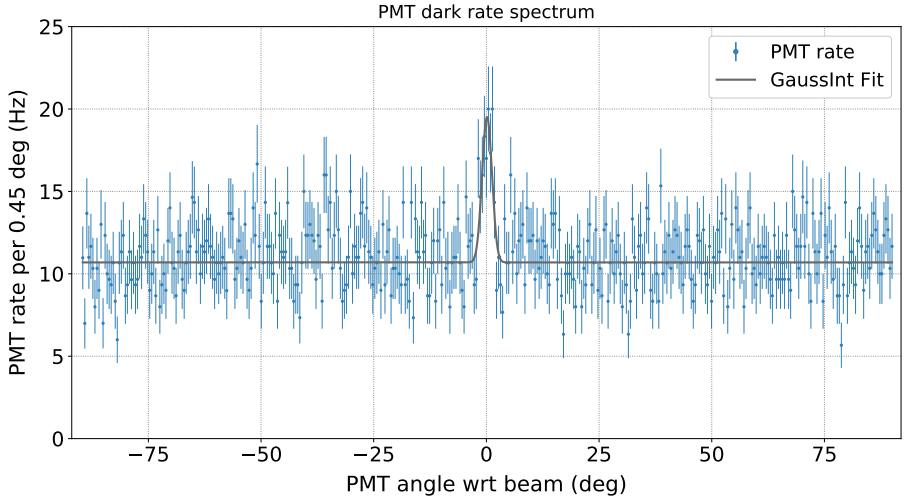

Figure 3.29.: The dark rate is independent of the PMT scanning angle except for the reference position where a small peak can be seen. This can be caused by afterglow effects of the MgF_2 window in the light guide system.

A second study has been performed to investigate the behaviour of the light source after being switched off. Additionally, the dark rate uniformity with scanning angle has been examined. Figure 3.28 shows a sudden drop of the PMT rate after the lamp shut down at about 5 minutes and a stable dark rate of 22.5 Hz afterwards. Based on the prompt shut down of the lamp, no pause has to be considered between two operation of the deuterium lamp. Nevertheless, a period of 1 hour has been

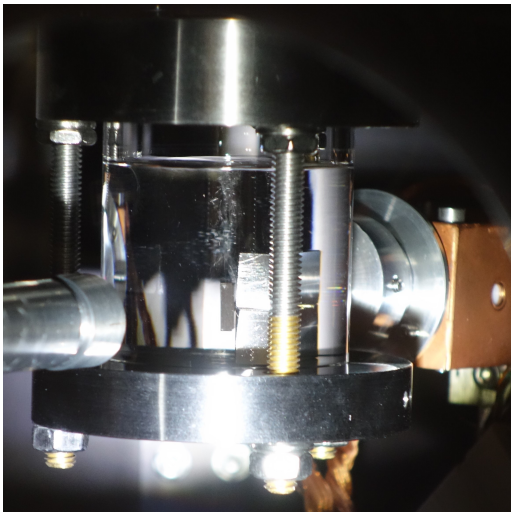

Figure 3.30.: Bubble streams originating from the pins of a VUV4 detector immersed in liquid xenon.

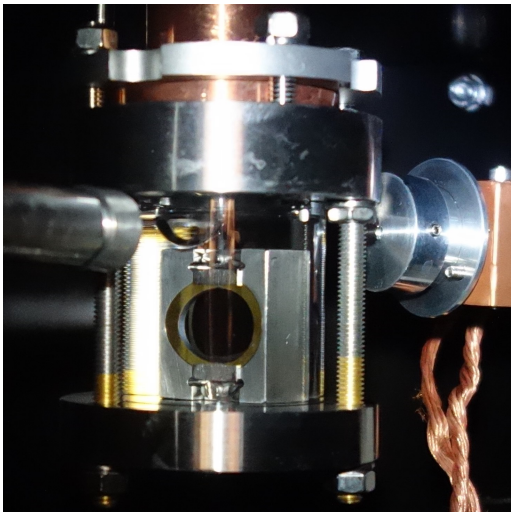

Figure 3.31.: A large bubble floating under the liquid xenon surface blocking the light path to the detector.

set up after each lamp shot down to properly operate the lamp and to warm up from cooled down conditions.
Figure 3.28 shows a drop at about 18 minutes when the PMT was manually moved out of the zero position vis-à-vis the beam collimator to an off-axis position. The rate drops to 9.9 Hz pointing to a scanning angle dependency of the dark rate. An angular spectrum has been performed under dark conditions and is shown in figure 3.29. The dark rate is stable over the entire scanned angle range except the zero position. Equation 3.9 has been fitted to the dark rate date and shows a 82 % increase when the PMT is facing the beam collimator. The observed increase is likely to originate from phosphorescence of the MgF_2 window – a material for which decay time constants of hours to days have been observed [305].
The observed variations are very tiny compared to the PMT rate under illumination. A systematic error of 1 % has been set to account for any dark rate variations.

3.4.2. Bubble formation

Bubbles in the liquid xenon can affect the path of the VUV beam and scatter photons thus blocking the PMT. Two kinds of bubbles can be observed.
First, streams of small bubbles have been observed originating from small or microscopic cracks and spikes in the sample or sample holder. These bubbles are gaseous xenon that face upward and especially occur outside of the thermodynamic equilibrium e.g. after a change of the xenon temperature. The xenon temperature and pressure has to be chosen carefully to avoid any bubble streams even in

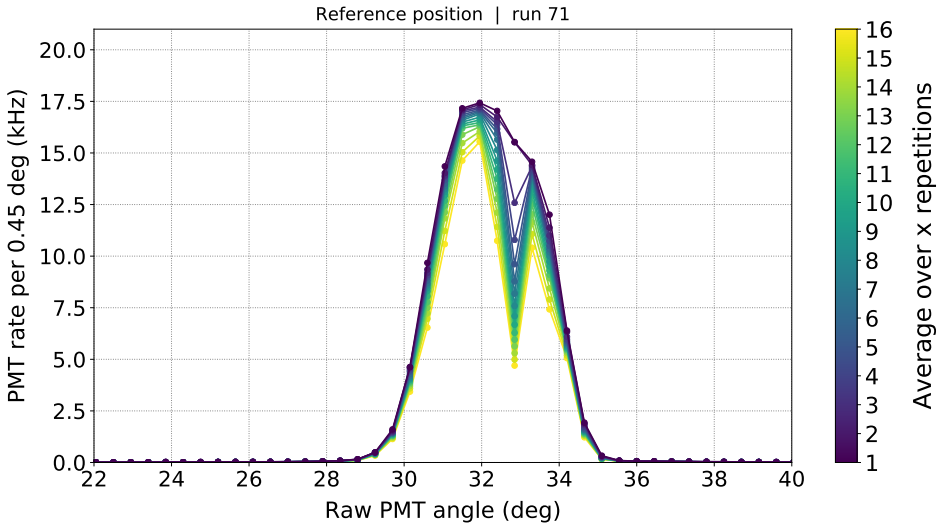

Figure 3.32.: Reference peaks of the APD run 71. The PMT rate has been evaluated 16 times for each angle step and averaged over x repetitions.

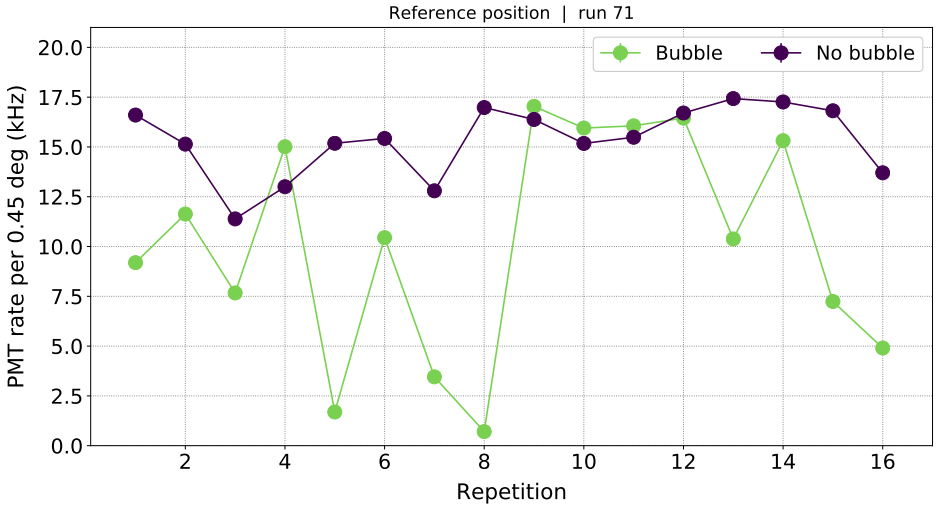

Figure 3.33.: PMT rate evolutions at two different PMT angle steps. The light green curve is affected by a bubble in the light path while the dark purple curve is unaffected. Statistical uncertainties are plotted but negligibly small.

equilibrium. This has been successful in all measurement runs. A picture of bubble streams origination from the pins of a VUV4 detector can be seen in figure 3.30. A second phenomenon is one single bubble floating under the surface of the liquid xenon. This bubble will grow slowly until it touches the sample holder, then bursts to reform again starting from several small surface bubbles. This kind of bubble

has been observed for several measurements. Adapting the xenon temperature and pressure will change the speed of the bubble growth and the velocity at which the bubble floats on the surface but did not prevent the bubble formation entirely. The bubble is believed to originate from impurities and vacuum residuals in the inner system. The impurities accumulate on the xenon surface and bend the gas-liquid phase transition downwards due to their weight. Xenon is known to have relatively large surface tension due to the large van-der-Waals forces which can explain the occurrence of such bubbles [274]. Such floating bubbles can be avoided if all components in the inner chamber including the quartz tube have been cleaned extensively with isopropanol prior to the measurements. A picture of a floating bubble above an APD sample detector can be seen in figure 3.31.
The impact of floating bubbles on the measurements can be seen in figure 3.32. This plot shows one reference run for the APD campaign during which the photograph in figure 3.31 was taken. 16 measurements have been taken for each angle step with an acquisition time of 2 s each before moving the PMT to the next angle. The average of the x highest PMT rates per angle step is plotted where x spans from 1 (only the highest PMT rate acquired) to 16 (average over all repetitions per angle step). If a bubble forms and moves into the beam during one angle step, a (larger) number of repetitions will be affected by light blockage and the average rate drops with an increasing number of repetitions. Apparently, the measurement is strongly affected by a large bubble while the PMT rested around 32.85°. Other angle steps look much more cleaner.
Figure 3.33 shows the PMT rate of the 31.95° (purple) and 32.4° (green) angle step plotted over the number of repetitions in chronological order. The purple curve is likely to only suffer from minor light blockage and the rate is quite constant. The green curve is strongly affected with several drops occurring whenever the bubble floats through the light beam. Strict cleaning procedures prior to any measurements are crucial to avoid this phenomenon and its systematic consequences.

3.4.3. Reference peak stability

A set of reference runs has been acquired during each campaign to monitor the stability of the reference peak integral. Instabilities can be due to PMT gain fluctuations or a change of the light source flux. Figure 3.34 shows the reference peaks over scanning angle for an FBK campaign with 6.5 hours acquisition time. The colour points to the reference run ID. Figure 3.35 shows the peak integrals and the peak position obtained from a fit with equation 3.9 to the reference spectra plotted over the time stamp of the individual reference runs. Apparently, there is some kind of evolution in the peak integral and position.
A standard deviation of 2.64 % and 0.67 % is obtained for the set of peak integrals and positions. This deviation can be set as systematic error on the reference

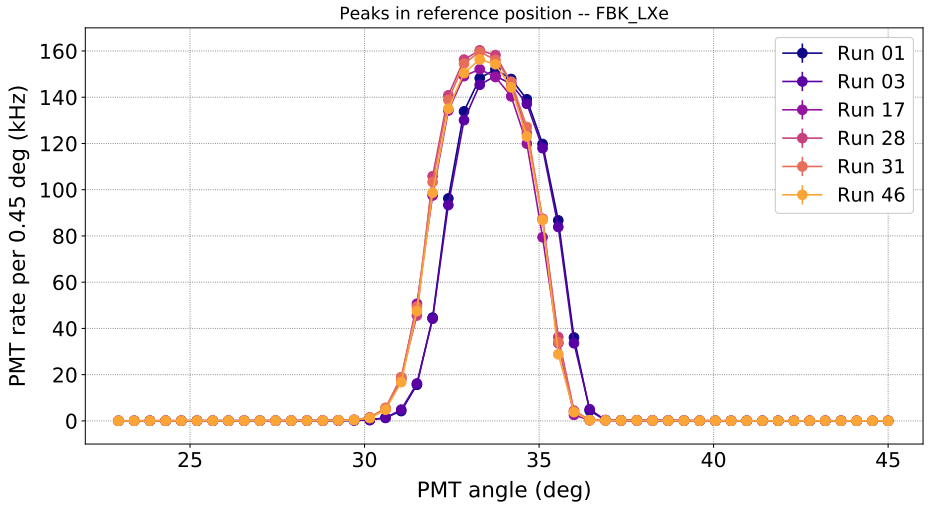

Figure 3.34.: A set of reference peaks measured at different time stamps during a reflection run with an FBK SiPM.

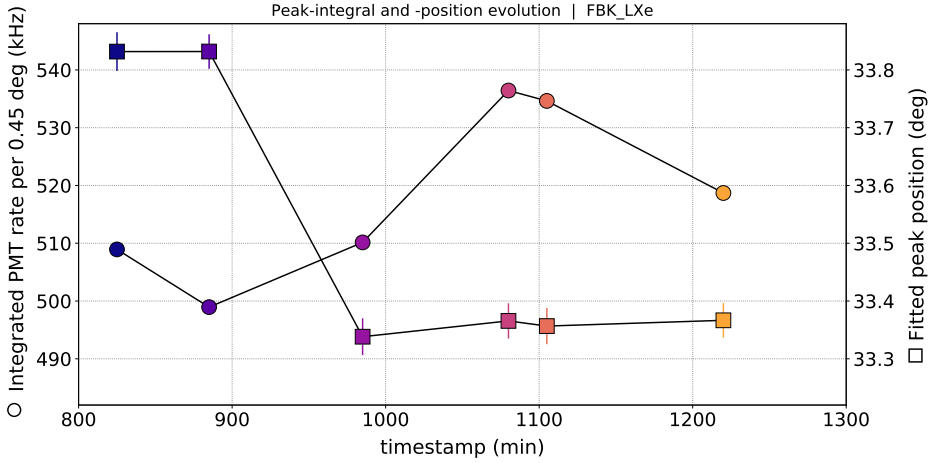

Figure 3.35.: Peak integrals and fitted peak positions of the same set of reference peaks as above. The reflction measurements in specular position are acquired between the reference runs. Both curves are interpolated to obtain the reference peak integral and PMT reference angle for each individual reflection run.

stability. A better way is to interpolate the curves and use the interpolated peak integral and position at the time stamps of the reflection runs to calculate the reflectivity for each AOI. This has been done for most of the reflectivity campaigns and a remaining systematic error of 1 % has been set to account for any inaccuracies introduced by the interpolation. For all other campaigns, the standard deviation of the peak integrals is taken.

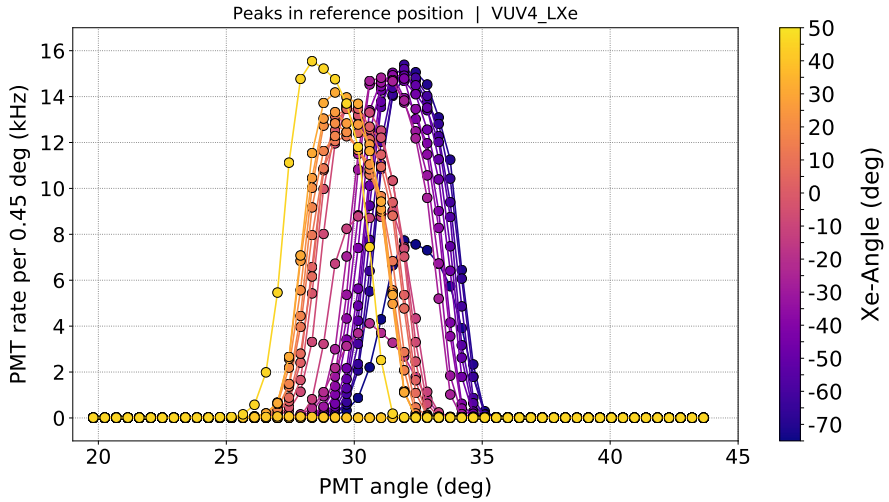

Figure 3.36.: A set of reference peaks at different xenon angles of the quartz tube. The maximum amplitude and the mean position are not constant for all curves.

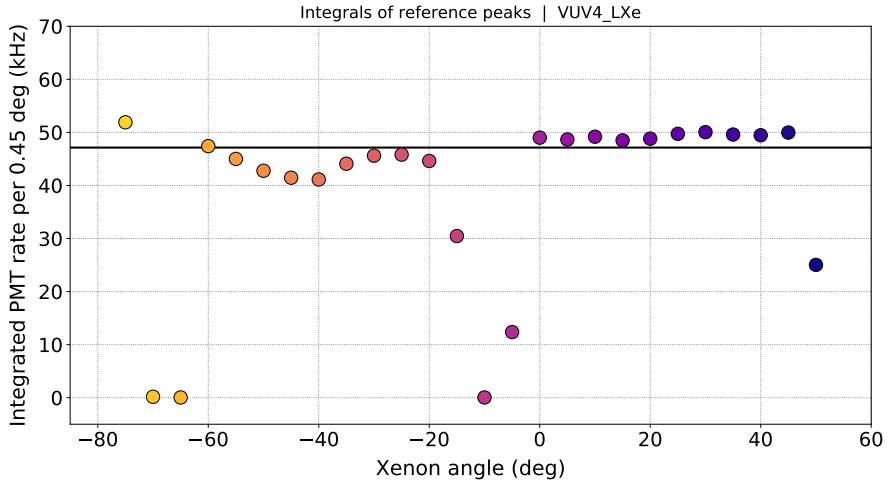

Figure 3.37.: Peak integrals of the same set of reference peaks. Equidistant drops in the integrated rate point to light blockage by the rods tightening the tube.

3.4.4. Zero point stability

Another set of reference runs has been used to investigate the stability of the PMT zero point (or reference angle) i.e. the position exactly vis-à-vis of the collimator (at θ_0 in figure 3.19). Figure 3.36 shows the individual reference peaks and figure 3.37 shows the peak integrals. The colour displays the xenon angle, i.e. the rotation angle of the quartz tube. The xenon angle range is limited by the xenon feed and bleed flexpipes as well as the cold head motor unit which all have to be rotated

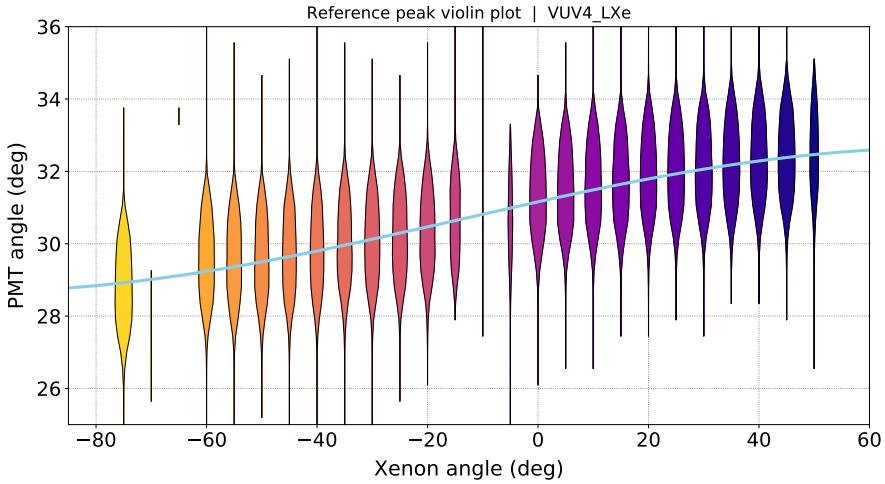

Figure 3.38.: Violin plot of the same data set. Reference spectra are shown vertically with filled curves. The x-axis shows the angle of the quartz tube (xenon angle) on an arbitrary scale. The blue curve is a sine fitted to the peak maximum positions.

along with the inner chamber. There are distinct gaps in the peak integrals caused by the rods tightening the quartz tube and blocking photons from arriving at the PMT. In total, there are three tightening rods as shown in figures 3.32 and 3.33. Any rod may block incident light when located between collimator and tube or block light exiting the quartz tube when located between tube and PMT. This yields an equidistant spacing of 60° between the gaps. The rate appears to be rather stable in between the gaps with a standard deviation of 6.4 % within the total acquisition time of about 4 hours.

Figure 3.38 shows a violin plot of the same data set where each peak is plotted as a vertical mirrored and filled curve for each individual xenon angle. Only data points with a rate higher than 15 Hz are shown to focus on the peaks. The plot reveals that the zero point of the PMT scanning angle scale depends on the xenon angle even though the quartz tube axis has been aligned with the axis of the PMT orbit. This can be explained with a small tilt of the quartz tube itself causing the tube to slightly wiggle perpendicularly to the light beam. It becomes clear from figure 3.23 that such a movement (up and down in the scheme) will move the focus point behind the quartz tube as well and therefore shift the PMT angle zero point. Equation 3.9 has been fitted to the individual peaks to derive the PMT angle where the peak maximum occurs. A sine function has been fitted to these angles and is shown in blue in figure 3.38. The sine has an amplitude of 2.00° and the deviation for the xenon angle range used in the measurement campaign in this work is ±1.136°. This value has been used as a systematic error on the AOI values at which the reflectivity of a given sample is investigated.

3.4.5. Rayleigh scattering

Rayleigh scattering is the elastic scattering of photons by particles smaller than the wavelength of these photons. It occurs for VUV light in xenon with typical scattering lengths of about 40 cm (see table 2.4). For a light path of the inner diameter of the quartz tube of 4.0 cm, about 91 % of photons travel without experiencing scattering. Rayleigh scattering affects both reference and reflection measurements. Since the light path is constant whether or not reflection occurs, the effect of Rayleigh scattering should affect both kinds of data in the same way and have no systematic impact on the reflectivity. The same is true for contaminations and impurities in the liquid xenon that absorb VUV photons.
A systematic error due to Rayleigh scattering is only considered for the last 2.0 cm where the VUV photons take different paths in reference and reflection measurements. For this path length, 95.12 % of light survives so 4.88 % has been set as a systematic error attributed to Rayleigh scattering.

3.5. Reflectivity Results

The following section presents the results obtained in various reflectivity studies with different samples. The measurements have been taken during several research trips and are not shown in chronological order.
The samples examined in the reflectivity setup are listed in table 3.2. The VUV3 and the VUV4 are VUV-sensitive SiPMs from Japanese manufacturer Hamamatsu. Italian manufacturer FBK provided samples from their VUV-HD LF model from 2016 and a bare silicon wafer sample covered with a 1.5 µm thick film of SiO_2. The APD is a mechanically and optically intact spare part from the assembly of the EXO-200 detector.
The acquisition time per angle step is set to several seconds or more for all angular spectra presented in the following. This and the strong intensity of the light source provides a large photon flux even in the limited VUV spectral width extracted by

Sample	Model	Manufacturer	Size	Pitch	Ref.
VUV4	MPPC S13370	Hamamatsu	$(6\,\mathrm{mm})^2$	50 µm	[146]
FBK	VUV-HD LF	FBK	$(10\,\mathrm{mm})^2$	35 µm	[147]
Wafer		FBK	$(20\,\mathrm{mm})^2$	plain	
APD	SD630-70-75-500	Advanced Photonix	⌀ 25.6 mm	plain	[226]

Table 3.2.: This list contains the samples of which the reflectivity has been studied in this work. References to literature are given where possible.

the monochromator. As a consequence, statistical uncertainties on the measured PMT rate are very small – even for parts of the angular spectra that present only small photons rates. Statistical uncertainties are plotted for all photon rate data but are mostly neglectable.

3.5.1. Beam profile

The first study reported here is the investigation of the 2D-profile of the reflected VUV beam. This has been accomplished in liquid xenon for a reflectivity campaign using the wafer sample at an AOI of +30°. The goal is to study the shape of the profile and compare it to earlier investigation performed with the same setup to validate the proper assembly of the setup components. The beam profile also allows to determine the refractive index of liquid xenon if fitted with the mathematical framework established in section 3.3.2.
The beam profile was obtained by varying the z-setpoint of the PMT orbit in steps of 0.25 mm and recording one angular spectrum for each z-point. The profile is plotted in figure 3.39 where the colour represents the PMT rate. The scanning angle has been converted to millimeter to be comparable to the PMT orbit z-points on the y-axis.
The beam profile is elliptic due to the focusing effect of the quartz tube and the liquid xenon. According to the discussion in section 3.3.2, the beam is compressed in the plane of incidence but not in the direction of the cylinder axis. The beam profile can be described with the 2-dimensional Gaussian integral function in equation 3.13. The width σ is scaled in one direction to account for the polar compression. The fit to the beam profile is shown in figure 3.40 along with projections of the peak on both parameter planes.
The analysis of the fit parameter yields a FWHM of 2.907 mm of the initial Gaussian beam. This compares well to the beam profile initially measured in [79] with the same setup (see figure 5.24 ibid.). The small difference may be due to the quartz tube since the studies in [79] have been performed in vacuum without any inner chamber. The scaling factor introduced in section 3.3.2 to account for the focusing power of the liquid xenon can be translated to a refractive index of LXe via equation 3.11 which yields 1.5667±0.0081 from the fit above. This value is well within the range of experimental measurements of the refractive index of liquid xenon summarised in table 2.4 and especially lies within the challenging uncertainties presented in [71].
The beam profile also reveals a slight tilt of the peak compared to a strict vertical symmetry. This is due to a small tilt of the quartz tube causing the peak centre to slightly shift with the z-point as already suggested in section 3.4.4. The tilt can be investigated by plotting the angular position of the peak maximum versus the z-point of each angular spectra. This is shown in figure 3.41. A linear dependency

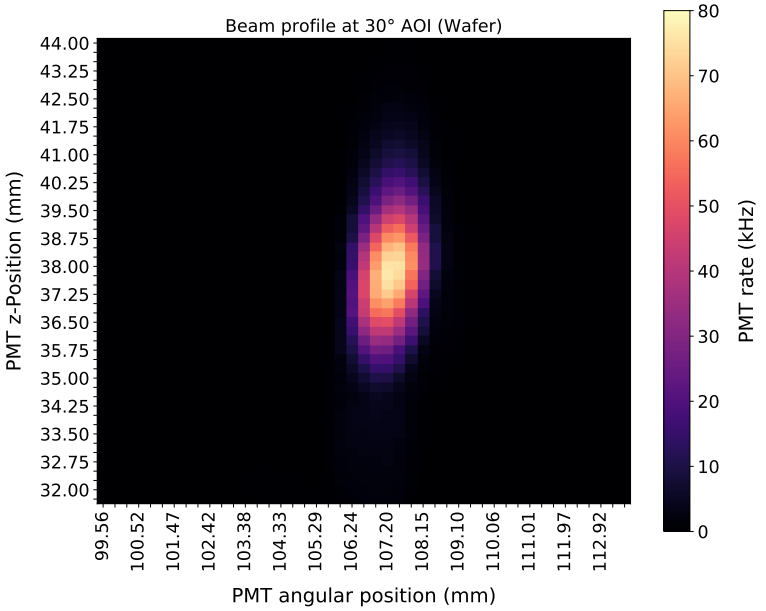

Figure 3.39.: VUV beam profile with the Wafer as reflection sample at an AOI of 30°. The PMT angle in the plane of incidence is converted to circle segments and plotted on the x-axis. The y-axis shows the z-position of the PMT orbit. The beam is compressed in the plane of incidence due to the focusing of the liquid xenon.

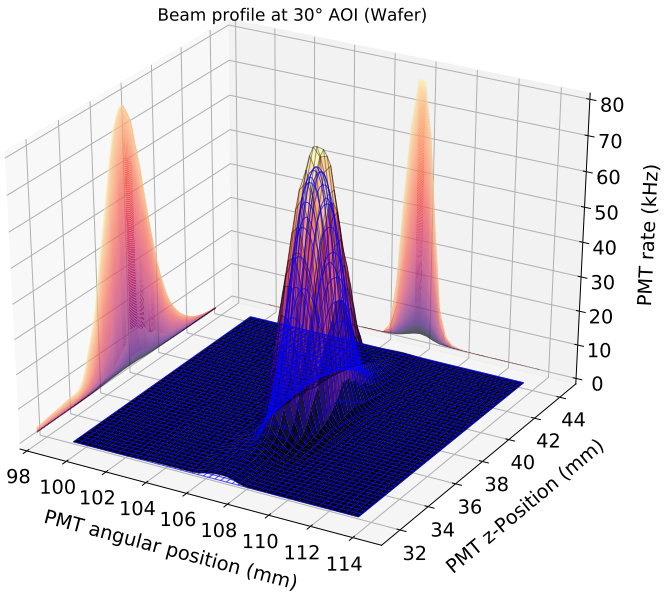

Figure 3.40.: The same beam profile as above but as 3-dimensional plot including a fit with equation 3.13 (blue) and planar projections to both abscissae.

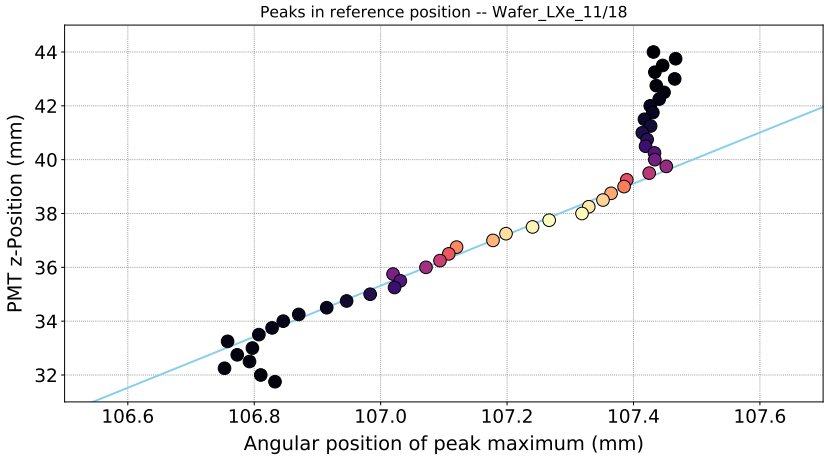

Figure 3.41.: Maximum position of the individual angular spectra forming the beam profile plotted versus their corresponding PMT z-setpoint. The beam profile is not exactly vertical due to a slight tilt of the quartz tube.

is expected in case of a tilt of the tube. A corresponding fit to the data points with peak integrals inconsistent with zero yields a tilt angle of $(6.02 \pm 0.03)°$. In figure 3.40, this angle is already used to rotate the data before applying the fit procedure with equation 3.13.

3.5.2. FBK Wafer

Studying the wafer sample provides a good approach to understand angular spectra in detail. The wafer sample exhibits a plain geometry and diffuse reflection is completely absent. The wafer has been examined both in vacuum and liquid xenon and differences in the corresponding spectra are pointed out in following. Oscillations appear in the wafer reflectivity curve due to a mismatch of the refractive indices and are discussed as well.

Acquisition of angular spectra

The bare silicon wafer sample has been provided by FBK and is equipped with a 1.5 µm thick SiO_2 coating on the surface. The wafer sample has been investigated in both vacuum and liquid xenon. Pieces from the same wafer have already been examined by P. Lv at al. in vacuum while also delivering simulations of the predicted reflectivity in liquid xenon [202].
A set of reference peaks each has been recorded for the vacuum and liquid xenon wafer campaigns (similar to the set shown in figure 3.36). Figure 3.42 shows one reference spectrum from each campaign. Several conclusions can be made:

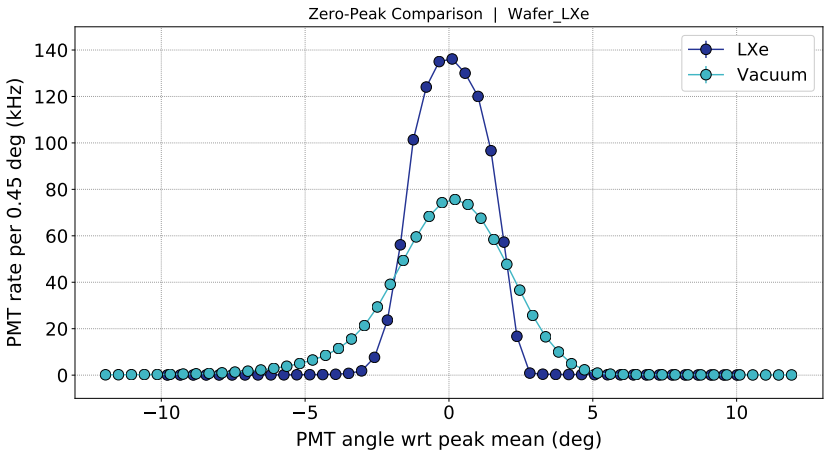

Figure 3.42.: Reference peaks in vacuum and liquid xenon (LXe) using the wafer sample. Both peaks are aligned in the peak maximum position (mean value). The peak in LXe is compressed due to the focusing effect of the xenon.

1. The peak integrals are very stable over time ($< 1\,\%$) for each campaign. Their average value was used as a reference point for the reflectivity calculation (including the uncertainty from section 3.4.3).

2. The reference peak in liquid xenon is significantly compressed compared to the vacuum peaks. This is caused by the focusing effect of the liquid in the quartz tube as discussed in section 3.5.1.

3. The peak integral in LXe campaigns is expected to be larger due to the matching refractive indices of fused silica and LXe. This is depicted in figure 3.43. In LXe campaigns, photons are unaffected at the LXe-FS-interface. At normal incidence, the reflectivity is $R = |(n_1\text{-}n_2)/(n_1{+}n_2)|^2$ according to the Fresnel equations. This yields $(1\text{-}R)^2$ more light in LXe campaigns which is about $5.21\,\%$ for the refractive index of the quartz tube.

4. On he other hand, the peak integral in LXe campaigns is also expected to be smaller due to Rayleigh scattering. Accordingly, the constant offset in the angular spectra should be higher given the non-directionality of Rayleigh scattering. Using the scattering length discussed in section 3.4.5, the fraction of scattered light is $9.52\,\%$ in liquid xenon.

All in all, reference peak integrals are expected to be slightly smaller in vacuum campaigns. This contradicts the measurements where the reference peak integral in LXe is $23\,\%$ larger. One explanation may be the light source which has been restarted in between both wafer campaigns. The light source has been seen before

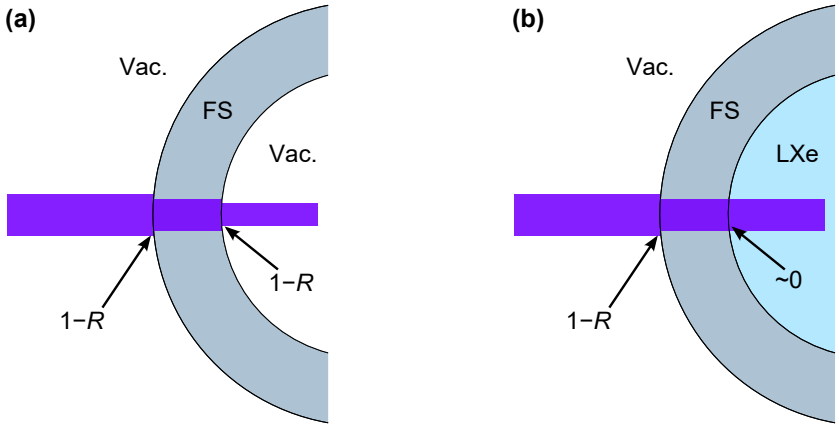

Figure 3.43.: A fraction R of VUV photons is reflected at normal incidence at the quartz tube (fused silica, FS) due to the mismatch of the refractive index to vacuum. Only a fraction of $(1\text{-}R)^2$ is transmitted in one tube crossing in vacuum campaigns (a). In LXe campaigns (b), the fraction is $(1\text{-}R)$ since the refractive indices of FS and LXe are very close.

to emit different levels of light for each launch. This can explain differences in the peak amplitude and integral between different campaigns.
Reflection spectra have been recorded for various AOIs in both campaigns – ranging from 17° to 87°. Smaller AOIs can not be realised in the setup since the beam collimator blocks the PMT housing. The spectra of the vacuum wafer campaign are plotted in figure 3.44. The upper plot shows the spectra including fits with equation 3.9. The peak amplitudes present an increasing trend but drop strongly at large AOIs. The lower plot shows the same data set in log-scale. The individual spectra are shifted with equidistant offsets for better visualisation. Only short spectra around the specular peak have been recorded for all but one AOI to save acquisition time. A secondary peak emerges for large AOI at the right hand side of the specular peak. Reflection spectra of the LXe campaign look very similar.
One full angle spectrum has been recorded for each wafer campaign (figures 3.45 and 3.46). There is one distinct specular peak and no sign of diffuse reflection following the cosine law in section 3.1.2. The spectra are again fitted with equation 3.9. The fits generally work well except for the base of the specular peak. The spectra are mostly flat apart from the peaks with a fitted offset of 41.9 Hz for the vacuum and 28.1 Hz for the LXe campaign. This contradicts the assumption from above, according to which Rayleigh scattering should result in a larger offset for LXe runs. The reason is likely to be a different dark rate of the PMT. The PMT temperature slowly decreased from −17 °C at the begin of the vacuum wafer campaign to −38 °C at the end of the LXe runs. The PMT dark rate is known to decrease with temperature [41]. This may explain the 33 % drop in the fitted offset.

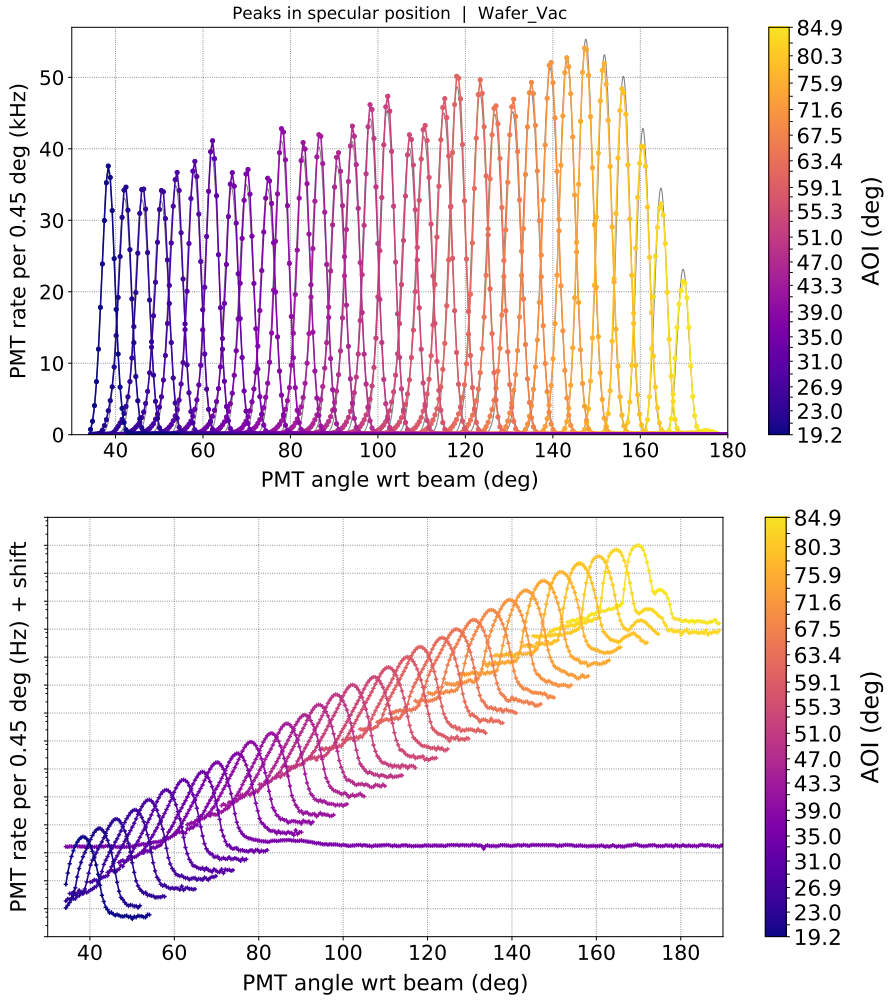

Figure 3.44.: Reflection spectra from the silicon wafer vacuum campaign with linear and logarithmic y-axis. The individual spectra are displaced by equidistant offsets in the lower plot to better display the entire measurement range.

A small secondary peak appears in the vacuum campaign but merges with the specular peak in LXe. This appears to be caused by the sample or sample holder where the reflected light is affected by the LXe focusing. Most likely, the outermost edge of the beam hits the edge of the sample holder where small chamfers have been cut into the material. This chamfers presents a different slope and therefore a different AOI resulting in a shifted secondary peak. These peaks are very small since both the projected surface of the chamfers and the fraction of photons hitting these are tiny. Their integral compared to the specular peaks grows with increasing AOIs due to the decreasing projected sample surface.

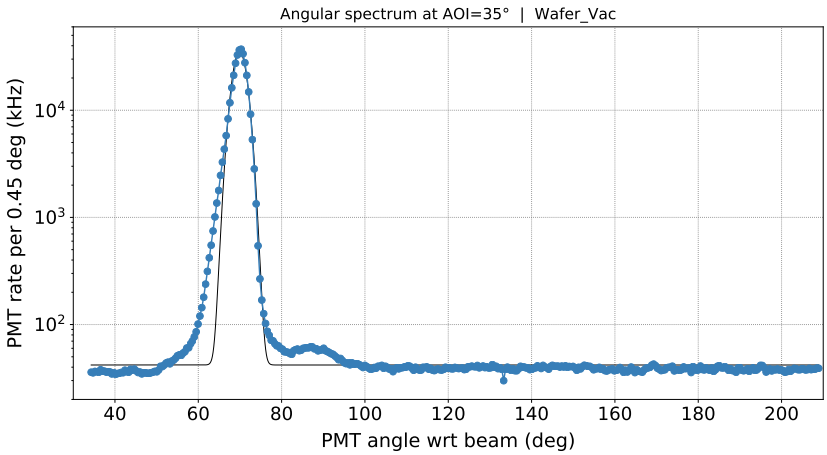

Figure 3.45.: Full angular spectrum of a wafer in vacuum under an AOI of 35°. No cosine-dependency indicating diffuse reflection can be observed.

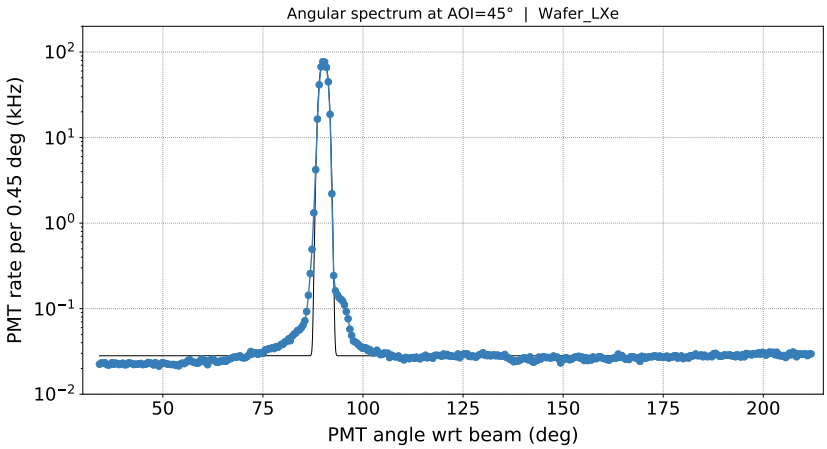

Figure 3.46.: Full angular spectrum of a wafer in LXe under an AOI of 45°.

Off-peak artefacts in angular spectra

A zoom into the base region of figure 3.46 reveals two additional features:

1. First, there is an exponential relationship in the offset rate at the right.
2. Secondly, a distinct jump in the offset rate can be seen at 135° with an amplitude of roughly 6 Hz.

A time constant of 257 min can be obtained for the exponential decrease within the darkened data. All angular spectra are recorded starting at small raw PMT angles and correspond to large PMT angles with respect to the beam according

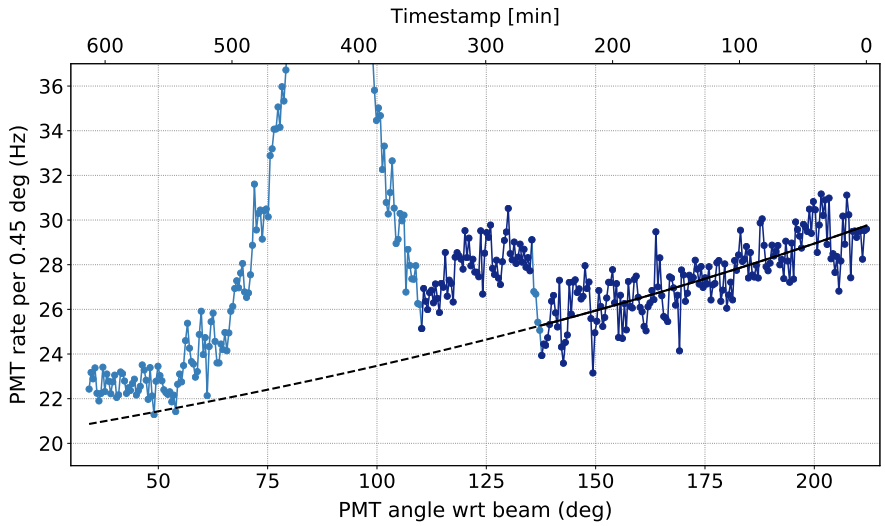

Figure 3.47.: Zoom on the baseline of the wafer LXe campaign in figure 3.47.

to figure 3.19. This means, the data acquisition takes place from right to left as indicated by the timeline on the top in figure 3.48. The PMT has been illuminated for 40 min straight prior to the acquisition of the plotted data for alignments and reference spectra measurements. The exponential decrease can be ascribed to phosphorescence of the bialkali photocathode after VUV-excitation for which similar relaxation time constants have been measured before [305]. No decrease has been seen in the case of the full angle spectrum of the vacuum campaign where no alignment or zero measurements have been performed previously.
The rate jump can be ascribed to the shadow of the sample holder. Behind the holder, Rayleigh scattered photons are effectively shielded from the PMT orbit. The PMT exits the shadow at θ_i+90° and promptly starts to detect these additional photons. This is shown in the scheme in figure 3.48. A mathematical evaluation can be set up by estimating the initial VUV photon flux F_i at the collimator. On their way to the quartz tube centre as well as from the centre to the other side of the tube, a photon fraction of f_Ray is scattered via Rayleigh scattering each. Only $F_\mathrm{i}{\cdot}(1\text{-}f_\mathrm{Ray})^2$ arrive at the PMT in reference position and only $F_\mathrm{i}{\cdot}R(1\text{-}f_\mathrm{Ray})^2$ in reflection position where the flux after the reflection is reduced by the reflectivity R. The total Rayleigh scattered light flux in reflection position is then:

$$F_\mathrm{Ray} = F_\mathrm{i} \cdot (f_\mathrm{Ray} + R(1 - f_\mathrm{Ray}){\cdot}f_\mathrm{Ray}) = F_\mathrm{add} \cdot \frac{4\pi r_\mathrm{PMT}^2}{\pi r_\mathrm{aptr}^2} \tag{3.17}$$

The last part describes the 4π solid angle integration of the additional rate F_add observed when exiting the sample holder shadow. r_PMT and r_aptr are the radii of the PMT orbit and PMT aperture. The total photon flux in the reference peak

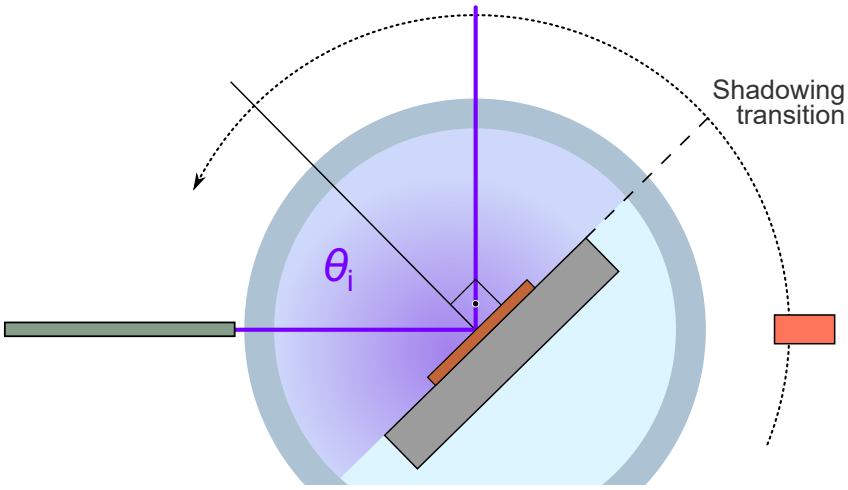

Figure 3.48.: Scheme showing the shadowing effect in the quartz tube. Scattered VUV photons can not be detected beyond a PMT angle of $\theta_i + 90°$ with respect to the collimator. The angle of incidence in the scheme is 45° as in the plot in figure 3.47.

F_{refr} can be obtained via a 3D integration using equation 3.13 and the parameters from the fits presented in figure 3.42. If only Rayleigh-scattering occurs, then:

$$F_i = F_{\text{refr}} + F_{\text{Ray}} \tag{3.18}$$

Combining both equations, f_{Ray} can be calculated based on the 4π integration of F_{add}, the 3D integration of the reference peak, and the reflectivity at 45° at which figure 3.48 was acquired. Putting this into the attenuation law:

$$(1 - f_{\text{Ray}}) = I(x)/I_0 = \exp\left(-x/\lambda_{\text{Ray}}\right) \tag{3.19}$$

yields a Rayleigh scattering length of about 76 cm. This value is in the same order of magnitude of dedicated measurements presented in table 2.4. With this result, it seems likely that scattered light is dominantly due to Rayleigh-scattering. Still, the dark rate was significantly higher for the wafer campaigns compared to the one measured in section 3.4.1.

Wafer Reflectivity

The specular reflectivity r is calculated according to equation 3.6 by dividing the specular peak integrals from the angular reflection spectra by the integrals derived from the reference spectra. The values for both wafer campaigns are plotted in figure 3.49. The reflectivity increases with AOI up to about 75° where the curves drop rapidly. At this angle, the beam containment becomes an issue and the projected sample surface decreases to roughly the beam width.

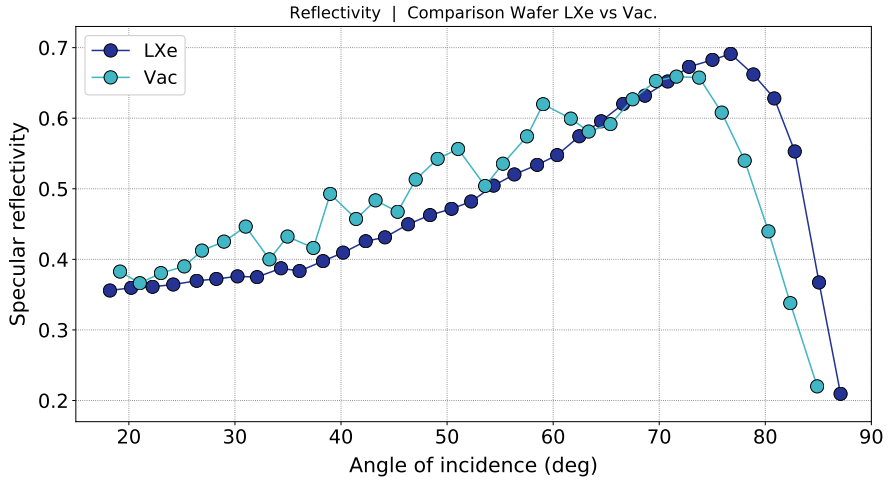

Figure 3.49.: Specular reflectivity over AOI for the wafer sample in vacuum and LXe.

Both campaigns produce quite similar reflectivity values however the vacuum data reveal an oscillation. This is due to a mismatch in the refractive indices of the sample surface and the test medium. The wafer sample is coated with 1.5 µm of SiO_2. A fraction of photons entering the sample experience back-reflection at the SiO_2-Si interface. In LXe these photons are not affected by the SiO_2-LXe interface due to the matching refractive indices and just travel back towards the collimator. In vacuum however, these photons start to interfere with the primary light beam depending on the AOI and SiO_2 thickness. This oscillation has been investigated before by P. Lv et al. [202]. Their results are compared to the studies from this work in figure 3.50. The grey data was obtained with a sample of the same wafer and a narrow unpolarised VUV spectrum around 175 nm. The oscillation frequency in the data from this work has been found to be 9.7° via Fourier analysis and agrees with [202]. The amplitude however does not agree since the spectral width used here is 5.3 nm while it was 0.8 nm in [202] resulting in less distinct oscillation features observed.

The data in [202] has been fitted with a Fresnel model of the wafer to obtain the refractive index n and extinction coefficient k of the SiO_2 coating. With these values, the reflectivity was simulated if the wafer was submerged in liquid xenon. Figure 3.51 compares the simulation results to the measurements presented previously and reveals a significantly different behaviour. In the simulation, total reflection occurs above 68° and a slight oscillation component can be seen – similar to the measurements in vacuum. This oscillation is again caused by a refractive index mismatch between the SiO_2 and the LXe. The most recent literature value 1.69 is used in the simulation for LXe (see table 2.4) while SiO_2 is reported to have indices around 1.59 at 178 nm (according to [262] and [106]).

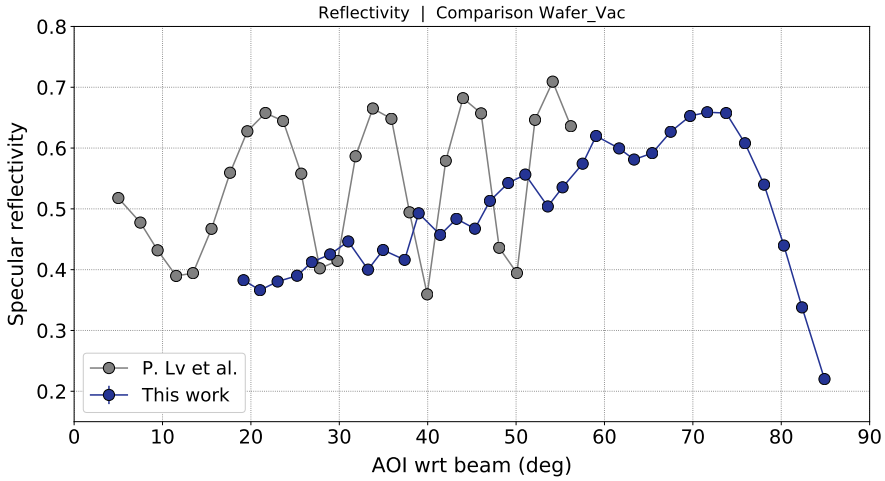

Figure 3.50.: Reflectivity over AOI for the wafer sample in vacuum. The data from this work (dark blue) is compared to measurements reported in [202] (grey).

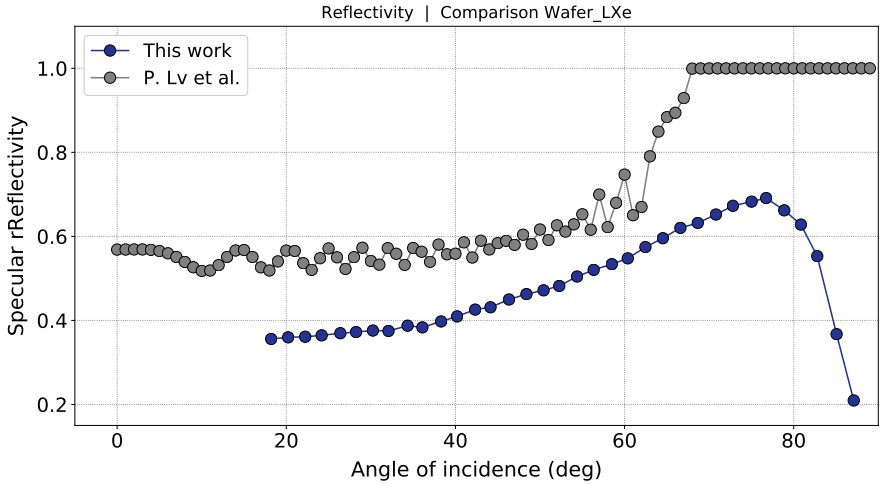

Figure 3.51.: Reflectivity over AOI for the wafer sample in LXe. The data from this work (dark blue) is compared to compared to simulations reported in [202] (grey).

The refractive index of LXe however is still experimentally unconstrained. Also, it increases drastically with wavelength in the VUV regime so only small variations of n_{LXe} result in strong differences of the reflectivity curve (see [165], Fig. 1). Indeed, the refractive index of 1.57 found in section 3.5.1 is very close to the one of SiO_2 so no oscillations and no total reflection are expected in this case which agrees much better with the measured data. The results from this work therefore suggest that the recent literature values for the refractive index of LXe at 178 nm are about 7 % too high.

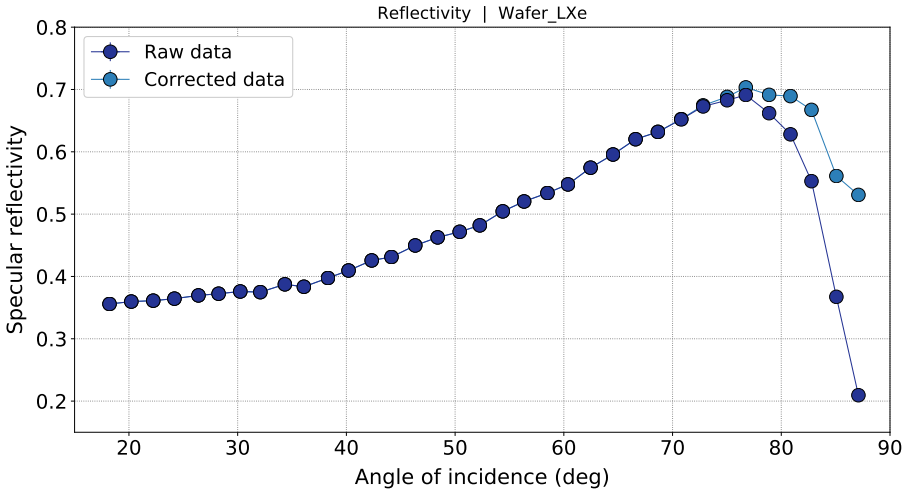

Figure 3.52.: Reflectivity over AOI of the wafer sample in LXe including a correction of the VUV beam containment on the sample surface.

The sudden drop of the reflectivity at large AOIs can be ascribed to the beam containment on the sample surface. At large angles, the projected surface of the sample becomes so small in lateral direction that the beam spot increasingly exceeds the sample and less light is reflected. This can be accounted for with the containment correction factor introduced in equation 3.15. The correction factor is 1 as long as the projected sample surface is significantly larger than the beam width in the quartz tube but decreases rapidly at high AOIs. Figure 3.52 compares the corrected and uncorrected reflectivity values. No drop can be seen in the corrected curve which appears to continue the data much more smoothly. No uncertainty is given for the correction factor but they can be assumed to be substantial for the highest AOIs due to the unknown exact beam shape in the LXe. The corrected values therefore are only of little benefit. Also, the angle range producing significant differences from the uncorrected reflectivity curve is limited.
Finally, it needs to be noted that equation 3.9 fits the vacuum peaks very well – including the scaling factor from equation 3.12. Fits tend to underestimate the peak widths for small AOI but yield slightly higher values for larger AOI. This indicates that the beam width increases with the angle of incidence. Peaks in LXe show more severe problems. The biggest one is a plateau-like flattening around the top of the peaks. The goodness-of-fit improves for slightly adapted r in equation 3.9 indicating an inaccuracy of the mathematical model to describe an aperture collimator. Indeed, the model works far better if data is obtained with the slit-collimator in front of the PMT housing as in the VUV4 campaigns.
Another reason is the astigmatic focus caused by a double cylindrical lens like the quartz tube. The astigmatism can not be described accurately with a simple scaling

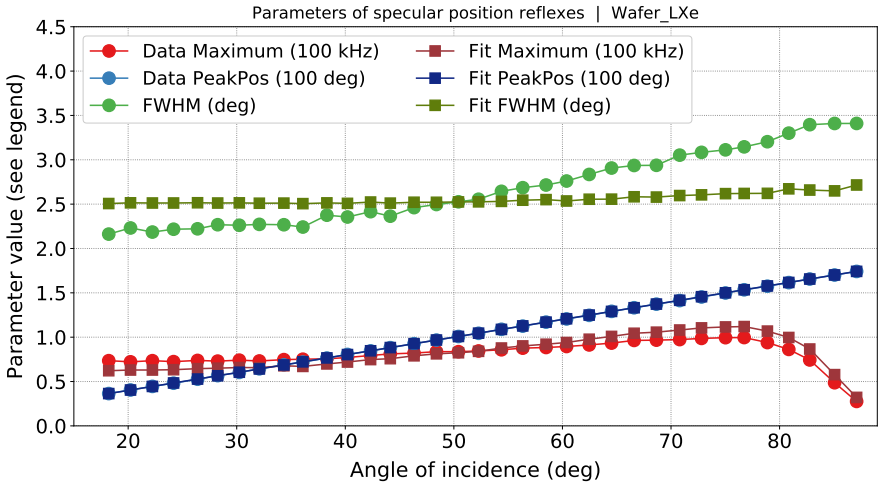

Figure 3.53.: Peak amplitude, position and FWHM of the reflection peak from the wafer LXe campaign. The values are obtained from raw data (circles) and Gauss integral fits (squares). There are discrepancies between the amplitude and FWHM sets since the plateaus at the specular peak are difficult to fit properly.

factor. Since the reflectivity calculation is purely data-driven, it does not depend on the fitting procedure apart from obtaining the peak position. The peak position is necessary to calculate the zero point of the raw PMT angle scale and the AOI of the reflection peaks. Figure 3.53 shows the LXe reflection peak parameters for the actual data (circles) and the Gauss integral fits (squares). The peak position is shown in blue and the same values are obtained via a data-driven analysis or the fit procedure. This means that the incapability of the fit to properly describe the peak shape does not affect the AOI calculation. On the other hand, fit amplitudes are smaller (larger) by roughly 9 % and the FWHM is larger (smaller) by about 12 % for small (large) AOIs. This shows that the fitted optimum derived with equation 3.9 does not fully capture the width of the peak plateaus. Considering the peak integrals, both effects mainly cancel each other out and fit integrals are in average 1.8 % short of the data integral.

All in all, the wafer sample presents clean angular reflection spectra. No diffuse reflection components was found. The incompatibility of the measured reflectivity and the simulation in [202] suggests that the optical parameters of the SiO_2 coating cannot be derived in vacuum and used to determine the reflectivity of the wafer in LXe. The wafer is suitable as a VUV mirror sample with which different reflection setups can be compared and validated. The Gaussian integral fit model established in section 3.3.1 only shows a decent capability to describe the specular peaks. This is no problem for the calculation of the reflectivity and the angle of incidence since the peak centres are described successfully.

3.5.3. FBK VUV-HD LF

The VUV-HD LF silicon photomultiplier model is manufactured from the same wafers investigated above and comprises an additional surface micro-structure for the electrical connections to the individual SPADs. Compared to the wafer, the VUV-HD reflectivity was found to be reduced by a constant factor independently from the angle of incidence. The reflectivity spectra present small, periodic oscillations that can be explained with the geometry of the micro-structure components that exhibit a regular scattering pattern.
The VUV-HD has been introduced in 2016 by FBK [147]. The development focused on an improved PDE in the near ultraviolet (NUV) region and a high fill factor (FF) achieved via a high density (HD) microcell array [147]. LF (*low field*) points to the low-noise focused doping profile. The FBK SiPMs have been manufactured from the silicon wafer sample investigated in section 3.5.2. The reflectivity in vacuum has been measured by P. Lv at al. [202].

Acquisition of angular spectra

Two LXe campaigns have been performed with one FBK SiPM: the first campaign with 37 reflection spectra where only a small angle range around the specular peak was scanned (*specular angle campaign*), and the second one with 12 full angular spectra (*full angle campaign*). This procedure was chosen to save acquisition time and end up with a large number of AOIs while still obtaining several full spectra for further analyses. Figure 3.54 shows the reference peak integrals and positions over the course of both campaigns. Grey data shows the reference runs recorded during the specular angle campaign, coloured data the ones from the full angle campaign. The reference integral is subject to significant oscillation although the lamp was not shut down during the entire acquisition time. Interpolated integral values have been used at the reflection peak timestamps to determine the reflectivity. The LabView protocol crashed three times and each time the step motor had to be turned back manually to the zero point of the raw PMT angle scale. This causes the distinct jump at around 900 min in the fitted reference peak position which has been taken into account for the AOI calculation.
All 12 full angular spectra are shown in figure 3.55 – again with an equidistant offset between the individual curves. As for the wafer, the specular peak is dominant with no sign of diffuse reflection. There are however secondary structures close to the peaks which didn't appear in the wafer campaign (see figure 3.44) and are caused by the micro-structure on the SiPM surface. The FBK micro-structure is quite compact and slim compared to other SiPM models. This explains why the secondary structures are not very prominent. The specular peak integral has been calculated by integrating over the entire spectrum and subtracting the fitted

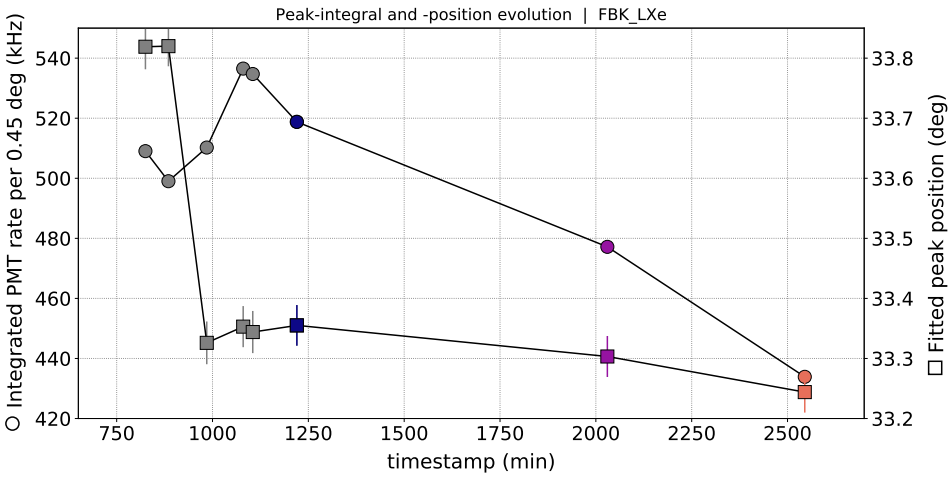

Figure 3.54.: Reference peak integral (circles) and position (squares) of the FBK campaigns. Grey data points have been obtained in the first campaign, coloured data points in the second campaign.

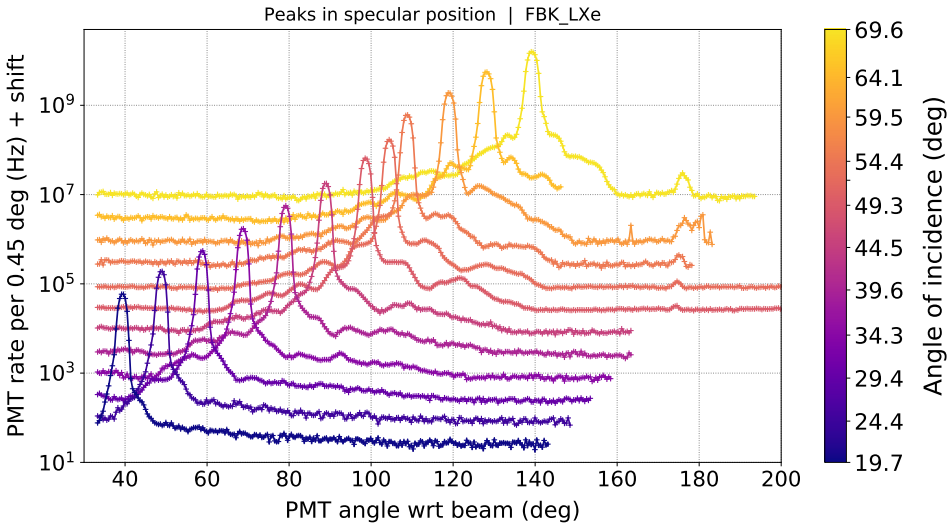

Figure 3.55.: Angular reflection spectra of the full angle FBK campaign. The distinct specular peaks are accompanied by small secondary structures which are caused by the micro-structure on top of the SiPM surface.

constant offset. The contribution of the spectral side structures to the integral is smaller than 2 % for all full angle spectra. The small artefacts just below 180° are likely due to VUV photons that miss the sample at large AOI and cross the tube unaltered eventually hitting the PMT in reference position. This also explains why this artefact gets increasingly distinctive with increasing AOI.

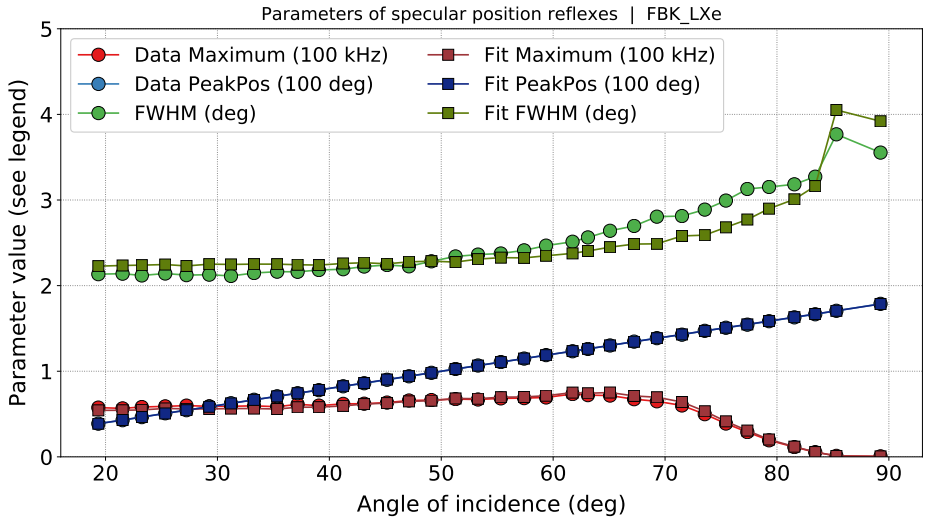

Figure 3.56.: Peak amplitude, position and FWHM of the reflection peak from the specular angle FBK campaign. The values are obtained from raw data (circles) and Gauss integral fits (squares).

The processing of the specular spectra data is done in the same way: fitting the peak with equation 3.9 and then integrating the data subtracted by the fitted offset. The fit maximum position is used to determine the AOI according to figure 3.19. The data-driven and fitted peak parameters are plotted in figure 3.56. As for the LXe wafer campaign, the fit struggles to reproduce the top plateaus depending on the AOI. The fitted amplitudes are within 5 % and the FWHM within 11 % of the peak values and in average fitted peak integrals are roughly 2 % smaller compared to the data integrals. The peak width increases at larger AOI and for the two largest values, the fit experiences problems due to the limited angle range of each specular spectrum. In any case, the peak maximum position is observed to follow the expected monotonic increase.

FBK Reflectivity

The specular reflectivity is again calculated via equation 3.6. The resulting curves for both FBK campaigns are plotted in figure 3.57. No beam containment correction has been applied yet. The data point at an AOI of 52.2° displays the largest discrepancy between both campaigns. The corresponding run however was acquired roughly 600 min after the last reference peak at the end of the campaign. The reference integral was extrapolated making this data point the least reliable one. For all other runs, the maximum deviation is about 9 % so both campaigns are entirely compatible within their systematic errors. As for the LXe wafer campaign, the

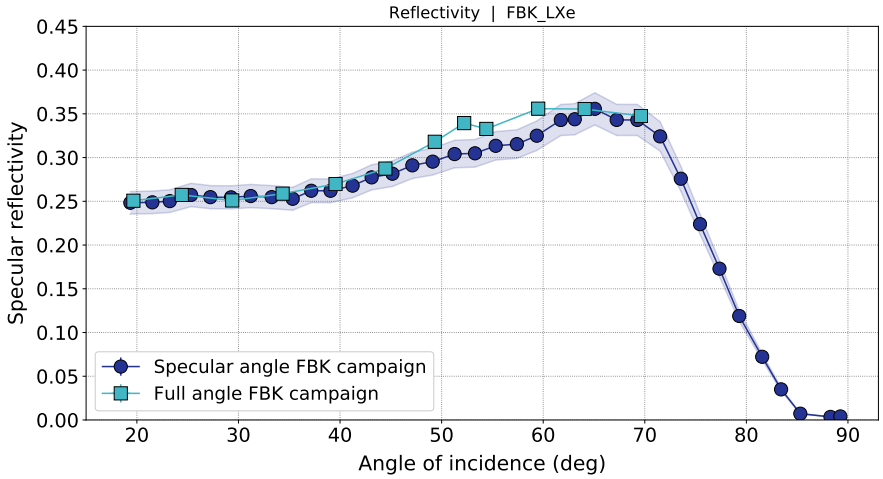

Figure 3.57.: Reflectivity over AOI of the FBK sample for both the specular angle and the full angle campaign. The systematic errors are calculated based on section 3.4 and is only plotted for the specular angle runs for better visualisation.

reflectivity is increasing steadily and drops at large AOI due to beam containment issues. The drop may also be caused by actual physical effects like unknown surface depositions which however cannot be resolved with the setup.
Applying the beam containment correction shows that a larger AOI range is affected for the FBK SiPM compared to the wafer campaigns since the edge length of the FBK is smaller than than of the wafer. As a result, the VUV beam starts to exceed the projected sample surface at smaller angles. Figure 3.58 shows a comparison of the FBK specular angle campaign and the LXe wafer campaign from figure 3.52. Both data sets present the same behaviour with AOI but the FBK reflectivity is reduced due to the surface micro-structure which has been added to the wafer during manufacture and is expected to not reflect any VUV photons under the specular angle. The reflectivity ratio is shown as a black line and is constant over AOI as expected in case of a mere loss of reflecting surface but drops for large AOI where the data becomes unreliable. The average ratio below 72° is 68 %. This is significantly smaller than the microcell surface ratio at about 90 % (calculated later) or the geometric fill factor (FF) at about 80 % [147]. This points to a different geometric effect which is yet to be resolved.

Effects of the surface micro-structure

On closer look, the reflection spectra show periodic wiggles that also affect the secondary structures. The wiggles are present in all reflection spectra. An example spectra at an AOI of 49.3° is shown in figure 3.59. Any periodicity within the

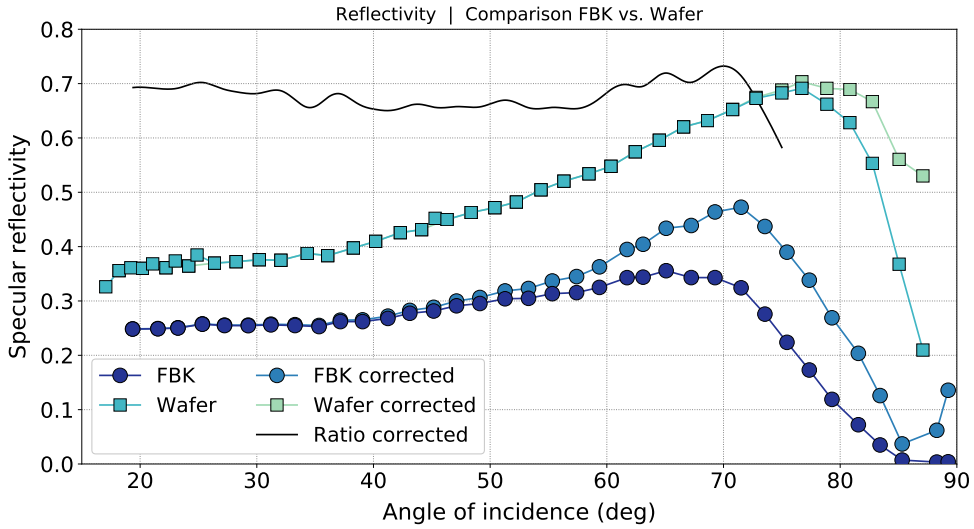

Figure 3.58.: Reflectivity over AOI of the FBK sample compared to the LXe wafer campaign. Both data sets are shown with and without beam containment correction. The black line shows the ratio between both corrected reflectivity datasets.

spectrum points to a periodic structure of the reflecting/scattering sample. In the case of SiPMs, this refers to the surface micro-structure. Consistently, there are no periodicities in the spectra recorded with the wafer sample without any micro-structure. To analyse the periodic components within the reflection spectra, a Fourier transform has been carried out (right in figure 3.59). The specular peak is excluded from the Fourier transform and only greyish underlaid data points are processed. The observed periodic wiggles correspond to a small peak at $1/0.13°$. A table-top scattering experiment has been performed to further investigate the angular scattering pattern of this SiPM. The photograph in figure 3.60 shows the scattering image of an FBK SiPM when exposed to green laser light at 532 nm under an AOI of 45°. The scattering image is complex with various maxima in two dimensions. Two periodicities can be seen in the plane of reflection: a fast one with a periodicity of 6.2 mm between two maxima and a slow one with a first maximum visible roughly 14 cm left from the bright specular spot. The scattering structure d can be derived via basic phase difference calculation:

$$\begin{aligned}\Delta &= \Delta_1 - \Delta_2 = \\ &= d\,\sin\theta - d\sin(\theta - \alpha) = \\ &= d\,\cdot\,(\sin\theta\,(1-\cos\alpha) + \cos\theta\,\sin\alpha) \\ &= \lambda\end{aligned} \tag{3.20}$$

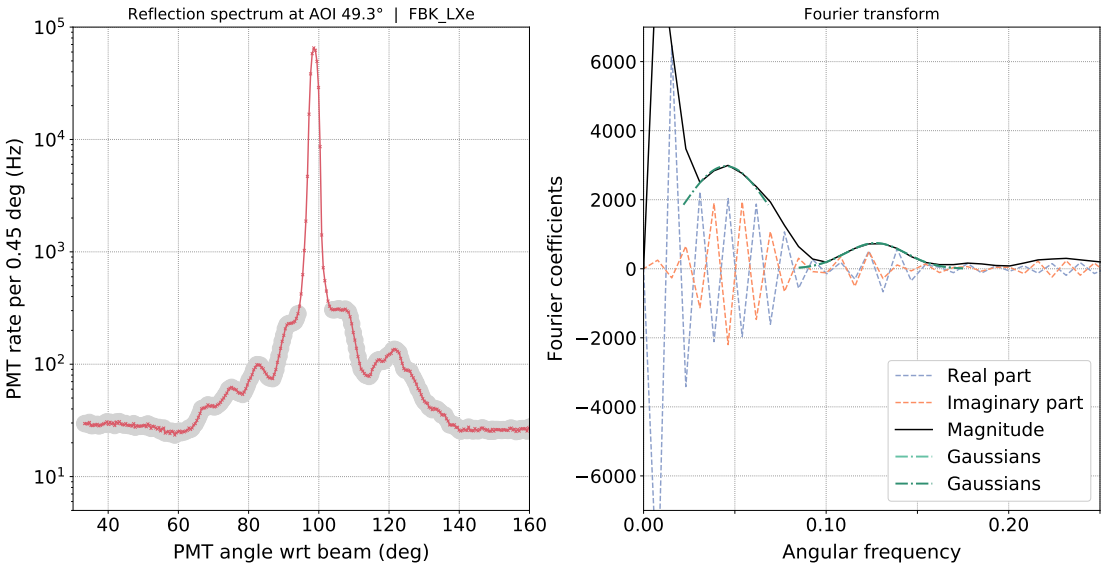

Figure 3.59.: Specular reflection full angle spectrum of an FBK SiPM in LXe at an angle of incidence of 49.3° (left). A Fourier analysis has been performed to analyse the periodicities within the angular spectrum (right). Only greyish underlaid data of the angular spectrum is processed to exclude the specular peak from the transform. The peaks in the Fourier magnitude is fitted with Gaussians to extract the angular frequency caused by the SiPM surface micro-structure.

where θ is the AOI and α the periodicity of the scattering pattern. The fast and slow components in figure 3.60 point to scattering structures with sizes 34.8 µm and 1.3 µm, respectively. The fast (and dominant) component corresponds to the SiPM pixel pitch at 35 µm of the FBK VUV-HD LF used in this work. This is verified with optical microscopy: in the picture in figure 3.61, horizontal bias lines act as common anode to distribute the bias voltage over the entire microcell array while vertical polysilicon resistors act as quenching resistor and connect the microcells on both sides of the bias lines. The pixel pitch is 35 µm, the microcell surface about $(32\,\mu\text{m})^2$. This gives a ratio very close to the geometric fill factor of 80 % [147]. The orientation of the micro-structure in the microscope picture corresponds to the choice of the azimuthal angle ϕ_i of the SiPM in figure 3.60. The polysilicon resistors are the vertical scattering structure and d is equal to the SiPM pixel pitch of 35 µm. This agrees very well with the structure size obtained from equation 3.20. If the SiPM orientation is rotated by 90°, the bias lines become the vertical structure and the scattering pattern is compressed. Equation 3.20 then yields $d = 69\,\mu\text{m}$ due to the fact that the bias line distance is twice the pixel pitch.

The fast component comes from the lateral dimension of the micro-structure components. The profile of the components are not stated by the manufacturer

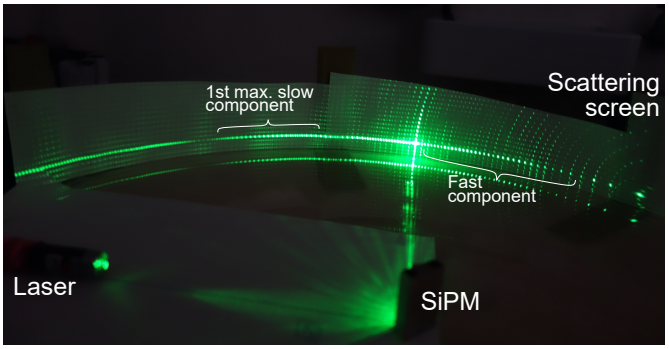

Figure 3.60.: Picture of the scattering pattern of an FBK VUV-HD LF SiPM. The SiPM was exposed with green laser light at 532 nm under an AOI of 45°. The scattering pattern shows a short-ranged fast component generated by the SiPM pixel pitch and a slow component from the electrical connectors on the SiPM surface.

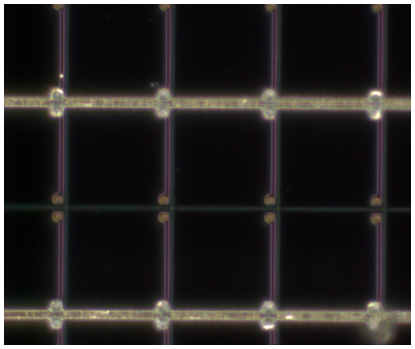

Figure 3.61.: 134 × 113 µm section of the same SiPM under the microscope. The bias lines are white, the polysilicon resistors purple and the grooves separating the microcells are green.

but is investigated with atomic force microscopy (AFM). A $(20\,\mu m)^2$ section of a micro-structure intersection is shown in figure 3.62. The vertical bias line (yellow) is connected to two polysilicon resistors (light purple) supplying the microcells (dark purple) which are mechanically separated by grooves (black) just next to the resistor lines. The grooves are assumed to represent the visible upper end of the SiPM trenches. Height profiles have been extracted of both bias lines and polysilicon resistors via averaging over about 100 line profiles and are shown in figure 3.63. Following the notation from section 3.63, the top width t is 2.14 and 1.19 µm, the height h is 0.975 and 0.198 µm and the slope α is 72 and 45° for the bias line and polysilicon resistor, respectively. The width of the polysilicon resistor fits very well to the scattering structure size derived from figure 3.60. The lateral dimension of the micro-structure indeed creates a visible scattering pattern.

The periodicity from the SiPM pixel pitch (fast component) cannot be resolved in the angular reflection spectra due to the small wavelength. Even at the highest AOI, the expected periodicity at 178 nm is 0.84° which is smaller than twice the smallest angle step size of 0.45° achievable in the setup. The slower periodicity from the micro-structure components however is observable and responsible for the two small peaks in the Fourier spectrum in figure 3.59. The right (secondary) peak is prominent in all reflection spectra at different AOI. The left (tertiary) peak is much fainter but still visible in all spectra. This indicates that two scattering patterns exist. Both peaks are fitted with a simple Gaussian to obtain the corresponding angular frequency. The responsible scattering structures d are then calculated from equation 3.20.

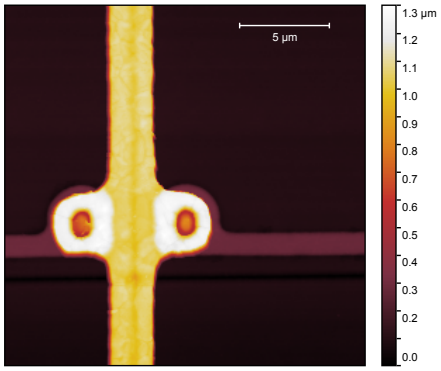

Figure 3.62.: AFM height image of a micro-structure intersection of an FBK SiPM. The vertical strip is one bias line which is connected to two polysilicon resistors on both sides.

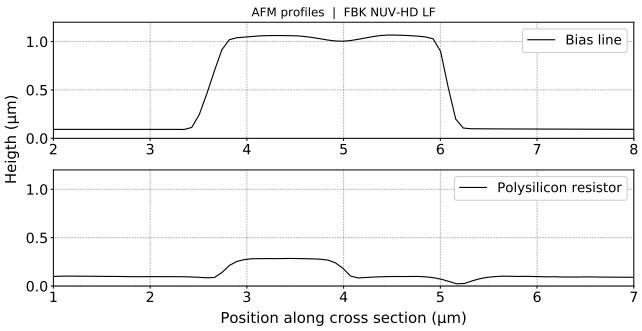

Figure 3.63.: AFM height profiles of the FBK micro-structure. The bias line profile is shown on the top and reveals two sub-strips separated by a small dip. The polysilicon resistor profile is on the bottom and also shows the microcell separation groove.

The data can be compared to the width of the micro-structure derived from the AFM image in figure 3.63. The orientation of the FBK SiPM during the FBK reflectivity campaigns was perpendicular to the orientation in figure 3.61 and the table-top scattering experiment in figure 3.60. The bias lines are the vertical structure responsible for any periodic pattern in the angular spectra. The geometric width of the bias line AFM profile is determined via the straight distance of the top corners to each other as well as from the top corners to the maxima of both sub-strips.

The result is shown in figure 3.64 where d is plotted via the corresponding AOI. Red data points show the periodicity in the angular spectra as derived via the Gaussian fit of the secondary peak in the corresponding Fourier spectra. The red band shows the average, minimum and maximum top width t of the bias lines as determined from the AFM cross section. Additionally, a less distinct tertiary peak can be seen at about half the angular frequency of the secondary peak in the Fourier spectrum in figure 3.59. This points to an additional structure less prominent than the bias line width. The tertiary peaks have been processed for all AOI and are plotted in figure 3.64 as well (blue data). They compare very well to the width of the bias line sub-strips (blue band). The sub-strips are separated by the small dip at 5 µm in figure 3.63 and are about half the total bias line width.

The AFM height image in figure 3.62 also allows to calculate the relative surfaces of the micro-structure components. For this, a height distribution of the image is extracted and scaled to one pixel. As a result, the microcell surface accounts for 90.2 % of the microcell surface, the bias lines for 5.0 % and the resistors and

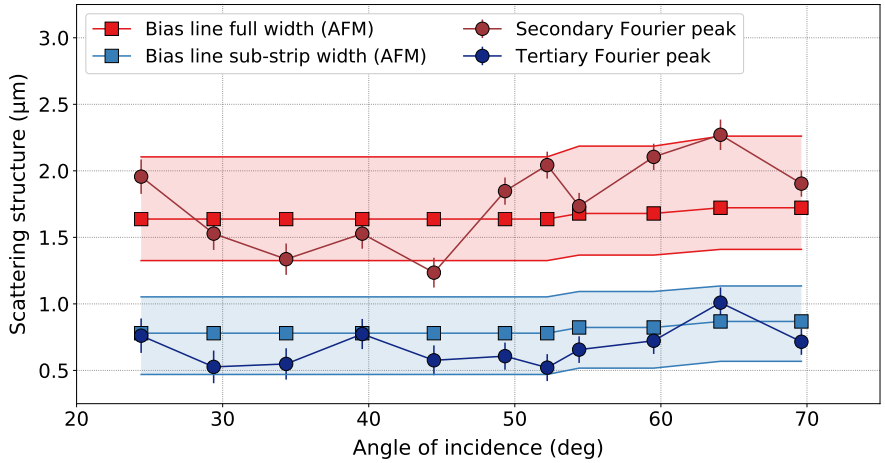

Figure 3.64.: Lateral size of the scattering structure on the FBK surface reconstructed from secondary (red) and tertiary (blue) peaks in the Fourier transformed angular reflection spectra (dots). The data is compared to the geometric size of the bias lines (red) and bias sub-strips (blue) as extracted from the AFM height profiles in figure 3.63 (squares). The bands correspond to the geometric uncertainties in the AFM profiles.

grooves for 4.8 %. The relative microcell surface is significantly larger than the value obtained above for the optical microscopy picture which is close to the fill factor at about 80 % [147]. The difference likely arises from surface depositions in the edges between the microcell surface and the bias/resistor lines. Such depositions are transparent for AFMs but visible as smoothed out edges in microscopy images as in figure 3.61 and are well known in atomic force microscopy.

In summary, the FBK VUV-HD SiPM presents a similar reflectivity over AOI as the wafer sample but reduced by a constant factor. This factor can be well understood from a geometric standpoint since the only difference between the VUV-HD and the wafer sample is the micro-structure added to the wafer surface during the SiPM manufacturing process. At the time of the submission of this thesis, the presented curves are the first and only reflectivity studies of an FBK VUV-HD in liquid xenon for VUV wavelengths.
A further feature of the VUV-HD are periodic oscillations in the reflectivity curves. The oscillations can be interpreted as scattering patterns invoked by the micro-structure components. The geometric dimensions of the scattering structure was determined via Fourier analysis and compare very well to results obtained with optical and atomic force microscopy. This proves that the angular spectra are well understood and validates the approach to investigate the reflectivity of SiPMs with the setup used in this work.

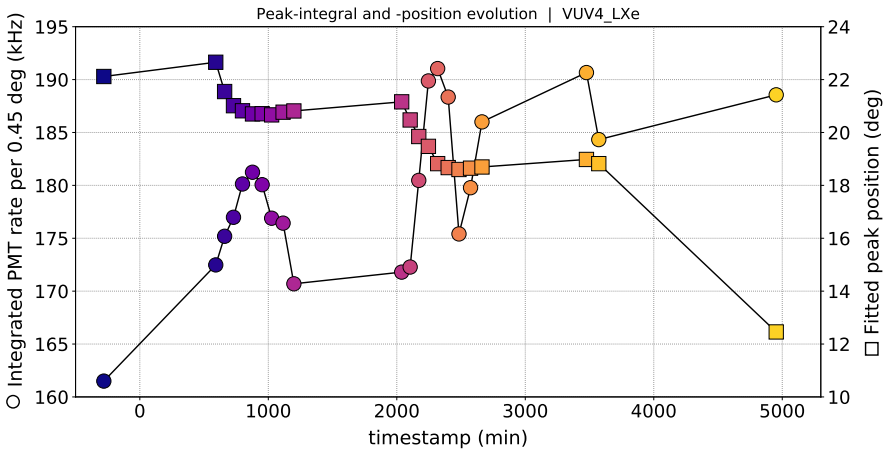

Figure 3.65.: Reference peak integral (circles) and position (squares) of the VUV4 campaigns in liquid xenon. The full angle runs have been acquired first, the specular angle runs between timestamps 3575 and 4080 min.

3.5.4. Hamamatsu VUV4

The Hamamatsu VUV4 SiPMs presents an entirely different micro-structure design compared to the FBK VUV-HD. Additionally, the AOI-dependence of the reflectivity curve is completely different. Diffuse reflection components are again absent as well as periodic oscillations in the reflectivity over AOI curve. In contrast, secondary peaks appear on both sides to the specular peak due to a symmetrically inclined shape of the surface micro-structure strips.
The VUV4 is the current flagship VUV SiPM from Hamamatsu. Various publications report on the properties of this SiPM model [141] including the reflectivity in vacuum [202] and liquid xenon [225]. Three LXe campaigns have been performed: the first with 29 specular angle spectra, the second with 21 full angular spectra and an additional full angle campaign discussed later. The reference peaks have been thoroughly monitored throughout both campaigns. This was of high importance in the case of the full angle campaign since it lasted for 3.5 days.
All VUV4 spectra have been obtained with a slit collimator instead of an aperture in front of the PMT housing. The slit was 1.5 mm wide and 24 mm in height and integrated over the entire axial dimension of the beam profile. The spatial width r in equation 3.9 was adapted accordingly.

Acquisition of angular spectra

Figure 3.65 shows the evolution of the reference integrals and positions during both campaigns. The specular angle campaign has been performed between timestamps 3575 and 4080 min. There are distinct jumps with at least two peaks of the reference

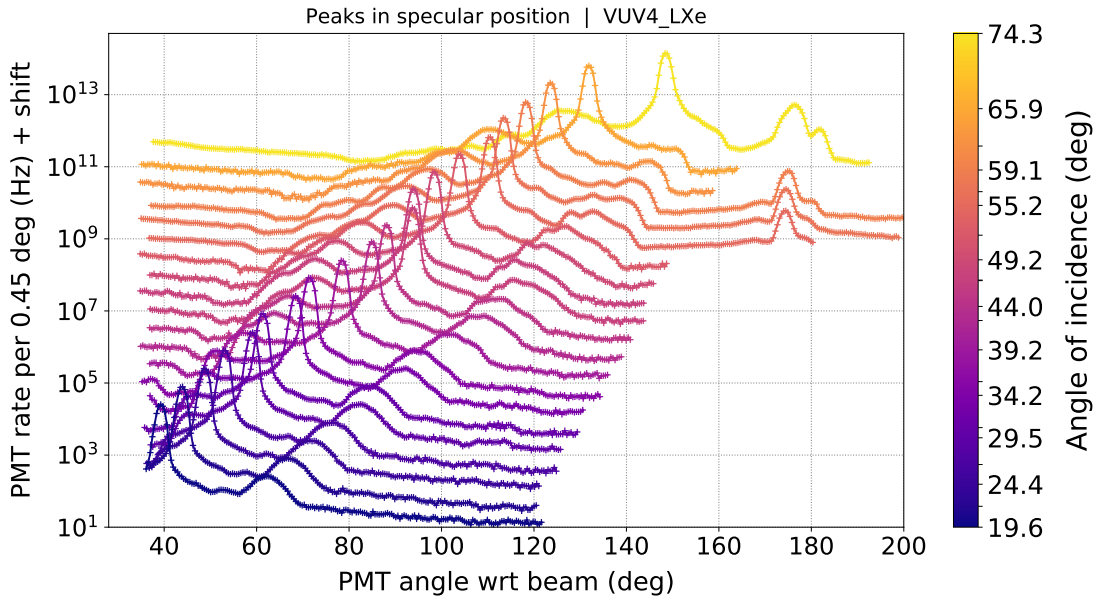

Figure 3.66.: Angular reflection spectra of the full angle VUV4 campaign. The distinct specular peaks are accompanied by distinct secondary structures on both sides of the dominant specular peaks. These secondary peaks are caused by the complex micro-structure on top of the VUV4 surface.

integral with a coincident drop of the reference position. Despite extensive efforts, the observation could not be traced back to a certain origin. A possible explanation is a correlating with the lab temperature which peaked each afternoon around 2 p.m. (timestamps 840, 2280 and 3720 min). A causal coupling between the deuterium lamp or the step motor to the temperature is yet to be resolved in detail. The variations in the reference data was again met via a linear interpolation and then analysed at the reflection spectrum timestamps. The fluctuations in both reference integral and position pose no problem due to this procedure. The reference angle for the last reflection spectrum was set to the last peak position recorded to account for the long gap to the last reference run.

The reflection spectra of the full angle campaign are plotted in figure 3.66. Specular peaks are again dominant but the secondary peaks on both their sides are much more pronounced compared to the FBK spectra since the VUV4 micro-structure is more complex as shown in figure 2.26. A larger fraction of the VUV4 surface presents slopes apart from the microcell surface and a larger number of photons are reflected under different angles. The peaks around 180° are artefacts caused by the part of the beam missing the sample holder and hitting the PMT in reference position. The beam can pass the sample holder on both sides resulting in a double peak with a gap at exactly 180°. This can be clearly seen in the highest AOI

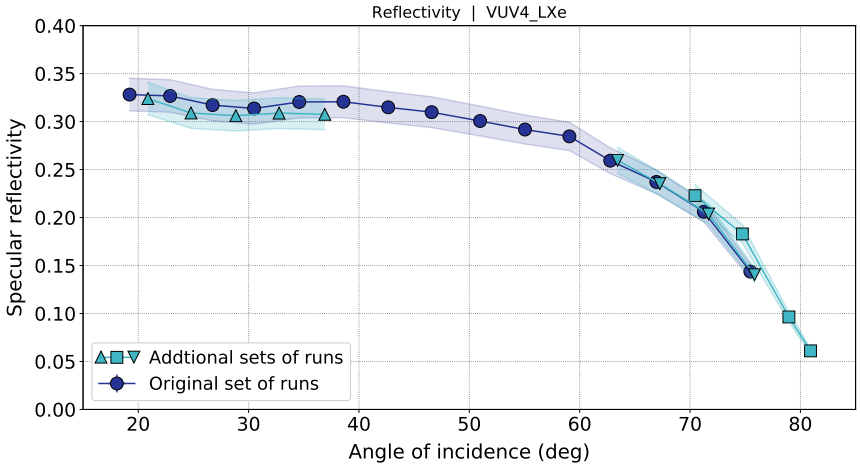

Figure 3.67.: Reflectivity over AOI of the VUV4 sample. Several sets of runs from the **specular** angle campaign are compared and agree within their uncertainties.

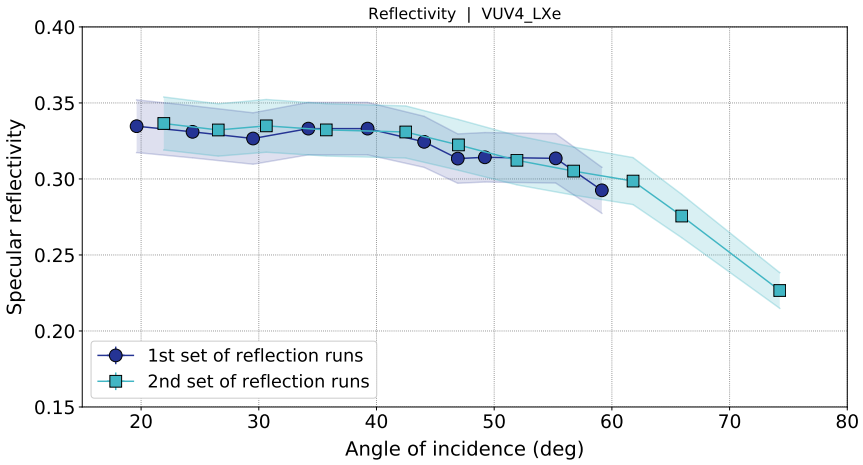

Figure 3.68.: Reflectivity over AOI of the VUV4 sample but with two sets of runs from the **full** angle campaign. Both sets again agree within their uncertainties.

spectra and provides proof of the proper alignment of the setup. The thickness of the sample holder is 1 cm so a larger part of the beam is blocked by the back side of the holder compared to the side holding the detector. Therefore, the right peak is significantly smaller. The holder is shown in figure 3.19.

VUV4 reflectivity

Several sets of runs have been acquired during each campaign to monitor the long-term stability of the reflectivity. Figure 3.67 shows the four run sets of the

specular angle campaign and figure 3.68 the two sets of the full angle campaign. Despite some differences among the run sets of the specular angle campaign they all agree within their systematic errors. A comparison of both campaigns is shown in figure 3.69. The VUV4 campaigns mostly agree within their systematic errors but the specular angle runs yield slightly lower reflectivity values. One reason might be the fluctuations of the reference integral within the acquisition time interval of the specular runs, which are about the same magnitude as the difference between both campaigns. Another reason is a shift of about 3° in the reference angle. The shift occurred during the specular angle campaign as shown in figure 3.65 and was caused by a twist in the stepping motor chain. The twist was untied after being discovered but might have slightly affected the z-position resulting in reduced specular peak integrals.
A striking feature of the VUV4 reflectivity is its decline over the entire AOI range. This differs from all other samples investigated in this thesis. There is no published information about the exact surface composition applied by Hamamatsu but it is possible that the VUV4 models are equipped with some VUV-absorbing protection layer. In this case, any incident light is attenuated by a factor $\exp(-\alpha{\cdot}L)$ before getting reflected where $\alpha = 4\pi k/\lambda$ is the absorption coefficient and k the extinction coefficient. The optical path L of photons crossing the surface film with thickness d is equal to $d{\cdot}\cos(\mathrm{AOI})$. This yields:

$$R_{\mathrm{obs}} = R_{\mathrm{act}} \cdot \exp\left(-\alpha d/\cos(\mathrm{AOI})\right) \tag{3.21}$$

where R_{obs} and R_{act} are the observed and actual reflectivity. Assuming that R_{act} is constant, a simple fit to the data in figure 3.67 yields a reflectivity of 43.1 % and an $\alpha{\cdot}d$ of 0.12. Energy dispersive X-ray spectroscopy (EDS) performed by a nEXO collaboration partner revealed small amounts of carbon on the microcell surface with about 6 % of the total pixel surface [priv. comm. with P. Nakarmi]. Carbon is unexpected in a doped semiconductor but might point to a very thin surface coating with silicon carbide (SiC). The fitted $\alpha{\cdot}d$ and $k_{\mathrm{SiC}} = 2.19$ yields an effective film thickness of 0.78 nm so only very few atomic layers. Such thin coatings are technologically achievable so these findings may indicate the application of SiC films or the admixture of SiC to the Si-substrate by Hamamatsu [192].
Both VUV4 campaigns agree within their uncertainties according to figure 3.69. The data from Nakarmi et al. present a very similar behaviour – however with reduced values for the reflectivity [225]. This data set has been acquired with the same SiPM model in liquid xenon at a different setup. Validation runs based on the reflectivity simulation of the wafer sample in LXe [202] and optical simulations have been performed to validate the approach. The uncertainties on the reflectivty lie between 0.9 and 1.2 $\%_{\mathrm{abs}}$. The disagreement of both data sets may be expalined with device-to-device differences regarding their individual surface reflectivities.

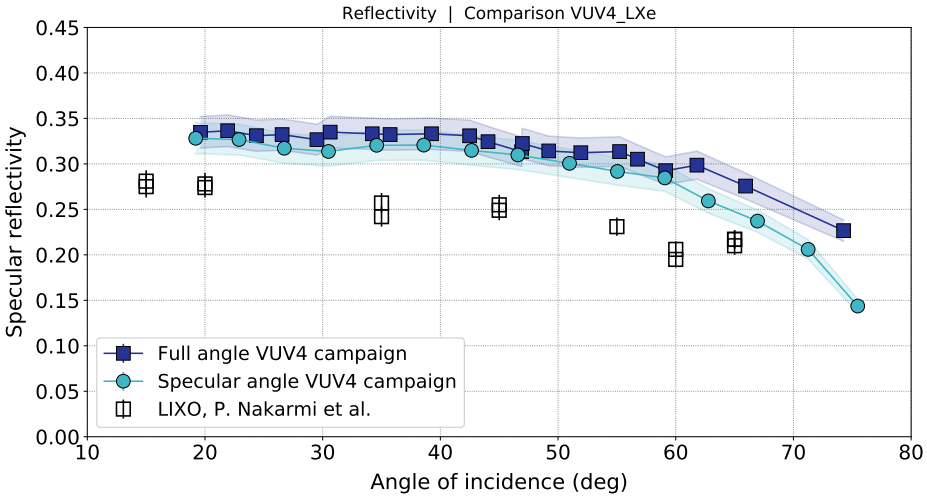

Figure 3.69.: Reflectivity over AOI of the VUV4 sample in LXe calculated from both VUV4 campaigns compared to measurements reported in [225]

Indeed, further unpublished studies with other VUV4 samples in the setup in [225] yield reflectivity values that comply much better with the data presented here [priv. comm. with P. Nakarmi]. This issue is yet to be investigated in more detail. In average, the measurements from [225] are 21.7 % lower than the reflectivity values found in this work.

Effects of the surface micro-structure

One further distinct feature of the VUV4 reflection spectra is the pronounced secondary peaks on both sides of the specular peak. As for the FBK, such off-peak features are caused by the surface micro-structure. The secondary peaks are significantly more prominent for the VUV4 compared to the FBK due to the stronger micro-structure strips as shown in the microscope photographs in figure 2.26. The influence of the secondary features and how to address them in a global model are discussed in the following.

Figure 3.70 shows two reflection spectra obtained with a VUV4 in liquid xenon in a different full angle campaign than above. The y-axes are limited to focus on the off-peak features. The upper plot shows a regular angular reflection spectra at an AOI of 42.23°. The lower polar plot was acquired at an AOI of 34.51° and includes a simple CAD inlet of the LXe-filled quartz tube (bluish), the sample and sample holder (brown, grey) as well as the bottom flange of the inner chamber (outer grey circle). The flange incorporates three evenly spaces holes for the tightening rods explained in section 3.2.1. Both plots show the following features:

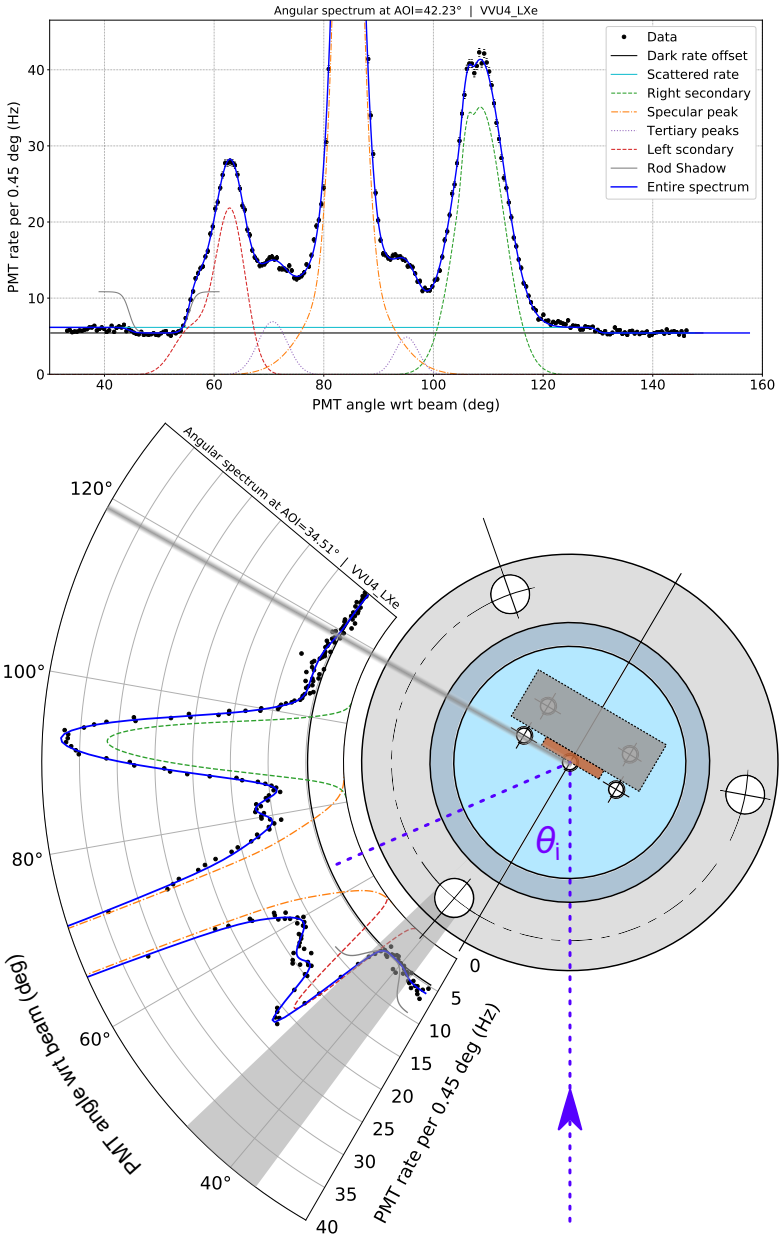

Figure 3.70.: Full angular reflection spectra of a VUV4 SiPM at an AOI of 42.23° (top) and 34.51° (bottom). The spectra present various features apart of the specular peak which are accounted for individually for a global fit model. Details are found in the text. The polar plot shows the relation of the shadowing features at roughly 120° and 40° to the geometry of the inner chamber.

- The specular peak at twice the angle of incidence is fitted as above but with a superposition of three function following equation 3.9 with identical maximum position. This presented the best fitting results and is motivated by three different domains with a slope of 0 identified on the VUV surface. The fit is shown as orange dot-dashed line.
- The spectra present a constant dark rate offset plotted with a black line. An additional offset due to Rayleigh scattered light is plotted in cyan. The additional rate due to these photons is smaller compared to the wafer spectrum in figure 3.47 due to the poor xenon purity in the second VUV4 full angle campaign.
- The recorded photon rate drops to the dark rate above 130° (top plot) and 117° (polar plot) where the PMT is located behind the sample holder and the scattered photons are shadowed. This is depicted by the grey bolt in the polar plot. The drop is mathematically expressed via an inverse error-function:

$$A_{\text{add}}/2 \cdot (1 - \text{erf}\left(\left(x - M_{\text{drop}}\right)/c_{\text{drop}}\right))$$

  where A_{add} is the additional amplitude, M_{drop} is the position where the drop occurs and c_{drop} scales the smoothness of the shadowing transition.
- The rate also drops to the dark rate when the PMT is located behind the tightening rod roughly perpendicular to the sample surface. The rod blocks any scattered or reflected photons from reaching the PMT and causes a roughly 11° dip in the angular spectra. The dip is located at 50° in the top plot and 42° in the polar plot where the rod shadow is indicated as grey circle segment. It is modelled with a double Fermi-function in the global fit:

$$\left(\exp\left(\frac{-x + M_{\text{dip}} + w/2}{c_{\text{dip}}}\right) + 1\right)^{-1} + \left(\exp\left(\frac{x - M_{\text{dip}} + w/2}{c_{\text{dip}}}\right) + 1\right)^{-1}$$

  where M_{dip} is the position of the shadow centre, w the dip width and c_{dip} again scales the transition. w is fixed through geometric considerations.
- There is one secondary peak approximately 23° to the right of the specular peak (green, dashed line). This peak increasingly splits into two close but separate peaks with increasing AOI. It is fitted with a superposition of two equations 3.9 with different amplitude, maximum position and width. This has been done for all angles of incidence even if the split is not visible as in the polar plot. The peak integral of the right secondary is decreased at large AOI when the position of the drop M_{drop} moves inside the secondary peak and the shadow of the sample holder starts to block the peak photons.

- A further secondary peak is visible about 21° to the left of the specular peak (red, dashed line). This peak shows less significant hints of two sup-peaks but is nevertheless accounted for with two functions again. The left secondary peak is cut by the holder shadow for small and medium angles of incidence as in the polar plot in figure 3.70.
- Additional tertiary peaks appear very close and to both sides of the specular peak. The contribution of these peak vary strongly with AOI from nearly zero to peak integrals similar to the ons of the secondary peaks. They are modelled with one function according to equation 3.9 each and plotted as dotted, purple curve.

The global fit model constitutes a superposition of all normalised Gaussian integrals listed above as well as the error function describing the holder shadow transition. The combined sum of all these components is then multiplied with the double Fermi-function to model the dip independently of its location relative to the peaks. The dark rate is included as global offset. The uncertainties on the rate values are Poissonian and plotted only in the top plot. χ^2 values are decent ranging from 4.24 to 35.03 with an average of 11.81.
The positions of the sample holder shadow and of the rod shadow centre depend on the geometry of the inner chamber as depicted in the polar plot in figure 3.70. If the angle of incidence is changed, both features move by the same angle in the reflection spectra. In contrast, the specular and all secondary peaks move by twice the AOI change. This shows, that the secondary (and tertiary) peaks are reflection phenomena in their own rights and do not originate from the inner chamber. It also means, that the relative position of the secondary peaks to the shadowing artefacts depend on the AOI. This is the reason why the right secondary peak is suppressed by the holder shadow at large AOI while the left secondary is diminished by the rod shadow at small and medium AOI e.g. in the polar plot above.
The secondary peaks are positioned almost symmetrically around the specular peak. Their origin lies in a symmetry of the VUV4 surface micro-structure causing these additional peaks. The symmetric secondary peaks are apparent in all reflection spectra in figure 3.66. To investigate the symmetry, both angular distances to the specular peak are subtracted and plotted in figure 3.71. The subtracted distance is close to zero for all AOIs where both secondary peaks appear. The plot also features the position of the shadow from the sample holder relative to its expected position at θ_i+90° according to figure 3.48. At large AOIS, data is not available since the drop cuts into the right secondary. The third curve in figure 3.71 shows the angular position of the rod shadow relative to its expected centre angle at $\theta_\mathrm{i} + 10°$. Both curves are below zero which means that the shadowing angles are slightly smaller than where they are supposed to occur. This is likely due to a slight misalignment of the photon beam. The shadowing angles are very sensitive

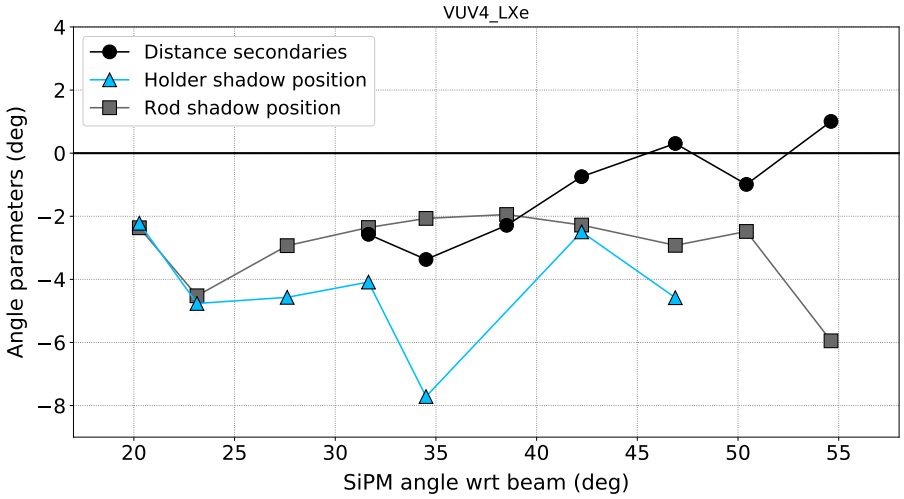

Figure 3.71.: Angle investigations based on the global fit parameters. Black dots present the difference of the distances of both secondary peaks to the specular peak which is zero in case of a perfect symmetry. The angular distance of the shadowing transition from the sample holder to the values expected from geometric considerations is plotted with blue triangles. Grey squares show the angular distance of the rod shadow centre to the expected location. Symmetry data is not available for small AOIs due to shadowing of the left secondary peak by the rod. Similarly, the holder shadow position cannot be yielded for large AOIs since it merges with the right edge of the right secondary peak.

to scenarios where the VUV photons do not hit exactly the centre of the reflection sample while angles associated with reflection features are less so.

The additional secondary peaks are very prominent for the VUV4 and result in an increase in the total reflectivity R compared to the specular reflectivity r. The difference of these two is explained in section 3.2.2. The increase in reflectivity scales with the integral of all peaks since the secondary peaks can be interpreted as additional specular peaks where incident photons merely experience a different surface slope from components of the SiPM micro-structure. The secondary and tertiary peak integrals relative to the primary specular peak integral are plotted in the histogram in figure 3.72 for all AOIs within the corresponding VUV4 campaign. The left secondary peak plotted in red cannot be modelled for small AOIs due to the rod shadow. Its integral can be assumed to be similar to the ones at larger AOIs. The right secondary peak in green is increasingly reduced by the sample holder shadow above an AOI of 54°. In general, the global fit accuracy decreases towards larger AOIs. This mainly manifests in extended tertiary components. All in all, figure 3.72 shows that the total reflectivity is up to 12.8 % larger than the specular reflectivity plotted in figure 3.68.

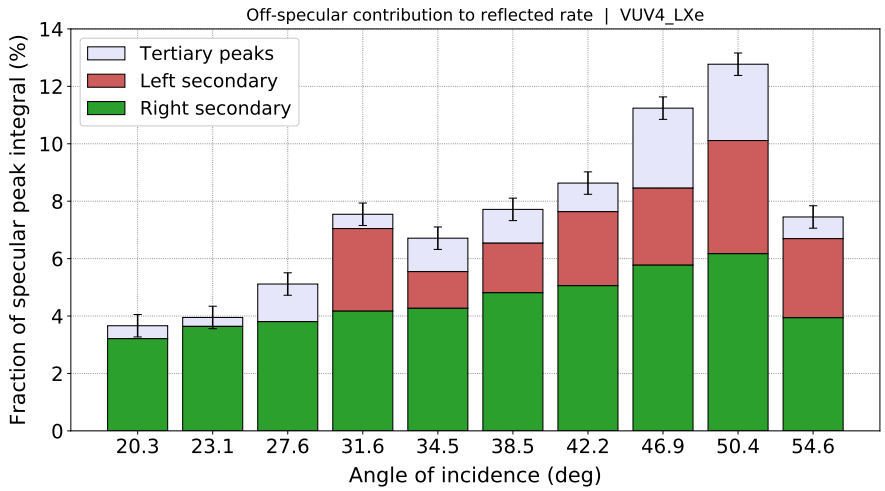

Figure 3.72.: Histogram of additional peak integrals in the angular spectra of the second full angle VUV4 campaign. The right (left) secondary peak integral is shown in green (red), the tertiary peak integrals in light purple. Error bars show the combined uncertainties of all integrals derived from the global fit model. The integrals are displayed as fraction relative to the specular peak integral.

The spectral components apart from the specular peak are again caused by the surface micro-structure as in the case of the FBK. Figure 3.73 shows a 45 µm squared AFM image of the VUV4. The micro-structure strips are significantly larger in height and width compared to the FBK (compare to figure 3.62). Figure 3.74 shows a profile of the micro-structure strip on the top. The aspect ratio is 1. The bottom plot presents a surface slope distribution of this strip where zero refers to the slope of the microcell surface. Two distinct peaks are located symmetrically around zero at roughly 10° and −10°. This indicates a dominant slope of the micro-structure lines and results in additional, symmetric secondary peaks at twice this angular distance from the specular peak. This is consistent with the findings in the angular spectra e.g. in figure 3.70. The smaller angular distance of the right peak in the slope distribution can explain why the left secondary peak is slightly closer to the specular peak than the right secondary peak.

To conclude, the reflectivity of the VUV4 was observed to unexpectedly decrease with the angle of incidence – unlike all other samples investigated in this work. This behaviour was validated by another publication in the meantime but the reason for this is yet to be determined. Distinct secondary peaks in the angular spectra can be explained with symmetric features of the surface micro-structure. This results in a significant angular rate beyond the specular angle and increases the total reflectivity by roughly 10 %.

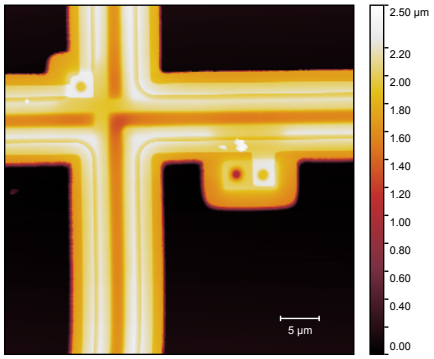

Figure 3.73.: AFM height image of a micro-structure intersection of a VUV4 SiPM. The micro-structure forms a striking quadratic pattern. The connector to the microcell can be seen right of the centre.

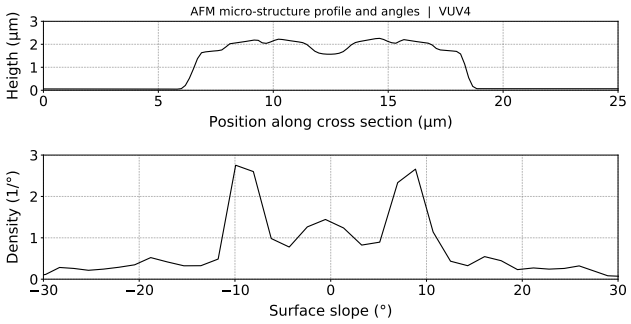

Figure 3.74.: AFM height profile of the VUV4 micro-structure. The bias lines are larger in height and width compared to the FBK. The bottom plot shows a distribution of surface slopes within the micro-structure strip.

3.5.5. APD

The last sample investigated in this work is a Large Area Avalanche Photon Detector (LA-APD) from the EXO-200 experiment [226]. EXO-200 employed 468 of these detectors in its two TPCs to read out the scintillation channel [58]. APDs are semiconductor avalanche sensors but unlike SiPMs without pixelisation and operated below the breakdown voltage. This allows to count more than one photon per APD but implies a much lower gain and higher noise rates. Details are outlined in section 2.4.1. APDs have been chosen over PMTs due to their substantially lower content of radioactive contaminations. The LA-APDs are conical with an outer diameter of about 20 mm and a diameter of the photosensitive area of 16 mm (see figure 3.31).

Figure 3.75 shows the reference measurements of the APD campaign. The reference angle is stable and the reference peak integral fluctuates are again accounted for via a spline interpolation. As explained in section 3.4.2, the reference runs in the APD campaign are affected by large bubbles floating on the LXe surface. This causes drops in the measured rate in reference position due to light blockage and prevents clean reference spectra. Instead, each angle step was scanned several times and only the measurement with the largest count rate was processed in the angular reference spectra. The fluctuation of the reference integrals might be an artefact of possible shortcomings of this procedure.

The APD campaign consists of 11 full angle reflections spectra plotted in figure 3.76. Only specular peaks can be seen with no signs of diffuse reflection and no secondary

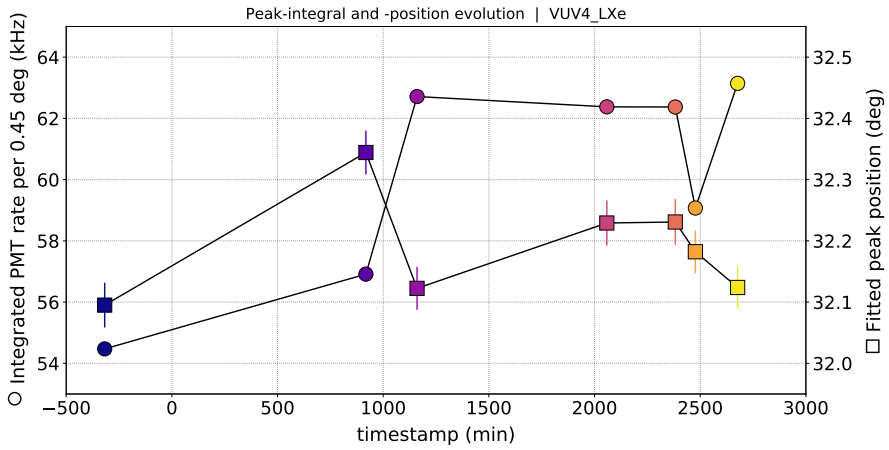

Figure 3.75.: Reference peak integral (circles) and reference position (squares) in liquid xenon from the APD campaign.

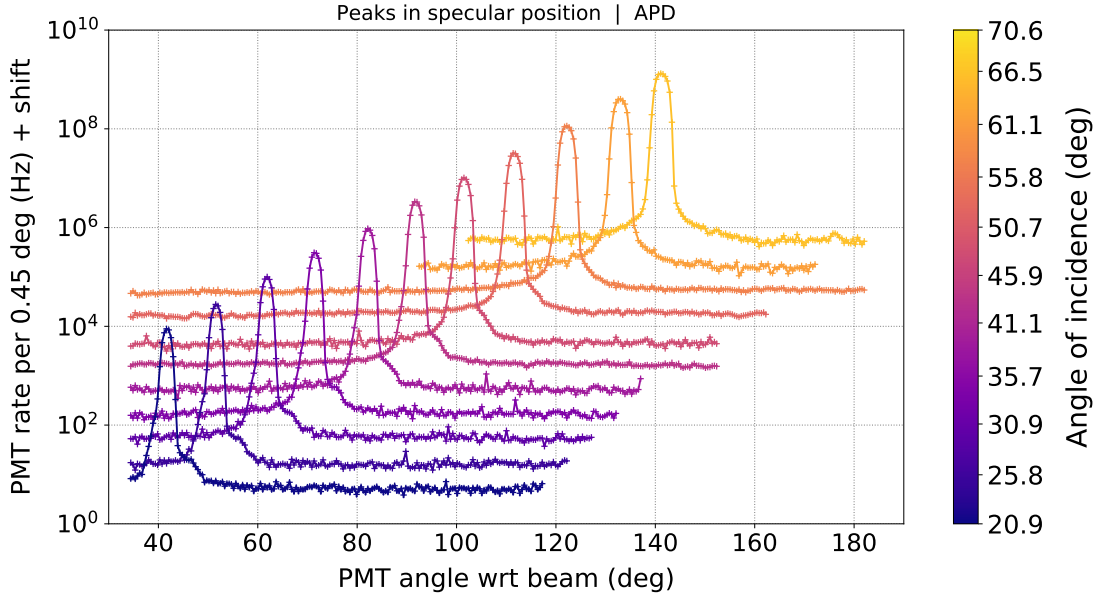

Figure 3.76.: Angular reflection spectra of the APD campaign. There are no secondary peaks since the APD has no surface micro-structure.

peaks – similar to the wafer campaigns. This is due to the missing micro-structure since the APD has a plain photosensitive area. The small spikes in the flat parts of the spectra are random fluctuations. They only appear for an acquisition time up to 18 s per each angle step and vanish entirely for larger time steps. The reflection runs at 45.9, 55.8 and 61.1° have been acquired over night with an acquisition time around 160 s per angle step and present no spikes in the flat spectral parts.

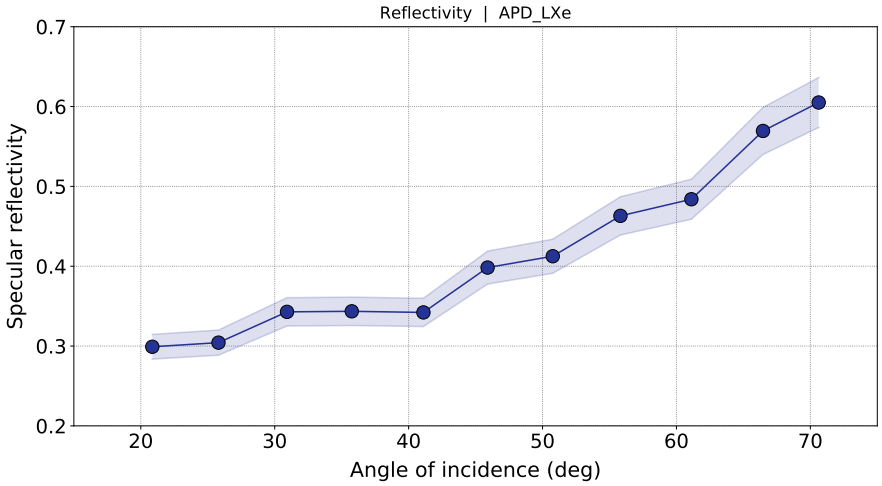

Figure 3.77.: Reflectivity over AOI for the APD sample in liquid xenon.

The reflectivity of the APD sample in LXe is shown in figure 3.77. The values increase within the entire AOI range. No sign of beam decontainment can be seen due to the large size of the sample.
Comparisons with literautre cannot be provided due to the difficultiy to find similar measurements. No information exists on the exact composition of the APD surface and the material and thickness of possible surface films as in the case of the wafer sample. On the other hand, the optical properties of doped silicon surfaces are known to depend strongly on the similarly unknown preparation conditions of the material [163]. Despite this, the APD reflectivity measurements will be used by the nEXO-collaboration to understand and learn from the EXO-200 light map which can be reconstructed in more detail based on these values.

3.5.6. Overview

The plot in figure 3.78 shows a comparison of the reflectivity in liquid xenon for all samples investigated within this thesis.
The most interesting curves for nEXO are the one for the FBK VUV-HD LF and the Hamamatsu VUV4. Both SiPM models are currently in the closer selection as baseline SiPM for the nEXO photo-detector system. As discussed in section 2.2.4, one prime goal of nEXO is to precisely simulate the photon collection efficiency to verify that the claimed energy resolution goal can be achieved. This requires a good knowledge of the optical behaviour of SiPMs in LXe as well as an optimal photon detection efficiency (PDE), i.e. the probability for photons to be absorbed and detected. The PDE is known to decline with AOI [225] but this can be partly compensated with an increasing reflectivity at larger AOI. Photons that are not

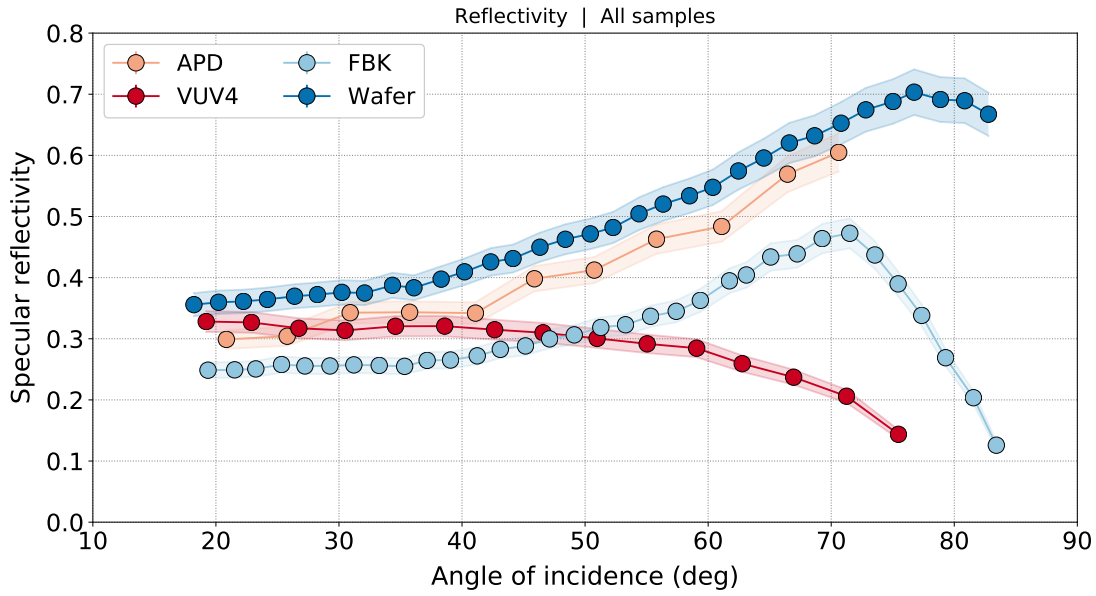

Figure 3.78.: Overview of the reflectivity in liquid xenon versus AOI of all samples investigated in this work.

absorbed in the sensor are reflected and get a second chance to be detected by a different SiPM. All photons that are neither detected nor reflected are still absorbed but fail to trigger an avalanche. This last quantity needs to be as small as possible. As a consequence, a mere focus on the reflectivity is insufficient to compare both SiPM models in terms of nEXO's physics goal. The position-dependent photon collection efficiency (the so-called light map) of the entire detector needs to be simulated including the probabilities of all reflection and absorption processes. The PDE of the FBK VUV-HD has been determined to saturate at nearly twice the value measured for the VUV4 [141]. This means, that less photons are available for reflection processes in case of the FBK SiPM and might explain the smaller reflectivity below 48°. At larger angles, up to 73 % of incident photons are either detected or reflected but large AOIs are rather unlikely in nEXO for geometric reasons. The different reflection behaviour of both SiPM models might therefore have little effect on the overall photon collection efficiency in nEXO. Detailed studies of all efficiencies and the relationship with the sensitivity goals of nEXO will be published soon in a dedicated sensitivity paper that makes use of the findings reported in this chapter.

4. SiPM Diode Characteristics

Table of contents:

Nearly all characteristic parameters of silicon photomultipliers (SiPMs) depend on temperature as explained in section 2.4. This requires additional efforts during SiPM studies since some observed effects may temperature-driven rather than true light signals or noise. Knowing the precise temperature of the SiPM is as important as difficult to measure since it is impossible to attach a temperature sensor right onto the pixel matrix. However, if certain temperature characteristics are measured precisely and carefully calibrated, the SiPM temperature can be derived directly without the need of temperature sensors.
This chapter presents the method to investigate calibrated current-voltage diode curves (IV-characteristics) to establish a probe of the pn-junction temperature of SiPMs with good precision as proposed by G. Collazuol [103]. Diode curves can also be used to determine characteristics as the breakdown voltage or the dynamic range. IV SiPM characteristics are an important tool to test large amounts of SiPMs due to the simple test setup, easy analysis and low time requirements [242]. This will be important for the final stage of the construction of nEXO, when $4.5\,\mathrm{m}^2$ of SiPMs need to be tested before the SiPM tile assembly.
Phenomenological explanations of diode IV-characteristics are given in sections 4.1 and a mathematical model is established. The model is fitted to IV-curves in

forward direction in section 4.3 to deduce key characteristic quantities of the SiPMs and establish a direct temperature calibration. Section 4.2 provides an overview of the test setup. Section 4.4 presents results with IV-curves in reverse direction.

4.1. IV-Characteristics

4.1.1. Diode IV characteristics

SiPMs present complex doping profiles as explained in section 2.4.3 with at least two pn-junction [208]. As any diode, electron current is only allowed in one direction: from the cathode (p-layer) to the anode (n-layer). When connected to an external bias voltage opposing the internal polarity, a diode is operated in forward direction and allows to conduct electricity. If the external polarity is set to enhance the internal polarity, the diode is operated in reverse regime where no macroscopic current is possible and only leakage currents occur. The current in forward direction kicks off as soon as the intrinsic pn-potential barrier is compensated by the external electric field (see section 2.4.1).
Figure 4.1 shows a schematic IV-characteristic curve. The diode is driven in reverse regime for negative voltages where the depletion layer is enlarged and only a small leakage current flows (strongly exaggerated in the figure). Below the breakdown voltage V_{bd}, the SPADs are able to discharge completely after an external trigger (see section 2.4.2). In forward direction, the current increases exponentially following the Shockley equation (see section 4.1.2) above the so-called turn-on-voltage V_{t} which is roughly 0.7 V for silicon. For light-emitting diodes (LEDs), this regime is used intentionally to stimulate photon emission. Silicon is an indirect semiconductor so SiPMs don't emit light in forward direction.
SiPMs are used as light sensors in the Geiger mode below V_{bd} while the forward region can be used to investigate several external parameters of SiPMs as the quenching resistance. The forward IV-curves can also be used to derive the true temperature of the SiPM pn-junction.

4.1.2. Mathematical model of IV-forward-characteristics

The forward regime of a diode can be described with the Shockley equation:

$$I_{\mathrm{D}}(V_{\mathrm{D}}, T) = I_{\mathrm{S}}(T) \cdot \left(\exp\left(\frac{V_{\mathrm{D}}}{n\, V_{\mathrm{T}}} \right) - 1 \right) \tag{4.1}$$

where the diode current I_{D} is calculated as the saturation current (or drift current) I_{S} multiplied by an exponential term that contains the external diode voltage V_{D}, the ideality factor n and the thermal potential V_{T} [281]. The ideality factor (or emission

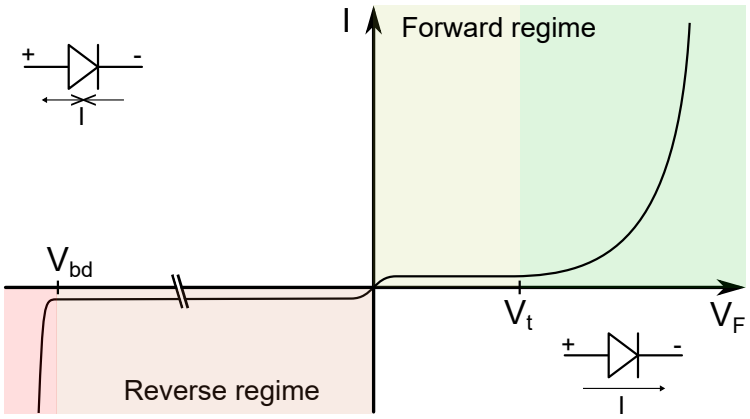

Figure 4.1.: Scheme of a diode IV-curve. There is only a small leakage current in the reverse regime (exaggerated here) before the SPADs break down in the Geiger-mode below V_{bd}. In the forward direction, the current increases exponentially with the forward bias which becomes particularly significant above the turn-on-voltage V_{t}.

coefficient) describes the quality of the junction and is typically between 1 (ideal diode) and 2 but can be higher for non-standard diode junctions. It depends on the semiconductor material, manufacturing process and diode geometry. The thermal potential is $V_{\mathrm{T}} = k_{\mathrm{B}}T/e$ where k_{B} and e are the Boltzman constant and the electron charge, respectively, and equals approximately 26 V at room temperature [299]. The saturation current shows an exponential temperature-dependence following:

$$I_{\mathrm{S}}(T) = I_{\mathrm{S}}(T_0) \cdot \exp\left(\left(\frac{T}{T_0} - 1\right)\frac{V_{\mathrm{G}}(T)}{n\,V_{\mathrm{T}}}\right) \cdot \left(\frac{T}{T_0}\right)^{\chi_T/n} \tag{4.2}$$

where V_{G} is the band gap voltage of the semiconductor (1.124 eV at 300 K for silicon [77]) and T_0 is a reference point for the saturation current characterisation typically set to 300 K [299]. The dimensionless temperature coefficient of the saturation current χ_T is approximately 3 for ideal diodes but may differ significantly. The Shockley equation describes the electric behaviour of a regular diode in forward direction. SiPMs are more complicated since they comprise four doping layers with large discrepancies in layer thickness and doping concentration. Additionally, each SPAD has a passive quenching resistor connected in series. Figure 4.2 shows a simplified circuit for one SPAD. Mathematically, it can be describes as:

$$\begin{aligned} V_{\mathrm{B}} &= V_{\mathrm{D}} + V_{\mathrm{R}} = \\ &= n\,V_{\mathrm{T}} \cdot \ln\left(I_{\mathrm{D}}/I_{\mathrm{S}} + 1\right) + R\,I_{\mathrm{R}} \end{aligned}$$

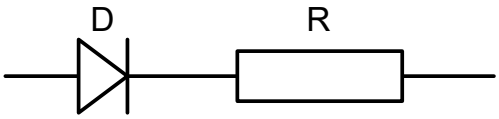

Figure 4.2.: Simplified circuit of a SPAD consisting of the avalanche diode D and the passive quenching resistor R connected in series.

where R is the quenching resistance and $I_\mathrm{D} = I_\mathrm{R} = I$ is the diode circuit. There is no trivial way to get an analytical solution for I but Lambert W-functions $\mathscr{W}_k(z)$ can be used to provide an exact solution [105] for the main branch $k = 0$:

$$I_\mathrm{SPAD}(T) = \frac{n\,V_\mathrm{T}}{R} \cdot \mathscr{W}\left(\frac{I_\mathrm{S}\,R}{n\,V_\mathrm{T}} \cdot \exp\left(\frac{I_\mathrm{S}\,R + V_\mathrm{B}}{n\,U_\mathrm{T}}\right)\right) - I_\mathrm{S} \tag{4.3}$$

The overall current, that can be measured at the SiPM pins, then is the sum over all SPADs assuming that all quenching resistors and diodes behave similarly:

$$I_\mathrm{SiPM}(T) = N_\mathrm{px} \cdot I_\mathrm{SPAD}(T) + I_\mathrm{off} \tag{4.4}$$

where N_px is the number of SPADs within the SiPM array and I_off is a global offset current generated by broken pixels or leakage currents within the sensor.

4.1.3. Mathematical model of IV-breakdown-characteristics

The mathematical description of the diode behaviour in the breakdown regime can be divided into a pre-breakdown and a post-breakdown regime. In the pre-breakdown regime, the saturation current shows a slow exponential increase due to potential dependencies of both surface and bulk dark currents [117]. Shockley-Read-Hall recombination only plays a minor role immediately below the breakdown voltage and is neglected. The pre-breakdown regime is modelled with:

$$I_\mathrm{pre\text{-}BD}(V) = A \cdot \exp\left(\frac{V}{c}\right) + I_0 \tag{4.5}$$

where A and c scale the exponential function and I_0 accounts for the saturation current in reverse direction. The current in the post-breakdown regime is equal to the space-charge in the SiPM doping layers $C \cdot \Delta V$ multiplied with the dark rate R. The triggering probability p_trig carries the overvoltage dependence of the probability to trigger avalanches. A correction factor CA is introduced to account for the contribution by correlated avalanches:

$$I_\mathrm{post\text{-}BD}(V) = C{\cdot}R{\cdot}\Delta V \;\cdot\; p_\mathrm{trig}(\Delta V) \;\cdot\; CA(\Delta V)$$

There are several attempts to parametrise the triggering probability reported in literature but one of the best working models for modern SiPMs is reported in [140]:

$$p_{\text{trig}}(\Delta V) = 1 - \left(\frac{1}{k_{\text{e1}} \cdot \Delta V \cdot \exp\left(-k_{\text{e2}}/\sqrt{\Delta V}\right)} \right)^2$$

where k_{e1} and k_{e2} are voltage-independent parameters. Correlated avalanches summarise crosstalk and afterpulsing events which both may contribute to an initial event and increase the reverse current. The contribution from crosstalk can be expressed with a certain voltage-dependent crosstalk contribution CT. The contribution from afterpulsing requires to take higher order events with a fixed single afterpulsing event contribution AP into account [243]:

$$p_{\text{AP}}(\Delta V) = AP + AP^2 + AP^3 + \ \cdots \ = \frac{AP}{1 - AP}$$

where AP needs to be multiplied with a certain factor f_Q to describe the average fraction of charge per afterpulsing event. This gives the final formula for the post-breakdown region:

$$I_{\text{post-BD}}(V) = C{\cdot}R{\cdot}\Delta V \ \cdot \ p_{\text{trig}}(\Delta V) \cdot \left(1 + \frac{f_Q{\cdot}AP(\Delta V)}{1 - f_Q{\cdot}AP(\Delta V)} + CT(\Delta V)\right) \quad (4.6)$$

The contributions through correlated avalanches need to be parametrised for a post-breakdown fit procedure. The crosstalk contribution depends quadratically on the overvoltage while the afterpulsing contribution increases approximately linearly [174, 203]. Equation 4.6 can then be written as:

$$\begin{aligned} I_{\text{post-BD}}(V) = & \underbrace{C\,R}_{\text{Par1}} \cdot \Delta V \ \cdot \ \left(1 - \left(\frac{1}{\underbrace{k_{\text{e1}}}_{\text{Par2}} \cdot \Delta V \cdot \exp\left(-\underbrace{k_{\text{e2}}}_{\text{Par3}}/\sqrt{\Delta V}\right)} \right)^2 \right) \cdot \\ & \left(1 + \frac{\Delta V \cdot \left[\frac{f_Q{\cdot}AP(\Delta V)}{\Delta V}\right]}{1 - \Delta V \cdot \underbrace{\left[\frac{f_Q{\cdot}AP(\Delta V)}{\Delta V}\right]}_{\text{Par4}}} + \Delta V^2 \cdot \underbrace{\left[\frac{CT(\Delta V)}{\Delta V^2}\right]}_{\text{Par5}} \right) \end{aligned} \quad (4.7)$$

The final post-breakdown fit contains 5 degrees of freedom: one scaling factor depending on the SiPM capacitance C, two factors for modelling the trigger probability and one parameter each for the afterpulsing and crosstalk dependence on overvoltage.

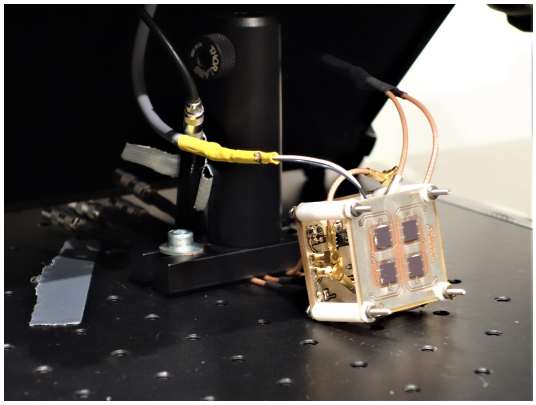

Figure 4.3.: Photograph of the black box used for IV-characteristics measurements. The cables to the power supply, current readout and temperature monitor are guided through light-tightened holes in the sides.

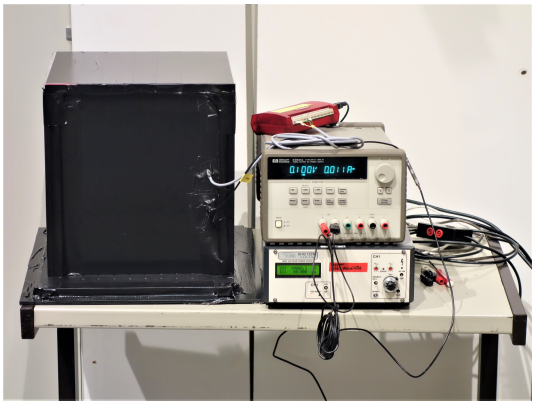

Figure 4.4.: Photograph of the SiPM stack. The SiPM can be connected to a pre-amplification board with two Kapton cables. The temperature is monitored with an RTD connected to the SiPM board.

The breakdown voltage V_{bd} is determined by analysing the full reverse curves for the characteristic kink when the diode enters Geiger-mode. Determining V_{bd} works best via the derivative of the logarithmic reverse current $\mathrm{d}_V(\log(I))$. The resulting curves increase sharply when breakdown sets in and drop exponentially afterwards. They are fitted with exponentially modified Gaussian functions (see [224]).

4.2. Setup for IV-Characteristics measurements

The IV-characteristics measurements have been performed in a custom-designed black box to provide dark conditions so that no photon triggers avalanches. The black box is shown in figure 4.3. It is equipped with threaded holes in the bottom plate to allow support structures to be attached and cable feedthrough holes in one side. All holes and slits are light-tightened with black duct tape during measurements. The SiPM can be connected to a detector stack consisting of a SiPM board and a pre-amplification (preamp) board which are connected via two short Kapton cables as shown in figure 4.4. The SiPM is either glued to the SiPM board using silver adhesives or contacted with metal pins on the SiPM bottom. The two-stage preamp board amplifies the SiPM pulses by a factor of 100.
The amplification stage is connected to the laboratory periphery via coaxial cables. The SiPM also can be contacted directly to study the electrical influence of the preamp board on the SiPM parameters (direct readout). A power supply is used to set the SiPM voltage and the current is measured with an ammeter. Both quantities

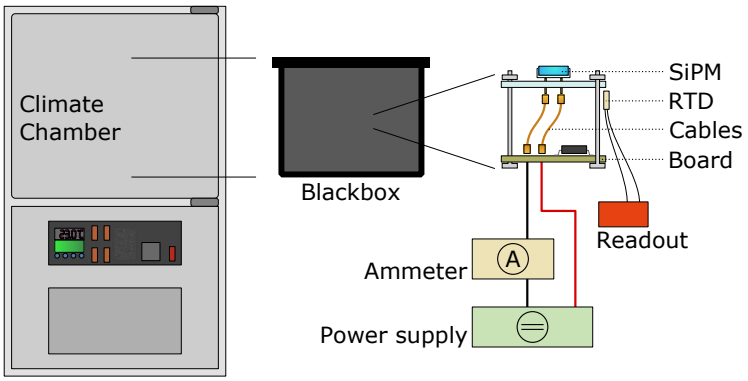

Figure 4.5.: Scheme of the setup used for IV-characteristics measurements. The SiPM is attached to a preamp board via a support structure and connected with two kapton wires. It is powered with a low-voltage power supply. The current is measured with a high precision ammeter. The SiPM board temperature is monitored with an RTD. The support structure is insulated from photons in a light-tight black box. The box is located in a climate chamber to be cooled down to $-70\,^{\circ}\mathrm{C}$.

are recorded digitally to derive the IV-characteristics. A resistance temperature detector (RTD) is attached closely to the SiPM to monitor the temperature stability of the photosensor.
Temperature-dependent measurements are accomplished by putting the black box in a climate chamber to cool down the entire setup. The power supply and ammeter are located outside of the chamber and the cables are guided to the black box via a thermally insulated hole in the chamber wall. The climate chamber is not light-tight so the black box is crucial for all measurements. This imposes a large thermal latent mass and increases the time necessary to reach thermal equilibrium after each change of the temperature set-point. The SiPM temperature is monitored with the RTD and measurements only start after the RTD reading has stabilised. The RTD is read out with a USB analog output module and displayed with TracerDAQPro. The entire setup is schematically shown in figure 4.5. Table 4.1 provides an overview of the devices used for the setup.
Data is acquired by setting a specific forward voltage with the power supply and measuring the resulting current with the ammeter. The Fluke ammeter is used for forward measurements, the Keithley ammeter for investigations of the reverse current. All devices are controlled with a computer via RS232 serial connections. The *serial* python class is used for the communication between PC and laboratory periphery. The current is read out several times to include statistical fluctuations. The standard deviation of those values is taken as statistical error and the ammeter accuracy as systematic error. The systematic error is not used for the further analysis since it can be determined and eliminated prior to the measurement runs.

4.3. IV-Characteristics in the Forward Regime

SiPM characterisation studies with IV-curves in forward direction are presented in this section. A method to use SiPMs as a direct temperature monitor for the temperature of the pn junction is developed and external parameters of the sensor are extracted from fits with equation 4.4. Several parts of this study have also been elaborated in the Bachelor thesis from N. Vogel [308].
Four SiPM models have been examined in the following studies. The SiPM models used here are:

- the 3$^{\text{rd}}$ generation VUV-MPPC from the S13370 series from Hamamatsu (in the following denoted as VUV3),
- the 4$^{\text{th}}$ generation VUV-MPPC from the S13370 series from Hamamatsu (in the following denoted as VUV4),
- the non-VUV sensitive PM3350 from KETEK (in the following denoted as KETEK),
- the VUV-HD SiPM from FBK in the LF version from the 2016 batch (in the following denoted as FBK).

The characterisation studies have been accomplished without preamplifier board (direct readout) – except for the KETEK where this was not possible. The investigations for using SiPMs as direct temperature sensors have to comply with the setup constellation including the pre-amp board in the LXe SiPM test stand [313]. This has been done for the VUV3 and the KETEK. The VUV4 and the FBK are only operated in direct mode. Nevertheless, they are examined and compared to the investigations including the pre-amp board. It will be shown later, that the method used in this work is quite insensitive to whether or not the pre-amp board is used.

Device	Brand	Model	Specifications	Man.
Chamber	Testequity	1007C	Down to $-75\,^{\circ}\text{C}$	[298]
PS 1	Keysight	E3631A	Stability: $< 0.01\,\% + 2\,\text{mV}$	[181]
PS 2	iseg	SHQ 122M	Error: $\pm(0.05\,\% + 0.4\,\text{V})$	[171]
Ammeter	Fluke	8846A	$0.01\,\%(\text{meas.}) + 0.02\,\%(\text{range})$	[134]
Ammeter	Keithley	6485	Acc. $0.1\,\% + 1\,\mu\text{A}$ for $I > 2\,\text{mA}$	[178]
RTD	Honeywell	HEL-705	$100\,\Omega$ platinum	[167]
RTD-ADC	RedLab	3104		[214]

Table 4.1.: Setup components used for the IV-characteristics studies including specifications used for the systematic error calculation and links to the manuals.

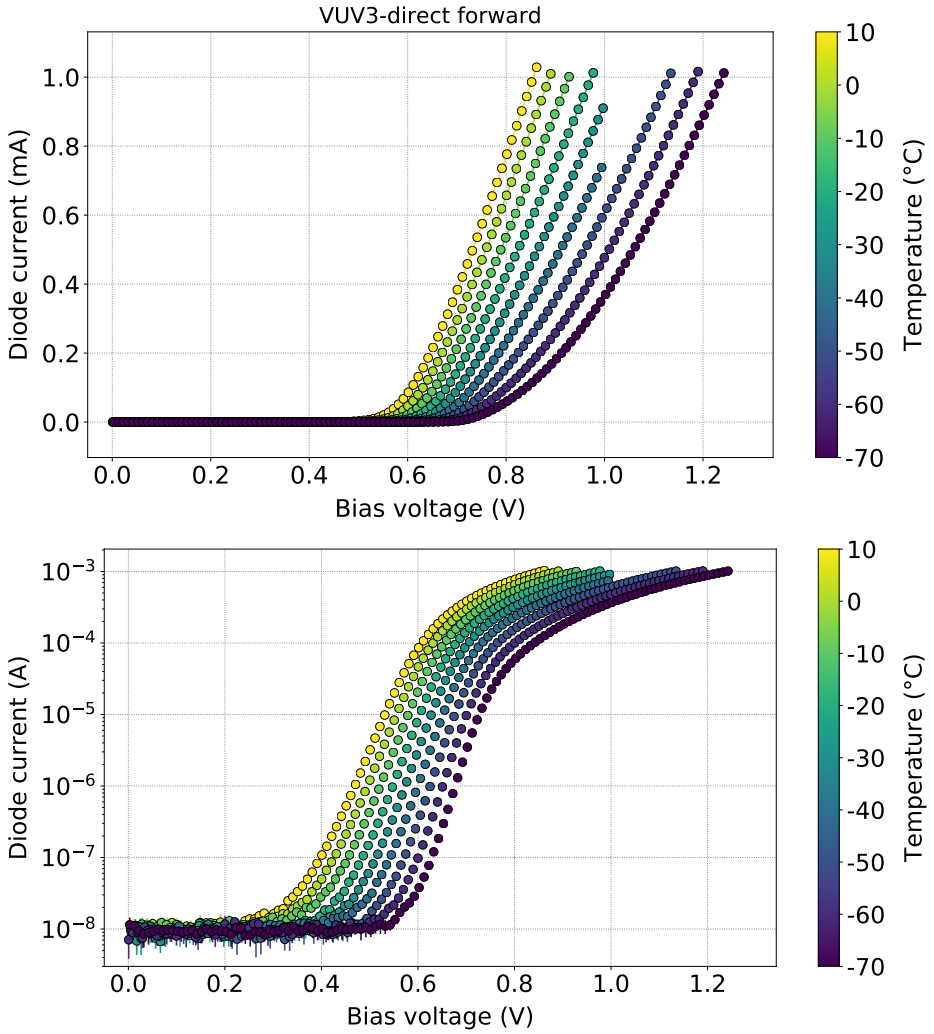

Figure 4.6.: IV-characteristics in forward direction of a VUV3 SiPM with direct readout and for different temperatures. The curves are plotted for a linear (top) and a logarithmic (bottom) y-axis. Current and voltage limits have been imposed in the control routines to protect the diode. The offset current I_{off} is around 10^{-8} A and the turn-on-voltage V_{t} lies between 0.3 and 0.6 V.

A typical set of IV-characteristics measurements is shown in figure 4.6. A VUV3 SiPM with direct readout has been used for this data set. The temperature range is +10 to −70 °C for all IV curves. The forward current is limited to protect the SiPM. The typical IV-characteristics behaviour displays a flat line at low voltages, where only the saturation current flows, a sharp increase in current around the turn-on voltage and a linear dependency at higher voltages. The saturation current I_{S} and the diode ideality factor n control the Shockley domain below and around V_{t}.

The resistor dominates the behaviour limiting the further excursion of the diode current. The resistance R corresponds to the inverse slope of the linear domains. Most SiPM parameters are temperature-dependent in some kind. Figure 4.6 shows a first glance that this is definitely true for the turn-on-voltage V_t and the resistance R. Other SiPM parameters also present such dependencies and will be investigated in the following.

4.3.1. Diode parameters from IV-curves

IV-characteristics can be used to deduce basic external parameters of the SiPM circuit and their dependence on the junction temperature. Two fit procedures are used for the data sets: first, a global fit via the Lambert W-function in equation 4.4 and, secondly, a regime fit. The regime fit uses the Shockley equation (equation4.1) for the lower part of the IV curves where the diode behaviour is dominant and a simple linear fit for the upper part where the resistor dominates. The fit functions contain the saturation current I_S, the ideality factor n and the resistance R as fit parameters. The offset current I_off induced by the devices and the circuit is taken into account as well. Additionally, the thermal potential $n\,V_\mathrm{T}$ and the turn-on-voltage V_t can be derived. The fit procedure is as follows:

1. The Shockley function in equation 4.1 is fitted to the lower branch of all IV-curves. An upper fit limit is set on the diode current so that the average χ^2 over all temperatures is about 1. The fit parameters I_S, n and I_off are completely unconstrained. The equation is scaled with the pixel number N_px based on the specifications of the individual SiPM model. All SPADs are assumed to be identical.
2. A linear fit is applied to the upper branch of the IV-curves. A global lower fit limit is set on the diode current so that the degrees of freedom is at least 3 for all IV-curves. The linear fit function is also scaled by N_px. The offset current I_off is fixed based on the value determined with the Shockley fit. Both Shockley and linear fit are part of the regime fit procedure.
3. The Lambert W-function in equation 4.4 is fitted to the entire data sets. The optimal regime fit parameters are taken as start parameters. I_off is again fixed to the optimal Shockley fit parameter. N_px is also fixed. All fits include the uncertainties on the current values outlined in section 4.2.
4. The goodness-of-fit is evaluated for a running upper (lower) fit limits on the Shockley (linear) fit in the regime fit procedure. This is to evaluate a possible alternative to the Lambert W-functions by combining both regime fits. In this case, the two regime fits are forced to be continuously differentiable at the regime transition.

5. All fit parameters and their uncertainties are plotted with respect to their individual fit routine (regime fit, Lambert fit).
6. The turn-on-voltage V_t is derived in two ways. First, via the x-intersection of the linear fit to the resistance branch of the IV-curves. Secondly, the average diode current and its averaged statistical uncertainty are calculated for small voltages ($< 0.2\,\mathrm{V}$). The averaged uncertainty is then multiplied by 3 and added to the average current. The voltage where the IV-curves exceed this 3σ level is interpreted as V_t as well.
7. All fit parameters except I_S are fitted with a linear function to analyse their temperature dependency. The saturation current I_S is fitted with equation 4.2 that only depends on the scaling factor χ.
8. Reduced χ^2 values are calculated for all IV-curve and parameter fits to examine the goodness-of-fit.

Figure 4.7 shows the forward-IV-characteristics of a VUV3 SiPM with direct readout. The fitted Lambert functions are plotted in the left, the regime fits are shown in the right plot. The corresponding χ^2-values are listed below in table 4.2. While the SiPM behaviour can be modelled very precisely with a Shockley function (red) around the turn-on voltage V_t, the resistance branch shows a very poor linearity and the linear fits (orange) yield rather high χ^2 values. The higher current regimes are also responsible for the poor result of the Lambert fit procedure – especially at lower temperatures.
The fit parameters for the Lambert and regime fit procedures can be found in figures 4.8 and 4.9, respectively. Due to the poor result of the Lambert fit at low temperatures, the fit parameters for the lowest three temperatures have been excluded from the investigation of the temperature dependency. Figures 4.10, 4.11 and 4.12 compare both fit procedures for the individual fit parameters I_S, n and R (in this order). Figure 4.13 shows the turn-on-voltage V_t derived with both methods explained above. I_S is fitted with equation 4.2, all other parameters are fitted with linear relationships. The coefficient χ_T from the I_S-fit and the slopes (i.e. temperature dependencies) of the linear fits of n, R and V_t are summed up in table 4.3 alongside their corresponding χ^2-values.
The fits for the KETEK, VUV4 and FBK SiPMs are shown in figures 4.14, 4.21 and 4.28, respectively. The corresponding χ^2-values are presented in tables 4.4, 4.6 and 4.8. The individual fit parameters I_S, n and R as well as the turn-on-voltage V_t are plotted over temperature in figures 4.15 to 4.20 for the KETEK, figures 4.22 to 4.27 for the VUV4, and figures 4.29 to 4.34 for the FBK SiPM. The fitted slopes as well as χ_T are listed in tables 4.5, 4.7 and 4.9, respectively, and so are the corresponding χ^2-values.

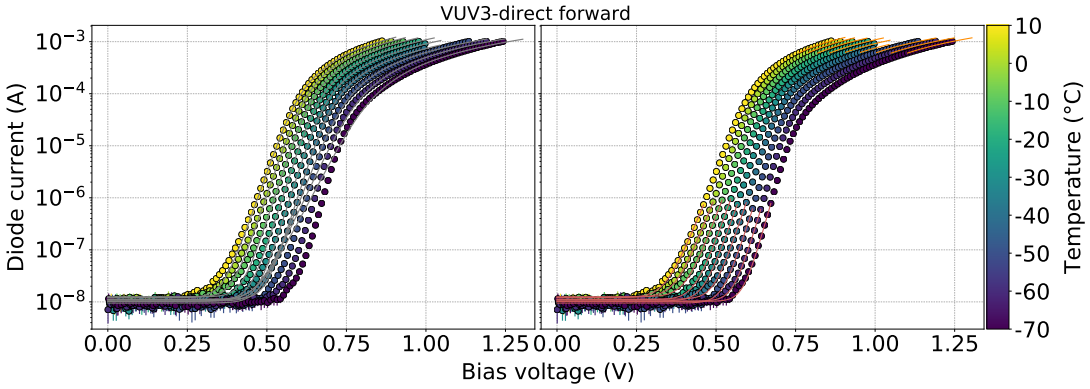

Figure 4.7.: Forward-IV-characteristics for a VUV3 SiPM with direct readout. Lambert W-functions (left, grey) are fitted as well as Shockley functions at low currents (right, red) and linear functions at higher currents (right, orange).

Temperature	χ^2_{red} (Lambert)	χ^2_{red} (Shockley)	χ^2_{red} (linear)
+10.0 °C	166.674	1.47088	286.052
+00.0 °C	159.590	1.81128	163.844
−10.0 °C	168.503	2.05776	199.688
−20.0 °C	130.598	1.67359	604.147
−30.0 °C	1405.51	1.58737	489.602
−40.0 °C	5613.88	1.48007	93.1133
−50.0 °C	40732.2	1.16370	2625.97
−60.0 °C	93792.6	0.906549	4901.63
−70.0 °C	126785	0.927385	4452.65

Table 4.2.: Reduced χ^2 values of the Lambert and regime fit procedures for a VUV3 SiPM with direct readout between +10 and −70 °C.

Fit parameter	**Lambert**		**Regime**	
	χ_T or slope	χ^2_{red}	χ_T or slope	χ^2_{red}
Saturation current I_S	3.768	39.16	7.018	3.483
Ideality factor n	$-3.026{\cdot}10^{-4}$/K	24.26	$-6.723{\cdot}10^{-4}$/K	2.128
Resistance R	−7421 Ω/K	392.3	−6022 Ω/K	67.81
	Resistance x-offset		**3σ Current-limit**	
Turn-on voltage V_{on}	−2.973 mV/K	328.8	−3.219 mV/K	0.1681

Table 4.3.: Fit results of the temperature dependency of the Lambert and regime fit parameters for a VUV3 SiPM with direct readout.

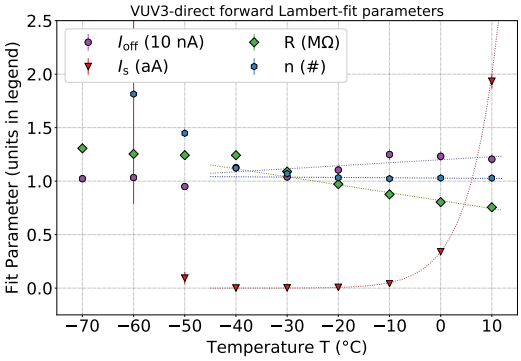

Figure 4.8.: Lambert fit parameters of forward IV-characteristics for a VUV3 SiPM with direct readout.

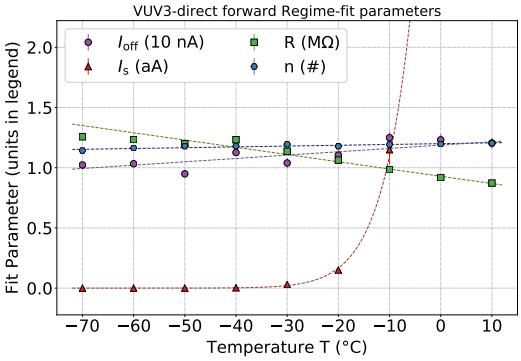

Figure 4.9.: Regime fit parameters of forward IV-characteristics for a VUV3 SiPM with direct readout.

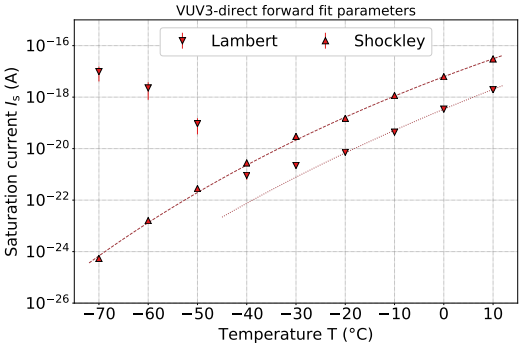

Figure 4.10.: Saturation current I_S of a VUV3 SiPM with direct readout.

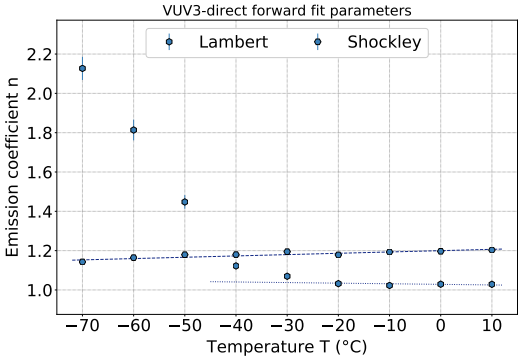

Figure 4.11.: Ideality factor n of a VUV3 SiPM with direct readout.

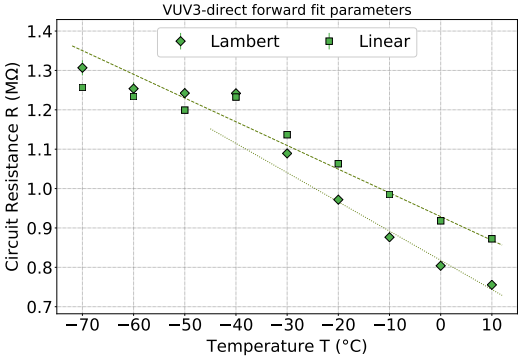

Figure 4.12.: Resistance R of a VUV3 SiPM with direct readout.

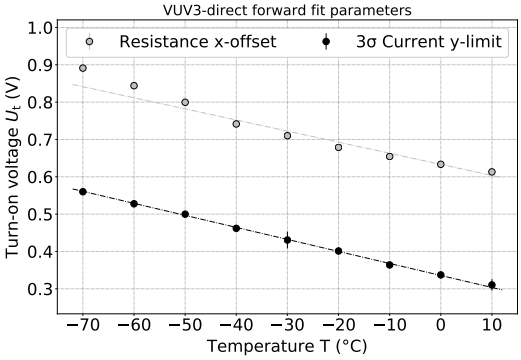

Figure 4.13.: Turn-on voltage V_{on} of a VUV3 SiPM with direct readout.

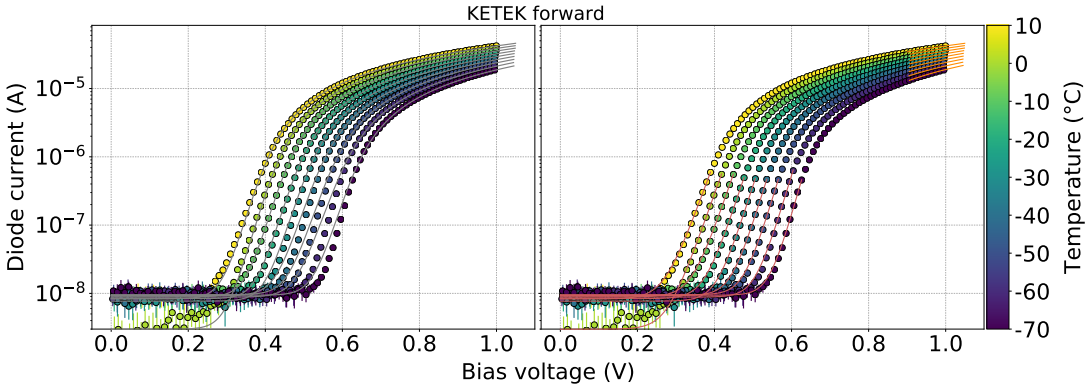

Figure 4.14.: Forward-IV-characteristics for a KETEK SiPM with preamp board. Lambert W-functions (left, grey) are fitted as well as Shockley functions at low currents (right, red) and linear functions at higher currents (right, orange).

Temperature	χ^2_{red} (Lambert)	χ^2_{red} (Shockley)	χ^2_{red} (linear)
10.0 °C	31.5702	1.90366	7.06618
0.0 °C	29.9425	1.03335	8.06462
−10.0 °C	85.8691	1.4427	14.7574
−20.0 °C	193.283	1.17558	19.263
−30.0 °C	380.919	0.949559	34.0895
−40.0 °C	522.068	0.709428	45.7952
−50.0 °C	620.573	0.96594	59.9055
−60.0 °C	552.639	2.40935	96.6507
−70.0 °C	440.741	1.26706	74.0114

Table 4.4.: Reduced χ^2 values of the Lambert and regime fit procedures for a KETEK SiPM with preamp board between +10 and −70 °C.

Fit parameter	**Lambert**		**Regime**	
	χ_T or slope	χ^2_{red}	χ_T or slope	χ^2_{red}
Saturation current I_S	−11.97	4.972	3.57	3.755
Ideality factor n	$-50.03{\cdot}10^{-4}\,/K$	10.23	$-11.24{\cdot}10^{-4}\,/K$	3.786
Resistance R	$-14140\,\Omega/K$	2.98	$-13320\,\Omega/K$	13.86
	Resistance x-offset		**3σ Current-limit**	
Turn-on voltage U_{on}	$-2.973\,\text{mV}/K$	8.181	$-3.445\,\text{mV}/K$	0.1034

Table 4.5.: Fit results of the temperature dependency of the Lambert and regime fit parameters for a KETEK SiPM with preamp board.

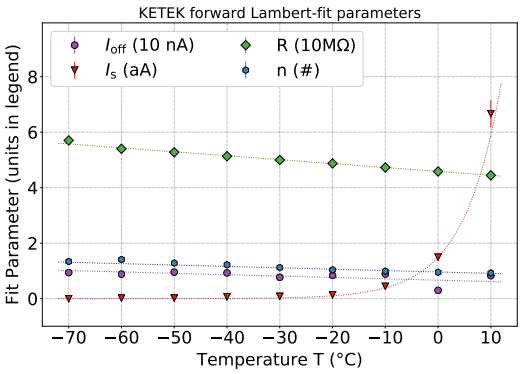

Figure 4.15.: Lambert fit parameters of forward IV-characteristics for a KETEK SiPM with preamp board.

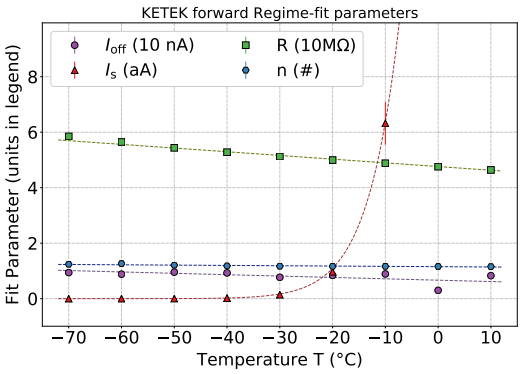

Figure 4.16.: Regime fit parameters of forward IV-characteristics for a KETEK SiPM with preamp board.

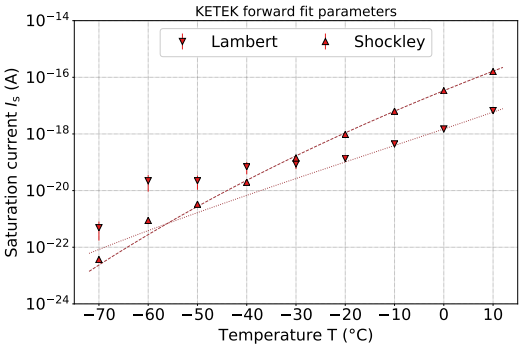

Figure 4.17.: Saturation current I_S of a KETEK SiPM with preamp board.

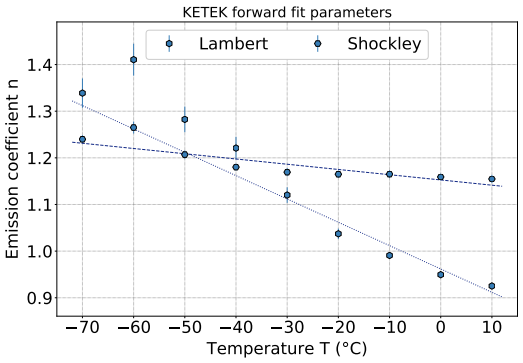

Figure 4.18.: Ideality factor n of a KETEK SiPM with preamp board.

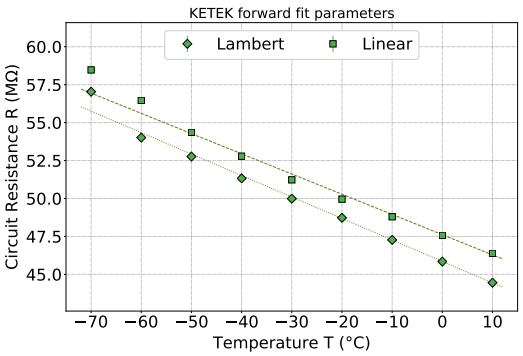

Figure 4.19.: Resistance R of a KETEK SiPM with preamp board.

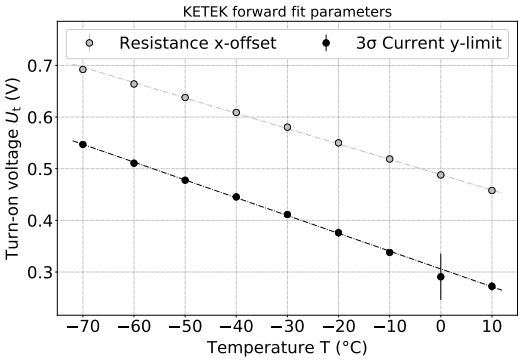

Figure 4.20.: Turn-on voltage V_{on} of a KETEK SiPM with preamp board.

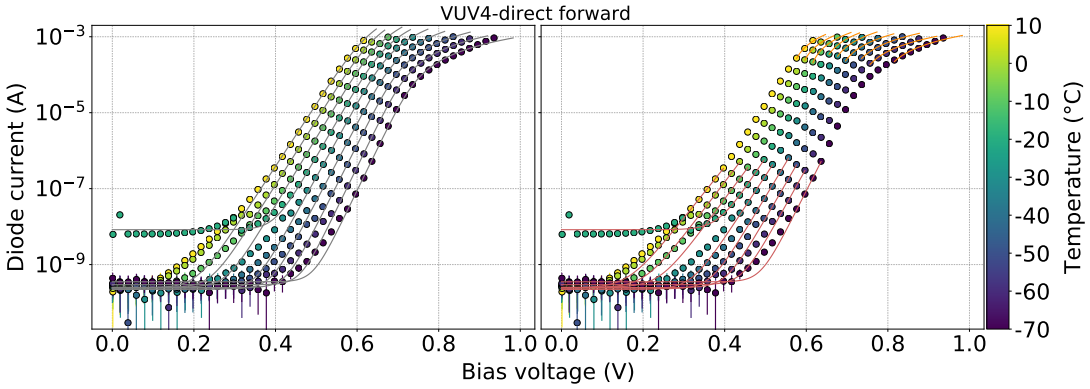

Figure 4.21.: Forward-IV-characteristics for a VUV4 SiPM with direct readout. Lambert W-functions (left, grey) are fitted as well as Shockley functions at low currents (right, red) and linear functions at higher currents (right, orange).

Temperature	χ^2_{red} (Lambert)	χ^2_{red} (Shockley)	χ^2_{red} (linear)
+10.0 °C	1293.92	83.4725	3596.97
+00.0 °C	1425.42	364.337	3453.98
−10.0 °C	1111.98	156.182	6284.8
−20.0 °C	900.748	388.287	943.625
−30.0 °C	797.296	123.395	944.255
−40.0 °C	585.72	78.7816	1095.99
−50.0 °C	435.739	74.5658	1296.18
−60.0 °C	534.53	55.4252	3236.88
−70.0 °C	2445.57	63.4229	3794.72

Table 4.6.: Reduced χ^2 values of the Lambert and regime fit procedures for a VUV4 SiPM with direct readout between +10 and −70 °C.

Fit parameter	**Lambert**		**Regime**	
	χ_T or slope	χ^2_{red}	χ_T or slope	χ^2_{red}
Saturation current I_S	7.054	1.01	12.56	1.957
Ideality factor n	$2.645{\cdot}10^{-4}\,/K$	1.741	$18.73{\cdot}10^{-4}\,/K$	1.255
Resistance R	$-26.78\,\text{k}\Omega/K$	62.86	$-20.6\,\text{k}\Omega/K$	6.299
	Resistance x-offset		3σ **Current-limit**	
Turn-on voltage U_{on}	$-2.446\,\text{mV}/K$	3.378	$-3.772\,\text{mV}/K$	1.046

Table 4.7.: Fit results of the temperature dependency of the Lambert and regime fit parameters for a VUV4 SiPM with direct readout.

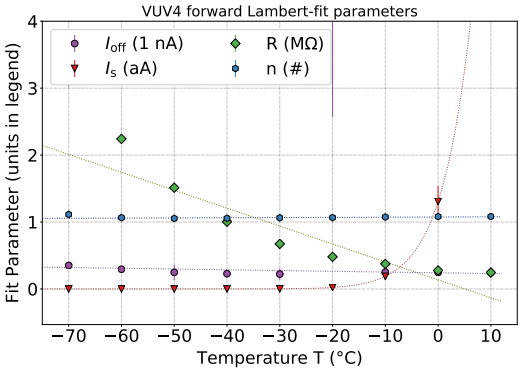

Figure 4.22.: Lambert fit parameters of forward IV-characteristics for a VUV4 SiPM with direct readout.

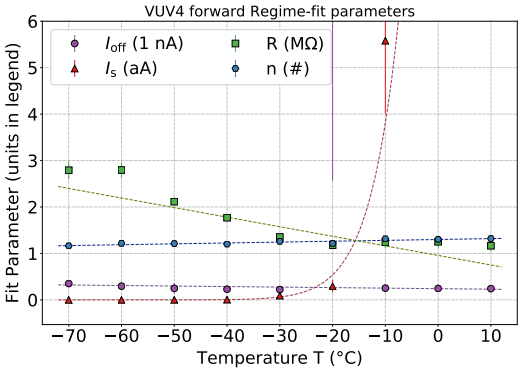

Figure 4.23.: Regime fit parameters of forward IV-characteristics for a VUV4 SiPM with direct readout.

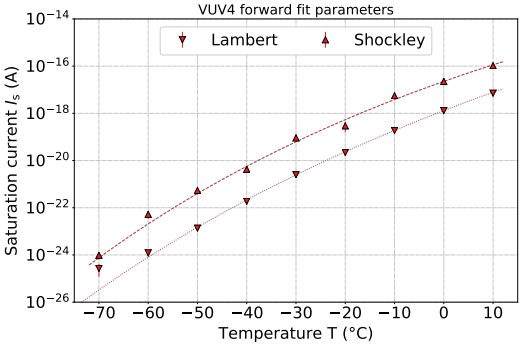

Figure 4.24.: Saturation current I_S of a VUV4 SiPM with direct readout.

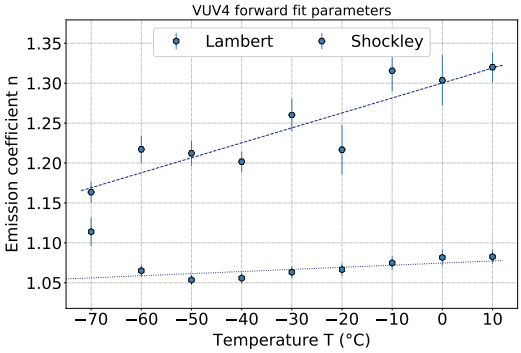

Figure 4.25.: Ideality factor n of a VUV4 SiPM with direct readout.

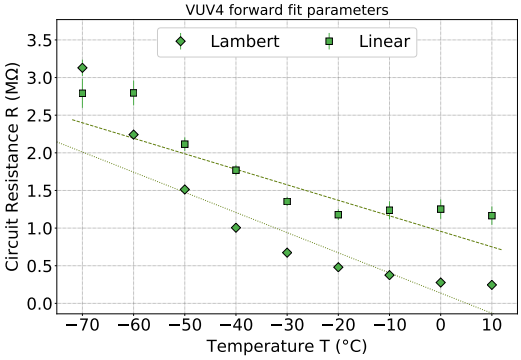

Figure 4.26.: Resistance R of a VUV4 SiPM with direct readout.

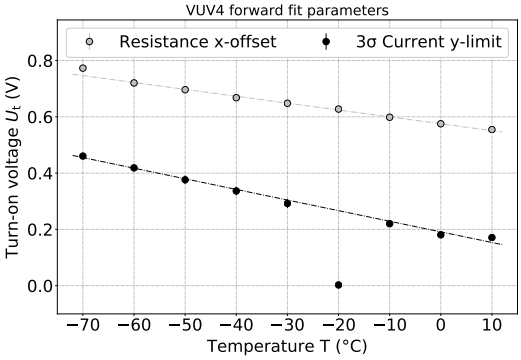

Figure 4.27.: Turn-on voltage V_{on} of a VUV4 SiPM with direct readout.

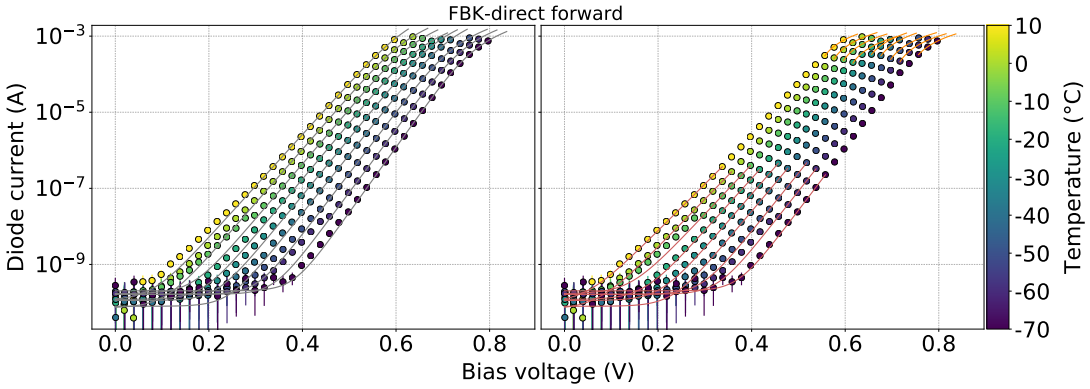

Figure 4.28.: Forward-IV-characteristics for an FBK SiPM with direct readout. Lambert W-functions (left, grey) are fitted as well as Shockley functions at low currents (right, red) and linear functions at higher currents (right, orange).

Temperature	χ^2_{red} (Lambert)	χ^2_{red} (Shockley)	χ^2_{red} (linear)
+10.0 °C	631.351	6.69107	3014.22
+00.0 °C	592.766	6.3463	4546.29
−10.0 °C	373.202	95.5367	4555.51
−20.0 °C	197.839	8.57871	3949.68
−30.0 °C	83.1495	12.0603	1709.02
−40.0 °C	57.9748	6.70842	2237.39
−50.0 °C	84.5271	15.4301	3043.23
−60.0 °C	162.977	43.0967	3651.9
−70.0 °C	133.095	4.71319	702.818

Table 4.8.: Reduced χ^2 values of the Lambert and regime fit procedures for an FBK SiPM with direct readout between +10 and −70 °C.

Fit parameter	**Lambert**		**Regime**	
	χ_T or slope	χ^2_{red}	χ_T or slope	χ^2_{red}
Saturation current I_S	−4.706	18.95	0.4594	3.135
Ideality factor n	$-17.83{\cdot}10^{-4}\,/K$	3.914	$-6.921{\cdot}10^{-4}\,/K$	4.082
Resistance R	$-4072\,\Omega/K$	38.05	$-1259\,\Omega/K$	1.324
	Resistance x-offset		**3σ Current-limit**	
Turn-on voltage U_{on}	$-2.449\,\text{mV}/K$	0.8577	$-2.837\,\text{mV}/K$	4.495

Table 4.9.: Fit results of the temperature dependency of the Lambert and regime fit parameters for an FBK SiPM with direct readout.

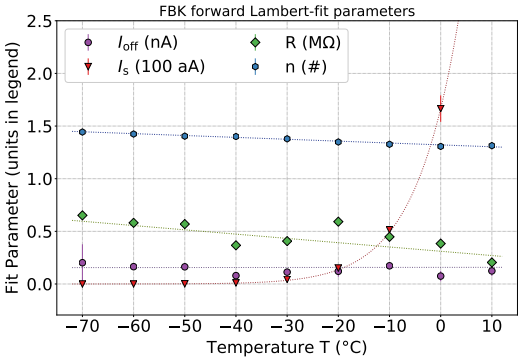

Figure 4.29.: Lambert fit parameters of forward IV-characteristics for an FBK SiPM with direct readout.

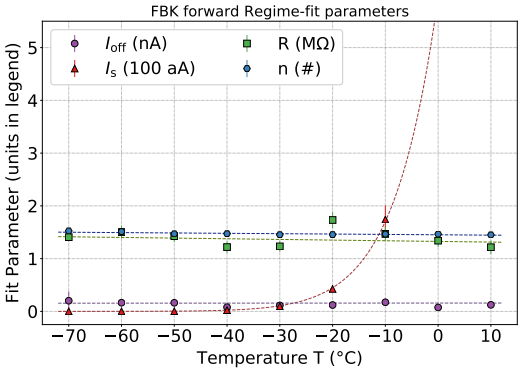

Figure 4.30.: Regime fit parameters of forward IV-characteristics for an FBK SiPM with direct readout.

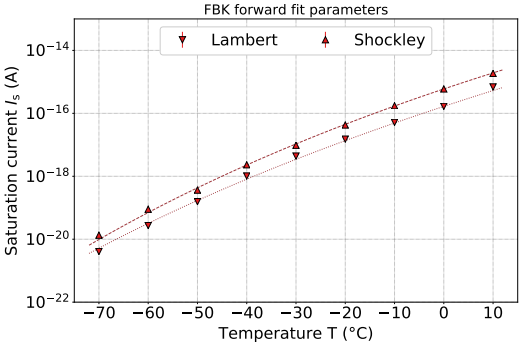

Figure 4.31.: Saturation current I_S of an FBK SiPM with direct readout.

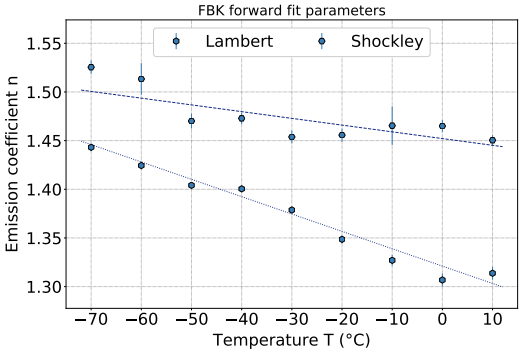

Figure 4.32.: Ideality factor n of an FBK SiPM with direct readout.

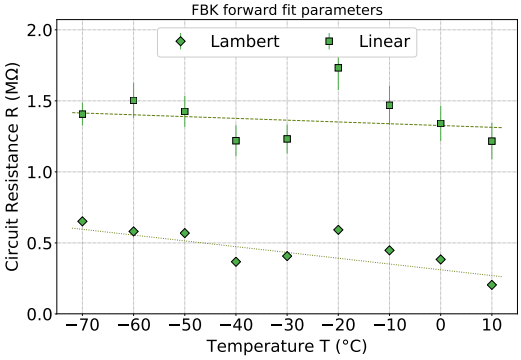

Figure 4.33.: Resistance R of an FBK SiPM with direct readout.

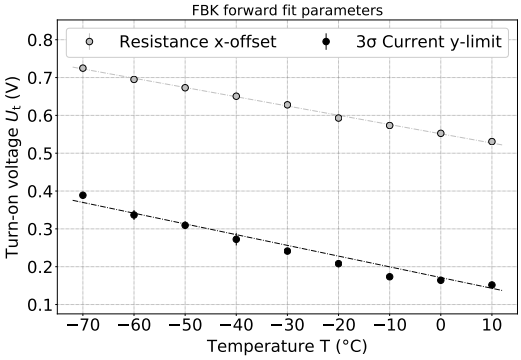

Figure 4.34.: Turn-on voltage V_{on} of an FBK SiPM with direct readout.

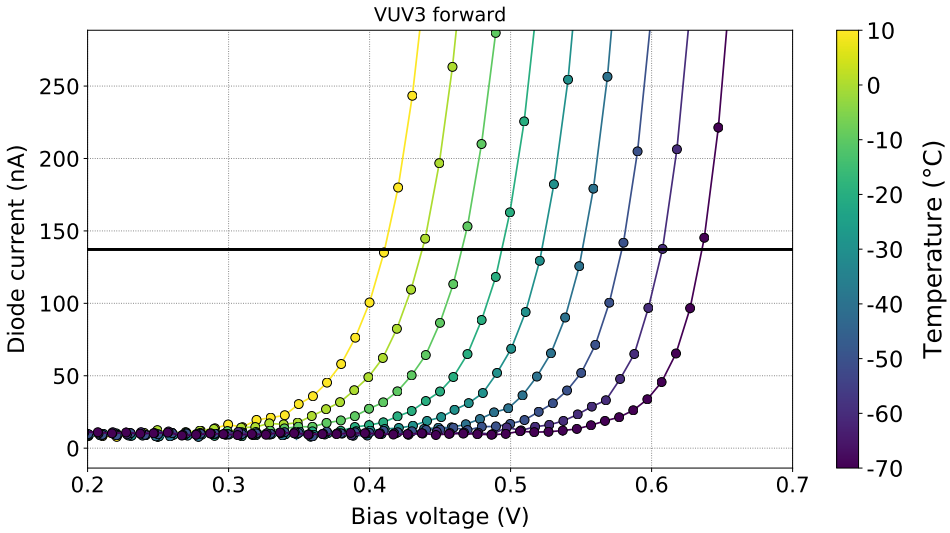

Figure 4.35.: IV-characteristics in forward direction for a VUV3 SiPM with preamp board. The evaluation current at 137.4 nA used for the temperature sensor calibration is shown as a horizontal black line.

4.3.2. SiPMs as temperature sensor

SiPMs can be used as direct probe for the pn-junction temperature via calibrated IV-characteristics. This allows to monitor the SiPM temperature during extended characterisation studies without having to rely on a temperature sensor. Temperature sensors as RTDs may be close to the SiPM in operation but impose an unknown systematic temperature deviation from the SiPM material itself. Since many SiPM parameters are temperature dependent, this method helps to get more precise knowledge of these parameters e.g. the breakdown voltage.

The method to calibrate IV-characteristics to use a SiPM as a direct temperature sensor is explained in figure 4.35. The plot shows the same VUV3 IV-curves as in figure 4.7 around the turn-on-voltage V_t. A fixed evaluation current $I_\mathrm{eva} = 137.4\,\mathrm{nA}$ is specified. At this current, the corresponding forward voltage $V_\mathrm{eva}(T)$ is derived via a spline interpolation for each curves i.e. each temperature.

Figure 4.36 shows the temperature dependence of $V_\mathrm{eva}(T)$ at the pre-defined I_eva and a fitted slope. The fit is used as a calibration curve which allows to extend the usability of SiPMs as direct temperature sensors to other temperatures T_0. For liquid xenon experiments, SiPMs will have to work around $-100\,^\circ\mathrm{C}$. This is beyond the temperature range of the available climate chamber. The linear fit is extrapolated to $V_\mathrm{extr}(T_0)$ as shown in figure 4.36. An evaluation voltage $V_\mathrm{eva}(-100\,^\circ\mathrm{C})$ of 715.22 mV is expected if the SiPM junction reached the desired LXe temperature T_0. Eventually, the temperature monitoring during SiPM characterisation studies

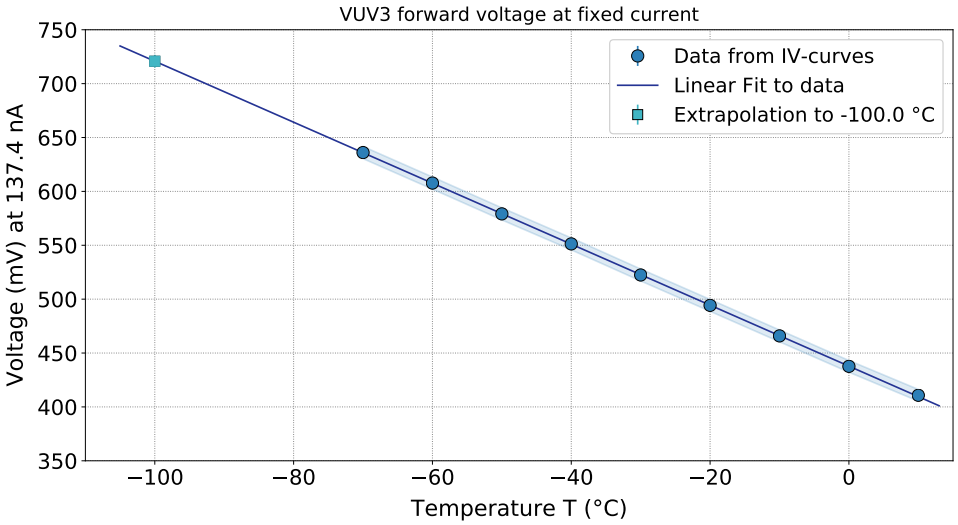

Figure 4.36.: Interpolated voltage values at fixed evaluation current I_{eva} over temperature. The values show a linear dependency on the temperature and can be extrapolated to a certain target temperature e.g. the temperature of liquid xenon.

can be accomplished via periodic measurements of the forward IV-curve and their evaluation at the same constant I_{eva} used for the IV-curve calibration.
The uncertainties on the $V_{\mathrm{eva}}(T)$ are calculated in the following way. At first, the statistical errors of each pair of current data values around I_{eva} are derived for each IV-curve. Their weighted average is calculated as uncertainty on I_{eva}. These values are converted into an uncertainty on V_{eva} via the local slope of the IV curve. These uncertainties ΔV_{eva} are used in the fit procedure in figure 4.36. The final statistical uncertainty on the extrapolated voltage V_{extr} is calculated from the uncertainties of the linear fit parameters. The uncertainty on the target temperature T_0 is calculated from $\Delta V_{\mathrm{extr}}(T_0)$ and the fit slope. This ΔT_0 describes the uncertainty on a temperature T_0 determined from a IV-curve recorded at T_0 and the linear fit from the set of IV-curves used for calibration. ΔT_0 can be interpreted as the quality of the direct SiPM temperature measurement method.
The χ^2_{red} value for the VUV3 with direct readout shown in figure 4.36 was 0.261. This indicates that the current uncertainties from which $V_{\mathrm{eva}}(T)$ is calculated are overestimated. This is reasonable since the uncertainty on the currents are based on the fluctuation of a set of current readings and are dominated by the device-wise fluctuations rather than the SiPM. The uncertainty on the target temperature is 0.423 K. This is good enough for further SiPM characterisation studies.
The target temperature uncertainty ΔT_0 depends on the slope and the fit parameter uncertainties of the linear calibration curve. The ideal evaluation current I_{eva} should be chosen in a minimum of these uncertainties while the slope of the calibration

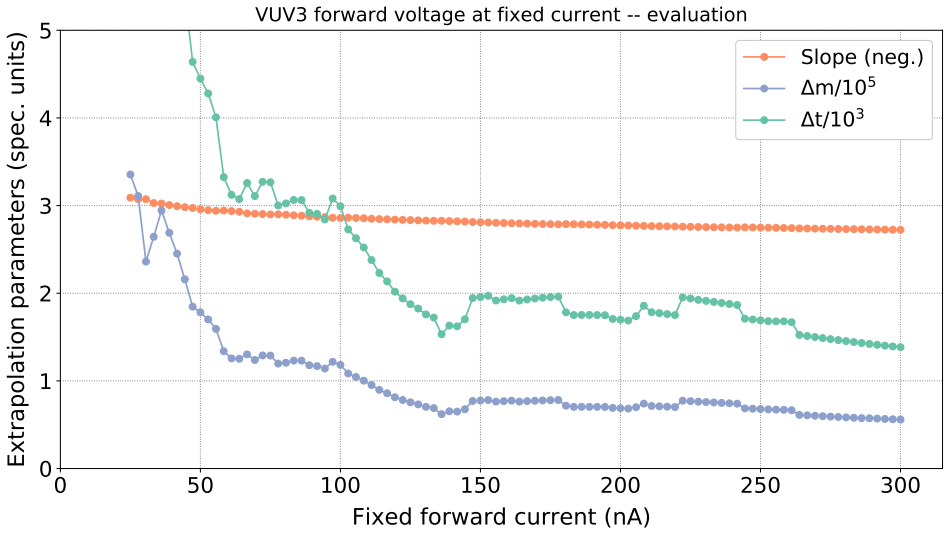

Figure 4.37.: The evaluation current I_{eva} is scanned up to 300 nA with a VUV3 and the slope and fit parameter uncertainties of the $V_{\mathrm{eva}}(T)$ calibration curve are plotted. The optimal evaluation current is at 137.4 nA, where the uncertainties are lowest.

curve should be large. For this, I_{eva} is scanned within the Shockley regime and the corresponding slope m and fit parameter uncertainties Δm and Δt are determined. These three curves are plotted in figure 4.37 over current. The slope of the calibration curve is almost flat while Δm and Δt present a larger variability. The evaluation current I_{eva} is set to 137.4 nA where the fit parameter uncertainties fall in a mutual minimum. The uncertainty on the target temperature T_0 is significantly higher for other I_{eva}. This demonstrates the practicability of the I_{eva} optimisation via current scans.

The SiPM calibration of $V_{\mathrm{eva}}(T)$ curves has been accomplished for two SiPM models including pre-amplifier board: the VUV3 and the KETEK. Including the preamp was assumed to be important since it is also contained in the Erlangen SiPM characterisation test stand [313] for which the temperature monitoring method is developed. Comparisons between IV-curves with and without pre-amplifier board however revealed, that the board has little to no influence on the evaluation current calibration. This is due to the DC nature of the forward current and the small values of I_{eva} for which the effect of the pre-amp board is small. The plot therefore also contains two curves acquired without pre-amplifier board (VUV4 and FBK). For both curves, the uncertainties and the individual optimal evaluation current have been derived via the presented techniques. The target temperature was $-100\,^{\circ}\mathrm{C}$ for all measurement sets.

All calibration curves are plotted in figure 4.38. Table 4.10 lists the corresponding evaluation current, χ^2 values and target temperature uncertainties. The χ^2 values

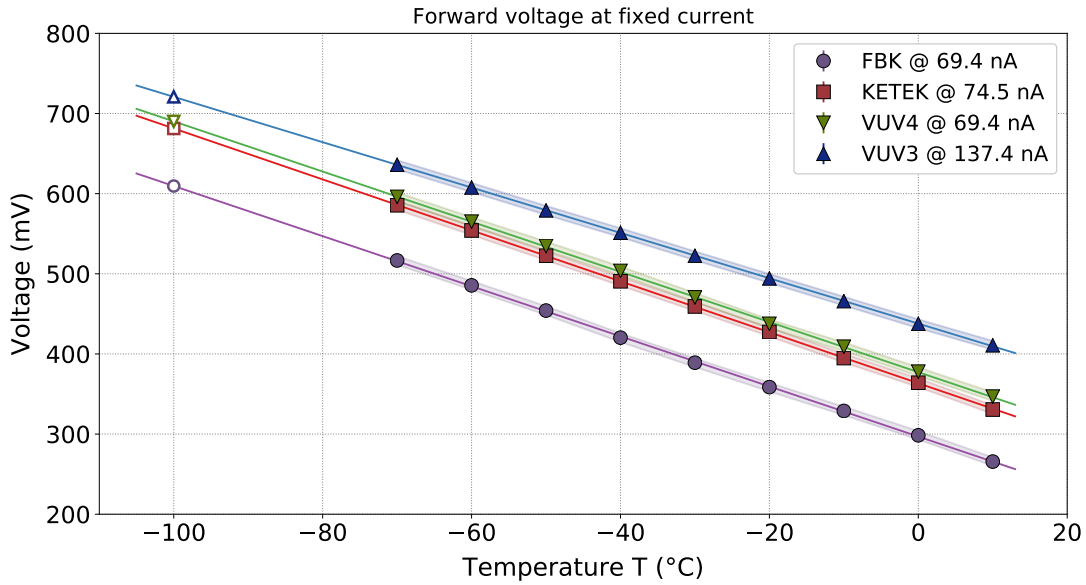

Figure 4.38.: Interpolated voltage values at fixed evaluation current I_{eva} over the temperature. The KETEK (red squares) and VUV3 (blue triangles) curves are acquired via a pre-amplifying stage, the FBK (purple circles) and VUV4 (green upside-down triangles) curves are directly connected. Each I_{eva} data set is extrapolated to the LXe-target temperature at −100 °C (open markers).

SiPM	I_{eva}	χ^2	ΔT
FBK	49.0 nA	108	1.59 K
KETEK	74.5 nA	0.417	0.586 K
VUV4	69.4 nA	165	1.41 K
VUV3	137.4 nA	0.692	0.519 K

Table 4.10.: List of the optimal evaluation current, reduced χ^2 value and target temperature uncertainty for the temperature calibration curves of all SiPMs.

are significantly larger for the FBK and VUV4 curves. This is due to an improved ammeter that allows more precise current readings. The much smaller χ^2-value for the VUV3 and the KETEK are therefore an artefact of the poor current measurements in the early studies. It may also indicate that the dependence of V_{eva} on T is not exactly linear. All in all, the target temperature accuracy for the FBK and VUV4 is more reliable in general. On the upside, the small variations between the four curves indicate that the calibration technique is rather insensitive to whether or not the pre-amp board is used. This simplifies future calibration studies since it is enough to only operate the SiPM itself in the climate chamber.

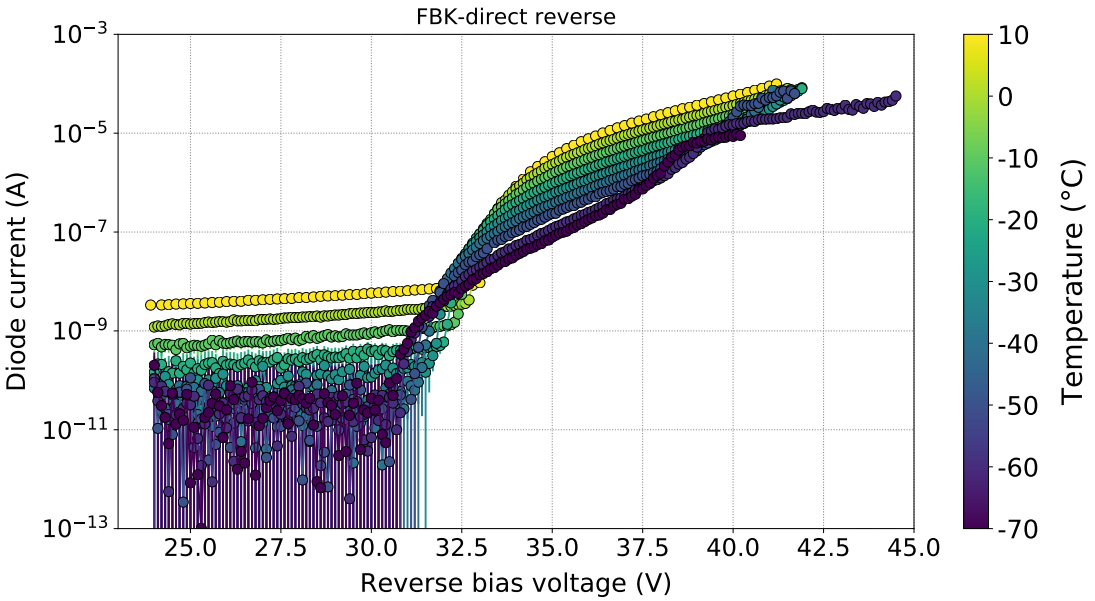

Figure 4.39.: IV-characteristics in reverse direction of an FBK VUV-HD SiPM with direct readout for different temperatures. Current and voltage limits have been imposed in the control routines to protect the diode. The breakdown voltage V_{bd} is around 32 V. The current increases drastically above due to avalanche breakdown.

4.4. IV-Characteristics in the Breakdown Regime

SiPM characterisation studies with IV-curves in reverse direction are presented in this section. The same SiPM samples as listed in section 4.3 are used – with exception of the KETEK model. The IV curves are acquired for a bias range of roughly $V_{\mathrm{bd}}\pm10\,\mathrm{V}$ and analysed using the fit models explained in section 4.1.3. Several parts of this study have also been elaborated in the Bachelor thesis from C. Rauch [256].

An example set of reverse IV-curves are obtained with an FBK VUV-LF and plotted in figure 4.39. The pre-breakdown regime presents a slow exponential rise while the post-breakdown regime shows a sharp rise when microplasmas discharge kicks in followed by an increasingly slower increase in current. Both pre-breakdown current level as well as the breakdown voltage increase with temperature. The first is due to the increased dark rate while the latter is governed by the smaller scattering length preventing conduction band electrons from gaining enough energy to sustain avalanches. At low temperatures, the saturation current gets smaller than parasitic noise induced by the power supply. This conceals the true exponential relationship of the pre-breakdown current as well as the true breakdown voltage. The curves at the lowest two temperature are omitted from further analysis due to this issue.

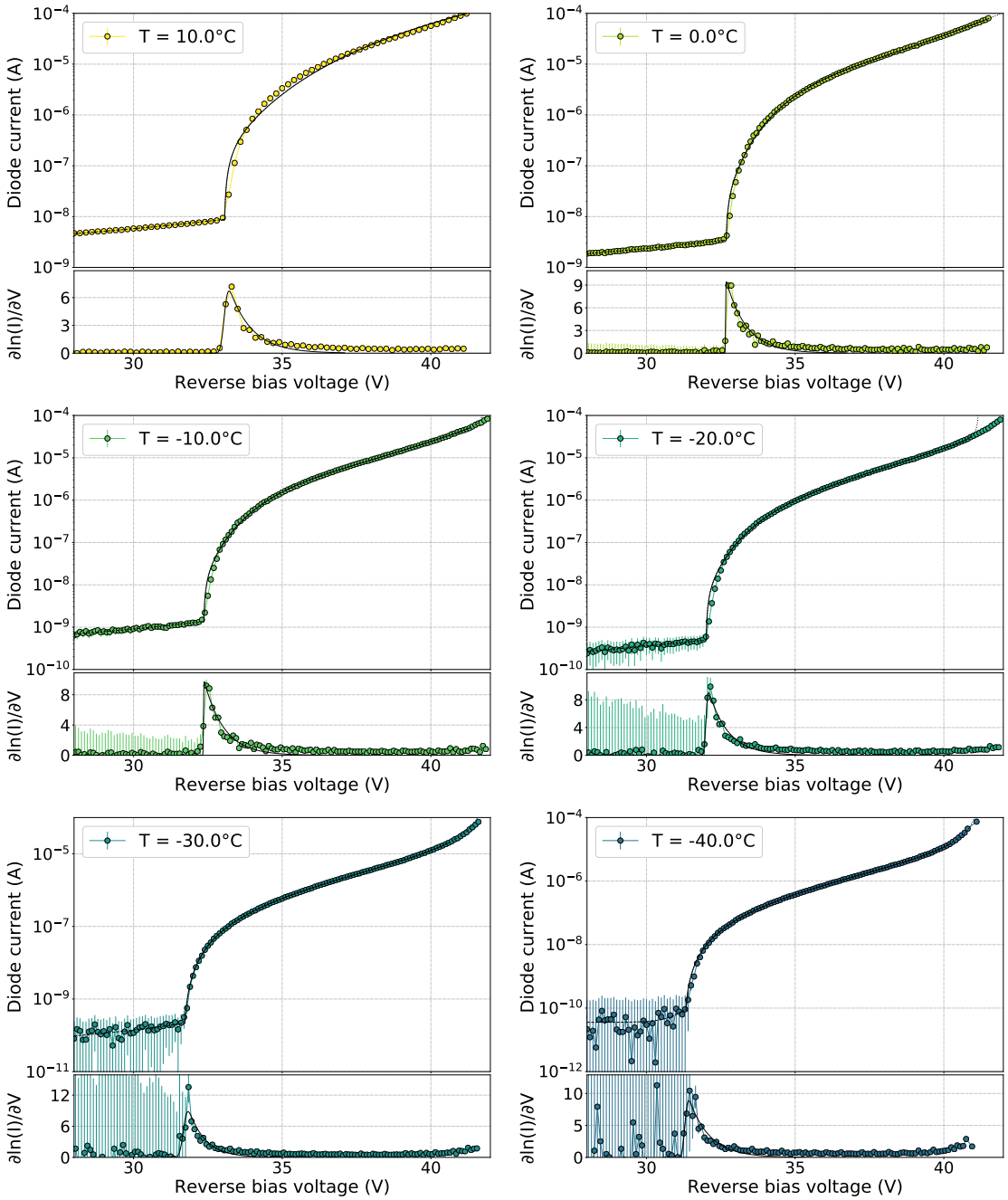

Figure 4.40.: Reverse IV-characteristics for an FBK SiPM with direct readout at different temperatures. The pre- and post-breakdown fits are plotted with a dashed and solid line, respectively. The bottom plot shows the derivative of the logarithmic reverse current and a fit with an exponentially modified Gaussian function from which the breakdown voltage is obtained.

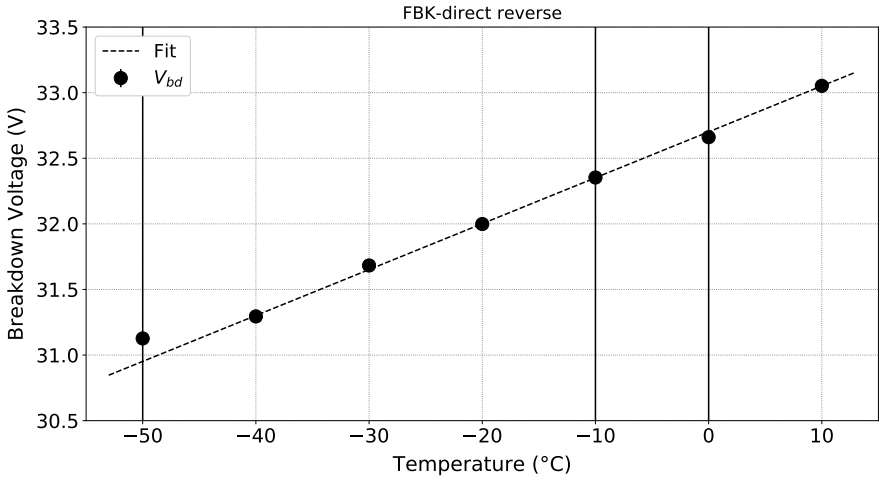

Figure 4.41.: Breakdown voltage over temperature for the FBK VUV-HD. The voltage values are derived via EMG-fits of the derivative of the logarithmic reverse current.

The plots in figure 4.40 show the individual reverse IV-characteristics near V_{bd} between +10 and −40 °C for the FBK SiPM. The pre-breakdown regime is fitted with equation 4.5 and plottted with a dashed black line. The post-breakdown regime follows equation 4.7 and is plotted with a solid line. The post-breakdown fit is limited to an overvoltage of 9 V. Above, self-sustaining avalanches occur which cannot be modelled correctly with the fit model or lead to a current overdrive in the ammeter and unplausible data. The upper limit has been chosen with respect to the dynamic range that allows a stable operation of the SiPM [256]. The bottom plots show the derivative of the logarithmic current with an exponentially modified Gaussian (EMG) fit to determine V_{bd} [224].

The pre-breakdown regime can be modelled well while the more complex post-breakdown fit struggles with the large current range. χ^2 values decrease with temperature due to the higher relative uncertainties on the decreasing reverse currents. For the FBK VUV-HD, χ^2 is 19296 at +10 °C but drops down to 32 at low temperatures. The goodness-of-fit is comparable to other studies (e.g. [117]) so the large χ^2 values might indicate underestimated current uncertainties.

The afterpulsing parameter $[f_Q{\cdot}AP/\Delta V]$ (Parameter 4 in equation 4.7) is almost independent of temperature. An extrapolation to LXe temperature yield a value of 0.1087±0.0144 which compares very well to the results presented in [174], Fig. 7 where the same SiPM model is used. The crosstalk parameter (Parameter 5) is far less stable. Its weighted mean is 0.6684 which is far larger than determined in [174], Fig. 5. The large uncertainties on this parameter further suggest, that significant fit instabilities are introduced due to the quadratic dependency on the overvoltage in equation 4.7 governed by the crosstalk parameter.

The breakdown voltage V_{bd} is determined via the fitted centroid of the Gaussian component in the EMG function (parameter t_{g} in [224]). The values for the FBK SiPM are plotted in figure 4.41 and present a linear dependency on the ambient temperature. An extrapolation to 168 K results in a value of 29.022±0.033 V for V_{bd}. This is consistent with the findings in [174] (tab. 1, LF) and is comparable to [313] (sec. 4.1.2).
The same analysis steps are accomplished for the Hamamatsu VUV3 and VUV4 SiPM with direct readout. The crosstalk factor is $\mathcal{O}(10^{-5})$ for both SiPMs. This indicates that the crosstalk contribution is small and rather linear than quadratic. This is consistent with the findings in [141] (Fig. 14). The afterpulsing factor is 0.0697±0.0024 for the VUV3 and 0.0867±0.0020 for the VUV4 at 163 K. The model in [141] suggests an afterpulsing slope of about 0.1 for small overvoltages but include delayed crosstalk events so the VUV4 afterpulsing factor can be considered consitent with literature as well. The breakdown voltage of the VUV3 is 45.85±0.40 at −100 °C and agrees with [256] where a different technique is used for the same dataset. For the VUV4, V_{bd} is 44.67±0.41 at 163 K and 45.21±0.37 at −100 °C – again consistent with [141] and [256].
Figure 4.42 shows several IV-characteristics around the breakdown voltage of a VUV3 and a VUV4 at ambient temperature +10, −10 and −30 °C. The dynamic range is significantly larger compared to the FBK. Accordingly, the post-breakdown fit range can be extended to 13.6 and 11 V above V_{bd}, respectively. Table 4.11 lists the V_{bd} linear fit parameters.

Sample	V_{bd} fit slope	V_{bd} fit offset
FBK	$(0.034990\pm0.000310)\ \frac{\mathrm{V}}{^\circ\mathrm{C}}$	(32.70 ± 0.01) V
VUV3	$(0.047216\pm0.003822)\ \frac{\mathrm{V}}{^\circ\mathrm{C}}$	(50.57 ± 0.11) V
VUV4	$(0.052487\pm0.003567)\ \frac{\mathrm{V}}{^\circ\mathrm{C}}$	(50.46 ± 0.10) V

Table 4.11.: List of the breakdown voltage fit parameters for all examined SiPMs.

To conclude, the investigation of the IV-characteristics in the breakdown regime allows to determine the breakdown voltage with good precision. The results are consistent with current literature and alternative methods. Additionally, the fit of the breakdown curves yield values for the afterpulsing scaling factor that, too, are validated through comparisons with dedicated SiPM studies. The examination of IV-characteristics – especially with a focus on the breakdown voltage – provides a valuable tool to test large numbers of SiPMs for uniformity in a reasonable time scale for the upcoming nEXO experiment.

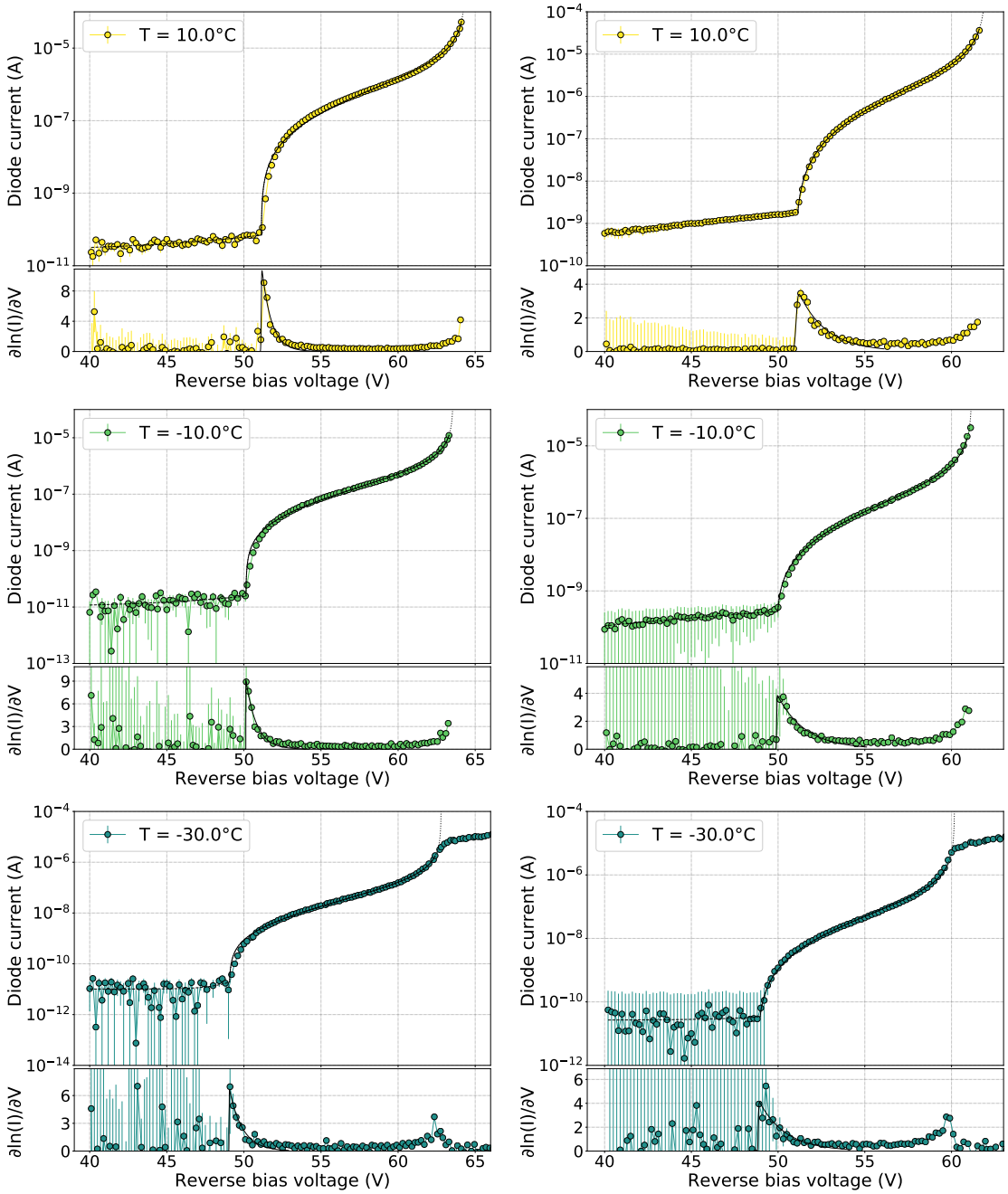

Figure 4.42.: Reverse IV-characteristics for a Hamamtsu VUV3 (left) and VUV4 (right) with direct readout at different temperatures. The pre- and post-breakdown fits are plotted with a dashed and solid line, respectively. The bottom plot shows the derivative of the logarithmic reverse current and a fit with an exponentially modified Gaussian function from which the breakdown voltage is obtained.

5. Conclusion

This work focused on the characterisation of VUV-sensitive SiPMs under cryogenic conditions. New investigations are reported contributing to the SiPM characterisation efforts within the nEXO collaboration. The first part of this thesis presents extended reflectivity studies with SiPMs and other samples in liquid xenon. The reflectivity has been examined at liquid xenon scintillation wavelengths in a specialised setup at the University of Münster. The second part deals with the investigation of IV-characteristics of SiPMs to gain knowledge of some basic SiPM parameters and establishes a method to use a SiPM as direct temperature sensor.

Chapter 3 focused on the reflectivity of VUV-sensitive SiPMs in liquid xenon. The phenomenology and the mathematical foundation of reflection processes are discussed. The reflectivity studies have been accomplished in a complex setup designed to investigate various reflection samples in vacuum or liquid xenon using a narrow spectrum in the VUV regime. The setup components and the measurement principle are explained in detail and a mathematical model to describe the angular reflection spectra is established. Several sources of systematic uncertainties are discussed and their effect on the measurements is calculated.
The angular reflectivity has been examined for a VUV-HD SiPM from FBK, a VUV4 SiPM from Hamamatsu and one of the APDs used in the EXO-200 experiment. A sample from the wafer material which is used by FBK as substrate to process SiPMs has also been investigated. This sample is suitable as plain and simple reflection mirror with which different reflection setups can be compared. The reflectivity has been measured to be between 24.9–36.0 % at the smallest angle of incidence of 20° achievable in the reflection setup. At an angle of incidence of 70°, the reflectivity increases to 46.7 % for the FBK, 60.0 % for the APD and 64.5 % for the wafer sample but drops to 21.5 % for the VUV4. The reflectivity is reduced at even higher angles due to an increasing fraction of the VUV beam missing the decreasing projected sample surface. The reflectivity curves for the FBK and wafer sample present a constant ratio as expected since the only difference is the SiPM micro-structure added to the wafer to process SiPMs. The VUV4 curve is unexpected but cross-checked by another group during the process of this thesis.
Oscillations in the angular spectra can be attributed to the micro-structure on the SiPM surface. A Fourier analysis of these oscillations successfully reconstructed the geometrical dimensions of the micro-structure derived from AFM images. Secondary

peaks on both sides of the specular peak are visible in VUV4 campaigns and are caused by the inclined surface of the micro-structure components. This effect increases the total reflectivity by roughly 10 %.
A beam profile after reflection has been examined for the wafer sample at an angle of incidence of 30°. The profile is found to be elliptical due to the focusing power of liquid xenon which results in a compression in the reflection plane. The refractive index of liquid xenon can be deduced from a complex mathematical fit to the beam profile yielding a value of 1.56671. This value is consistent with literature but significantly lower than most recent measurement for which however doubts have been raised by other groups.

Chapter 4 presented the use of IV-characteristics of SiPMs to obtain information about several basic properties of SiPMs as the quenching resistance or the saturation current in forward direction and the breakdown voltage and afterpulsing scaling factor in reverse direction. The setup is explained and two fit model are established for both voltage regimes. Three SiPM models are examined between +10 and −70 °C: a VUV3 and a VUV4 sample from Hamamatsu as well as an VUV-HD from FBK. The SiPM parameters obtained from the fits are plotted over temperature. The fit parameters reveal a good linear relationship and the expected exponential increase for the saturation current for most of the temperature range. The breakdown voltage is extracted from the reverse curves and is extrapolated to the temperature of liquid xenon which agrees well with other reports.
A method is established to use a SiPM as direct sensor for the temperature of its own pn-junction. IV-characteristics are evaluated at a fixed forward current and well-known temperature to obtain voltage calibration curves. These curves can then be used to derive the temperature in different studies when IV-characteristics are acquired and evaluated at the same forward current.

Zusammenfassung

Diese Arbeit beschäftigt sich mit der Charakterisierung VUV-sensitiver SiPMs unter kryogenen Bedingungen. Die neuartigen Studien tragen zu den Bemühungen der nEXO-Kollaboration bei, ein geeignetes Sensor-Model für den nEXO Photodetektor zu bestimmen. Der erste Teil dieser Arbeit dreht sich um die ausführlichen Studien zur Reflektivität von SiPMs und anderen Proben in flüssigem Xenon. Die Reflektivität wurde für Wellenlängen untersucht, bei welchen flüssiges Xenon szintilliert. Die Messungen fanden in einem speziellen experimentellen Apparat an der Universität Münster statt. Der zweite Teil stellt die Vermessung von Dioden-Kennlinien von SiPMs vor, um damit auf grundlegende Parameter von SiPMs Rückschlüsse zu ziehen. Zudem wurde eine Methode entwickelt, SiPMs anhand dieser Kennlinien als direkten Temperatur-Sensor zu betreiben.

Kapitel 3 behandelt das Reflexionsvermögen VUV-sensitiver SiPMs in flüssigem Xenon. Die Phänomenologie sowie die mathematischen Grundlagen zu Reflexionsprozessen werden anfangs diskutiert. Sämtliche Studien zur Reflexion fanden in einem komplexen Setup statt, welches zur Untersuchung des Reflexionsvermögens beliebiger Proben im Vakuum oder in flüssigem Xenon konzipiert wurde. Das Reflexionsvermögen wurde in einem schmalen Wellenlängenabschnitt im VUV-Regime untersucht. Die Komponenten des Versuchsaufbaus sind ebenso detailliert erläutert wie das mathematische Model, das zur Beschreibung der gewonnenen Winkelspektren entwickelt wurde. Mehrere Quellen systematischer Unsicherheiten sind aufgeführt und deren Auswirkung auf die Messungen berechnet.
Das Reflexionsvermögen in Abhängigkeit des Einfallswinkels wurde für einen VUV-HD SiPM von FBK, einen VUV4 von Hamamatsu und eine APD des EXO-200 Experiments vermessen. Außerdem wurde eine Probe des Wafers untersucht, aus welchem FBK ihre Sensoren fertigt, um eine plane, gut verstandene Probe zu etablieren, anhand derer verschiedene Versuchsaufbauten zur Reflexionsmessung miteinander verglichen werden können. Das Reflexionsvermögen der vermessenen Problem liegt zwischen 24.9–36.0 % bei dem kleinsten Einfallswinkel bei 20°, der mit dem Versuchsaufbau erzielt werden kann. Wird der Einfallswinkel auf 70° erhöht, steigt die Reflektivität des FBK SiPMs auf 46.7 %, die der APD auf 60.0 % und die der Wafer Probe auf 64.5 %, während die Reflektivität des VUV4 SiPMs auf 21.5 % abfällt. Wird der Einfallswinkel weiter erhöht, sinkt das Reflexionsvermögen für alle Proben stark ab, da ein wachsender Anteil des VUV Strahls die projizierte

Oberfläche der untersuchten Probe verpasst. Die Reflektivitätskurve des FBK SiPMs und der Wafer Probe zeigen ein konstantes Verhältnis auf. Dies entsprach der Erwartung, da der einzige Unterschiede beider Proben die Mikrostruktur auf der Oberfläche des SiPMs darstellt, welche einen Teil der Oberfläche einnimmt. Die abfallende Verlauf der Reflektivitätskurve des VUV4 SiPMs war dagegen unerwartet und wurde mittlerweile von einer weiteren Gruppe ebenso vermessen.
Oszillationen in den Winkelspektren können der Mikrostrukturen auf der SiPM Oberfläche zugeordnet werden. Die geometrischen Dimensionen dieser Strukturen wurde mit einer Fourier-Analyse der Oszillationen bestimmt und erfolgreich mit AFM Aufnahmen der SiPM Oberfläche verglichen. Winkelspektren des VUV4 SiPMs weisen deutliche, sekundäre Maxima zu beiden Seiten des spekularen Peaks auf, die schrägen Oberflächen der Mikrostruktur zugeschrieben werden können. Dieser Effekt erhöht das totale Reflexionsvermögen bei etwa 10 %.
Ein Profil des VUV-Strahls wurde bei einem Einfallswinkel von 30° auf die Wafer Probe untersucht. Das Profil weist eine elliptische Form auf, da der fokussierende Effekt von flüssigem Xenon zu einer Stauchung des Strahls in der Einfallsebene führt. Der Brechungsindex von flüssigem Xenon wurde über einen komplexen mathematischen Fit an das Strahlprofil zu einem Wert von 1.56671 bestimmt. Dieser Wert ist konsistent mit Literaturangaben, jedoch deutlich geringer als Ergebnisse jüngerer Messungen, welche allerdings von anderer Gruppen angezweifelt werden.

Kapitel 4 befasst sich mit der Vermessung von SiPMs mittels Dioden-Kennlinien. Anhand solcher Kennlinien können Rückschlüsse auf grundlegende Parameter der untersuchten SiPMs gezogen werden, wie z.B. des Quenching Widerstands oder des Sperrstroms in Vorwärts-Richtung und der Durchbruchspannung oder des Afterpulsing Skalierungsfaktors in Rückwärts-Richtung. Der Versuchsaufbau und die Fit-Modelle für beide Betriebsarten sind erläutert. Drei SiPM Modelle wurden zwischen +10 und −70 °C untersucht: ein VUV3 und ein VUV4 SiPM von Hamamatsu sowie ein VUV-HD von FBK. Die aus dem Fit erhaltenen SiPM Parameter hängen linear von der Temperatur ab, während der Sperrstrom eine exponentielle Abhängigkeit aufzeigt. Die Durchbruchspannung wurde aus der Ableitung des Stroms in Rückwärts-Richtung bestimmt und für die Temperatur von flüssigem Xenon extrapoliert. Die gefunden Werte sind konsistent zu anderen Studien mit den gleichen SiPM Modellen.
Des Weiteren wird eine Methode einwickelt, SiPMs als direkten Sensor für die Temperatur des eigenen pn-Übergangs zu nutzen. Dioden-Kennlinien werden bei einer festen Stromstärke in Vorwärts-Richtung und einer definierten Temperatur ausgewertet. Die daraus erstellten Kalibrationskurven gestatten die Bestimmung der Temperatur in anderen Versuchsaufbauten, wenn dort Kennlinien aufgenommen und bei derselben Stromstärke ausgewertet werden.

A. List of Figures

B. List of Tables

C. List of Abbreviations

$0\nu\beta\beta$	Neutrinoless double beta
$2\nu\beta\beta$	Neutrino-accompanied double beta
AFM	Atomic Force Microscopy
AP	Afterpulsing
AOI	Angle of Incidence
APD	Avalanche Photo-Diode
ASIC	Application-Specific Integrated Circuit
$\beta\beta$	Double beta decay
CAD	Computer Aided Design
CF	ConFlat (vacuum standard)
C.L.	Confidence Level
CSDA	Continuous Slowing Down Approximation
CT	Crosstalk
DAQ	Data Acquisition
DCR	Dark Count Rate
DM	Dark matter
DN	Dark noise
EC	Electron capture
EMG	Exponentially modified Gaussian
EXO	Enriched Xenon Observatory
FWHM	Full Width at Half Maximum
FS	Fused Silica
HFE	Hydrofluoroether
ISO-K	International Organization for Standardization - K (vacuum standard)
LAr	Liquid Argon
LN	Liquid Nitrogen
LXe	Liquid Xenon
KF	Klein Flange (vacuum standard)
m.w.e.	meters water equivalent

nEXO next Enriched Xenon Observatory
NME Nuclear Matrix Element
PDE Photon Detection Efficiency
p.e. Photoelectron equivalent
PMNS Pontecorvo–Maki–Nakagawa–Sakata
PMT Photomultiplier Tube
PTE Photon transport efficiency
PTFE Polytetrafluorethylen
QE Quantum Efficiency
QRPA Quasiparticle Random Phase Approximation
RHC Right Handed Current
ROI Region of Interest
RTD Resistance Temperature Detector
SiPM Silicon Photomultiplier
SM Standard Model of Particle Physics
SPAD Single-photon Avalanche Diode
UV Ultra-Violet
VUV Vacuum Ultra-Violet
WIMP Weak Interacting Massive Particle

Bibliography

[1] Aalbers J. et al. [DARWIN Collaboration]. DARWIN: towards the ultimate dark matter detector. *Journal of Cosmology and Astroparticle Physics*, **2016** (11):017, (2016). doi:10.1088/1475-7516/2016/11/017.

[2] Aalseth C. E. et al. [DarkSide Collaboration]. DarkSide-20k: A 20 tonne two-phase LAr TPC for direct dark matter detection at LNGS. *The European Physical Journal Plus*, **133**(3):131, (2018). doi:10.1140/epjp/i2018-11973-4.

[3] Aalseth C. E. et al. [Majorana Collaboration]. Search for Neutrinoless Double-β Decay in ^{76}Ge with the Majorana Demonstrator. *Physical Review Letters*, **120**(13):132502, (2018). doi:10.1103/PhysRevLett.120.132502.

[4] Abe K. et al. [XMASS Collaboration]. XMASS detector. *Nuclear Instruments and Methods A*, **716**:78, (2013). doi:10.1016/j.nima.2013.03.059.

[5] Acciarri R. et al. [DUNE Collaboration]. Long-Baseline Neutrino Facility (LBNF) and Deep Underground Neutrino Experiment (DUNE) – Conceptual Design Report Volume 4: The DUNE Detectors at LBNF. *arXiv:1601.02984*, (2016).

[6] Acerbi F. et al. Silicon Photomultipliers: Technology Optimizations for Ultraviolet, Visible and Near-Infrared Range. *Instruments*, **3**(1):15, (2019). doi:10.3390/instruments3010015.

[7] Ackerman N. et al. [EXO-200 Collaboration]. Observation of Two-Neutrino Double-Beta Decay in ^{136}Xe with the EXO-200 Detector. *Physical Review Letters*, **107**(21):212501, 2011. doi:10.1103/PhysRevLett.107.212501.

[8] Adams D. Q. et al. [CUORE Collaboration]. Improved Limit on Neutrinoless Double-Beta Decay in ^{130}Te with CUORE. *Physical Review Letters*, **124**(12): 122501, (2020). doi:10.1103/PhysRevLett.124.122501.

[9] Aghanim N. et al. [Planck Collaboration]. Planck 2018 results. VI. Cosmological parameters. *Astronomy & Astrophysics*, **641**(A6):67, (2020). doi:10.1051/0004-6361/201833910.

[10] Agostini F. et al. [DARWIN Collaboration]. Sensitivity of the DARWIN observatory to the neutrinoless double beta decay of ^{136}Xe. *The European Physical Journal C*, **80**(808):11, (2020). doi:10.1140/epjc/s10052-020-8196-z.

[11] Agostini M., Benato G. and Detwiler J. A. Discovery probability of next-generation neutrinoless double-β decay experiments. *Physical Review D*, **96**(5):053001, (2017). doi:10.1103/PhysRevD.96.053001.

[12] Agostini M. et al. [GERDA Collaboration]. Background-free search for neutrinoless double-β decay of ^{76}Ge with GERDA. *Nature*, **544**:47, (2017). doi:10.1038/nature21717.

[13] Agostini M. et al. [GERDA Collaboration]. Improved limit on neutrinoless double-β decay of ^{76}Ge from gerda phase ii. *Physical Review Letters*, **120** (13):132503, (2018). doi:10.1103/PhysRevLett.120.132503.

[14] Akerib D. S. et al. [LUX Collaboration]. The Large Underground Xenon (LUX) experiment. *Nuclear Instruments and Methods A*, **704**:111, (2013). doi:10.1016/j.nima.2012.11.135.

[15] Akil N. et al. A multimechanism model for photon generation by silicon junctions in avalanche breakdown. *IEEE Transactions on Electron Devices*, **46**(5):1022, (1999). doi:10.1109/16.760412.

[16] Akimov D. Yu. et al. [RED-100 Collaboration]. Status of the RED-100 experiment. *Journal of Instrumentation*, **12**(06):C06018, (2017). doi:10.1088/1748-0221/12/06/c06018.

[17] Alanssari M. et al. Single and Double Beta-Decay Q Values among the Triplet ^{96}Zr, ^{96}Nb and ^{96}Mo. *Physical Review Letters*, **116**(7):072501, (2016). doi:10.1103/PhysRevLett.116.072501.

[18] Albert J. B. et al. [EXO-200 Collaboration]. Improved measurement of the $2\nu\beta\beta$ half-life of ^{136}Xe with the EXO-200 detector. *Physical Review C*, **89** (1):015502, (2014). doi:10.1103/PhysRevC.89.015502.

[19] Albert J. B. et al. [EXO-200 Collaboration]. Search for Majorana neutrinos with the first two years of EXO-200 data. *Nature*, **510**:229, (2014). doi:10.1038/nature13432.

[20] Albert J. B. et al. [EXO-200 Collaboration]. Search for $2\nu\beta\beta$ decay of ^{136}Xe to the 0_1^+ excited state of ^{136}Xe with the EXO-200 liquid xenon detector. *Physical Review C*, **93**(3):035501, (2016). doi:10.1103/PhysRevC.93.035501.

[21] Albert J. B. et al. [EXO-200 Collaboration]. Cosmogenic backgrounds to $0\nu\beta\beta$ in EXO-200. *Journal of Cosmology and Astroparticle Physics*, **2016**: 029, (2016). doi:10.1088/1475-7516/2016/04/029.

[22] Albert J. B. et al. [EXO-200 Collaboration]. First search for Lorentz and CPT violation in double beta decay with EXO-200. *Physical Review D*, **93** (7):072001, (2016). doi:10.1103/PhysRevD.93.072001.

[23] Albert J. B. et al. [EXO-200 Collaboration]. Measurement of the drift velocity and transverse diffusion of electrons in liquid xenon with the EXO-200 detector. *Physical Review C*, **95**(2):025502, (2017). doi:10.1103/PhysRevC.95.025502.

[24] Albert J. B. et al. [EXO-200 Collaboration]. Searches for double beta decay of ^{134}Xe with EXO-200. *Physical Review D*, **96**(9):092001, (2017). doi:10.1103/PhysRevD.96.092001.

[25] Albert J. B. et al. [EXO-200 Collaboration]. Search for Neutrinoless Double-Beta Decay with the Upgraded EXO-200 Detector. *Physical Review Letters*, **120**(7):072701, (2018). doi:10.1103/PhysRevLett.120.072701.

[26] Albert J. B. et al. [EXO-200 Collaboration]. Search for nucleon decays with EXO-200. *Physical Review D*, **97**(7):072007, (2018). doi:10.1103/PhysRevD.97.072007.

[27] Albert J. B. et al. [nEXO Collaboration]. Sensitivity and discovery potential of the proposed nEXO experiment to neutrinoless double-β decay. *Physical Review C*, **97**(6):065503, (2018). doi:10.1103/PhysRevC.97.065503.

[28] Alduino C. et al. [CUORE Collaboration]. CUORE-0 detector: design, construction and operation. *Journal of Instrumentation*, **11**(07):P07009, (2016). doi:110.1088/1748-0221/11/07/p07009.

[29] Alduino C. et al. [CUORE Collaboration]. First Results from CUORE: A Search for Lepton Number Violation via $0\nu\beta\beta$ Decay of ^{130}Te. *Physical Review Letters*, **120**(13):132501, (2018). doi:10.1103/PhysRevLett.120.132501.

[30] Al Kharusi S. et al. [EXO-200 Collaboration]. Measurement of the Spectral Shape of the β-decay of ^{137}Xe to the Ground State of ^{137}Cs in EXO-200 and Comparison with Theory. *Physical Review Letters*, **124**(23):232502, (2020). doi:10.1103/PhysRevLett.124.232502.

[31] Al Kharusi S. et al. [EXO-200 Collaboration]. The EXO-200 detector, part II: Auxiliary systems. *unpublished*, (2020).

[32] Al Kharusi S. et al. [nEXO Collaboration]. nEXO Pre-Conceptual Design Report. *arXiv:1805.11142v2*, (2018).

[33] Althueser L. et al. VUV Transmission of PTFE for Xenon-based Particle Detectors. *Journal of Instrumentation*, **15**:P12021, (2020). doi:10.1088/1748-0221/15/12/P12021.

[34] Amaudruz P. et al. Pixelated Geiger-Mode Avalanche Photo-Diode Characterization Through Dark Current Measurement. *IEEE Transactions on Nuclear Science*, **61**(3):1369, (2014). doi:10.1109/TNS.2014.2319080.

[35] Andreotti E. et al. [CUORICINO Collaboration]. 130Te neutrinoless double-beta decay with CUORICINO. *Astroparticle Physics*, **34**(11):822, (2011). doi:10.1016/j.astropartphys.2011.02.002.

[36] Angle J. et al. [XENON Collaboration]. First Results from the XENON10 Dark Matter Experiment at the Gran Sasso National Laboratory. *Physical Review Letters*, **100**(2):021303, (2008). doi:10.1103/PhysRevLett.100.021303.

[37] Anton G. et al. [EXO-200 Collaboration]. Search for Neutrinoless Double-Beta Decay with the Complete EXO-200 Dataset. *Physical Review Letters*, **123**(16):161802, (2019). doi:10.1103/PhysRevLett.123.161802.

[38] Anton G. et al. [EXO-200 Collaboration]. Measurement of the scintillation and ionization response of liquid xenon at MeV energies in the EXO-200 experiment. *Physical Review C*, **101**(6):065501, (2020). URL 10.1103/PhysRevC.101.065501.

[39] Aprile E. and Doke T. Liquid xenon detectors for particle physics and astrophysics. *Review of Modern Physics*, **82**(3):2053, (2010). doi:10.1103/RevModPhys.82.2053.

[40] Aprile E. et. al. *Noble Gas Detectors*. Wiley-VCH, Weinheim, (2006). ISBN: 978-3-527-40597-8.

[41] Aprile E. et al. Measurement of the quantum efficiency of Hamamatsu R8520 photomultipliers at liquid xenon temperature. *Journal of Instrumentation*, **7**(10):P10005, (2012). doi:10.1088/1748-0221/7/10/p10005.

[42] Aprile E. et al. [XENON100 Collaboration]. The XENON100 dark matter experiment. *Astroparticle Physics*, **35**(9):573, (2012). doi:10.1016/j.astropartphys.2012.01.003.

[43] Aprile E. et al. [XENON Collaboration]. The XENON dark matter search experiment. *New Astronomy Reviews*, **49**(2):289, (2005). doi:10.1016/j.newar.2005.01.035.

[44] Aprile E. et al. [XENON Collaboration]. Physics reach of the XENON1T dark matter experiment. *Journal of Cosmology and Astroparticle Physics*, **2016**:027, (2016). doi:10.1088/1475-7516/2016/04/027.

[45] Aprile E. et al. [XENON Collaboration]. Observation of two-neutrino double electron capture in ^{124}Xe with XENON1T. *Nature*, **568**:532, (2019). doi:10.1038/s41586-019-1124-4.

[46] Argyriades J. et al. [NEMO-3 Collaboration]. Measurement of the two neutrino double beta decay half-life of Zr-96 with the NEMO-3 detector. *Nuclear Physics A*, **847**(3):168, (2010). doi:10.1016/j.nuclphysa.2010.07.009.

[47] Armengaud E. et al. [CUPID Interest Group]. CUPID pre-CDR. *arXiv:1907.09376v1*, (2019).

[48] Arnold R. et al. [NEMO-3 Collaboration]. Measurement of the $\beta\beta$ Decay Half-Life of ^{130}Te with the NEMO-3 Detector. *Physical Review Letters*, **107** (6):062504, (2011). doi:10.1103/PhysRevLett.107.062504.

[49] Arnold R. et al. [NEMO-3 Collaboration]. Results of the search for neutrinoless double-β decay in ^{100}Mo with the NEMO-3 experiment. *Physical Review D*, **92**(7):072011, (2015). doi:10.1103/PhysRevD.92.072011.

[50] Arnold R. et al. [NEMO-3 Collaboration]. Measurement of the double-beta decay half-life and search for the neutrinoless double-beta decay of ^{48}Ca with the NEMO-3 detector. *Physical Review D*, **93**(11):112008, (2016). doi:10.1103/PhysRevD.93.112008.

[51] Arnold R. et al. [NEMO-3 Collaboration]. Measurement of the $2\nu\beta\beta$ decay half-life of ^{150}Nd and a search for $0\nu\beta\beta$ decay processes with the full exposure from the NEMO-3 detector. *Physical Review D*, **94**(7):072003, (2016). doi:10.1103/PhysRevD.94.072003.

[52] Arnold R. et al. [NEMO-3 Collaboration]. Measurement of the $2\nu\beta\beta$ decay half-life and search for the $0\nu\beta\beta$ decay of ^{116}Cd with the NEMO-3 detector. *Physical Review D*, **95**(1):012007, (2017). doi:10.1103/PhysRevD.95.012007.

[53] Arnold R. et al. [NEMO-3 Collaboration]. Search for Neutrinoless Quadruple-β Decay of ^{150}Nd with the NEMO-3 Detector. *Physical Review Letters*, **119**(4):041801, (2017). doi:10.1103/PhysRevLett.119.041801.

[54] Arnold R. et al. [NEMO-3 Collaboration]. Final results on ^{82}Se double beta decay to the ground state of ^{82}Kr from the NEMO-3 experiment. *The European Physical Journal C*, **78**(10):821, (2018). doi:10.1140/epjc/s10052-018-6295-x.

[55] Asaf U. and Steinberger I. T. Photoconductivity and electron transport parameters in liquid' and solid xenon. *Physical Review B*, **10**(10):4464, (1974). doi:10.1103/PhysRevB.10.4464.

[56] Asakura K. et al. [KamLAND-Zen Collaboration]. Results from KamLAND-Zen. *AIP Conference Proceedings*, **1666**(1):170003, (2015). doi:10.1063/1.4915593.

[57] Aspnes D. E. and Studna A. A. Dielectric functions and optical parameters of Si, Ge, GaP, GaAs, GaSb, InP, InAs, and InSb from 1.5 to 6.0 eV. *Physical Review B*, **27**(2):985, (1983). doi:10.1103/PhysRevB.27.985.

[58] Auger M. et al. [EXO-200 Collaboration]. The EXO-200 detector, part I: Detector design and construction. *arXiv:1202.2192v2*, (2011).

[59] Auger M. et al. [EXO-200 Collaboration]. Search for Neutrinoless Double-Beta Decay in ^{136}Xe with EXO-200. *Physical Review Letters*, **109**(3):032505, (2012). doi:10.1103/PhysRevLett.109.032505.

[60] Aull B. F. et al. Geiger-Mode Avalanche Photodiodes for Three-Dimensional Imaging. *Lincoln Laboratory Journal*, **13**(2):335, (2002).

[61] Avignone F. T., Elliott S. R. and Engel J. Double beta decay, Majorana neutrinos, and neutrino mass. *Review of Modern Physics*, **80**(2):481, (2008). doi:10.1103/RevModPhys.80.481.

[62] Aziz R. A., Bowman D. H. and Lim C. C. Sound velocity in the inert gas liquids and the law of corresponding states. *Canadian Journal of Chemistry*, **45**(18):2079, (1967). doi:10.1139/v67-335.

[63] Azzolini O. et al. [CUPID-0 Collaboration]. First result on the neutrinoless double-β decay of ^{82}Se with cupid-0. *Physical Review Letters*, **120**(23):232502, (2018). doi:10.1103/PhysRevLett.120.232502.

[64] Baldini A. et al. Absorption of scintillation light in a 100l liquid xenon γ-ray detector and expected detector performance. *Nuclear Instruments and Methods in Physics Research A*, **545**(3):753, (2005). doi:10.1016/j.nima.2005.02.029.

[65] Baldini A. et al. [MEG II Collaboration]. The design of the MEG II experiment. *The European Physical Journal C*, **78**(5):380, (2018). doi:10.1140/epjc/s10052-018-5845-6.

[66] Barabash A. S. Average and recommended half-life values for two-neutrino double beta decay. *Nuclear Physics A*, **935**:52, (2015). doi:10.1016/j.nuclphysa.2015.01.001.

[67] Barabash A. S. et al. Results of the experiment on the search for double beta decay of ^{136}Xe, ^{134}Xe and ^{124}Xe. *Physics Letters B*, **223**(2):273, (1989). doi:10.1016/0370-2693(89)90252-9.

[68] Barabash A. S. et al. Final results of the aurora experiment to study 2β decay of ^{116}Cd with enriched $^{116}CdWO_4$ crystal scintillators. *Physical Review D*, **98**(9):092007, (2018). doi:10.1103/PhysRevD.98.092007.

[69] Barabash A. S. et al. [NEMO-3 Collaboration. Investigation of double-beta decay with the NEMO-3 detector. *Physics of Atomic Nuclei*, **74**(2):312, (2011). doi:10.1134/S1063778811020062.

[70] Barbarino V. *Photodiodes – World Activities in 2011*, chapter 9, page 458. IntechOpen, (2011). doi:10.5772/21521. Editor: J. W. Park, ISBN: 978-953-307-530-3.

[71] Barkov L. M. et al. Measurement of the refractive index of liquid xenon for intrinsic scintillation light. *Nuclear Instruments and Methods in Physics Research A*, **379**(3):482, (1996). doi:10.1016/0168-9002(99)00518-5.

[72] Beattie J. A. *Argon, Helium and the Rare Gases*, page 251. Interscience Publishers, (1961). Editor: G. A. Cook.

[73] Bellotti E. et al. A search for lepton number non-conservation in double beta decay of ^{136}Xe. *Physics Letters B*, 221(2):209, (1989). doi:10.1016/0370-2693(89)91500-1.

[74] Bethe H. A. and Bacher R. F. Nuclear Physics A. Stationary States of Nuclei. *Reviews of Modern Physics*, **8**(2):82, (1936). doi:10.1103/RevModPhys.8.82.

[75] Bilenky S. M. and Giunti C. Neutrinoless double-beta decay: A probe of physics beyond the Standard Model. *International Journal of Modern Physics A*, **30**(4-5):1530001, (2015). doi:10.1142/S0217751X1530001X.

[76] Bilenky S. M. and Pontecorvo B. Lepton mixing and neutrino oscillations. *Physics Reports*, **41**(4):225, (1978). doi:10.1016/0370-1573(78)90095-9.

[77] Bludau W., Onton A. and Heinke W. Temperature dependence of the band gap of silicon. *Journal of Applied Physics*, **45**(4):1846, (1974). doi:10.1063/1.1663501.

[78] Bohren C. F. and Albrecht B. A. *Atmospheric Thermodynamics*. Oxford University Press, New York, (1998). ISBN: 0-19-509904-4.

[79] Bokeloh K. *Calibration of hot and cold dark matter experiments: An angular-selective photoelectron source for the KATRIN experiment and an apparatus to determine the reflection properties of PTFE for vacuum UV light*. PhD thesis, Westfälische Wilhelms-Universität Münster, Germany, (2013).

[80] Bolotnikov A. and Ramsey B. The spectroscopic properties of high-pressure xenon. *Nuclear Instruments and Methods in Physics Research A*, **396**:360, (1997). doi:10.1016/S0168-9002(97)00784-5.

[81] Braem A. et al. Observation of the UV scintillation light from high energy electron showers in liquid xenon. *Nuclear Instruments and Methods in Physics Research A*, **320**(1-2):228, (1992). doi:10.1016/0168-9002(92)90780-8.

[82] Bressi G. et al. Infrared scintillation in liquid Ar and Xe. *Nuclear Instruments and Methods in Physics Research A*, **440**(1):254, (2000). doi:10.1016/S0168-9002(99)01021-9.

[83] Bressi G. et al. Infrared scintillation: a comparison between gaseous and liquid xenon. *Nuclear Instruments and Methods in Physics Research A*, **461**(1):378, (2001). doi:10.1016/S0168-9002(00)01249-3.

[84] Bude J., Sano N. and Yoshii A. Hot-carrier luminescence in Si. *Physical Review B*, **45**(11):5848, (1992). doi:10.1103/PhysRevB.45.5848.

[85] Butcher A. et al. A method for characterizing after-pulsing and dark noise of PMTs and SiPMs. *Nuclear Instruments and Methods in Physics Research A*, **875**:87, (2017). doi:10.1016/j.nima.2017.08.035.

[86] Buzhan P. et al. The Advanced Study of Silicon Photomultiplier. *Advanced Technology and Particle Physics*, **610**:717, (2002). doi:10.1142/9789812776464_0101.

[87] Buzhan P. et al. The cross-talk problem in SiPMs and their use as light sensors for imaging atmospheric Cherenkov telescopes. *Nuclear Instruments and Methods in Physics Research A*, **610**(1):131, (2009). doi:10.1016/j.nima.2009.05.150.

[88] CAEN. N1145, . URL https://www.caen.it/products/n1145/. Accessed: 14.01.2020.

[89] CAEN. N470, . URL http://www.tunl.duke.edu/documents/public/electronics/CAEN/caen_n470.pdf. Accessed: 14.01.2020.

[90] CAEN. N840, . URL https://www.caen.it/products/n840/. Accessed: 14.01.2020.

[91] CAEN. N979, . URL https://www.caen.it/products/n979/. Accessed: 14.01.2020.

[92] Chambers C. et al. [nEXO Collaboration]. Imaging individual Ba atoms in solid xenon for barium tagging in nEXO. *Nature*, **569**:203, (2019). doi:10.1038/s41586-019-1169-4.

[93] Chen H. H., Lim C. C. and Aziz R. A. The enthalpy of vaporization and internal energy of liquid argon, krypton, and xenon determined from vapor pressures. *J. Chem. Thermodynamics*, **7**:191, (1975). doi:10.1016/0021-9614(75)90268-2.

[94] Chen X. et al. Rayleigh scattering in fused silica samples for gravitational wave detectors. *Optics Communications*, **284**:4732, (2011). doi:10.1016/j.optcom.2011.06.014.

[95] Chepel V. and Araujo H. Liquid noble gas detectors for low energy particle physics. *Journal of Instrumentation*, **8**(04):R04001, (2013). doi:10.1088/1748-0221/8/04/r04001.

[96] Chepel V. Y. et al. Purification of liquid xenon and impurity monitoring for a PET detector. *Nuclear Instruments and Methods in Physics Research A*, **349**(2-3):500, (1994). doi:10.1016/0168-9002(94)91217-3.

[97] Chung C.-Y. et al. Temperature dependence of absorption cross-section of H_2O, HOD, and D_2O in the spectral region 140–193 nm. *Nuclear Instruments and Methods A*, **467-468**:1572, (2001). doi:10.1016/S0168-9002(01)00762-8.

[98] Chynoweth A. G. and McKay K. G. Photon Emission from Avalanche Breakdown in Silicon. *Physical Review*, **102**(2):369, (1956). doi:10.1103/PhysRev.102.369.

[99] Clayton G. F. and Benson J. L. Atomic Masses from Phosphorus through Manganese. *Physical Review*, **110**(3):712, (1958). doi:10.1103/PhysRev.110.712.

[100] Clusius K. Über Trennversuche der Xenonisotope durch Rektifikation; der Tripelpunktsdruck des Xenons [German]. *Zeitschrift für Physikalische Chemie B*, **50**:403, (1941).

[101] Clusius K. and Riccoboni L. Atomwärme, Schmelz- und Verdampfungswärme sowie Entropie des Xenons [German]. *Zeitschrift für Physikalische Chemie B*, **38**:81, (1938).

[102] Clusius K. and Weigand K. Die Schmelzkurven der Gase A, Kr, X, CH_4, CH_3D, CD_4, C_2H_4, C_2H_6,COS und PH_3 bis 100 Atm. Druck [German]. *Zeitschrift für Physikalische Chemie B*, **46**:1, (1940).

[103] Collazuol G. Low temperature and timing properties of SIPMs. In *LIGHT 2011*, (2011). Editors: E. Lorenz, R. Mirzoyan.

[104] Conti E. et al. [EXO-200 Collaboration]. Correlated fluctuations between luminescence and ionization in liquid xenon. *Physical Review B*, **68**(5):054201, (2003). doi:10.1103/PhysRevB.68.054201.

[105] Corless R. M. et al. On the LambertW function. *Advances in Computational Mathematics*, **5**(1):329, (1996). doi:10.1007/BF02124750.

[106] Corning Semiconductor Optics. HPFS Standard Grade 7980. URL http://valleydesign.com/Datasheets/Corning-Fused-Silica-7980.pdf. Accessed: 17.12.2019.

[107] Corsi F. et al. Modelling a silicon photomultiplier (SiPM) as a signal source for optimum front-end design. *Nuclear Instruments and Methods in Physics Research A*, **572**(1):416, (2007). doi:10.1016/j.nima.2006.10.219.

[108] Cova S. et al. Avalanche photodiodes and quenching circuits for single-photon detection. *Applied Optics*, **35**(12):1956, (1996). doi:10.1364/AO.35.001956.

[109] Cova S., Lacaita A. and Ripamonti G. Trapping phenomena in avalanche photodiodes on nanosecond scale. *IEEE Electron Device Letters*, **12**(12):685, (1991). doi:10.1109/55.116955.

[110] Crawford R. K. *Rare Gas Solids Vol. II*, chapter 11, page 663. Academic Press, London, (1977). Editors: M. L. Klein and J. A. Venables.

[111] Cui X. et al. [PandaX-II Collaboration]. Dark Matter Results from 54-Ton-Day Exposure of PandaX-II Experiment. *Physical Review Letters*, **119**(18):181302, (2017). doi:10.1103/PhysRevLett.119.181302.

[112] Danevich F. A. et al. Search for 2β decay of cadmium and tungsten isotopes: Final results of the Solotvina experiment. *Physical Review C*, **68**(3):035501, (2003). doi:10.1103/PhysRevC.68.035501.

[113] Davis C. G. et al. [EXO-200 Collaboration]. An optimal energy estimator to reduce correlated noise for the EXO-200 light readout. *Journal of Instrumentation*, **11**(07):P07015, (2016). doi:10.1088/1748-0221/11/07/p07015.

[114] de Kort K., Damink P. and Boots H. Spectrum emitted by hot electrons in p-i-n cold cathodes. *Physical Review B*, **48**(16):11912, (1993). doi:10.1103/PhysRevB.48.11912.

[115] Delaquis S. et al. [EXO-200 Collaboration]. Deep neural networks for energy and position reconstruction in EXO-200. *Journal of Instrumentation*, **13**(08):P08023, (2018). doi:10.1088/1748-0221/13/08/p08023.

[116] Dick K. et al. Leptogenesis with Dirac Neutrinos. *Physical Review Letters*, **84**(18):4039, (2000). doi:10.1103/PhysRevLett.84.4039.

[117] Dinu N., Nagai A. and Para A. Breakdown voltage and triggering probability of SiPM from IV curves at different temperatures. *Nuclear Instruments and Methods A*, **845**:64, (2017). doi:10.1016/j.nima.2016.05.110.

[118] Dobi A. et al. [EXO-200 Collaboration]. A xenon gas purity monitor for EXO. *Nuclear Instruments and Methods A*, **659**(1):215, (2011). doi:10.1016/j.nima.2011.09.017.

[119] Doke T. et al. Estimation of Fano Factors in Liquid Argon, Krypton, Xenon and Xenon-doped Liquid Argon. *Nuclear Instruments and Methods*, **134**(2): 353, (1976). doi:10.1016/0029-554X(76)90292-5.

[120] Doke T. et al. Absolute Scintillation Yields in Liquid Argon and Xenon for Various Particles. *Japanese Journal of Applied Physics*, **41**:1538, (2002). doi:10.1143/jjap.41.1538.

[121] Douysset G. et al. Determination of the ^{76}Ge Double Beta Decay Q Value. *Physical Review Letters*, **86**(19):4259, (2001). doi:10.1103/PhysRevLett.86.4259.

[122] Dueck A., Rodejohann W. and Zuber K. Neutrinoless double beta decay, the inverted hierarchy, and precision determination of θ_{12}. *Physical Review D*, **83**(11):113010, (2011). doi:10.1103/PhysRevD.83.113010.

[123] Du Y. and Retière F. After-pulsing and cross-talk in multi-pixel photon counters. *Nuclear Instruments and Methods in Physics Research A*, **596**(3): 396, (2008). doi:10.1016/j.nima.2008.08.130.

[124] Edmund Optics. Uncoated UV Fused Silica Double-Convex Lens #48-297. URL https://www.edmundoptics.com/p/25mm-dia-x-100mm-fl-uncoated-uv-double-convex-lens/8537/. Accessed: 13.12.2019.

[125] Eguchi K. et al. [KamLAND Collaboration]. First Results from KamLAND: Evidence for Reactor Antineutrino Disappearance. *Physical Review Letters*, **90**(2):021802, (2003). doi:10.1103/PhysRevLett.90.021802.

[126] Elliott S. R. et al. [LEGEND Collaboration]. LEGEND: The Large Enriched Germanium Experiment for Neutrinoless Double-Beta Decay. *Bulletins of the American Physical Society*, **64**(3), (2019).

[127] Engel J., Šimkovic F. and Vogel P. Chiral two-body currents and neutrinoless double-β decay in the quasiparticle random-phase approximation. *Physical Review C*, **89**(6):064308, (2014). doi:10.1103/PhysRevC.89.064308.

[128] Engelmann E., Popova E. and Vinogradov S. Spatially resolved dark count rate of SiPMs. *European Physical Journal C*, **78**(971), (2018). doi:10.1140/epjc/s10052-018-6454-0.

[129] ESTAR. Stopping Power and Range Tables for Electrons. URL https://physics.nist.gov/PhysRefData/Star/Text/ESTAR.html. Accessed: 25.07.2019.

[130] Fano U. Ionization Yield of Radiations. II. The Fluctuations of the Number of Ions. *Physical Review*, **72**(1):26, (1947). doi:10.1103/PhysRev.72.26.

[131] Firestone R. B. and Shirley V. S., editors. *Table of Isotopes*, volume 1. Wiley, New York, 8 edition, (1996). ISBN: 0-471-07730-5.

[132] Fischer V. et al. [SNO+ Collaboration]. Search for neutrinoless double-beta decay with SNO+. *arXiv:1809.05986v1*, (2018).

[133] Fluck E. and Heumann K. G. Periodensystem der Elemente, (2002). ISBN: 3-527-30716-8, With regard to the IUPAC recommendations until 2002.

[134] Fluke. Fluke 8845A/8846A 6.5 Digit Precision Multimeters. URL https://www.fluke.com/en-us/product/precision-measurement/bench-instruments/fluke-8845a-8846a. Accessed: 30.08.2019.

[135] Fonseca I. M. A. and Lobo L. Q. Thermodynamics of Liquid Mixtures of Xenon and Methyl Fluoride. *Fluid Phase Equilibria*, **47**:249, (1989). doi:10.1016/0378-3812(89)80178-5.

[136] Freeman M. P. and Halsey, Jr. G. D. The Solid Solution Krypton-Xenon from 90 to 120 K, The vapor pressures of Argon, Krypton and Xenon. *Journal of Physical Chemistry*, **60**(8):1119, (1956). doi:10.1021/j150542a022.

[137] Fukuda Y. et al. [Super-Kamiokande Collaboration]. Evidence for Oscillation of Atmospheric Neutrinos. *Physical Review Letters*, **81**(8):1562, (1998). doi:10.1103/PhysRevLett.81.1562.

[138] Gallego L. et al. Modeling crosstalk in silicon photomultipliers. *IJournal of Instrumentation*, **8**(5):P05010, (2013). doi:10.1088/1748-0221/8/05/p05010.

[139] Gallego Manzano L. et al. XEMIS2: A liquid xenon detector for small animal medical imaging. *Nuclear Instruments and Methods A*, **912**:329, (2018). doi:10.1016/j.nima.2017.12.022.

[140] Gallina G. et al. Characterization of SiPM Avalanche Triggering Probabilities. *IEEE Transactions on Electron Devices*, **66**(10):4228, (2019). doi:10.1109/TED.2019.2935690.

[141] Gallina G. et al. [nEXO Collaboration]. Characterization of the Hamamatsu VUV4 MPPCs for nEXO. *Nuclear Instruments and Methods*, **940**:371, (2019). doi:10.1016/j.nima.2019.05.096.

[142] Gando A. et al. [KamLAND-Zen Collaboration]. Search for Majorana Neutrinos Near the Inverted Mass Hierarchy Region with KamLAND-Zen. *Physical Review Letters*, **117**(8):082503, (2016). doi:10.1103/PhysRevLett.117.082503.

[143] Gando A. et al. [KamLAND-Zen Collaboration]. Precision Analysis of the ^{136}Xe Two-Neutrino $\beta\beta$ Spectrum in KamLAND-Zen and Its Impact on the Quenching of Nuclear Matrix Elements. *Physical Review Letters*, **122**(19): 192501, (2019). doi:10.1103/PhysRevLett.122.192501.

[144] Gautam D. K., Khokle W. S. and Garg K. B. Effect of absorption on photon emission from reverse-biased silicon p-n junctions. *Solid-State Electronics*, **31**(6):1119, (1988). doi:10.1016/0038-1101(88)90415-7.

[145] Gavrilko V. G. and Manzhelii V. G. Density of crystalline xenon. *Soviet Physics – Solid State*, **6**(7):1734, (1965).

[146] Ghassemi A., Sato K. and Kobayashi K. MPPC. *Hamamatsu Technical Note*, (2017). Cat. No KAPD9005E01.

[147] Gola A. et al. NUV-Sensitive Silicon Photomultiplier Technologies Developed at Fondazione Bruno Kessler. In *Sensors* ***2019***, 19(2), 308. doi:10.3390/s19020308.

[148] Gómez-Cadenas J. J. et al. Sense and sensitivity of double beta decay experiments. *Journal of Cosmology and Astroparticle Physics*, **06**, (2011). doi:10.1088/1475-7516/2011/06/007.

[149] Gómez-Cadenas J. J. et al. The search for neutrinoless double beta decay. *Rivista del Nuovo Cimento*, **35**:29, (2012). doi:doi: 10.1393/ncr/i2012-10074-9.

[150] Grace E. et al. Index of refraction, Rayleigh scattering length, and Sellmeier coefficients in solid and liquid argon and xenon. *Nuclear Instruments and Methods in Physics Research A*, **867**:204, (2017). doi:10.1016/j.nima.2017.06.031.

[151] Gruhn C. R. and Loveman R. A Review of the Physical Properties of Liquid Ionization Chamber Media. *IEEE Transactions on Nuclear Science*, **NS-26**(1):110, (1979). doi:10.1109/TNS.1979.4329620.

[152] Gupta R. P. et al. A new avalanche-plasma Si light emitter and its physical analysis. *Journal of Physics D*, **14**(3):L31, (1981). doi:10.1088%2F0022-3727%2F14%2F3%2F004.

[153] Gushchin E. M. et al. Electron emission from condensed nobel gases. *Soviet Phyiscs JETP*, **49**(5):856, (1979).

[154] Gushchin E. M., Kruglov A. A. and Obodovskii I. M. Electron dynamics in condensed argon and xenon. *Soviet Phyiscs JETP*, **55**(4):650, (1982).

[155] Gushchin E. M., Kruglov A. A. and Obodovskii I. M. Emission of hot electrons from liquid and solid argon and xenon. *Soviet Phyiscs JETP*, **55** (5):860, (1982).

[156] Habgood H. W. and Schneider W. G. PVT Measurements in the Critical Region of Xenon. *Can. J. Chem.*, **32**:98:164, (1954). doi:10.1139/v54-017.

[157] Haecker W. Infrared radiation from breakdown plasmas in Si, GaSb, and Ge: Evidence for direct free hole radiation. *Physica Status Solidi*, **25**(1):301, (1974). doi:10.1002/pssa.2210250129.

[158] Haitz R. H. Model for the Electrical Behavior of a Microplasma. *Journal of Applied Physics*, **35**(5):1370, (1964). doi:10.1063/1.1713636.

[159] Haitz R. H. Mechanisms Contributing to the Noise Pulse Rate of Avalanche Diodes. *Journal of Applied Physics*, **36**(10):3123, (1965). doi:10.1063/1.1702936.

[160] Hamamatsu. PMT R852–406. URL https://www.hamamatsu.com/eu/en/product/type/R8520-406/index.html. Accessed: 20.12.2019.

[161] Heastie R. and Lefebvre C. Phase Equilibria in Condensed Mixtures of Argon and Xenon. *Proceedings of the Physical Society*, **76**(2):180, (1960). doi:10.1088/0370-1328/76/2/302.

[162] Heath D. F. and Sacher P. A. Effects of a Simulated High-Energy Space Environment on the Ultraviolet Transmittance of Optical Materials between 1050 Å and 3000 Å. *Applied Optics*, **5**(6):937, (1966). doi:10.1364/AO.5.000937.

[163] Hilbrich S. et al. The influence of the doping level on the optical properties of porous silicon. *Thin Solid Films*, **276**(1):231, (1996). doi:10.1016/0040-6090(95)08060-0.

[164] Hitachi A. et al. Effect of ionization density on the time dependence of luminescence from liquid argon and xenon. *Physical Review B*, **27**(9):5279, (1983). doi:10.1103/PhysRevB.27.5279.

[165] Hitachi A. et al. New approach to the calculation of the refractive index of liquid and solid xenon. *Journal of Chemical Physics*, **123**(23):234508, (2005). doi:10.1063/1.2136879.

[166] Hollis Hallett A. C. *Argon, Helium and the Rare Gases*, page 313. Interscience Publishers, (1961). Editor: G. A. Cook.

[167] Honeywell. HEL-705-T-0-12-00. URL https://sensing.honeywell.com/HEL-705-T-0-12-00-rtd-sensors. Accessed: 30.08.2019.

[168] Horoi M. and Brown B. A. Shell-Model Analysis of the ^{136}Xe Double Beta Decay Nuclear Matrix Elements. *Physical Review Letters*, **110**(22):222502, (2013). doi:10.1103/PhysRevLett.110.222502.

[169] Hudson R. D. and Mahle S. H. Photodissociation rates of molecular oxygen in the mesosphere and lower thermosphere. *Journal of Geophysical Research*, **77**(16):2902, (1972). doi:10.1029/JA077i016p02902.

[170] Hwang S.-C. and Weltmer W. R. *Kirk-Othmer Encyclopedia of Chemical Technology*, page 1. Wiley, 4 edition, (1995).

doi:10.1002/0471238961.0701190508230114.a01. Editors: J. I. Kroschwitz, M. Howe-Grant.

[171] ISEG. SHQ 122M. URL https://iseg-hv.com/en/products/detail/SHQ. Accessed: 09.09.2019.

[172] ISHIDA N. et al. Attenuation length measurements of scintillation light in liquid rare gases and their mixtures using an improved reflection suppresser. *Nuclear Instruments and Methods in Physics Research A*, **384**(2-3):380, (1997). doi:10.1016/S0168-9002(96)00740-1.

[173] IWATA Y. et al. Large-Scale Shell-Model Analysis of the Neutrinoless ββ Decay of ^{48}Ca. *Physical Review Letters*, **116**(11):112502, (2016). doi:10.1103/PhysRevLett.116.112502.

[174] JAMIL A. et al. [nEXO collaboration]. VUV-Sensitive Silicon Photomultipliers for Xenon Scintillation Light Detection in nEXO. *IEEE Transactions on Nuclear Science*, **65**(11):2823, (2018). doi:10.1109/TNS.2018.2875668.

[175] JEWELL M. et al. [nEXO Collaboration]. Characterization of an Ionization Readout Tile for nEXO. *Journal of Instrumentation*, **13**(01):P01006, (2018). doi:10.1088/1748-0221/13/01/p01006.

[176] JORTNER J. et al. Localized Excitations in Condensed Ne, AI, Kr, and Xe. *Journal of Chemical Physics*, **42**(12):4250, (1965). doi:10.1063/1.1695927.

[177] KANNULUIK W. G. and CARMAN E. H. The Thermal Conductivity of Rare Gases. *Proceedings of the Physical Society B*, **65**:701, (1952). doi:10.1088/0370-1301/65/9/307.

[178] KEITHLEY. Keithley Series 6400 Picoammeters. URL https://www.tek.com/keithley-low-level-sensitive-and-specialty-instruments/keithley-series-6400-picoammeters. Accessed: 29.07.2020.

[179] KEMP R. C. et al. The Triple Point of Xenon as a Possible Defining Point on an International Temperature Scale. *Metrologia*, **21**:43, (1985). doi:10.1088/0026-1394/21/2/001.

[180] KEYES F. G. Thermal Conductivity of Gases. *Transactions of the ASME*, **77**:1395, (1955).

[181] KEYSIGHT. E3630 Series Bench Power Supply. URL https://www.keysight.com/de/de/products/dc-power-supplies/bench-

power-supplies/e3630-series-bench-power-supply-80-200w.html. Accessed: 30.08.2019.

[182] Klapdor-Kleingrothaus, H. V. et al. Latest results from the HEIDELBERG-MOSCOW double beta decay experiment. *The European Physical Journal A*, **12**(2):147, (2001). doi:10.1007/s100500170022.

[183] Klein M. L. and Venables J. A, editor. *Rare Gas Solids Vol I+II*. Academic Press, London, (1977). ISBN: 0-12-413502-1.

[184] Kolhinen V. S. et al. Double-β decay Q value of ^{150}Nd. *Physical Review C*, **82**(2):022501, (2010). doi:10.1103/PhysRevC.82.022501.

[185] Korpiun P. and Lüscher E. *Rare Gas Solids Vol. II*, chapter 12, page 729. Academic Press, London, (1977). M. L. Klein and J. A. Venables.

[186] Krupskii I. N. and Manzhely V. G. Multiphonon interactions and the Thermal Conductivity of Crystalline Argon, Krypton, and Xenon (translated from Russian). *Soviet Physics JETP*, **28**:1097, (1969).

[187] Kubota S. et al. Evidence for a triplet state of the self-trapped exciton states in liquid argon, krypton and xenon. *Journal of Physics C*, **11**(12):2645, (1978). doi:10.1088/0022-3719/11/12/024.

[188] Kubota S. et al. Recombination luminescence in liquid argon and in liquid xenon. *Physical Review B*, **17**(6):2762, (1978). doi:10.1103/PhysRevB.17.2762.

[189] Kubota S. et al. Dynamical behavior of free electrons in the recombination process in liquid argon, krypton, and xenon. *Physical Review B*, **20**(8):3486, (1979). doi:10.1103/PhysRevB.20.3486.

[190] Lacaita A. L. et al. On the bremsstrahlung origin of hot-carrier-induced photons in silicon devices. *IEEE Transactions on Electron Devices*, **40**(3): 577, (1993). doi:10.1109/16.199363.

[191] Lakeshore. Temperature Controller 336. URL https://shop.lakeshore.com/index.php/temperature-products/temperature-controllers.html. Accessed: 20.12.2019.

[192] Larruquert J. I. et al. Self-consistent optical constants of SiC thin films. *Journal of the Optical Society of America*, **28**(11):2340, (2011). doi:0.1364/JOSAA.28.002340.

[193] Leonard D. S. et al. [EXO-200 Collaboration]. Systematic study of trace radioactive impurities in candidate construction materials for EXO-200. *Nuclear Instruments and Methods A*, **591**:490, (2008). doi:10.1016/j.nima.2008.03.001.

[194] Leonard D. S. et al. [EXO-200 Collaboration]. Trace radioactive impurities in final construction materials for EXO-200. *Nuclear Instruments and Methods A*, **871**:169, (2017). doi:10.1016/j.nima.2017.04.049.

[195] Levy C. *Light propagation and Reflection off Teflon in Liquid Xenon Detectors for the XENON100 and XENON1T Dark Matter Experiment*. PhD thesis, Westfälische Wilhelms-Universität Münster, Germany, (2014).

[196] Leybold. RPK 1500 E, . URL http://www.wordentec.com/manuals/leybold/rpk.pdf. Accessed: 20.12.2019.

[197] Leybold. Scrollvac SC 5 D, . URL https://www.leyboldproducts.com/media/pdf/24/72/13/GA01423_002_C0_SCROLLVAC_EN.pdf. Accessed: 13.01.2020.

[198] Leybold. Leybold-TW300, . URL http://www.ptb-sales.com/manuals/leybold/tw300.pdf. Accessed: 20.12.2019.

[199] Lide D. R., editor. *CRC Handbook of Chemestry and Physics*. CRC press, Boca Raton, 85 edition, (2004). ISBN: 0-8493-0485-7.

[200] Li Z. et al. [nEXO Collaboration]. Simulation of charge readout with segmented tiles in nEXO. *Journal of Instrumentation*, **14**(9):P09020, (2019). doi:10.1088/1748-0221/14/09/p09020.

[201] Lovejoy D. R. Some Boiling and Triple Points below 0°C. *Nature*, **197**: 353, (1963). doi:10.1038/197353a0.

[202] Lv P. et al. [nEXO Collaboration]. Reflectance of Silicon Photomultipliers at Vacuum Ultraviolet Wavelengths. *IEEE Transactions on Nuclear Science*, **67**:2501, (2020). doi:10.1109/TNS.2020.3035172.

[203] Maderer L. Analyse des Crosstalks von Siliziumphotomultiplier [German]. Bachelor's thesis, University Erlangen-Nürnberg, Germany, (2017). URL https://ecap.nat.fau.de/index.php/research/publications/theses/.

[204] Maki Z., Nakagawa M. and Sakata S. Remarks on the Unified Model of Elementary Particles. *Progress of Theoretical Physics*, **28**(5):870, (1962). doi:10.1143/PTP.28.870.

[205] Martín-Albo J. et al. [NEXT Collaboration]. Sensitivity of NEXT-100 to neutrinoless double beta decay. *Journal of High Energy Physics*, **2016**(159), (2016). doi:J. High Energ. Phys.

[206] Mazur P. and Mandel M. On the Theory of the Refractive of non-polar Gases. *Physica*, **XXII**(1-5):299, (1956). doi:10.1016/S0031-8914(56)80041-4.

[207] McCowan P. M. and Barber R. C. Q value for the double-β decay of ^{136}Xe. *Physical Review C*, **82**(2):024603, 2010. doi:10.1103/PhysRevC.82.024603.

[208] McIntyre R. J. Theory of Microplasma Instability in Silicon. *Journal of Applied Physics*, **32**(6):983, (1961). doi:10.1063/1.1736199.

[209] McIntyre R. J. On the avalanche initiation probability of avalanche diodes above the breakdown voltage. *IEEE Transactions on Electron Devices*, **20** (7):637, (1973). doi:10.1109/T-ED.1973.17715.

[210] McKeen D. and Nirmal R. Monochromatic dark neutrinos and boosted dark matter in noble liquid direct detection. *Physical Review D*, **99**(10): 103003, (2019). doi:10.1103/PhysRevD.99.103003.

[211] McKinsey D. N. et al. [LZ Collaboration]. The LZ dark matter experiment. *Journal of Physics: Conference Series*, **718**:042039, 2016. doi:10.1088/1742-6596/718/4/042039.

[212] McPherson. McPherson Model 632 Deuterium lamp. URL `https://www.mcphersoninc.com/pdf/632.pdf`. Accessed: 13.12.2019.

[213] Meija J. et al. Atomic weights of the elements 2013 (IUPAC Technical Report). *Pure and Applied Chemistry*, **88**(3):265, (2016). doi:10.1515/pac-2015-0305.

[214] Meilhaus. RedLab 3104 USB Analog Output Module. URL `https://www.meilhaus.de/en/redlab-3000.htm`. Accessed: 30.08.2019.

[215] Michels A. and Prins C. The Melting Lines of Argon, Krypton and Xenon up to 1500 atm; Representation of the results by a law of Corresponding States. *Physica*, **28**(2):101, (1962). doi:10.1016/0031-8914(62)90096-4.

[216] Michels A. and Wassennar T. Vapour Pressure of Liquid Xenon. *Physica*, **XVI**(3):253, (1950). doi:10.1016/0031-8914(50)90023-1.

[217] Michels A. et al. Thermodynamic properties of xenon as a function of density up to 520 amagat and as a function of pressure up to 2800 atmospheres, at temperatures between 0 °C and 150 °C. *Physica*, **22**(1):17, (1956). doi:10.1016/S0031-8914(56)80005-0.

[218] Michels A., Wassennar T. and Louwerse P. Isotherms of xenon at temperatures between 0°C and 150°C and at densities up to 515 Amagats (pressures up to 2800 atmospheres). *Physica*, **20**(1):99, (1954). doi:10.1016/S0031-8914(54)80019-X.

[219] Mihara S. et. al. Development of a liquid-xenon photon detector — towards the search for a muon rare decay mode at Paul Scherrer Institute. *Cryogenics*, **44**(4):223, (2004). doi:10.1016/j.cryogenics.2003.12.002.

[220] Miller L. S., Howe S. and Spear W. E. Charge Transport in Solid and Liquid Ar, Kr, and Xe. *Physical Review*, **166**(3):871, (1968). doi:10.1103/PhysRev.166.871.

[221] Mirzoyan R., Kosyra R. and Moser H.-G. Light emission in Si avalanches. *Nuclear Instruments and Methods in Physics Research A*, **610**(1):98, (2009). doi:10.1016/j.nima.2009.05.081.

[222] Mong B. et al. [nEXO Collaboration]. Spectroscopy of Ba and Ba^+ deposits in solid xenon for barium tagging in nEXO. *Physical Review A*, **91**(2):022505, (2015). doi:10.1103/PhysRevA.91.022505.

[223] Morikawa E. et al. Argon, krypton, and xenon excimer luminescence: From the dilute gas to the condensed phase. *Journal of Chemical Physics*, **91**(3): 1469, (1989). doi:10.1063/1.457108.

[224] Naish P. J. and Hartwell S. Exponentially Modified Gaussian functions – A good model for chromatographic peaks in isocratic HPLC? *Chromatographia*, **26**(1):285, (1988). doi:10.1007/BF02268168.

[225] Nakarmi P. et al. [nEXO Collaboration]. Reflectivity and PDE of VUV4 Hamamatsu SiPMs in Liquid Xenon. *Journal of Instrumentation*, **15**(1): P01019, (2020). doi:10.1088/1748-0221/15/01/P01019.

[226] Neilson R. et al. Characterization of Large Area APDs for the EXO-200 Detector. *Nuclear Instruments and Methods A*, **608**:68, (2009). doi:10.1016/j.nima.2009.06.029.

[227] Newman R. Visible Light from a Silicon p-n Junction. *Physical Review*, **100**:700, (1955). doi:10.1103/PhysRev.100.700.

[228] Nicodemus F. E., Richmond J. C. and Hsia J. J. Geometrical Considerations and Nomenclature for Reflectance. *National Bureau of Standards monograph*, **160**:2, (1977).

[229] Nikzad S. and Hoenk M. E. High-performance silicon imagers, back illumination using delta and superlattice doping, and their applications in astrophysics, medicine, and other fields. *High Performance Silicon Imaging (Second edition)*, page 473, (2020). doi:10.1016/B978-0-08-102434-8.00015-5. ISBN: 978-0-08-102434-8.

[230] NIST. Standard Reference Data. URL https://webbook.nist.gov/cgi/cbook.cgi?ID=C7440633&Units=CAL&Mask=384. Accessed: 12.07.2019.

[231] Njoya O. et al. [nEXO Collaboration]. Measurements of electron transport in liquid and gas Xenon using a laser-driven photocathode. *Nuclear Instruments and Methods in Physics Research A*, **972**:163965, (2020). doi:10.1016/j.nima.2020.163965.

[232] Nxumalo J. N. et al. Energy available for the double beta decay of ^{82}Se. *Physics Letters B*, **302**:13, (1993).

[233] Obodovskii I. M. and Pokachalov S. G. Average ion pair formation energy in liquid and solid xenon [Russian]. *Soviet Journal for Low Temperature Physics*, **445**(8):829, (1979).

[234] Oldham W. G., Samuelson R. R. and Antognetti P. Triggering phenomena in avalanche diodes. *IEEE Transactions on Electron Devices*, **19** (9):1056, (1972). doi:10.1109/T-ED.1972.17544.

[235] Ootani W. et al. Development of deep-UV sensitive MPPC for liquid xenon scintillation detector. *Nuclear Instruments and Methods in Physics Research A*, **787**:220, (2015). doi:10.1016/j.nima.2014.12.007.

[236] Ostrovskiy I. and O'Sullivan K. Search for neutrinoless double beta decay. *Modern Physics Letters A*, **31**(18):1630017, (2016). doi:10.1142/S0217732316300172.

[237] Ostrovskiy I. et al. Characterization of Silicon Photomultipliers for nEXO. *IEEE Transactions on Nuclear Science*, **62**(4):1825, (2015). doi:10.1109/TNS.2015.2453932.

[238] Otono H. et al. On the basic mechanism of Pixelized Photon Detectors. *Nuclear Instruments and Methods in Physics Research A*, **610**(1):397, (2009). doi:10.1016/j.nima.2009.05.139.

[239] Otte A. N. et al. On the basic mechanism of Pixelized Photon Detectors. *Nuclear Instruments and Methods in Physics Research A*, **846**:106, (2017). doi:10.1016/j.nima.2016.09.053.

[240] Otte N. On the efficiency of photon emission during electrical breakdown in silicon. *Nuclear Instruments and Methods in Physics Research A*, **610**(1): 105, (2009). doi:10.1016/j.nima.2009.05.085.

[241] Otte N. et al. The potential of SiPM as photo detector in astropaticle physics experiments like MAGIC and EUSO. *Nuclear Physics B (Proc. Suppl.)*, **150**: 144, (2006). doi:10.1016/j.nuclphysbps.2004.10.084.

[242] Pagano R. et al. Optimized silicon photomultipliers with optical trenches. *Proceedings of the European Solid-State Device Research Conference*, page 183, (2011). doi:10.1109/ESSDERC.2011.6044204.

[243] Para A. et al. Afterpulsing in Silicon Photomultipliers: Impact on the Photodetectors Characterization. *arXiv:1503.01525*, (2015).

[244] Päs H. and Rodejohann W. Neutrinoless double beta decay. *New Journal of Physics*, **17**:115010, (2015). doi:10.1088/1367-2630/17/11/115010.

[245] Patterson H. S., Cripps R. S. and Whytlaw-Gray R. The critical constants and orthobaric densities of xenon. *Proceedings of the Royal Society A*, **86**:579, (1912). doi:10.1098/rspa.1912.0050.

[246] Pfeiffer Vacuum. Pfeiffer TMU 071. URL `http://www.nanophys.kth.se/nanophys/facilities/nfl/aja/manuals-pdf/PFEIFFER_TMU_071_TURBO_PUMP.pdf`. Accessed: 20.12.2019.

[247] Piemonte C. A new Silicon Photomultiplier structure for blue light detection. *Nuclear Instruments and Methods in Physics Research A*, **568**(1):224, (2006). doi:10.1016/j.nima.2006.07.018.

[248] Platzman R. L. Total Ionization in Gases by High-Energy Particles: An Appraisal of Our Understanding. *International Journal of Applied Radiation and Isotopes*, **10**(2-3):116, (1961). doi:10.1016/0020-708X(61)90108-9.

[249] Popova E. et al. Amplitude and timing properties of a Geiger discharge in a SiPM cell. *Nuclear Instruments and Methods in Physics Research A*, **787**: 270, (2015). doi:10.1016/j.nima.2014.12.050.

[250] Rahaman S. et al. Q values of the ^{76}Ge and ^{100}Mo double-beta decays. *Physics Letters B*, **662**(2):111, (2008). doi:10.1016/j.physletb.2008.02.047.

[251] Rahaman S. et al. Double-beta decay Q values of ^{116}Cd and ^{130}Te. *Physics Letters B*, **703**(4):412, (2011). doi:10.1016/j.physletb.2011.07.078.

[252] Rajkanan K., Singh R. and Shewchun J. Absorption coefficient of silicon for solar cell calculations. *Solid-State Electronics*, **22**(9):793, (1979). doi:10.1016/0038-1101(79)90128-X.

[253] Ramilli M. Characterization of SiPM: Temperature dependencies. *IEEE Nuclear Science Symposium Conference Record*, page 2467, (2008). doi:10.1109/NSSMIC.2008.4774854.

[254] Ramilli M. et al. *Silicon Photomultipliers: Characterization and Applications*, chapter 4, page 460. IntechOpen, (2012). Editor: S. Gateva.

[255] Ramson B. J. et al. [DUNE Collaboration]. The Photon Detection System (PDS) at ProtoDUNE. *APS April Meeting 2019*, **64**(3), (2019). URL http://meetings.aps.org/Meeting/APR19/Session/L17.4.

[256] Rauch C. Temperature dependent reverse bias IV-curve measurements of VUV sensitive SiPMs. Bachelor's thesis, University Erlangen-Nürnberg, Germany, (2019). URL https://ecap.nat.fau.de/index.php/research/publications/theses/.

[257] Rech I. et al. A New Approach to Optical Crosstalk Modeling in Single-Photon Avalanche Diodes. *IEEE Photonics Technology Letters*, **20**(5):330, (2008). doi:10.1109/LPT.2007.915654.

[258] Redshaw M. et al. Mass and Double-Beta-Decay Q Value of ^{136}Xe. *Physical Review Letters*, **98**(5):053003, (2007). doi:10.1103/PhysRevLett.98.053003.

[259] Renker D. Geiger-mode avalanche photodiodes, history, properties and problems. *Nuclear Instruments and Methods in Physics Research A*, **567**(1):48, (2006). doi:10.1016/j.nima.2006.05.060.

[260] Renker D. and Lorenz E. Advances in solid state photon detectors. *Journal of Instrumentation*, **4**(4):P04004, (2009). doi:10.1088/1748-0221/4/04/p04004.

[261] Robertson R. G. H. Empirical Survey of Neutrinoless Double Beta Decay Matrix Elements. *Modern Physics Letters A*, **28**(08):1350021, (2013). doi:10.1142/S0217732313500211.

[262] Rochester Institute of Technology. SiO_2 material optical properties. URL https://www.rit.edu/kgcoe/microsystems/lithography/thinfilms/cgi-bin/database.cgi?SiO2.csv. Accessed: 04.02.2020.

[263] Rodejohann W. Neutrinoless double-beta decay and neutrino physics. *Journal of Physics G*, **39**(12):124008, (2012). doi:10.1088/0954-3899/39/12/124008.

[264] Romo-Luque C. et al. [PETALO Collaboration]. PETALO: Time-of-Flight PET with liquid xenon. *Nuclear Instruments and Methods in Physics Research A*, **958**:162397, (2020). doi:10.1016/j.nima.2019.162397.

[265] Rosado J. Performance of SiPMs in the nonlinear region. *Nuclear Instruments and Methods in Physics Research A*, **912**:39, (2018). doi:10.1016/j.nima.2017.10.031.

[266] Rose D. J. Microplasmas in Silicon. *Physical Review*, **105**(2):413, (1957). doi:10.1103/PhysRev.105.413.

[267] SAES. MonoTorr PS3-MT3. URL https://www.entegris.com/shop/en/USD/products/gas-filtration-and-purification/gas-purifiers/GateKeeper-HGU-Heated-Getter-Gas-Purifiers/p/GateKeeperHGUHeatedGetterGasPurifiers. Accessed: 20.12.2019.

[268] Saveliev V. *Silicon Photomultiplier – New Era of Photon Detection*, chapter 14, page 364. IntechOpen, (2010). in: Advances in optical and photonic devices, Editor: K. Y. Kim.

[269] Schechter J. and Valle J. W. F. Neutrinoless double-β decay in SU(2)×U(1) theories. *Physical Review D*, **25**(11):2951, (1982). doi:10.1103/PhysRevD.25.2951.

[270] Schmidt S. Analyses of the Electron Motion and Recombination in the EXO-200 Experiment. Master's thesis, University Erlangen-Nürnberg, Germany, (2017). URL https://ecap.nat.fau.de/index.php/research/publications/theses/.

[271] Schmidt W. F. *The International Workshop on Technique and Application of Xenon Detectors*, chapter 1, page 1. World Scientific, (2001). Editors: Y. Suzuki at al.

[272] Schmitz N. *Neutrinophysik*. Teubner, Stuttgart, (1997). ISBN: 978-3-519-03236-6.

[273] Schonkeren J. M. *Photomultipliers, Part I*. Philips Gloeilampenfabrieken, Eindhoven, (1970).

[274] Schrobilgen G. J. *Encyclopedia of Physical Science and Technology*, page 449. Academic Press, 3 edition, (2003). doi:10.1016/B0-12-227410-5/00480-4. Editor: R. A. Meyers.

[275] Schwalbe L. A. et. al. Thermodynamic consistency of vapor pressure and calorimetric data for argon, krypton, and xenon. *Journal of Chemical Physics*, **66**:4493, (1977). doi:10.1063/1.433701.

[276] Seidel G. M., Lanou R. E. and Yao W. Rayleigh scattering in rare-gas liquids. *Nuclear Instruments and Methods in Physics Research A*, **489**(1-3): 189, (2002). doi:10.1016/S0168-9002(02)00890-2.

[277] Senitzky B. and Moll J. L. Breakdown in Silicon. *Physical Review*, **110** (3):612, (1958). doi:10.1103/PhysRev.110.612.

[278] SENSE Project. SENSE ROADMAP v1.3. URL `https://www.sense-pro.org/documents/roadmap`.

[279] Serra N. et al. Experimental and TCAD Study of Breakdown Voltage Temperature Behavior in n^+/p SiPMs. *IEEE Transactions on Nuclear Science*, **58**(3):1233, (2011). doi:10.1109/TNS.2011.2123919.

[280] Serra N. et al. Characterization of new FBK SiPM technology for visible light detection. *Journal of Instrumentation*, **8**(3):P03019, (2013). doi:10.1088%2F1748-0221%2F8%2F03%2Fp03019.

[281] Shockley W. The Theory of p-n Junctions in Semiconductors and p-n Junction Transistors. *Bell System Technical Journal*, **28**(3):435, (1949). doi:10.1002/j.1538-7305.1949.tb03645.x.

[282] Shutt T. et al. Thermodynamic Properties of Xenon from the Triple Point to 800 K with Pressures up to 350 MPa. *Journal of Physical and Chemical Reference Data*, **23**(63):63, (1994). doi:10.1063/1.555956.

[283] Shutt T. et al. Performance and Fundamental Processes at Low Energy in a Two-Phase LiquidXenon Dark MatterDetector. *Nuclear Physics B (Proc. Suppl.)*, **173**:160, (2007). doi:10.1016/j.nuclphysbps.2007.08.140.

[284] Smirnov A. Yu. Solar neutrinos: Oscillations or No-oscillations? *arXiv:1609.02386v2*, (2017).

[285] Smith N. J. T. The SNOLAB deep underground facility. *The European Physical Journal Plus*, **127**(9), (2012). doi:10.1140/epjp/i2012-12108-9.

[286] Solovov V. N. et al. Measurement of the refractive index and attenuation length of liquid xenon for its scintillation light. *Nuclear Instruments and Methods in Physics Research A*, **516**(2-3):462, (2004). doi:10.1016/j.nima.2003.08.117.

[287] Spinelli A. and Lacaita A. L. Physics and numerical simulation of single photon avalanche diodes. *IEEE Transactions on Electron Devices*, **44**(11): 1931, (1997). doi:10.1109/16.641363.

[288] Sprenger A. Aufbau und Charakterisierung eines Experiments für Reflektionsmessungen mit Vakuum-UV-Licht (German). Master's thesis, Westfälische Wilhelms-Universität Münster, Germany, (2011).

[289] Sprenger F. Set-up and test of the slow control and calibration of the photomultiplier of an apparatus to measure the reectivity of teflon in LXe at VUV wavelengths. Bachelor's thesis, Westfälische Wilhelms-Universität Münster, Germany, (2013).

[290] Streett W. B. and Sagan L. S. An experimental study of the equation of state of liquid xenon. *Journal of Chemical Thermodynamics*, **5**(5):633, (1973). doi:10.1016/S0021-9614(73)80004-7.

[291] Subtil J. L. et al. VUV Optical Constants of Liquid and Solid Xenon at the Triple Point. *Physica Status Solidi*, **143**(2):783, (1987). doi:10.1002/pssb.2221430239.

[292] Sun X. L. et al. [nEXO Collaboration]. Study of silicon photomultiplier performance in external electric fields. *Journal of Instrumentation*, **13**(09): T09006, (2018). doi:10.1088/1748-0221/13/09/t09006.

[293] Swagelok. Bellows seald Valve SS-8BG-TW-3C. URL `https://www.swagelok.de/en/catalog/Product/Detail?part=SS-8BG-TW-3C`. Accessed: 20.12.2019.

[294] Sze S. M. and Gibbons G. Avalanche Breakdown Voltages of Abrupt and linearly graded p-n Junctions in Ge, Si, GaAs, and GaP. *Applied Physics Letters*, **8**:111, (1966). doi:10.1063/1.1754511.

[295] Szydagis M. et al. NEST: a comprehensive model for scintillation yield in liquid xenon. *Journal of Instrumentation*, **6**(10):P10002, (2011). doi:10.1088/1748-0221/6/10/p10002.

[296] Takahashi T. et al. Average energy expended per ion pair in liquid xenon. *Physical Review A*, **12**(5):1771, (1975). doi:10.1103/PhysRevA.12.1771.

[297] Tanabashi M. et al. [Particle Data Group]. Review of Particle Physic. *Physical Review D*, **98**(3):030001, (2018). doi:10.1103/PhysRevD.98.030001. URL http://pdg.lbl.gov/2019/AtomicNuclearProperties/HTML/liquid_xenon_Xe.html.

[298] Testequity. TestEquity 1007C Temperature Chamber (Environmental Chamber). URL https://www.testequity.com/product/TestEquity-1007C-Temperature-Chamber-Environmental-Chamber-13039-1. Accessed: 30.08.2019.

[299] Tietze U., Schenk C. and Gamm E. *Halbleiter-Schaltungstechnik [German]*. Springer, Heidelberg, 13 edition, (2010). ISBN: 978-3-642-01621-9.

[300] Toriumi A. et al. A study of photon emission from n-channel MOSFET's. *IEEE Transactions on Electron Devices*, **34**(7):1501, (1987). doi:10.1109/T-ED.1987.23112.

[301] Trefny J. U. and Serin B. Specific Heat of Solid Xenon. *Journal of Low Temperature Physics*, **1**(3):231, (1969). doi:10.1007/BF00628411.

[302] Tretyak V. I. and Zdesenko Y. G. Tables of Double Beta Decay Data – An Update. *Atomic Data and Nuclear Data Tables*, **80**(1):83, (2002). doi:10.1006/adnd.2001.0873.

[303] Umehara S. et al. [CANDLES Collaboration]. Neutrino-less double-β decay of ^{48}Ca studied by caf$_2$(eu) scintillators. *Physical Review C*, **78**(5):058501, (2008). doi:10.1103/PhysRevC.78.058501.

[304] Vacheret A. et al. Characterization and simulation of the response of Multi-Pixel Photon Counters to low light levels. *Nuclear Instruments and Methods in Physics Research A*, **656**(1):69, (2011). doi:10.1016/j.nima.2011.07.022.

[305] Viehmann W. et al. Photomultiplier window materials under electron irradiation: fluorescence and phosphorescence. *Applied Optics*, **14**(9):2104, (1975). doi:10.1364/AO.14.002104.

[306] Villa S., Lacaita A. L. and Pacelli A. Photon emission from hot electrons in silicon. *Physical Review B*, **52**(15):10993, (1995). doi:10.1103/PhysRevB.52.10993.

[307] Vinogradov S. Analytical models of probability distribution and excess noise factor of solid state photomultiplier signals with crosstalk. *Nuclear Instruments and Methods in Physics Research A*, **695**:247, (2012). doi:10.1016/j.nima.2011.11.086.

[308] Vogel N. Temperature Measurement of Silicon Photomultipliers via Calibrated IV Characteristics. Bachelor's thesis, University Erlangen-Nürnberg, Germany, (2018). URL https://ecap.nat.fau.de/index.php/research/publications/theses/.

[309] Wong H. T. et al. New limit on neutrinoless double β decay in ^{136}Xe with a time projection chamber. *Physical Review Letters*, **67**(10):1218, (1991). doi:10.1103/PhysRevLett.67.1218.

[310] XCOM. NIST Photon Cross Section Data. URL https://physics.nist.gov/PhysRefData/Xcom/html/xcom1.html. Accessed: 29.07.2019.

[311] Zabrodskii V. et al. SiPM prototype for direct VUV registration. *Nuclear Instruments and Methods in Physics Research A*, **787**:348, (2015). doi:10.1016/j.nima.2015.01.070.

[312] Zhang Y. Corrected Values for Boiling Points and Enthalpies of Vaporization of Elements in Handbooks. *J. Chem. Eng. Data*, **2011**(56):328, (2011). doi:110.1021/je1011086.

[313] Ziegler T. Characterisation of Silicon Photomultipliers with Xenon Scintillation Light for the nEXO Experiment. Master's thesis, University Erlangen-Nürnberg, Germany, (2016). URL https://ecap.nat.fau.de/index.php/research/publications/theses/.

[314] Zollweg J. et. al. Surface Tension and Viscosity of Xenon Near Its Critical Point. *Physical Review Letters*, **27**:18:1182, (1971). doi:10.1103/PhysRevLett.27.1182.

[315] Zuber K. Consensus Report of a Workshop on "Matrix elements for Neutrinoless Double Beta Decay". *arXiv:nucl-ex/0511009*, (2005).

Acknowledgements

I would like to pass my thanks to the following persons, who helped me in many different ways in my life, in my academic carrier and throughout the process of this thesis:

- **Gisela Anton** for her academic supervision, excellent support and advice in various matters and for giving me the possibility to contribute to the research projects at her chair,
- **Thilo Michel** for his topical supervision, thorough and extensive advice and many great discussion topics around and beyond particle physics,
- **Christian Weinheimer** for the wonderful opportunity to perform reflectivity measurements at his group in Münster,
- **My parents** for their never-ending love, support and motivation,
- **Nici** for her self-sacrificing support, all-embracing love plus being my backbone for most of the final months,
- **Meinen Großeltern** für ihre Leichtigkeit, Weitsicht und immerwährende Unterstützung,
- **Thorsten Kühn**, **Alfred Kaluza** and **Hennry Schott** for their fantastic technical skills and assistance in every possible way,
- **Thomas Spona** and his colleagues from the mechanics workshop for their manufacturing skills – especially for all too often short-term orders,
- **Jutta Dziwis** and **Sabine Link** for their patience with my red tape shortcomings,
- **Tobias**, **Ako**, **Sebastian**, **Patrick**, **Dennis**, **Andreas**, **Judith**, **Johannes**, **Federico**, **Naomi** and **Franziska** for the enjoyable atmosphere in our offices and scientific discussions,
- **Alexander Fieguth**, **Michael Murrah**, **Denny Schulte**, **Lutz Althüser** and **Christian Huhmann** for their supportive help and guidance during the reflectivity measurements in Münster,

- The **nEXO collaboration** for the stimulating, cooperative research in cutting-edge science,
- **Fabrice Retière** for the opportunity to work at TRIUMF at the beginning of my PhD time,
- **Naomi Vogel** and **Constantin Rauch** for their fruitful Bachelor theses,
- **Benjamin Hacker** and **Martin Siebert** for their support with the AFM,
- **Simon Kurz**, **Robinson Perić** and **Sebastian Schmidt** for proof-reading,
- All my **great friends** for a fantastic time in Erlangen and beyond,
- Everyone from the **ECAP board**, the **Departmentsversammlung**, the **ESFZ**, the **Lange Nacht der Wissenschaften** and the **GPT** for providing the rewarding opportunity to contribute to university life beyond my research topics.